January 2016

Modeling and Fundamental Design Considerations for Portable, Wearable and Implantable Electronic Biosensors

Piyush Dak
Purdue University

Graduate School Form 30
(Revised 08/14)

PURDUE UNIVERSITY
GRADUATE SCHOOL
Thesis/Dissertation Acceptance

This is to certify that the thesis/dissertation prepared

By Piyush Dak

Entitled: Modeling and Fundamental Design Considerations for Portable, Wearable and Implantable Electronic Biosensors

For the degree of Doctor of Philosophy

Is approved by the final examining committee:

MUHAMMAD A. ALAM

MARK S. LUNDSTROM

ZHIHONG CHEN

RASHID BASHIR

To the best of my knowledge and as understood by the student in the Thesis/Dissertation Agreement, Publication Delay, and Certification/Disclaimer (Graduate School Form 32), this thesis/dissertation adheres to the provisions of Purdue University's "Policy on Integrity in Research" and the use of copyrighted material.

MUHAMMAD A. ALAM

Approved by Major Professor(s): _____

_____

Approved by: V. Balakrishnan 07/25/2016

Head of the Department Graduate Program Date

MODELING AND FUNDAMENTAL DESIGN CONSIDERATIONS FOR PORTABLE, WEARABLE AND IMPLANTABLE ELECTRONIC BIOSENSORS

A Dissertation

Submitted to the Faculty

of

Purdue University

by

Piyush Dak

In Partial Fulfillment of the

Requirements for the Degree

of

Doctor of Philosophy

August 2016

Purdue University

West Lafayette, Indiana

Dedicated to my parents

ACKNOWLEDGMENTS

First and foremost, I would like to express my sincere gratitude to my supervisor, Prof. Muhammad Ashraful Alam. He introduced me to biosensors, and provided guidance with his knowledge and vision. I developed many good problem solving skills from him, notably the ability to break a complex problem into smaller pieces, understand the smaller pieces first, and then integrate those to solve the complex problem. Also, I learned the need to present simulation results in a compact form to capture the essence of the problem and to guide experiments. Further, I have inherited his ability to draw connections between the problems in different research fields through mathematical formulations. I learned from him how to present my research in a crisp form to a broad range of audience. I admire his patience, and his willingness to work with students is unparalleled. As such, I consider myself very fortunate to have him as my thesis adviser.

Prof. Rashid Bashir has offered me much advice and insights on nanobiosensors and pH sensors, and I have had close collaborations with his group. I would like to thank him and his previous graduate students, Vikhram Swaminathan and Eric Salm. Prof. Mark S. Lundstrom evinced keen interest in my work and I acknowledge the encouragement and support he provided through various stages of my graduate life. I would particularly like to thank him for giving me an opportunity to be part of the Nano-engineered electronic device simulation (NEEDs) node, and to be his teaching assistant for edX course which gave me much insights into nano-transistors and compact modeling. Special thanks are also due to Prof. Zhihong Chen for serving in my doctoral advisory committee and providing valuable feedback.

In addition, I would also like to thank Prof. Sunkook Kim for the collaborative work on MoS_2 biosensors. I would also like to thank Prof. Babak Ziaie and his student Hongjie Jiang for helping me develop a better understanding about hydro-

gel based sensors. I gratefully acknowledge the funding agencies - National Science Foundation (NSF) and SRC through NEEDS (Nano-engineered electronic device simulation node), National Institute of Health (NIH) and Intel. I am thankful for the efficient assistance from administrative staff: Vicki Johnson and Matt Golden. They assisted me on countless occasions, and I am amazed by their dedication, energy, and cheerfulness.

I am indebted to many former and current members of Prof. Alam's research group. Special thanks to my past group-mates: Biswajit Ray, Ankit Jain, Sambit Palit, Sourabh Dongaonkar, Pradeep R. Nair, Jonghyun Go, Md. Masuduzzaman and Md. Abdul Wahab for discussion on research, and their advice. I would like to thank all my current group-mates: Raghu Vamsi Chavali, Aida Ebrahimi, Md. Ryyan Khan, Sang Hoon Shin, Xingshu Sun, Reza Asadpour, Xin Jin, Hai Jiang, Woojin Ahn; and office colleagues: Evan Witkoske, Xufeng Wang, Mohit Singh, and Orchi Hassan, for insightful discussions on many interesting research projects.

In addition, I would like to credit my friends at Purdue: Gautham Madenoor Ramapriya, Krishna Singhal, Kartavya Neema, Punyashloka Debashis, Kevin Mugo, Lidia Mrad, Nancy Hernandez and Jonathan Chavez Casillias, for making my stay at Purdue enjoyable; and my friends back home: Tanuj Gigras and Shreyansh Jain, for providing me constant motivation during my PhD.

Finally and most importantly, I would like to express my heartiest gratitude towards my parents: Shri. Jaiprakash and Smt. Kamla Dak, for their unconditional love and unparalleled support that made it possible for me to pursue PhD. I would also like to thank my siblings: Sandeep, Vivek and Pooja Dak for their love and encouragement throughout my life.

TABLE OF CONTENTS

Page

LIST OF TABLES x

LIST OF FIGURES xi

ABSTRACT xxiii

1 INTRODUCTION 1

1.1 Classical approaches to address response time, sensitivity and selectivity 4

1.2 Review of droplet based portable sensors 5

1.3 Review of continous monitoring devices 8

1.3.1 Wearable sensors 8

1.3.2 Implantable sensors 11

1.4 System integration 13

1.5 Outline of the thesis 15

1.6 List of associated publications 16

2 CHARACTERIZATION OF EVAPORATING DROPLETS 20

2.1 Introduction 20

2.2 Device structure and Principle of operation 22

2.3 Frequency dependence of droplet impedance for different droplet sizes 26

2.4 Dynamics of droplet evaporation 32

2.5 Time evolution of impedance/conductance 37

2.5.1 Solution Resistance decreases and Conductance increases as droplet evaporates 37

2.5.2 Double Layer Capacitance increases as droplet evaporates . 38

2.5.3 Geometry Capacitance decreases as droplet evaporates . . . 38

2.6 Application of the model to a droplet based sensor 39

2.6.1 Frequency-dependent time response of Biosensors 39

Page

2.6.2 Implications of parasitic impedance of the substrate, Z_{par} . . 44
2.7 Experimental verification 47
2.8 Limitations of the impedance model 50
2.9 Conclusions 50
3 DROPLET DESALTING FOR BIOLOGICAL APPLICATIONS 52
3.1 Introduction 52
3.2 Concept and Operational Principle 55
3.3 Theory of Electrostatic Desalting 56
3.3.1 Numerical Model 58
3.3.2 Analytical Model 59
3.3.3 Comparison between proposed theory and traditional theories 64
3.4 Design rules for droplet desalting 65
3.5 Experimental Demonstration of Desalting by Collaborators at UIUC 66
3.5.1 Imaging surface ionic changes during desalting 67
3.5.2 High-surface area electrodes for enhanced desalting 68
3.5.3 Determination of desalting capacity by ionic current measurement 69
3.6 Applications of desalting for biological applications 71
3.6.1 Improvement in sensitivity of charge-based sensor 71
3.6.2 Electrostatic denaturation of DNA 73
3.6.3 Protein separation 74
3.7 Conclusion 75
4 DROPLET HEATING FOR BIOLOGICAL APPLICATIONS 76
4.1 Introduction 76
4.2 Device Structure and Operational Principle 77
4.3 Theory of dielectric heating and Model System 78
4.3.1 Electrostatic Simulation Shows Localized Fields 79
4.3.2 Thermal Simulation Shows Localized Heating 82

Page

4.3.3 Maximum droplet temperature does not depend on droplet size 85
4.3.4 Droplet heats in milli-seconds 87
4.4 Model Validation 88
4.5 Applications of Dielectric-Heating demonstrated by collaborators at UIUC 90
4.5.1 Distinguishing single-base pair mismatch 91
4.5.2 Selective sensing of probe-target hybridization 92
4.6 Conclusion 93
5 FLEXIBLE DEVICES FOR WEARABLE SENSING 94
5.1 Introduction 94
5.2 Device Structure and Operational Principle 96
5.3 Experimental Work by Collaborators at Kyung Hee University . . . 97
5.3.1 Device Fabrication by Mechanical Exfoliation 97
5.3.2 MoS_2 does not require surface functionalization 98
5.3.3 Biomolecule Physiosorption 99
5.3.4 Demonstration of biomolecular detection using Human-IgG . 99
5.3.5 PSA Detection 101
5.4 Theoretical Analysis 103
5.4.1 Model 104
5.4.2 Device Characteristics 108
5.4.3 Determination of Surface Densities of Biomolecules 113
5.5 Device Improvement by reduction of interface traps 114
5.6 Conclusion 115
6 HYDROGEL BASED IMPLANTABLE BIOCHEMICAL SENSORS . . . 117
6.1 Introduction 118
6.2 Device and Operational Principle 121
6.3 Model System 122
6.3.1 Numerical Framework 122

Page

6.3.2 Analytical Framework 129
6.4 Results and Discussions 133
6.4.1 Role of Ionizable Group Density (N_f) 133
6.4.2 Role of dissociation constant (pK_a) of ionizable groups . . . 136
6.4.3 Effect of environment variables 139
6.5 Design strategy to improve dynamic range 141
6.6 Glucose Sensor 143
6.7 Mechanical Deformation of Hydrogel 145
6.8 Conclusions 148
7 COMPACT MODELING FOR SYSTEM INTEGRATION OF FET BASED SENSORS 150
7.1 Introduction 151
7.2 Model System 153
7.2.1 DC Compact Model 155
7.2.2 Transient Model 160
7.2.3 Small-signal Compact Model 162
7.2.4 Noise Compact Model 163
7.3 Results And Discussions 166
7.3.1 Sensitivity of pH sensor is independent of the device operating point 166
7.3.2 Noise due to Different Sources in ISFET 167
7.3.3 Point of minimum pH resolution occurs near on-set of inversion 170
7.3.4 Impact of MOSFET Scaling 171
7.3.5 Scaling considerations for Extended-Gate FET pH sensors . 173
7.4 Circuit Demonstration by Collaborators at Purdue 179
7.5 Conclusions 181
8 SUMMARY AND FUTURE WORK 182
8.1 Summary of the thesis and key contributions 182
8.1.1 Lab-on-a-chip droplet based portable biosensors 182

Page

8.1.2 Wearable Sensors 184
8.1.3 Implantable Sensors 185
8.1.4 System Integration 185
8.2 Future work 186
8.2.1 System integration of Sensors 186
8.2.2 Electroceuticals 187
8.2.3 Transient Electronics 189
8.3 Concluding Remarks 190
REFERENCES 192
A CODES 220
A.1 Droplet Characterization 220
A.2 Droplet Desalting 223
A.3 Droplet Heating 226
A.3.1 Sentaurus Code for Solving Electrical Equations 226
A.3.2 Matlab Code for Solving Thermal Equation 228
A.4 MoS_2 Code 233
A.5 Hydrogel Code 237
A.5.1 Numerical Model 237
A.5.2 Analytical Model 247
A.6 Compact Model for pH-FET Sensor 248
A.6.1 DC Model: 248
A.6.2 Transient Model: 250
VITA 253

LIST OF TABLES

Table		Page
2.1	Equivalence between electrostatics and molecular diffusion system	34
2.2	Table of physical constants	36
2.3	Table of geometry parameters	37
3.1	Numerical model for calculating ion profiles during desalting	59
3.2	Desalting capacities of various electrodes measured in bulk and micro-droplet	69
4.1	Numerical Equations for Electrostatic Simulation	81
4.2	Description of Symbols	82
4.3	Parameters for electrostatics simulation	82
4.4	Thermal Simulation Parameters	85
5.1	Numerical equations for MoS_2 sensor	105
5.2	Simulation parameters	106
5.3	List of Symbols for charge transport in MoS_2	106
5.4	Number of charged amino acids in human IgG, anti-PSA and PSA and their corresponding pK [221, 222]	108
5.5	Determination of protein sequence	109
5.6	List of symbols for protein charge calculation	109
6.1	List of fitting parameters for match of analytical expressions to numerical model	135
6.2	Description of Symbols	149
7.1	Noise Model for ISFET	165
7.2	Parameter values for noise simulation	171

LIST OF FIGURES

Figure Page

1.1 Convolution of electronics and biosensors for miniaturized heathcare devices. Figure for the chip on bottom center is adapted with permission from Nature Publishing Group [2]. Figure on top right adapted with permission from Nature Publishing Group [3]. 2

1.2 A droplet-based LoC platform must be integrated with highly sensitive and selective sensors. (a) General configuration of digital microfluidics platforms. Digital microfluidics offers a broad range of droplet operations (e.g., generation, transport, mixing, sensing, etc.). (b) In a closed microfluidic system, sensors analyze the droplets as they flow past the sensors; (c) In an open microfluidic system, the droplet is placed on the sensor surface, and no continuous flow is required. 6

1.3 An illustration of advantages of a continuous health-monitoring device (CMD): The sensor can be either be implanted into the patient's body or worn as part of clothing. The real-time health information is wirelessly transmitted to the clinician and the patient's family. Figure adapted from Patel *et al.* [42] under the terms of the Creative Commons Attribution License which permits unrestricted distribution. 9

2.1 (a) Model system for numerical/analytic modeling, (b) Top view and side view of a pinned elongated evaporating droplet sitting on a substrate with a set of electrodes forming anode and cathode (at $t = 4$ min and $t = 14$ min) [27]. The droplet volume and its parallel/perpendicular contact angles ($\theta_{||}$/ $\theta_{\perp}$) decrease as it evaporates, while the contact line remains pinned by design, (c) Equivalent circuit representation of the system. . 23

2.2 Evaporation dynamics of droplet: As the droplet evaporates, the contact angle (θ) decreases while the contact line remains pinned. The concentration of the chemical/biomolecules (ρ) increases as the volume (V) decreases with time (t) with number of chemical/biomolecules (N) remaining constant 24

2.3 (a) Initial and (b) final shape of a droplet sitting on a surface with three wettable strips surrounded by dry strips. 25

Figure Page

2.4 (a) Geometry capacitance (C_{geo}) as a function of contact angle (θ), (b) Geometry factor as a function of contact angle (θ), (c) Double layer capacitance (C_{dl}) as a contact angle (θ) for different applied bias (V_e) i.e red 0.08 V, green 0.12 V, blue 0.16 V and black 0.20 V (circles are from numerical simulation and lines are from analytic estimate), (d) Solution resistance (R_{sol}) as a function of contact angle (θ) for constant conductivity. 29

2.5 (a) Impedance of the droplet as a function of frequency. C_{dl} dominates at $f < f_{\text{low}}$, R_{sol} dominates for $f_{\text{low}} < f < f_{\text{high}}$ and C_{geo} dominates the impedance at very high frequency ($f > f_{\text{high}}$). Similar trend (2(b)) is visible in the admittance vs. frequency response. 31

2.6 (a) Experimentally observed parallel and perpendicular contact angle for a 3μ L droplet as a function of time for the patterned surface described in [27], (b) Simulation results for the contact angles for the simplified geometry. The model results are in qualitative agreement with the experimentally observed trend as shown in (a). 33

2.7 Evolution of droplet contact angle (θ) (right) and droplet volume (V) (left) as a function of time. The variation of droplet volume as a function of time can analytically be approximated as $V = V_0(1 - \frac{t}{\tau})^n$ [141] with $n = 3/2$ where V_0 is the initial volume of the droplet and τ the total evaporation time. Simulation Parameter: $(c_s - c_\infty)/c_s = 0.88$ 35

2.8 (a) Time dependence of solution resistance (left) and solution conductance (right) (b) Time evolution of double layer capacitance (left) and Geometry capacitance (right) for $n_0 = 10$ μM and $V_0 = 3$ μL. 38

2.9 Sensitivity as a function of evaporation time for (a) low frequency operation (b) intermediate frequency operation (c) high frequency operation (d) Evolution of cut-off frequencies as a function of time for $n_0 = 10$ μ M and $V_0 = 3$ μL. 40

2.10 Simulation of parasitic capacitance for two different substrates. Geometry used for the simulation for glass substrate (a) and SOI substrate (d). Variation of parasitic capacitance as a function of (b) , (e) electrode separation and (c), (f) electrode width for glass and SOI substrate respectively. . . 46

2.11 Experimental data for (a) magnitude and (b) phase of the parasitic impedance as a function of frequency. 47

2.12 Impedance Magnitude and Phase vs. Frequency (calibration curves) at $t = 2$ min for different DNA concentration (a),(b) 330 fM; (c),(d) 3.3 pM; and (e), (f) 33 pM. 48

Figure Page

2.13 Impedance Magnitude and Phase vs. Time for different DNA concentration: 330 fM (red), 3.3 pM (black) and 33 pM (blue). Lines and circles represent simulation and experiment respectively. 49

3.1 Schematics (a) and (b) of electronic desalting in microdroplets. (b) By absorbing salt ions in the EDLs of desalting electrodes, the bulk of the droplet can be depleted. (c) Micrograph of two pairs of on-chip desalting electrodes patterned around a transducer and encapsulated within a droplet. The transducer's salt-dependent response can be modulated using this construct. 55

3.2 Domain for (a) Numerical, (b) Analytical Simulation 58

3.3 Numerical calculation of potential (ψ), and positive (p) and negative ion profile (n) in a 300 pL droplet 6100 μm^2 electrode area) for 1 μM concentration at 2 different desalting biases (V_e), i.e., 0.4 V ((a), (b), (d)) and 1.0 V ((d), (e), (f)) 60

3.4 Numerical calculation of positive (p) and negative (n) ion profile in a 300 pL droplet 6100 μm^2 electrode area) for two different ionic concentrations, i.e., 1 μM ((a) and (b)), and 10 μ M ((c) and (d)) at 1 V desalting bias (V_e). 61

3.5 Numerical calculation of ion profile showing negative ion density in a 300 pL droplet 6100 μm^2 electrode area) at (a) 1 μM and (b) 10 μM background strength under 1 V desalting bias. 62

3.6 (a) Maximum surface excess ionic charge that may be absorbed into the EDL over an electrode (10^4 μm^2) from various solutions at non-Faradaic conditions, (b) Ion density at the center of the droplet is plotted as a function of salt concentration for different desalting bias. 63

3.7 Comparison between different theories: ionic charge absorption vs. desalting bias 65

3.8 (a) Ratio of the volume of droplet to the area of the electrode required for desalting the droplet by 50%, as a function of desalting voltage and ionic concentration. Desalting at 100 mM concentration under 1 V desalting bias requires an aspect ratio of 1 μm, (b) n_i/n_0 as a function of enhancement in area ($\eta = A_{fractal}/A_{Projected}$) due to high-surface electrodes for different ionic concentrations 66

3.9 (a1-a4) Images of desalting in a droplet ([NaCl] = 1.174mM) in 4-electrode configuration, using surface functionalized SNARF-5F dye. 67

Figure Page

3.10 Imaging of electrode surfaces. (a) Images of Platinum-black (HSA) microelectrodes patterned in test structures (circular electrodes as well as multi-electrode systems) through controlled electro-deposition process. (b) SEM image at high magnification (70,000X) shows a highly branched, dendritic nanostructure on the surface that leads to high surface area; Electrochemical characterization and performance testing of HSA electrodes. (c) EIS measurements show increased surface area available for desalting due to the nanostructures and subsequent improvement after cyclic voltammetry treatments that enable >100-fold available area increase. (d) Desalting current at 0.5 V and 1 V bias in nano-liter volume droplets show the increased ionic current flow due to the area enhancement of HSA electrodes over smooth electrodes. Inset shows the ratio of rough to smooth electrode transient at each time point. 70

3.11 (a) Dependence of sensitivity on the ionic concentration. Figure reproduced from Nair *et al.* with permission from [126]. Copyright (2008) American Chemical Society, (b) The ionic concentration as a function of desalting bias for a droplet with high surface area electrodes (100X area enhancement), (c) Sensitivity improvement with desalting bias 72

3.12 (a) Dependence of melting temperature (T_m) of the DNA oligomer on the sodium ion concentration ($[Na^+]$), (b) Bias dependence of $Na^+]$ in the droplet center (right) for a droplet with 30 μm radius and 30X electrode area enhancement, and T_m variation upon application of desalting bias. 73

3.13 Application of electrode bias pulls $[H^+]$ ions towards the electrode thereby depleting the droplet bulk of the $[H^+]$. (a) The pH gradient can potentially be used to separate prostate specific antigen (PSA) from Immunoglogin (IgG) protein. Labeled contours show the Isoelectric point (IP) for the two proteins. The proteins stabilize their position along their respective IP contour lines. (b) The pH in droplet bulk (left) and protein charge (right) as a function of desalting bias. 75

4.1 (a) Cross-section of device showing electrical schematic with an AC voltage applied between the device and the bulk silicon. (b) A top-view of $\sim$ 225pL droplet placed on a heating element. The heating element is 2 μm wide in a 20 μm $\times$ 20 μm release window. Scale bar, 100 μm. 78

4.2 Structure for electrostatic and thermal simulation. 79

4.3 Electric Field within the droplet for different applied biases. Right hand side figures are the zoomed version of left hand side figures near the core of the droplet. 80

Figure Page

4.4 Temperature within the droplet for different applied biases. Right hand side figures are the zoomed version of left hand side figures near the core of the droplet. 83

4.5 Temperature within the droplet at X=0 μm for 20, 30 and 36 V. 84

4.6 Temperature within the droplet at X=0 μm for different droplet radius. 86

4.7 Time dependence of temperature in the core of the droplet. Temperature saturates to the steady state value within ms. 87

4.8 Graphic depiction of the FRET construct calibration concept. The device on the right is not heated. The DNA molecules in the droplet remain in their double-stranded state. Due to high FRET efficiency, the observed fluorescence is low. The device on the left is heated, resulting in denaturation of the DNA molecules. This causes separation of the FRET acceptor and donor which increases the observed fluorescence. 88

4.9 (a) A melting curve from commercial real-time PCR machine shows an increase in fluorescence as the FRET construct denatures (b) Derivative of (a), the peak of which gives the melting temperature of the FRET construct. (c) On-chip fluorescence data through a voltage sweep from 0-40V_{rms}. (d) Derivative of plot (c) showing the melting voltage of the constructs. 89

4.10 Bias dependence of temperature in the core of the droplet 90

4.11 Derivative of fluorescence w.r.t. voltage for 3 DNA strands, the red and black curves correspond to DNA samples with fully-complementary strands and the blue curve corresponds to a hetroduplex with a single-base pair mismatch. The hetroduplex showed the peak at lower voltage, thereby indicating a base pair mismatch (because of lower melting temperature) 91

4.12 Probe sequence rehydrated with a complementary sequence, a noncomplementary sequence, or water. A distinct peak in the derivative of fluorescence implies a matching sequence. 92

5.1 Schematic of a MoS_2 biosensor configured as PSA detecting label-free immunoassay, illustrating PSA antibody functionalized MoS_2 surface (top) and subsequent binding of PSA antigen with antibody receptors. The MoS_2 nanosheet biosensor consists of a gate insulator of SiO_2(300 nm) and a drain-source metal contact of Ti/Au (15 nm / 300 nm) 97

Figure Page

5.2 The water contact angle measurement to confirm hydrophobic characteristic of different substrates: the water contact angle of MoS_2, Au, and SiO_2 substrate are 75.75, 75.72, and 23.1, respectively. The contact angle of MoS_2 surface, which is more hydrophobic than Si-based substrates, is very comparable to that of Au surface. This suggests that MoS_2 nanosheet is an efficient candidate for functionalizing antibody and protein due to its highly hydrophobic surface. 98

5.3 Adsorption of human IgG onto MoS_2 sensor surface: (a) Transfer characteristics under various concentration of the human IgG from 0 to 100 μg/mL at V_{ds} = 1 V. (b) Plots of off-current versus human IgG concentration show an increase of off-current with increasing concentration of the human-IgG and abrupt increase of off-current at specific concentration of 10 fg/mL for V_{gs} = -20 V and V_{ds} = 1 V. Arrows indicate appropriate axis (red: log-scale, blue: linear-scale). (c), (d) Output characteristics under human IgG conditions of 0 and 100 μg/mL from V_{gs} = -32 V to V_{gs} = 0 V in steps of 8 V, respectively. Following adsorption of human IgG on MoS_2 surface, the drain current exhibits 6-fold increase at a high drain voltage and saturation currents disappear due to the immobile charge of human IgG on the MoS_2 nanosheet. 100

5.4 MoS_2 nanosheet biosensor for PSA detection: (a) Transfer characteristics of MoS_2 transistor biosensor functionalized by anti-PSA (Ab) of 100 μg/mL under various PSA concentrations. "None" refers to device without any biomolecule attachment. (b) Change of the off-current vs. various PSA concentrations for an anti-PSA (Ab) modified n-type MoS_2 transistor at the condition of V_{gs} = - 40 V and V_{ds} = 1 V. Inset shows an AFM image of MoS_2 device with thickness of $\sim$70 nm, width of 12.48 μm and length of 11.64 μm. (c), (d) Output characteristics of MoS_2 nanosheet biosensor with functionalized anti-PSA concentration of 100 μg/mL and PSA concentration of 1 ng/mL from V_{gs} = -32 V to V_{gs} = 0 V in steps of 8 V, respectively. 103

5.5 Schematic of the device used for numerical simulation of device characteristics. 104

5.6 (a) Human IgG, anti-PSA, and (b) PSA charge as a function of pH. The isoelectric point (IP) of human IgG, anti-PSA and PSA are 8.12, 7.94 and 7.46, respectively. 107

Figure Page

5.7 Simulated MoS_2device characteristics for PSA detection: (a) Transfer characteristics at $V_{ds} = 1$ V; (b) Off-current at $V_{ds} = 1$ V and $V_{gs} = -40$ V as a function of PSA concentration; (c) Average Subthreshold swing (between -10 V and -20 V) as a function of the PSA concentrations; and (d) Output characteristics of MoS_2 sensor with and without PSA on a surface, which has been pre-functionalized with anti-PSA. On-current decreases due to negative charge of PSA. 110

5.8 Band diagram of the MoS_2 channel in different operation regimes (a) Off-current regime, (b) On-current regime 111

5.9 Comparison of sensitivity based on 4 different device parameters: The base value used is for a MoS_2 surface with anti-PSA bound on its surface. The off-current shows a considerably larger change upon PSA binding as compared to the subthreshold-swing , threshold voltage and on-current. 112

5.10 (a) The surface potential at top (ψ_{top}) surface as a function of gate bias for different biomolecule concentrations at$V_{ds} = 1$ V. (b). Variation of MoS_2 potential at top ($\Delta\psi_{top}$) for $V_g = -40$ V and $V_g = 40$ V as a function of biomolecule concentration. The change in ψ_{top} at high gate bias is negligible leading to a small change in on-current upon PSA binding. . 112

5.11 (a) Calibration curve for surface charge density due to anti-PSA/PSA binding as a function of PSA bulk concentration. (b) The fraction of anti-PSA molecules bound to PSA molecules as a function of PSA concentration. Symbols are values obtained from (a) and fit corresponds to expression $f \sim \zeta \log(\frac{\rho}{\rho_0} + 1)$. 114

5.12 Improving the sensitivity by interface passivation: (a) Variation of MoS_2 sensitivity as a function of interface trap densities at top surface of MoS_2 for different PSA concentration (with $D_{\text{it,bot}} = 8 \times 10^{11}$ $\text{eV}^{-1}\text{cm}^{-2}$)) b) Variation of MoS_2 sensitivity as a function of interface trap density at MoS_2-oxide interface (with $N_{\text{it,top}} = 4 \times 10^{10}$ $\text{eV}^{-1}\text{cm}^{-2}$) for different PSA concentration 115

6.1 Schematic of a Hydrogel based Wireless Implantable Biochemical Sensor System: The sensor (blue) is implanted into a human body. The sensor is composed of an LC resonator with a hydrogel sandwiched between a rigid porous membrane and a deformable membrane. The hydrogel is pendent with the ionizable groups (with density, N_f and dissociation constant, K_a) which are responsive to analyte (say, proton) molecules. As the analyte concentration changes, the pressure exerted by hydrogel on deformable membrane changes which can be wirelessly detected. 119

Figure Page

6.2 1D approximation for simulation of hydrogel sensor. The area of the sensor (y-z plane) is assumed to be much larger than the thickness (x-direction). 123

6.3 Equilibrium Solution of the Poisson Equation: a) Potential (ψ) and electric field (E), b) H^+ and OH^- ion concentration, c) The concentration of Na^+ and Cl^- ions, d) Ionizable group density, N_a and fixed charge density, ρ_F. The hydrogel thickness is 20 μm and porous layer thickness is 5 μm. Salt concentration, c_s =100 mM, pH=5. 127

6.4 Experimental validation of static pressure change as a function of pH for (a) cationic and (b) anionic hydrogel. Lines represent the numerical simulation results and circle/polygon represent experimental data obtained from Ref. [87] and [77], respectively. 128

6.5 Effect of drift term on S and τ: Numerically simulated pressure change (ΔP) upon increase in pH, with and without drift term included. . . . 132

6.6 Effect of slow diffusion in porous membrane: Numerically simulated pressure change upon increase in pH, with different diffusion coefficients for H^+ in porous membrane. 132

6.7 (a) Normalized change in pressure as a function of pH for two different ratios of anionic density (N_f) to salt concentrations (c_s). The sensitivity is maximum near the pK_a (i.e., apparent pK_a) of the anionic groups. (b) Change of dynamic range (ΔpH_{range}) and the difference between the apparent pK_a and real pK_a (ΔpK_a) as a function of the N_f/c_s ratio. As the ratio increases, the dynamic range of the sensor increases. Symbols are the numerical simulation results and the lines are guide to eye. . . . 133

6.8 (a) Change in pressure as a function of time for two different anionic densities upon pH step from 5 to 5.1 ($pK_a = 5$), (b) Fit of analytical expression for S vs. N_f (line) in Eq. (6.24) to numerical simulation (symbols). S increases with increases in N_f, (c) Fit of analytical expression, $N_f = k\tau$ (line) to the numerical simulation (symbols). τ degrades with increase in N_f, (d) Tradeoff between sensitivity and response time: As the sensitivity increases, the response time also increases. Symbols represent numerical simulation and line represents fit using Eq. (6.26). Hydrogel thickness is 20 μm, Porous membrane thickness is 5 μm. 135

Figure Page

6.9 (a) Change in pressure as a function of time for a pH change from $5 \rightarrow 5.1 \rightarrow 5$ for anionic groups with different pK_a values, (b) The change in response time (τ) and pressure change (ΔP) as a function of pK_a. While S is high for pK_a close to the desired pH range, τ is also high. Blue and red symbols represent numerical simulation result, and blue line represent fit using Eq. (6.25) . Red line is a guide to eye. Hydrogel thickness is 20 μm, Porous membrane thickness is 5 μm, N_f =100 mM. 137

6.10 (a)Change in pressure as a function of time for large changes in pH values (from $pH = 4 \rightarrow 5 \rightarrow 4$) for different choice of anionic groups (i.e., different $pK_a's$), (b) The rise (τ_{rise}) and (c) fall (τ_{fall}) time and (d) the change in pressure as a function of the pK_a. While the sensor is most sensitivity for pK_a close to the base pH value (i.e., $pH = 5$), the response time is also high. Further, the asymmetry (i.e., $\tau_{\text{rise}} \neq \tau_{\text{fall}}$) is high when pK_a is close to the desired pH range. The symbols show numerical simulation and smooth lines show the fit to the analytical expression (see Eq. (6.25)) for τ_{rise} and τ_{fall}. 138

6.11 Effect of salt concentration (c_s) on the sensor response: S decreases with increase in c_s for both (a) pK_a <pH and (c) pK_a >pH. (b),(d) τ decreases with increase in c_s for pK_a <pH, and increases with increase in c_s for pK_a >pH. 140

6.12 Effect of buffer ion concentration on the sensor response. While the sensitivity remains same, the response of the sensor becomes faster as the buffer concentration increases. Simulation conditions: pH is stepped from 9 to 6 for a cationic gel with N_f = 100 mM and pK_a =7.4 and buffer, $pK_{\text{buff}} = 4$ 141

6.13 (a) Comparison of sensitivity of mono-ionic gel (only one type of ionizable monomer) with poly-ionic gel (two different ionizable monomers) as a function of pH. pK_a and N_f for mono-ionic gel were chosen to be 5.0 and 100 mM respectively, and the pK_a's and N_f values for poly-ionic gel were pK_{a1}=4.3, pK_{a2}=5.7, N_{f1}=68 mM, N_{f2}=32 mM. (b) Normalized response of the sensor as a function of time. The response of the poly-ionic gel is faster than that of mono-ionic gel. 142

6.14 (a) ΔP as a function of glucose concentration (G). Experimental data obtained from Lei *et al.* [75]. (b) The pressure for two different glucose concentrations, i.e., 2 mM (black) and 4 mM (blue) as a function of pH-pK_a. The sensitivity is maximum close to the $pK_h \sim$ pH of the acidic groups. Parameters: N_f = 50 mM, c_s = 100 mM. 144

Figure Page

6.15 (a) Effect of the affinity constant ($1/K_g$) of acidic group with the glucose. A_1 (PBA), A_2 (A pyridinium Derivative) and A_3 (A diboronic acid) are three different acids (HA) with increasing association constants [251]. . 145

6.16 Mechanical deformation of hydrogel. The dashed line shows the displaced grid within the hydrogel. u is the displacement of the i^{th} grid point from its equilibrium position. 146

7.1 (a) Sketch of different MOSFETs used for pH sensing, (b) Operation of an pH-FET sensor: The (-OH) groups protonate/deprotonate to give a net surface charge density. This leads to a shift in threshold voltage of the device. 154

7.2 Sketch of pH-FET and depiction of different voltages 155

7.3 Compact model for (a) DC, (b) AC/Transient, and (c) Noise analysis of FET pH sensors. 156

7.4 DC Model Validation: Match of experimental data (symbols) with compact model: (a) I-V characteristics obtained from Martinoia *et al.* [264]. Parameters: $pK_a = -2$, $pK_b = 6$, $pK_n = 10$, $N_{OH} = 2 \times 10^{14}$ cm^{-2}, $N_{NH_2} = 4 \times 10^{14}$ cm^{-2}, (b) I-V characteristics obtained from Go *et al.* [11]. Parameters: $pK_a = 6$ $pK_b = 10$ $N_s = 8 \times 10^{14}$ cm^{-2} [133] 159

7.5 Comparison between the transient model and the dc model for a gate voltage sweep. Excellent agreement between the DC (solid lines) and transient model (Symbols) shows that MOSFET charge can be assumed negligible, especially for pH values farther away from point of zero charge (pH_{pzc}=2) 161

7.6 Small-signal model validation: Inverse capacitance vs. pH for different ionic concentration for a metal-oxide-electrolyte system. Exp. data (symbols) is obtained from Bousse *et al.* [133]. Solid lines: DC operating point, Dashed lines: Transient operating point 163

7.7 (a) Transfer characteristics of 130 nm process with L=10 μm and W=100 μm, (b) Transconductance (g_m) as a function of gate bias for 130 nm bulk CMOS with L=10 μm and W=100 μm 166

7.8 (a) Absolute change in surface potential as a function of pH, and (b) Sensitivity as a function of pH 167

7.9 Input Referred Electrolyte Thermal Noise Spectral density. Electrolyte noise decreases with increase in ionic concentration and increase in gate area 168

7.10 Input Referred Thermal Noise Spectral density for different drain biases 169

Figure Page

7.11 Input referred flicker noise spectral density. The sold lines show the results obtained from HSPICE simulation, while the dashed lines show the match to the simplified model (for thermal noise) and Δn-$\Delta\mu$ model (for flicker noise) 169

7.12 Input referred noise voltage as a function of gate bias. FET thermal noise dominates below subthreshold, while FET flicker noise dominates above threshold. Electrolyte thermal noise remains constant 170

7.13 pH resolution as a function of gate bias. Minimum pH resolution occurs near onset of inversion. Solid line and Symbol shows simulation using dc and transient operating point, respectively. 171

7.14 (a) Scaling dependence of the sensor noise: Total input referred noise voltage as a function of the gate bias for different channel lengths (b) FET flicker (at V_{lg} =1 V) , FET thermal (V_{lg} = 0 V) and electrolyte thermal noise as a function of channel length for fixed gate width (W=100 μm) 172

7.15 (a) Scaling dependence of the sensor noise: Total input referred noise voltage as a function of the gate bias for different channel widths, (b) FET flicker (at V_{lg} = 1 V) , FET thermal (V_{lg} = 0 V) and electrolyte thermal noise as a function of channel width for fixed channel length (L=10 μm). 172

7.16 (a) Sketch of Extended Gate ion-sensitive FET (Not to scale). The design is more reliable since the gate oxide is not directly exposed to the fluid. Labeled are area of the sensing layer (A_{sensor}), active device area (A_{ox}) and the interconnect area (A_{int}). The area of the parasitic capacitance is $A_{\text{par}} = A_{\text{int}} + A_{\text{sensor}}$. (b) Ion-Torrent extended gate pH sensor design. . 174

7.17 Matching of experimental data [273] with Eq. (7.41). When the sensor area is small, the parasitic capacitances degrade the device sensitivity. As the sensor area becomes large, irrespective of the parasitic capacitances the device sensitivity reaches its maximum value. 176

7.18 (a) HSPICE simulation of pH sensitivity for an EGFET as a function of Z for $A_{\text{int}} \gg A_{ox}$, (b) Sensitivity as a function of scaling factor, Z for two scenarios (i) For negligible A_{int}, S remains constant with Z. (ii) For $A_{\text{int}} \gg A_{ox}$, S scales with Z (shown in the inset) in $Z \ll$ 1regime and saturates to the ISFET response at $Z \gg 1$ 177

7.19 Comparison of (a) noise and (b) pH resolution of EGFET with ISFET. 178

7.20 Block diagram for the sensor interface 179

7.21 Timing diagram for the sensor interface 180

Figure Page

7.22 Simulated pulse width versus pH. 181

8.1 Illustration of an electroceutical implant: Neurons are stimulated using an implanted electrical device to treat an array of conditions. Adapted by permission from Macmillan Publishers Ltd: Nature [276], copyright (2013) 188

8.2 Illustration of transient electronic devices: (a) Devices include transitors, diodes, inductors, capacitors, and resistors, with interconnects, all on silk substrate, (b) Schematic illustration in 3D, (c) Images showing time sequence of dissolution in water. From Hwang *et al.* [278]. Reprinted with permission from AAAS. 190

ABSTRACT

Dak, Piyush PhD, Purdue University, August 2016. Modeling and Fundamental Design Considerations for Portable, Wearable and Implantable Electronic Biosensors. Major Professor: Muhammad Ashraful Alam.

Chronic diseases such as cancer, diabetes, acquired immune deficiency syndrome (AIDS), etc. are leading causes of mortality all over the world. Portable, wearable and implantable biosensors can go a long way in preventing these premature deaths by frequent or continuous self-monitoring of vital health parameters.

Integration of different laboratory operations, such as mixing, sorting, transport and sensing (conducted to perform biomedical testing) onto a chip will allow development of portable hand-held diagnostic devices. In addition, if these device are flexible and/or bio-compatible, then these could either be worn as part of clothing or implanted into body for continuous health monitoring.

While considerable work has been done to evaluate and enhance sensing performance of classical diagnostic devices, electrical sensing properties of miniaturized portable, wearable and implantable diagnostic devices remain poorly understood. Thus, the need of the hour is to come up with a predictive theoretical framework that can provide design guidelines to improve the sensing performance of these devices. Towards this goal, we explore the physics and interpret experiments: 1) to manipulate small droplets for lab-on-chip portable sensors, 2) to improve the sensing performance of transition-metal dichalcogenides based flexible wearable sensors, 3) to determine the performance trade-offs in hydrogel based implantable biochemical sensors, and 4) to develop compact models for system level integration of biosensors. The guidelines resulting from this framework can be used to design and optimize the performance of these next-generation sensors.

1. INTRODUCTION

Chronic diseases, such as cancer, diabetes, acquired immune deficiency syndrome (AIDS), etc. are leading causes of mortality all over the world. Nearly 36 million people die each year due to chronic diseases of which 80% of the deaths occur in the developing countries [1]. Portable, Wearable and Implantable Biosensors can go a long way in preventing these premature deaths by frequent or continuous self-monitoring of vital health parameters.

While the primary concern for semiconductor industry has been building faster logic-switches, high-gain amplifiers and high capacity storage elements (see Fig. 1.1), the key concern for biosensor industry is to build sensors with high sensitivity, high specificity and lower response time. *Sensitivity* refers to the minimum amount of analyte (biomolecule or chemical molecule) that can be detected using the sensor. *Specificity* refers to the ability of the sensor to distinguish between the analyte and any parasitic molecule present in the sensing solution. *Response time* refers to the time it takes for the analyte to cause a distinguishable change in the sensor signal. Miniaturization of transistor has made it possible to embed different components such as processor, memory, etc. into a chip enabling portable electronic devices, such as iPhone. It has also enabled integration of many sensors such as pressure sensor, temperature sensor, gyroscope, etc. into hand-held devices, such as smart watch. However, integration of chemical/biosensors into these devices is still at a very early stage. Even today, the dominant model of medical diagnostics involves collection of blood samples into test tubes, which are sent to centralized laboratories to perform specialized tests for detection of disease markers. As such, patients have to do frequent hospital visits making their treatment slow, stressful and expensive, particularly for chronic diseases such as diabetics or cancer.

The need of the hour is to be able to integrate different laboratory operations, conducted to perform biomedical sensing such as sample preparation, mixing, dilution, heating, sensing, etc. into a chip. This will allow medical diagnostics to be performed at point-of-care, i.e., at a physician's office, in an ambulance, in the home, the field or in the hospital. Point-of-care testing would enable automated test operations by untrained personnel, and the results would be easily interpreted by the end users.

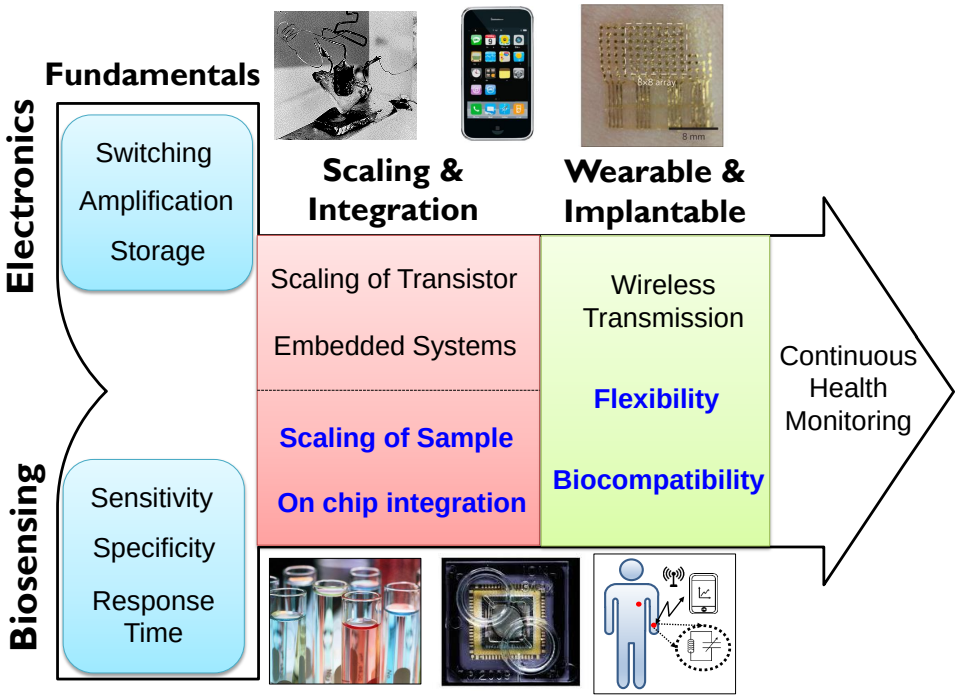

Fig. 1.1.: Convolution of electronics and biosensors for miniaturized heathcare devices. Figure for the chip on bottom center is adapted with permission from Nature Publishing Group [2]. Figure on top right adapted with permission from Nature Publishing Group [3].

Advantages of droplet based technologies: In this regard, droplet based lab-on-chip technologies have attracted significant attention due to their ability to perform a complete set of biomedical protocols to achieve cost-effective, high-throughput, sensitive, point-of-care diagnostics. The small volume of analyte brings many benefits like reduced footprint, smaller volumes of required reagents, faster analysis and

response time, faster and power efficient thermal cycling and improved reliability through redundant sensor design.

Advantages of wearable and implantable sensors: In addition to portable lab-on-chip sensors for rapid testing, another recent trend over the past decade for biosensors is the development of wearable and implantable sensors to enable continuous monitoring of vital health parameters. This could allow round the clock (24 hours) monitoring of the patient's heath enabling the patient to follow a normal life. Wearable sensors involve non-invasive monitoring of health parameters by either embedding the sensor into the fabric of the clothes or wearing an independent device (for example, a smart watch). This involves monitoring of the electrical signals of the body or determining the concentration of a biomolecule (for example, glucose) in a body fluid. The advantages are obvious: the device could be worn whenever required, and could be replaced conveniently. However, wearable sensors often suffer from low signal due to measurement of vital parameters in body fluids such as tear and sweat which have significantly less concentration of analyte in comparison to the blood. For example, the concentration of glucose in tear fluid (0.1-0.6 mM) is 10-20 times smaller than in blood (3.3 - 6.5 mM) [4]. On the other hand, implantable sensors involve invasive monitoring by placing the sensor under skin, or at specialized location in body, such as tumor site. However, since the measurement is done with sensor in direct contact with blood, these devices have the advantage of better signal as compared to wearable sensors.

Organization of the chapter: In this chapter[1], we review the recent trends in portable, wearable and implantable sensors in the literature. In Section 1.1, we discuss the approaches to address response time, selectivity and selectivity in classical sensors. In Section 1.2, we discuss state of art droplet-based sensing technologies for portable sensing devices. We review some recent efforts on the development of biosensors, compatible with both 'open' and 'closed' digital microfluidic systems. In Section 1.3, we discuss the progress in wearable and implantable sensing devices for

[1] Parts of this chapter are adapted from Ref. [5] with permission from Multidisciplinary Digital Publishing Institute (MDPI).

continuous monitoring of health parameters. In Section 1.4, we review some recent efforts towards system integration of MOSFET based sensors. In Section 1.5, we define our approach and outline for the thesis. Finally, we conclude with Section 1.6 with a list of journal and conference publications resulting from the work.

1.1 Classical approaches to address response time, sensitivity and selectivity

Approaches to overcome diffusion limited time-response: For a classical system, regardless of the detection mechanism, the response time is limited by the physical diffusion of molecules towards the sensor surface [6]. Approaches to overcome these limitations have involved either signal-amplification by increasing the number of biomarkers through amplification schemes such as Polymerase Chain Reaction (PCR) or Circular Strand-Replacement Polymerization (CSRP) [2, 7] or by decreasing the effective distance between the target and probe as in biobarcode assay [8, 9].

Approaches to mitigate screening limted response: Another concern with classical sensors is the screening limited response of potentiometric biosensors [10–13]. Since the target molecules conjugate with the probe molecules (usually immobilized on the sensor surface) only in salt-based electrolyte solutions, screening by these ions fundamentally limits the sensitivity of charge-based (potentiometric) biosensors. Various approaches have been adopted to mitigate this fundamental screening-limited sensitivity of potentiometric sensors in bulk based systems. Commonly used techniques include detection in low-ionic strength electrolyte, either by performing binding-sensing steps at low ionic strength [14] or using a flow-through apparatus that performs the binding and the sensing steps at different ionic strengths [15]. Both the approaches, however, reduce the binding affinity of the target molecule to the probe attached to the sensor, which may degrade selectivity, namely, the ability of a sensor to differentiate between target vs. parasitic molecules. Other approaches include detection of

biomolecular dipoles using high-frequency measurement [16] or engineering antibody capture fragments to bind the analytes close to the sensor surface [17].

Approaches to improve selectivity: Finally, the third important concern with biosensors is selectivity. In order to improve sensor selectively, three approaches have traditionally been used. *First*, and perhaps the most popular, is the use of amperometric sensors to detect analytes. These sensors monitor the current associated with oxidation or reduction of electroactive species involved in the recognition process. Since the electroactive species is specific to the target biomolecule, amperometric sensors have a very high specificity. The *second* approach relies on sample purification to capture the analytes of interest and release them in the sensing solution. For example, Stern *et al.* [18] developed a micropurification chip that captures the cancer biomarkers (antigens) from blood and, after washing, releases the antigens into a pure buffer solution to be detected by a silicon nanoribbon sensor. Finally, the third approach focuses on reducing non-specific binding by covering the gaps among receptors by small molecules, see Nair *et al.* [19] for a quantitative analysis.

To summarize, this section described several methodologies adopted to improve response-time, selectivity and sensitivity for classical sensors. We will see later through the research efforts in this thesis, how these concerns could be addressed in a droplet-based lab-on-chip platform.

1.2 Review of droplet based portable sensors

Advantages of Digital-microfluidics (DMF): Over the past two decades, there have been numerous reports of microfluidic systems integrated onto a lab-on-chip (LoC) platform [20–23]. Among them, DMFs offers a comprehensive set of fluidic operations, such as dispersing, transport, mixing, merging and splitting by programmable activation of a series of actuation electrodes [20, 24, 25], as shown in Fig. 1.2(a). DMF retains the advantages of traditional, continuous-flow microfluidic systems, namely, small sample volume, low reagent consumption and waste produc-

tion, rapid analysis and portability. Moreover, compared to other techniques, DMF systems operate at lower power, and are amenable to parallel processing and data acquisition for high throughput screening [25–32]. Being highly reconfigurable, DMF-based systems also satisfy the needs of various biochemical applications, e.g., chemical and enzymatic reactions, immunoassays, proteomics, DNA detection, single-cell studies, and so on [24, 28, 29, 33–37].

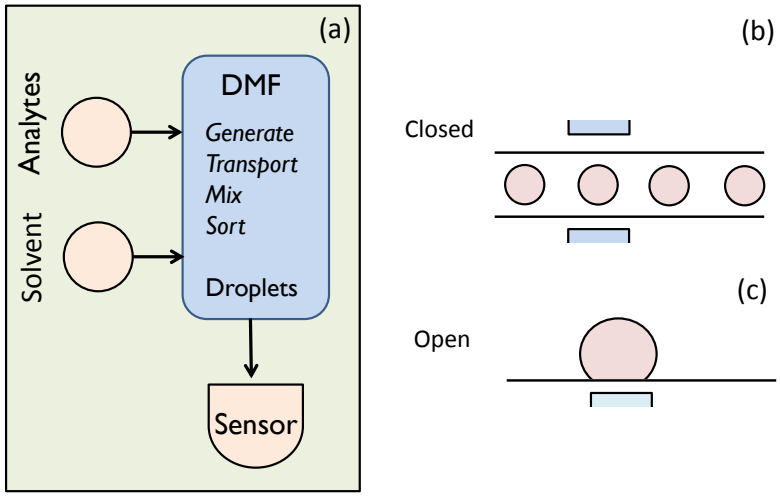

Fig. 1.2.: A droplet-based LoC platform must be integrated with highly sensitive and selective sensors. (a) General configuration of digital microfluidics platforms. Digital microfluidics offers a broad range of droplet operations (e.g., generation, transport, mixing, sensing, etc.). (b) In a closed microfluidic system, sensors analyze the droplets as they flow past the sensors; (c) In an open microfluidic system, the droplet is placed on the sensor surface, and no continuous flow is required.

There are two types of droplet-based sensing platforms:

Closed-microfluidic (CMF) Systems: For CMF systems (see Fig. 1.2(b)), the sensors straddle the channel, collecting data as droplets flow past the sensor. Such systems are well developed, offer high throughput, and simple integration. Numerous works have been reported on CMF based sensing systems [28, 38, 39]. For example, Srinivasan *et al.* have demonstrated a fully integrated lab-on-a-chip platform for detection of glucose in human physiological fluids such as serum, plasma and saliva [38]. Xiang *et al.* have reported a CMF fluorescence based colorimetric biosensor for

DNA detection by using graphene oxide (GO) nanoprobe as a quencher for the ssDNA probes labeled with carboxy fluorescein (FAM) and 6-carboxy-X-rhodamine (ROX), respectively [39]. As an another example, Kemna *et al.* reported a impedance based detection method for cells in droplets using on-chip coplanar electrodes. Using their approach, they were able to distinguish between viable-cells containing conducting cytoplasm vs. non-viable cells [28].

Open-microfluidic (OMF) Systems: In contrast to CMF systems, OMF systems (see Fig. 1.2(c)) involve planar (often, multifunctional) sensors where analytes within the droplets are interrogated. Although for on-chip droplet dispensing a 'closed system' with a top plate is required, the open system is easier and costs less to fabricate, is more flexible in terms of reconfigurability, and offers faster sample handling and also direct access to droplets for analyte extraction if necessary [20]. Inspite of these advantages, it is a bit surprising that there have been relatively fewer reports of sensing using OMF systems: De Angelis *et al.* reported the detection of attomolar concentration of λ-DNA using an integrated Surface-Enhanced Raman Scattering (SERS) sensor [26]. Although detection below the diffusion limit was achieved, the intricate design and nanofabrication of the Raman probe, localization of the sessile droplet, complex instrumentation, and scaling to smaller sizes for portable applications remain challenging. Moreover, the approache relies on single end-point detection of ultra-low concentrations; therefore, the statistical robustness of the result at highly diluted solutions is unknown.

Need of electrical approaches for fast and sensitive detection: Eventually, the goal of any LoC technology is to achieve fast and highly sensitive detection of a specific analyte with the smallest possible sample/reagent volume at comparatively low cost. Unfortunately, these otherwise sophisticated LoC technologies either rely on relatively simple sensors, e.g. colorimetric, rudimentary flow cytometry, UV-Vis absorbance spectroscopy, etc. [38, 40, 41] or are unable to address the fundamental response time and screening limited response of classical sensors (discussed earlier) using a label-free approach. Real-time, rapid, label-free detection of sub-femtomolar

concentration of biomolecules is critical in various areas, such as, biomedical diagnostics/therapeutics, food safety, environmental monitoring, and homeland security. Therefore, the need is to be able to come up with electrical approaches for fast and sensitive detection of biomarkers using a miniaturized sensor. This will be one of the primary topics to be addressed in Chapters 2, 3 and 4 of the thesis.

1.3 Review of continous monitoring devices

While portable lab-on-a-chip diagnostic devices offer high precision analysis, the data is obtained only when someone decides to do the test. For chronic illness or for patients under emergency conditions, a continuous monitoring device (CMD) capable of monitoring the vital health parameters in real-time can be very useful. Fig. 1.3 illustrates the conceptual framework for continuous monitoring of patient's health. A wearable sensor or a sensor implanted into patient's body is used to gather physiological data in real-time which is wirelessly transmitted through a smartphone to the caregivers, i.e., patient's family and the clinician. Emergency situations are detected via an automated server, and an alarm message is sent to an emergency vehicle for timely attention. As discussed earlier, CMD fall under two categories as follows.

1.3.1 Wearable sensors

Wearable sensors do not require any surgical procedure and can be worn as part of clothing, worn as an independent device (for example, a smart watch) or used as a patch over skin (for example, a smart bandage). These sensors avoid complications associated with implantation such as inflammation, foreign body rejection, etc. Some examples of wearable devices include glucose sensors for iontophoretic extraction of glucose through the skin, visible [43] or near-infrared [44] absorption spectrometry, and polarimetry [45].

A key desirable attribute of a wearable biosensor is that the sensor should be flexible while retaining its sensing capability to non-deformable state. The flexibility of

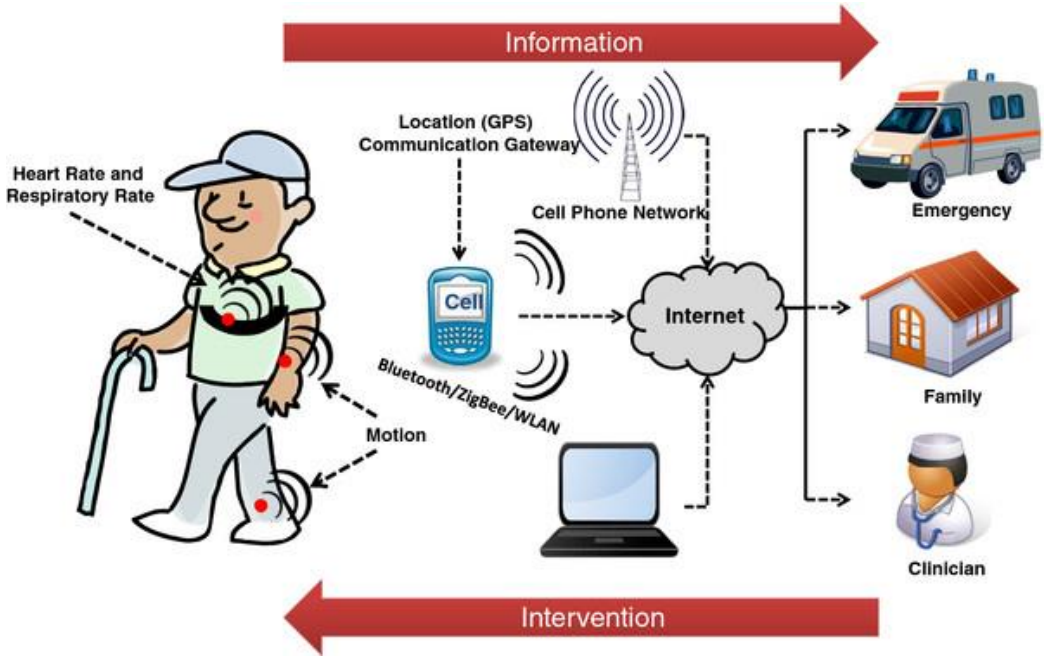

Fig. 1.3.: An illustration of advantages of a continuous health-monitoring device (CMD): The sensor can be either be implanted into the patient's body or worn as part of clothing. The real-time health information is wirelessly transmitted to the clinician and the patient's family. Figure adapted from Patel *et al.* [42] under the terms of the Creative Commons Attribution License which permits unrestricted distribution.

the device enables the sensor to adapt to the curvilinear surfaces of the human body, and hence probe the physiological parameters over a wider surface area, and ensures signal stability. In order for the sensor to be flexible, ideally all of the components comprising the device, i.e., the active device, the substrate and the packaging material should be flexible. Traditionally, silicon has been an ideal choice for non-flexible electronics, both for the active device and the substrate. However, silicon does not have good mechanically flexibility: a strain of even 10% causes an irreversible plastic deformation in crystalline silicon [46]. Therefore, other materials, such as thin glass, polymer foils and metals, have been explored over past couple of decades for fabricating flexible devices. Among these, polymer foils are very promising since they are highly flexible, have light weight and are amenable to roll-to-roll processing which enables low cost fabrication. Candidate polymers for flexible substrate

are polyethylene terephthalate (PET), polyethylene naphthalate (PEN), polyethersulphone (PES), polydimethylsiloxane (PDMS) and polyamide (PI) [47].

There have been several reports of electronic sensors fabricated on flexible substrates. For example, several researchers have reported the continuous detection of glucose in the tear fluid of eyes by fabricating an electrochemical sensor on a contact lens made up of PDMS [48], PET [49, 50] and hydrogel [4]. However, in all these devices, the active device, i.e., the electrochemical sensor, was made up of metal electrodes which are not very flexible. In another work, Swisher *et al.* [51] developed a flexible impedance based electrochemical sensor with inkject printed gold electrodes fabricated on PEN, which non-invasively maps pressure-induced tissue damage, and can potentially be used as a smart-bandage.

Two-dimensional (2D) materials are promising candidates: Recently, 2D nanomaterials, such as graphene and transition metal dichalcogenide (TMDCs): MX_2=Mo, W; X=S, Se, Te, have attracted significant attention for the choice of active device due to their unique electronic properties and mechanical flexibility [52–61]. These materials can easily be transferred to soft polymeric or plastic substrates [46,52], such as PET or fabricated on ultra-slim (thickness less than 200 μ m) flexible glass substrate [62]. 2D materials are preferred over silicon because they have a higher yield strain ($\sim$ 25-30%) as compared to silicon ($\sim$ 10%). Further, reports on biocompatbility of these materials [63–66] suggest that they may subsequently be used for biomonitoring on open-wounds as smart-bandages or as implantable flexible sensors.

Graphene, a 2D sheet of carbon, has been studied intensely for biosensor applications because of its high conductivity and unique optical properties [67]. For exmaple, Kwak *et al.* [68] reported a flexible graphene-based field effect transistor glucose sensor. Graphene was grown using chemical vapor deposition (CVD), transferred to a polyethylene terephthalate (PET) substrate and functionalized with linker molecules to immobilize glucose oxidase. Through measurement of the Dirac point shift, authors were able to determine the glucose concentration. In another work, Dong *et al.* [69]

reported a graphene FET to detect DNA. However, the zero bandgap of graphene limits the sensitivity of graphene FET [70].

In contrast, TMDs with non-zero bandgap could enable highly sensitive detection of biomolecular targets by TMD FET-based biosensors [70]. These materials exhibit desirable properties including mechanical flexibility, high mobility (>100 $cm^2V^{-1}s^{-1}$) and wide band gap (E_g >1 eV) [52–55], which makes them promising candidates for flexible and stretchable integrated sensors. Further, layered nature of TMDs allows them to have channel thickness on the orders of atomic dimensions which is significantly smaller as compared to the 3D materials, like silicon. This reduced channel thickness allows for an excellent electrostatic control of the channel. Some important work has been reported on use of TMD materials as a choice for channel material in FET based sensors. For example, Sarkar *et al.* [70] reported detection of streptadavin using an MoS_2 biosensor with HfO_2 gate dielectric functionalized with biotin. In another work, Wang *et al.* [71] reported detection of prostate specific antigen (PSA) using MoS_2 FET with HfO_2 gate oxide functionalized with anti-PSA. However, the sensitivity in both these works was limited due to oxide-layer separating the biomolecular charge and the MoS_2 channel, leading to partial screening of the charge by the ions in the solution. Therefore, novel sensing methodologies need to be explored for reducing the ion-screening effect in such kind of sensors. This will be addressed in Chapter 5 of the thesis.

1.3.2 Implantable sensors

Implantable sensors have the advantage of probing the physiological parameters inside the body which allows the sensor to be in direct contact with blood. When a sensor is implanted into the body, the body suffers from foreign body response which leads to the adsorption of blood and tissue proteins onto the sensor. This causes subsequent inflammation of the tissue surrounding the sensor, and loss of sensor functionality. Therefore, the most important attributes of an implantable sensor

are its biocompatibility (i.e., the sensors should not trigger immune response) and biostability (the device should tolerate harsh biological environement, and reliably function over a long period of time).

Most widely used medical implants include the cardiac pacemaker [72] for regulating the heart-beat and the cochlear implant [73] which simulates the cochlear nerve to provide a sensation of sound of hear-impaired patients. Both these implants use metallic leads and casing. For example, a pacemaker includes a metal casing for packaging, microelectronics, and the leads, all of which are made of biocompatible materials. Inert metals, such as titanium and platinum, are an excellent choice of metals [74] because of their resistance to corrosion and in-toxicity to the biological environment. Even though these implants are biocompatible due to inertness of the metal to the biological environment, these materials themselves are passive, i.e., they are not environmentally responsive, hence cannot be used as a biorecognition element for sensing of biological parameters, such as proteins and pH.

Smart biocompatible hydrogel for implantable sensors: In this regard, hydrogel based implantable sensors [75–78] have attracted significant attention because they are not only biocompatbile [79–83] but also responsive to environmental changes such as pH [77, 84–88], ionic concentration [87], temperature [85], glucose [75, 89, 90] and antigen [91]. Their high biocompatibilty orignates from their ability to hold large amount of water and their physiochemical similarity with the native extracellular matrix both compositionally and mechanically [79]. Further, these materials retain their sensing properties within the body [82], and therefore are ideal candidates for continuous monitoring of vital health parameters. The properties of hydrogel such as density, mass, volume or stiffness can change upon change in environment variables. These changes can be measured by using optical, mechanical or electrical transducers. Optical transducers measure the change in transmission coefficient, refractive index, diffraction wavelength, etc. as the pH of the solution changes. Mechanical transducers monitor the change in the bending (static mode) or resonance frequency (dynamic mode) as the hydrogel changes its volume or exerts pressure. Electrical transducers

measure the change in thickness of the hydrogel layer upon swelling due to environmental changes. For example, Lei *et al.* demonstrated a hydrogel based micromachined transponder for detection of glucose in interstitial fluid [75]. They embedded a hydrogel with phenyl-boronic acid (PBA) groups and sandwiched the hydrogel between stiff nanoporous plate and a thin glass diaphragm. Swelling and deswelling of hydrogel in response to glucose concentration deflects the glass membrane, which causes change in capacitance of a passive LC resonator. Glucose concentration is measured as the change in the resonance frequency of the oscillator.

Inspite of these efforts, hydrogel based sensors still show a very sluggish response (few hours), and the correlation between the different performance parameters, such as sensitivity and response time, are not clearly understood. Obviously, it would be difficult to design and optimize the sensor for fast and sensitive detection without detailed understanding of these correlations. This will be one of the areas that is addressed in Chapter 6 of the thesis.

1.4 System integration

The design cycle of any diagnostic device goes through two phases: 1) Prototype phase where the sensor is modeled, fabricated and its performance evaluated and optimized, 2) Integration phase in which the sensor is integrated with other components within the chip to yield the desired diagnostic device. In Section 1.2 and Section 1.3, we reviewed devices for portable lab-on-chip sensors, flexible wearable sensors and implantable sensors. Similar to the semiconductor industry where integration of individual transistors into complex circuits requires time-efficient compact models, the electrical and non-electrical components comprising the diagnostic device must also be represented by compact models for integration at system level.

Among various biosensing platforms, biosensors based on field effect transistors (FETs) have been widely investigated to detect a variety of target analytes due to their high sensitivity, label-free detection capability, and compatibility with commer-

cial planar processes for large-scale circuitry [92–94]. These sensors can be easily integrated into lab-on-a-chip platforms. For example, Choi *et al.* reported the integration of a field-effect transistor (FET) biosensor and digital microfluidic device to detect avian influenza virus without a labeling process in real time. Droplets containing the target protein molecules were transported using electro-wetting-on-dielectric (EWOD) platform with a pre-charging method [24]. Recently, Rothberg *et al.* demonstrated a commercial DNA sequencing technology in which minaturized H^+ ion sensitive field-effect transistors (ISFETs) are used to perform non-optical DNA seqeuncing of genomes [2]. The chip consists of tens of millions of micrometer-sized wells containing DNA-beads for massively-parallel sequencing. By injecting bases repeatedly and measuring the resulting signal due to step-by-step hybridization of DNA and subsequent release of protons, sequencing of 25 million bases is accomplished within a couple of hours.

There are several reports of compact modeling for analysis of sensitivity of FET based sensors. For example, Massobrio *et al.* [95], Grattarola *et al.* [96] and Martinoia *et al.* [97] developed physical models for DC analysis of planar ISFET and incorporated them into SPICE to predict response of different oxides to pH sensing and analyze non-ideal effects in ISFETs. Fernandes *et al.* [98] extended the DC model for incorporation of biomolecule charge as an ion-permiable charged membrane, and implemented in HSPICE. Livi *et al.* [99] proposed a Verilog-A model for DC analysis of silicon nanowire pH sensors. These early works are certainly useful, however, the utility of the existing models will broaden significantly if we can incorporate small-signal and noise analysis, so that the one may predict signal-to-noise performance of the sensor, integrated within a complex signal processing environment. This will be one of the areas that is addressed in Chapter 7 of the thesis, where as an illustrative example, we describe the signal-to-noise response of FET-based pH sensor using a versatile, industry standard compact modeling language, Verilog-A. This illustration should serve as a general purpose guideline for compact modeling of other components (such as droplet based sensors) for system integration.

1.5 Outline of the thesis

The overall goal of the research is to provide a comprehensive framework for embedding the chemical and biological sensors for portable, implantable and wearable applications. This necessitates scaling of both the analyte sample and transducer, ensuring biocompatibility and device flexibility. The outline of the thesis is described as follows:

- In Chapter 2, we discuss a comprehensive framework for non-faradaic impedance characterization of small evaporating droplets. We determine the time-dynamics of droplet evaporation using a gas-diffusion model, and develop a semi-analytical model to relate the impedance characteristics to the droplet shape, size and its composition. We discuss the application of model in determining the sensitivity enhancement of a droplet-based impedimetric nano-biosensor which can overcome the fundamental diffusion limited time response of classical sensor [27,100].

- In Chapter 3, we demonstrate a method for localized electronic desalting on a field effect transistor biosensor by using on-chip polarizable electrodes to locally deplete salt ions near the sensor region. We develop a theoretical numerical and analytical model to predict the degree and extent of desalting in the miniaturized droplets. We describe the effect of biasing voltage, droplet size and electrode area in determining the desalting efficiency of the sensor. We discuss the utility of desalting for various applications including overcoming fundamental screening limited response of charge-based sensors [100, 101].

- In Chapter 4, we demonstrate an approach to locally heat the droplet using an on-chip miniaturized FET based dielectric heater. We discuss the approach and develop a theoretical framework to provide guidelines for achieving a specific temperature within the droplet. We discuss the application of localized heating to specifically detect DNA probe-target hybridization and detect single-base pair mismatch between DNA strands [102].

- In Chapter 5, we describe the capability of two-dimensional layered transition metal dichalcogenides as a channel material for highly sensitive detection of cancer biomarkers in a label-free manner. We propose a scheme to enhance device sensitivity by using an oxide-free operation. We develop a theoretical model to interpret the experimental results, determine the performance bottlenecks and suggest strategies to improve the sensitivity [12].

- In Chapter 6, we discuss hydrogel based implantable biochemical sensors. We develop a numerical and analytical framework to show that there is a fundamental trade-off between the performance parameters, i.e., sensitivity/dynamic range vs. response-time/response-asymmetry in hydrogel sensors. Specifically, we consider the effect of the hydrogel preparation gel parameters and environmental factors in dictating the sensor performance [103, 104].

- In Chapter 7, we discuss time-efficient physics based behavioral compact models for system integration of FET based pH sensors [105]. Using the compact model, we analyse the noise performance of ISFET and EGFET sensors. The model should enable in design optimization of the biosensors which rely on pH measurement, such as genome-sequencing by Ion Torrent.

- In Chapter 8, we provide a summary of the thesis and possible direction for the future research.

1.6 List of associated publications

Patent

- M. Alam, **P. Dak**, "Electrostatic control of ionic environment in a droplet-based platform for biological applications," United States Patent Application no. 15/054176 (2016).

Journals

1. **P. Dak**, W. Seo, B. Jung, M. A. Alam, "A Physics-based (Verilog-A) Compact Model for DC, Small-Signal, Transient and Noise Analysis of FET based pH Sensors," IEEE Transactions on Electron Devices (In review).

2. **P. Dak** and M. A. Alam , "Numerical and Analytical Modeling to Determine Performance Trade-offs in Hydrogel based pH Sensors," IEEE Transactions on Electron Devices, vol. 63, pp. 6 (2016) [104].

3. **P. Dak***, A. Ebrahimi*, V. Swaminathan, C.-D. Guevara, R. Bashir and M. A. Alam, "Droplet-based Biosensing for Lab-on-a-Chip, Open Microfluidic Platforms," Biosensors, vol. 6, pp. 14 (2016) (*Equal Contributors) [5].

4. J.-S. Rhyee, J. Kwon, **P. Dak**, J. H. Kim, S. M. Kim, J. Park, W. Song, H.-J. Kwon, Y. K. Hong, I. Omkaram, M. A. Alam, S. Kim, "High-mobility transistors based on large-area and highly crystalline MoSe2 nanosheets directly grown onto insulating substrates," Advanced Materials, vol. 28, pp. 2316 (2016) [54].

5. V. Swaminathan, **P. Dak**, B. Reddy, E. Salm, C. D-Guevara, Y. Zhong, A. Fischer, Y.-S. Liu, M. A. Alam, R. Bashir, "Electrostatic desalting for controlling the ionic environment in droplet based biosensing platforms," Applied Physics Letters , vol. 106, pp. 053105 (2015) [106].

6. J. Lee*, **P. Dak***, Y. Lee*, H. Park, W. Choi, M. Alam, S. Kim, "Two-dimensional Layered MoS2 Biosensors Enable Highly Sensitive Detection of Biomolecules," Scientific Reports (Nature Publishing Group) vol. 4, pp. 7352 (2014) (*Equal Contributors) [12].

7. **P. Dak**, A. Ebrahimi and M. A. Alam, "Non-Faradaic Impedance Characterization of an Evaporating Droplet for Microfluidic and Biosensing Applications," Lab Chip vol. 14, pp. 2469 (2014) [100].

8. A. Ebrahimi, **P. Dak**, E. Salm, S. Dash, S. Garimella, R. Bashir, M. A. Alam, "Nanotextured Superhydrophobic Electrodes enable Detection of attomolar-scale DNA concentration within a Droplet by non-Faradaic Impedance Spectroscopy," Lab Chip, vol. 13, pp. 4248 (2013) [27].

9. E. Salm, C. D. Guevara, **P. Dak**, B. Dorvel, B. Reddy, M. A. Alam, R. Bashir, "Ultra-localized Thermal Reactions in Sub-Nanoliter Droplets-in-Air," Proceedings of National Academy of Sciences , vol. 110, pp. 3310 (2013) [102].

Conferences

1. M. A. Alam, **P. Dak**, M. A. Wahab and X. Sun, "Physics-based Compact Models for Insulated-Gate Field-Effect Biosensors, Landau-Transistors, and Thin-Film Solar Cells," IEEE Custom Integrated Circuits Conference (CICC) (2015) (Invited Talk) (All authors contributed equally) [107].

2. **P. Dak** and M. A. Alam, "A Predictive Model for Hydrogel Based Wireless Implantable Bio-Chemical Sensors," Device Research Conference (DRC) (June 21st - June 24th, 2015, Columbus, OH) [103].

3. **P. Dak** and M. A. Alam, "Electrostatic desalting of micro-droplets to enable novel chemical/biosensing applications," Device Research Conference (DRC) (June 22nd - June 25th, 2014, Santa Barbara, California) [108].

4. V. Swaminathan, **P. Dak**, B. R. Reddy Jr. E. Salm, C. D. Guerara, Y. Zhong, A. Fisher, Y. Liu, M. A. Alam, R. Bashir, "Localized Electrostatic Desalting Around Field-Effect Sensors for Molecular Detection in Droplets with Enhanced Sensitivity," Engineering in Medicine and Biology Society (EMBC) (2014) [101].

5. **P. Dak**, P. Nair, J. Go and M. A. Alam , "Extended-gate biosensors achieve fluid stability with no loss in charge sensitivity," Device Research Conference (DRC) (June 23rd - June 26th, 2013, Notre Dame, IN) [109].

Online Tools

1. **P. Dak**, M. A. Alam, "Non-Faradaic Impedance-based Biosensor Model 1.0.0," nanoHUB (2015) (>200 Users) [110].

2. **P. Dak**, M. A. Alam, "FET pH Sensor Model 1.0.1," nanoHUB (2014) (>500 Users) [105].

3. P. Nair, J. Go, G. J. Landells, T. R. Pundit, M. Alam, X. Jin, **P. Dak**, A. Jain, "BiosensorLab," nanoHUB (2014) (>950 Users) [111].

2. CHARACTERIZATION OF EVAPORATING DROPLETS

2.1 Introduction

Droplets are used in a broad range of applications: Droplets[1] are found in broad range of natural and engineered systems. In natural systems, for example, a drop of water on a lotus leaf forms a spherical shape to minimize the surface energy [112]. When a drop of liquid with suspended particles dries on a substrate, it leaves a ring-shaped stain on the surface generally known as the " coffee-ring effect" [113–115]. On the other hand, in the engineered systems, micro/nano-liter sized droplets have been used in various applications including drop-on-demand inkjet printing [116], molecule transport [117], single-cell analysis and sorting [118] through microfluidic channels, electrically-addressable biochemical reactions in sub-nanoliter droplets [102], etc.

Evaporating droplets have distinct advantages: When droplets are reduced in size, they evaporate faster. While this might be a concern for some systems, *Evaporating* droplets offer unique opportunities for a number of interesting applications. For example, Jing et al. have used tiny evaporating droplets to elongate and fix DNA molecules on derivatized surfaces [119]. De Angelis *et al.* have reported attomolar-detection of DNA concentration by concentrating few copies of DNA to a localized surface plasmon resonance (SPR) sensor by evaporation of droplet [26]; and most recently Ebrahimi *et al.* have reported a label-free on-chip non-faradaic impedance based detection of attomolar (aM) concentration of DNA [27]. The concentration

[1] For the purpose of this thesis, we define droplet as fluid with volume few micro-liters or less. At such small volume of liquid, the surface tension beings to dominate the shape of the droplet and gravitational effect on the droplet shape can be ignored.

of biomolecules was enhanced through evaporation of the droplet and an enhanced signal was obtained for even a few copies of DNA in micro-liter sized droplets.

Previous techniques to characterize droplets: Optical techniques such as high-speed imaging [120], confocal microscopy [121] and laser light scattering [122,123] have been used to characterize the geometry and composition of droplets. For probing the droplet on a surface, an electrical characterization technique such as impedance spectroscopy can provide complementary information. In this regard, it is desirable to have a theoretical model that can map the system parameters like the droplet composition, shape and size to an electrical signal (i.e. impedance) as the droplet evaporates.

Non-faradaic impedance spectroscopy provides a simple approach for droplet characterization: Faradaic impedimetric sensors [124] have long been used for highly selective detection of biomolecules. If the analyte is known and only its concentration is desired, non-Faradaic Impedance spectroscopy (NFIS) provides a simple non-intrusive way to obtain wealth of information regarding the composition of the droplet and the kinetics of evaporation. Important initial work on NFIS has been already reported. For example, Sadeghi *et al.* performed on-chip impedance based droplet characterization for a parallel plate electrode system [125]. However, the time dynamics of impedance components was not discussed. Also, effects due to accumulation of ionic charge (double layer formation) were not considered and sensitivity of the system for differentiating salt solution was limited to ∼pM. Therefore, for a broader range of applications, all droplet models must be generalized to include accumulation of ionic charges (double layer) near the electrode surface, arbitrary geometry of electrodes, the time dynamics and droplet shape dependence of impedance components, including all the parasitic components.

Our work: In this chapter[2], we formulate a comprehensive theory for droplet impedance with focus on nano-biosensing [26,27,119]. We solve for the time dynamics of droplet evaporation and relate the composition, size and shape of the droplet to

[2] The content of this chapter is adapted/reproduced from Ref. [100] and Ref. [27] with permission from The Royal Society of Chemistry.

the time-varying impedance. We demonstrate that the approach can be used to optimize an evaporating droplet based sensor for attomolar detection of DNA in DI water. Indeed, the model is general and can be used in a broad range of microfluidic systems.

Organization of chapter: The chapter is arranged as follows. In Section 2.2, we describe the device structure and operation principle of the evaporating-droplet based impedance sensor. Next, we describe the shape of the droplet sitting on a patterned structure. In Section 2.3, we describe the impedance/admittance response of the system for a fixed droplet geometry. In Section 2.4, we describe the time dynamics of droplet evaporation and describe the geometry variation as a function of time. In Section 2.5, we provide the time dependence of circuit components/impedance for the system. In Section 2.6, we explain the sensitivity enhancement of the droplet based sensor in various operation regimes and discuss the implications of parasitic impedance respectively. Finally, the model is validated with the experiments on droplets containing DNA molecules in Section 2.7.

2.2 Device structure and Principle of operation

Device Structure: As a model system for the theoretical framework, we consider an evaporating droplet containing chemical/biomolecules resting on a substrate with co-planar electrodes, as shown in Fig. 2.1(a). We assume that the surface is designed in such a way that the droplet is pinned and maintains constant contact line as it evaporates. The contact width (r) and the contact angle (θ) that the droplet makes with the surface depends on the surface wettability and the droplet volume. Recently, Ebrahimi *et al.* [27] fabricated a similar device with a droplet sitting on an array of nanotextured superhydrophobic electrodes having a pinned contact line as shown in Fig. 2.1(b).

Principle of Operation: The electrical impedance of the droplet is measured by applying a small ac signal (with a dc bias) between the electrodes. The impedance of

the droplet, $Z_{\text{drop}}(n_0, f, t)$, depends on the time-dependent (t) shape of the droplet, the initial concentration of ions (n_0), and the characterization frequency (f). As the droplet evaporates, Z_{drop} changes due to two distinct but correlated effects: the increase in ionic concentration associated with decrease in the droplet volume, and the change of the droplet geometry due to evaporation. The changes in Z_{drop} can be used as a characterization tool for many droplet-based problems and applications discussed earlier. For droplet-based nanobiosensors, the positive implications are

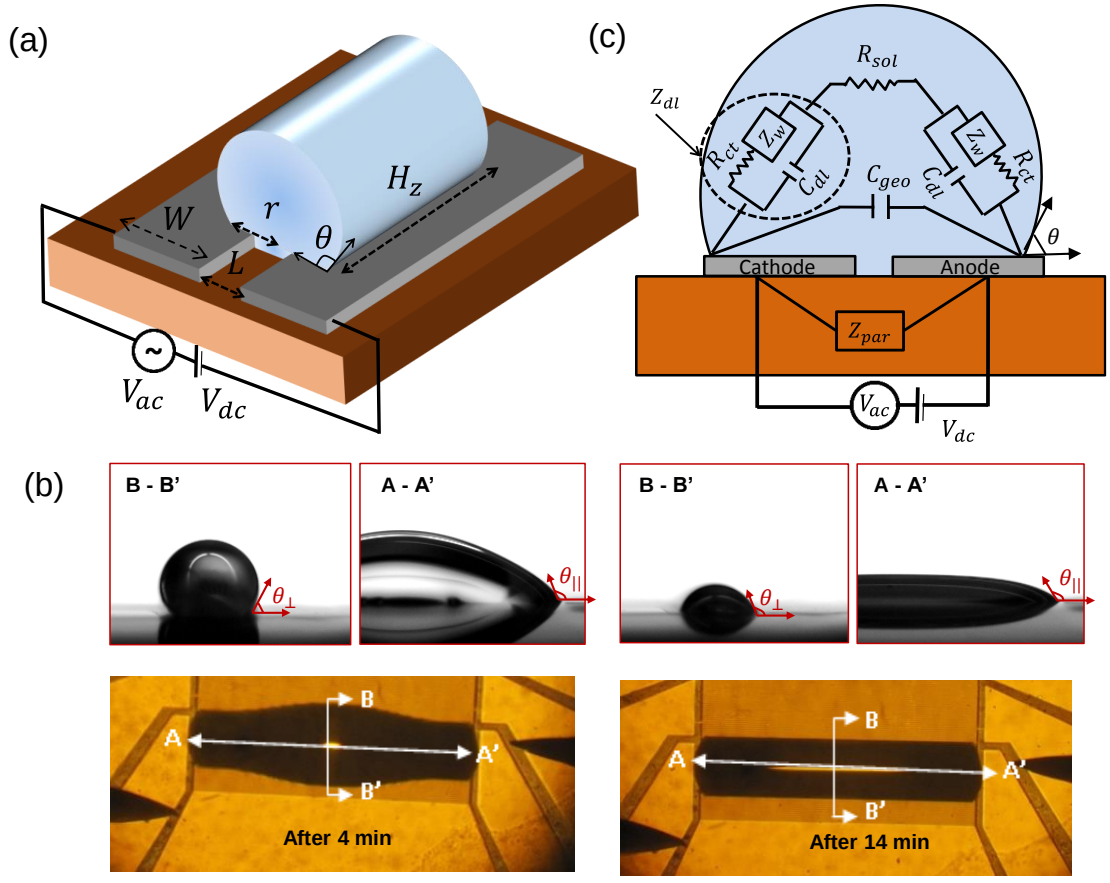

Fig. 2.1.: (a) Model system for numerical/analytic modeling, (b) Top view and side view of a pinned elongated evaporating droplet sitting on a substrate with a set of electrodes forming anode and cathode (at $t = 4$ min and $t = 14$ min) [27]. The droplet volume and its parallel/perpendicular contact angles ($\theta_{||}$/ $\theta_\perp$) decrease as it evaporates, while the contact line remains pinned by design, (c) Equivalent circuit representation of the system.

obvious (see Fig. 2.2): the shrinking droplet brings the analyte biomolecules close to the sensor surface faster than the diffusion limit [6]. As a result, the concentration of the biomolecules increases inversely with the volume of the droplet and this increased concentration is reflected in enhanced sensitivity [126], $S(t)$ defined as change in conductance ($\Delta Y(t)$) with respect to known reference solution (DI water).

Model assumptions: For simplicity, we assume that the droplet is self-aligned to the coplanar electrodes, as shown in Fig. 2.1(a). The conclusions of the chapter, however, are general and would apply to any electrode geometry. The electrodes are multi-functional: they define the superhydrophobic surface that pins the droplet and can also be used as an addressable heater. If the electrodes are simultaneously used as heater and prober, a complex interaction is likely. Therefore, for simplicity of model development, we use the electrodes exclusively for impedance measurement, and the heating effects are not considered. The applied voltage is presumed small to suppress the Faradaic current [127]. However, if a higher applied voltage is necessary, electrodes maybe coated with a thin dielectric layer to block any charge transfer between the electrodes and the solution.

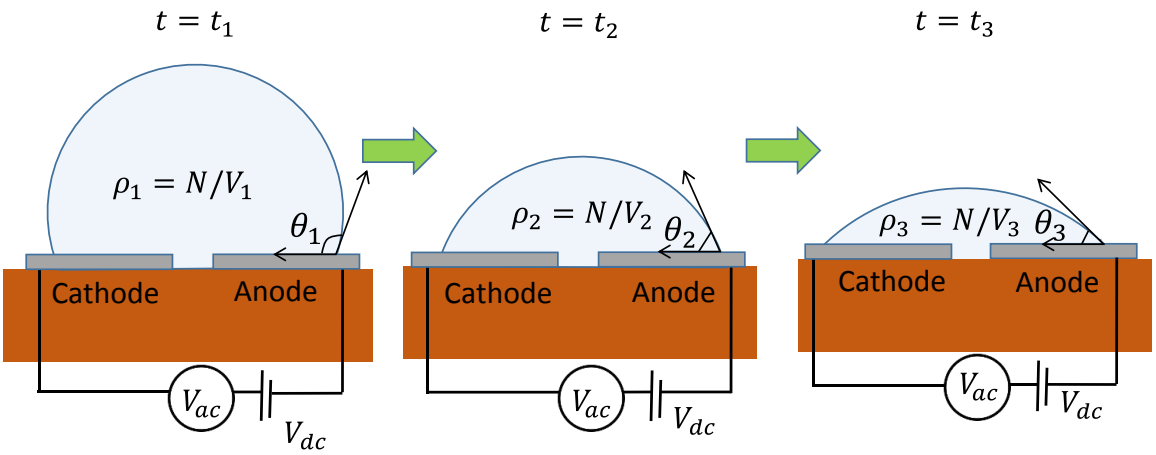

Fig. 2.2.: Evaporation dynamics of droplet: As the droplet evaporates, the contact angle (θ) decreases while the contact line remains pinned. The concentration of the chemical/biomolecules (ρ) increases as the volume (V) decreases with time (t) with number of chemical/biomolecules (N) remaining constant

Role of parasitics: Finally, the substrate offers a parasitic path between the electrodes (see Fig. 2.1(c)) and thereby defines the upper limit for the frequency of operation. At high enough frequencies, the impedance of the overall system, Z_{net} is dictated by the parasitic impedance, Z_{par} and becomes insensitive to the properties of the droplet itself. Depending on the substrate (e.g. glass vs. silicon-on-insulator, SOI), the parasitic impedance may change by orders of magnitude; therefore, the choice of the substrate is important in defining the sensitivity of the sensor.

In order to determine the magnitude of various parameters in Fig. 2.1(c), we first need to describe the volume, shape and size of the droplet immediately after the droplet has been placed, and then as a function of the evaporation time.

Initial droplet Shape

Droplet forms as a result of balance of surface tensions at the triple contact line between air, liquid and surrounding medium. Equivalently, the shape of the droplet can be determined by energy minimization [128]. Experimental results (see Fig. 2.1(b)) show that the droplet placed on nanotextured-superhydrophobic electrodes assumes a nearly ellipsoidal shape with pinned contact lines at the edges of the droplet [27]. Contact line pinning of droplet is critical for highly stable impedance characterization. A constant contact width for evaporating droplet can also be obtained using chemically heterogeneous striped surface [129].

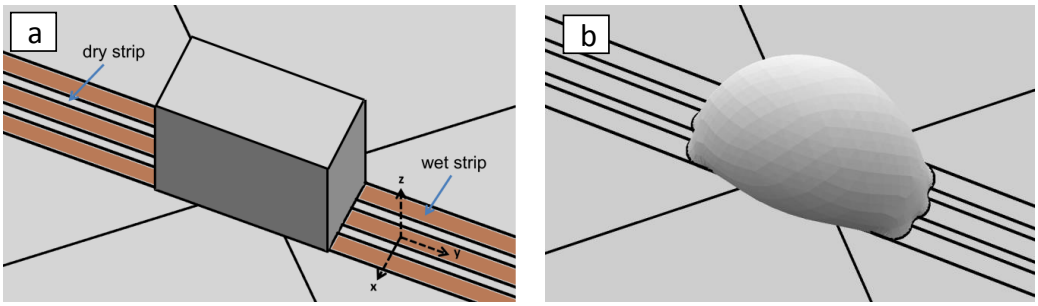

Fig. 2.3.: (a) Initial and (b) final shape of a droplet sitting on a surface with three wettable strips surrounded by dry strips.

Simulation Approach: In order to determine the shape of the droplet on the fabricated electrode array, we carried out simulations using the public domain software, Surface Evolver [130]. Although the fabricated structure has grooves and ridges, we consider a simpler surface defined by alternate patches of hydrophobic and hydrophilic regions. Such a mapping reduces computational complexity, while retaining the essential features of the original problem (For a more rigorous analysis see [128]). Our goal here is to understand the qualitative features of the droplet shape, such as elongation of droplet in the direction parallel to the electrode array and the trend that parallel and perpendicular contact angles follow with respect to time.

Simulation results agree qualitatively with the experiments: The simulation is initiated with a drop of given volume resting on a surface with three wettable strips surrounded by dry strips on either side. The aspect ratio of wettable and dry strips was chosen to be the aspect ratio of the electrode fins [27]) used in the experiments. The surface tensions of the wettable and dry strips are specified to reflect their corresponding contact angles on a flat homogeneous surface. Fig. 2.3 shows the initial and final droplet shapes for a given droplet volume. The initial shape of the droplet is assumed to be a parallelopiped whose length in the y direction is two times that in x direction. The ellipsoidal shape observed in the numerical simulation qualitatively agrees with the experimental results (see Fig. 2.1(b)) reported by Ebrahimi *et al.* [27].

2.3 Frequency dependence of droplet impedance for different droplet sizes

Let us now consider the frequency dependence of impedance of a droplet (see Fig. 2.1(a)) with a known geometry (defined by its constant contact angle θ) resting on a substrate with two planar electrodes. For an arbitrary electrode (faradaic/non-faradaic), the different components that can affect the impedance are shown in Fig. 2.1(c). Here, R_{ct} denotes the charge transfer resistance [127], Z_{w} the Warburg

impedance [131], $C_{\rm dl}$ double layer capacitance, $R_{\rm sol}$ denotes resistance of the solution and $C_{\rm geo}$ the dielectric (geometric) capacitance of the droplet. The net impedance of the system is therefore given by,

$$Z_{\rm net} = (R_{\rm sol} + 2Z_{\rm dl})||(\frac{1}{j\omega C_{\rm geo}})||(Z_{\rm par}), \tag{2.1}$$

where, $Z_{\rm dl} = (R_{\rm ct} + Z_{\rm w})||(\frac{1}{j\omega C_{\rm dl}})$ represents the double layer impedance and $Z_{\rm par}$ the parasitic impedance. For a non-faradaic electrode, there is no charge transfer at the surface, so that $R_{\rm ct} \to \infty$ and hence the net impedance of the system simplifies to

$$Z_{\rm net} \approx (R_{\rm sol} + \frac{2}{j\omega C_{\rm dl}})||(\frac{1}{j\omega C_{\rm geo}})||(Z_{\rm par}). \tag{2.2}$$

The rest of the chapter will focus on this reduced 'non-faradaic' model, with the understanding that it can be easily generalized to include Faradaic contributions as well. We first discuss the contact angle depedence of each of these circuit components, i.e. $C_{\rm geo}(\theta)$, $C_{\rm dl}(\theta)$, and $R_{\rm sol}(\theta)$. Once the dependence of circuit components on the contact angle (θ) is determined, we determine the frequency response of the sensor for a particular contact angle, θ.

Geometric Capacitance, ($C_{\rm geo}(\theta)$)

For a parallel plate system, the geometric (dielectric) capacitance is given by $C_{\rm geo} = A\varepsilon/d$, where A is the area of the electrodes, ε permittivity of the medium separating the electrodes and d the separation between the electrodes. This results from the solution of Poisson equation and is determined by the ratio of charge Q on the electrode and voltage $V_{\rm dc} = 2V_e$ between the electrodes. For any given contact angle θ, the geometrical capacitance can be determined in similar way. We solve for the Poisson equation ($-\overrightarrow{\nabla}.(\varepsilon\overrightarrow{\nabla}\varphi) = 0$) within the droplet with the boundary condition $\varphi = \pm V_e$ at the two electrodes using Sentaurus [132]. The capacitance is given by $C_{\rm geo} = Q/2V_e = \int_{\Omega_e} \varepsilon \overrightarrow{E}.d\overrightarrow{S}/2V_e$, where $\overrightarrow{E}$ is the electric field at the surface

of the electrode. Ω_e denotes the surface of the electrode. Fig. 2.4(a) shows the plot of the geometric capacitance as a function of contact angle θ of droplet with the surface.

We can generalize this solution for any droplet size (H_z) in z direction, by defining $C_{\text{geo}} = H_z\varepsilon/g(\theta)$, where $g(\theta)$ is dependent on the droplet shape. For a parallel plate capacitor, $g = d/W$, where W is the width of the electrodes and d the separation between them. Geometry factor can be interpreted as $g = 2\frac{H_z V_e}{\int_{\Omega_e} \overrightarrow{E}.d\overrightarrow{S}}$. Fig. 2.4 (b) shows the dependence of geometry function of the droplet contact angle (θ). This definition of geometry factor would be useful in evaluation of solution resistance which is discussed later. Note, that C_{geo} would be only impedance component of the droplet if it is non-conducting (which is dominant at high frequency when the ions don't respond to the ac signal). However, when electrolyte is conductive (at low/intermediate frequency), the solution will also have a double layer capacitance and solution resistance which are discussed next.

Double Layer Capacitance ($C_{\text{dl}}(\theta)$)

An electrode in contact with electrolyte forms a layer of surface ionic charge near its surface. This results in a formation of a diffuse layer due to columbic attraction to the surface charge. This double layer results in a net capacitance, $C_{\text{dl}} = (\frac{1}{C_S} + \frac{1}{C_{\text{diff}}})^{-1}$, where C_S is the Stern capacitance [133] and C_{diff} is the diffuse layer capacitance [134]. If the debye length is much larger than the thickness of the stern layer than, $C_S \gg C_{\text{diff}}$, so that $C_{\text{dl}} \approx C_{\text{diff}}$. For any given contact angle θ, this capacitance, $C_{\text{dl}}(\theta)$ is evaluated by solving Poisson equation $-\overrightarrow{\nabla}.(\varepsilon\overrightarrow{\nabla}\varphi) = \rho = p - n$, where $p(x, y, z)$ and $n(x, y, z)$ is the concentration of positive and negative ions in the solution respectively. Again, the capacitance is evaluated by evaluating the charge on the electrode, Q and differentiating it with respect to electrode voltage, V_e i.e. $C = dQ/dV_e$. Fig. 2.4(c) shows the variation of capacitance as a function of contact angle θ with $n_0 = 10^{-7}M$ for different applied biases. Also, shown is the plot of C_{dl} vs. θ from the analytic solution of Poisson equation in semi-infinite medium i.e.

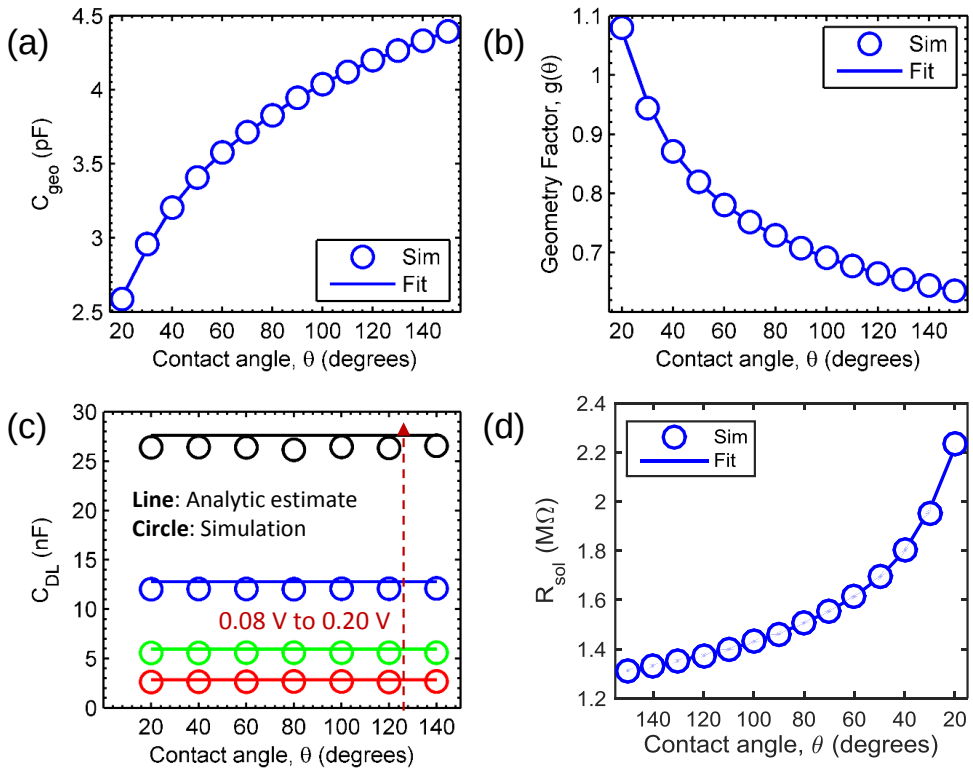

Fig. 2.4.: (a) Geometry capacitance (C_{geo}) as a function of contact angle (θ), (b) Geometry factor as a function of contact angle (θ), (c) Double layer capacitance (C_{dl}) as a contact angle (θ) for different applied bias (V_e) i.e red 0.08 V, green 0.12 V, blue 0.16 V and black 0.20 V (circles are from numerical simulation and lines are from analytic estimate), (d) Solution resistance (R_{sol}) as a function of contact angle (θ) for constant conductivity.

$C_{\text{dl}} = A\sqrt{2q^2\varepsilon\frac{n_0}{kT}}\cosh(\frac{qV_e}{2kT})$ [134]. The numerical solution is in excellent agreement with the analytic approximation. Therefore, we conclude that C_{dl} is independent of droplet geometry (different droplet shapes with same ionic concentration n_0). This is true as long as the droplet dimensions are much larger than the Debye length $\lambda = \sqrt{\frac{\varepsilon kT}{2n_0q^2}}$ in the ionic solution (maximum debye length is for pure water $n_0 = 100$ nM, i.e., $\lambda \approx 1$ μm). Finally, as the droplet evaporates the concentration of the electrolyte increases $n_i = n_i(\theta(t)) = n_0V_0/V(\theta(t))$, which we will be discuss in Section 2.4.

Solution Resistance, $(R_{\mathbf{sol}}(\theta))$

Solution resistance results from potential drop in the solution because of its finite resistivity. The resistance of a system with two parallel electrodes of area A separated by a distance d is given by $R_{\text{sol}} = d/\sigma A$, where $\sigma = qn_i(\mu_n + \mu_p)$ is the conductivity of the solution. This is the result of solution of Poisson equation and evaluation of $R_{\text{sol}} = \frac{V}{I} == \frac{V}{\int_{\Omega_e} \overrightarrow{J}.d\overrightarrow{S}}$, where $\overrightarrow{J} = \sigma \overrightarrow{E}$ is the current density. This can be related to the geometry factor that we defined earlier as $R_{\text{sol}} = \frac{g(\theta)}{\sigma H_z}$. Fig. 2.4(d) shows the dependence of solution resistance on the droplet contact angle (θ).

The conductivity (σ) of the solution is assumed to be constant. Note that in addition to the change in solution resistance due to geometry factor $g(\theta)$, there is an additional component $\sigma(\theta(t))$ that comes because of the increasing ionic concentration of the solution as the droplet evaporates. This is accounted for by considering the time evolution of the droplet volume which will be discussed in Section 2.4.

Once the droplet/electrode geometry are specified, the fluid properties are given e.g. $(\varepsilon_{\text{fluid}})$, and the salt (n_0) /analyte concentrations (ρ) is known, Z_{drop} is fully determined, and can be plotted, among other variables, as a function of frequency f.

Frequency Response

Response of ideal system shows three distinct regions: Frequency response of an ideal system (with no parasitic losses) at a particular contact angle, θ can be divided into three distinct regions (see Fig. 2.5(a)), such that the impedance components R_{sol}, C_{dl} and C_{geo} are dominant in one of the three regions. For $f < f_{\text{low}} = \frac{2}{2\pi R_{\text{sol}} C_{\text{dl}}}$, C_{dl} dominates the net impedance, for $f_{\text{low}} < f < f_{\text{high}} = \frac{1}{2\pi R_{\text{sol}} C_{\text{geo}}}$, R_{sol} is the dominant component, and finally for $f > f_{\text{high}}$, C_{geo} dominates. For a conductivity based sensor, we should be operating in either regime I or II, while detection can be done in the regime III if the change in permittivity of the solution upon addition of biomolecules is considerable.

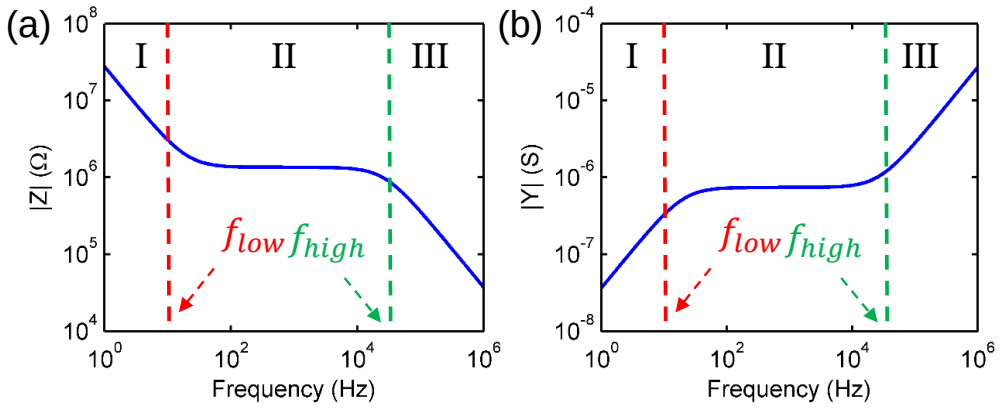

Fig. 2.5.: (a) Impedance of the droplet as a function of frequency. C_{dl} dominates at $f < f_{\mathrm{low}}$, R_{sol} dominates for $f_{\mathrm{low}} < f < f_{\mathrm{high}}$ and C_{geo} dominates the impedance at very high frequency ($f > f_{\mathrm{high}}$). Similar trend (2(b)) is visible in the admittance vs. frequency response.

The admittance of the droplet (see Fig. 2.5(b)) is defined as $Y_{\mathrm{drop}} = 1/Z_{\mathrm{drop}}$. We can define the limit of detection as the minimum measurable change in conductance ΔY_{drop} of the droplet upon introduction of salt/biomolecules.

Parameters affecting the limit of detection: In order to improve the limit of detection several design parameters can be considered, *i.e.* electrode separation (L), electrode width (W), electrode length (H_z) in contact with droplet. These factors have been considered by Hong *et al.* albeit for a bulk solution. The longer the electrode length and the smaller the electrode spacing, the better is the sensitivity [135]. However, for ultra-low concentration of biomolecules, the diffusion of the ions limits the detection time. Therefore, in order to improve the sensitivity and response time of the system, we need to explore droplet volume (V) (or contact angle (θ)) as an additional design parameter. This can be achieved by evaporation of the droplet which is considered next.

2.4 Dynamics of droplet evaporation

Simulations confirm a pinned contact line as droplet evaporates: In order to ensure that the signal is stable during measurement, we first must ensure that the droplet remains pinned and maintains a constant shape as it evaporates. We use Surface Evolver simulations to calculate the contact angles that the droplet makes with the electrodes as a function of time. We use a quasi-static approach: we first obtain the volume of the droplet for several different instants of time from the experimental data, and then simulate the equilibrium shape (and the contact angles) of the droplet for volumes associated with specific times. Fig. 2.6(b) shows the variation of the computed parallel ($\theta_{||}$) and perpendicular ($\theta_{\perp}$) contact angles as a function of time. Although the simplified model (secondary roughness is ignored, and the fin-structure of the electrodes is represented by wet/dry stripes) cannot reproduce quantitatively the experimental results in Fig. 2.6(a), the simulations correctly anticipate the key features of the experiments [27]: Both $\theta_{||}$ and $\theta_{\perp}$ decrease as a function of time and the decrease in $\theta_{\perp}$ is steeper than that of $\theta_{||}$. Further, $\theta_{\perp} >> \theta_{||}$, and therefore, the droplet maintains a nearly ellipsoidal shape.

Approximations for numerical determination of time-dependence of $V(t)$ and $\theta(t)$: For determining the time-dependence of droplet volume and contact angle numerically, we approximate the elongated ellipsoid as a truncated cylinder with contact width r and contact angle $\theta = \theta_{\perp}$, while keeping all other constraints (e.g. initial volume) unaltered, see Fig. 2.1(b). Our model is directly applicable in scenarios where the elongation of the droplet parallel to the coplanar electrodes is large as compared to that in direction perpendicular to the electrodes. However, the 'cylindrical' approximation is not restrictive - the formulation is general and can be applied to any system where the evolution of droplet shape (i.e. the geometry factor, $g(t)$) and droplet volume ($V(t)$) is known through numerical simulation [130] or high-speed imaging [120].

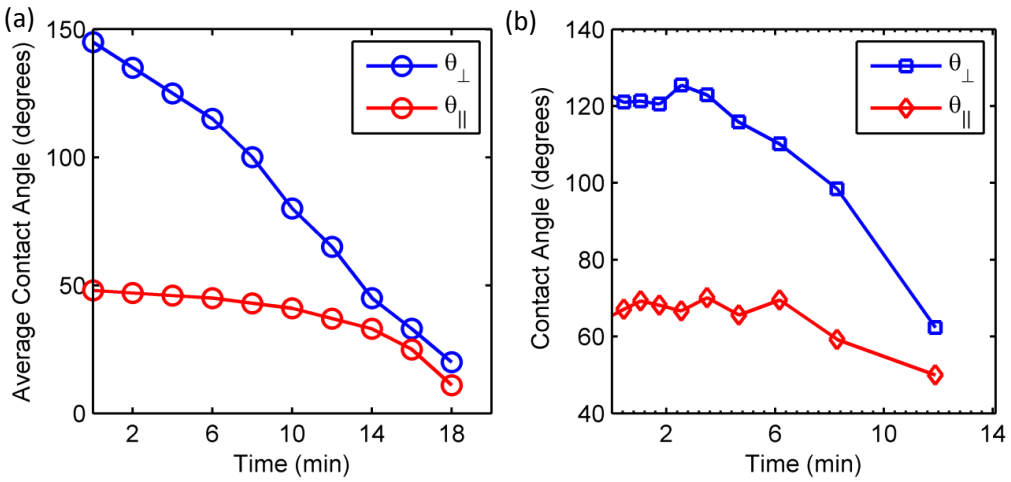

Fig. 2.6.: (a) Experimentally observed parallel and perpendicular contact angle for a 3μ L droplet as a function of time for the patterned surface described in [27], (b) Simulation results for the contact angles for the simplified geometry. The model results are in qualitative agreement with the experimentally observed trend as shown in (a).

Gas diffusion model used to determine $V(t)$ and $\theta(t)$: Similar to Rowan *et al.* [136] and Birdi *et al.* [137], we consider droplet evaporation as a gas diffusion process and assume that the rate of mass loss from droplet is given by $\Phi_D = \int_\Omega \overrightarrow{J}.d\overrightarrow{S}$, where $\overrightarrow{J}$ is the diffusion flux of liquid molecules away from the surface and integral of the flux is taken over the surface (Ω) of the droplet. The diffusion flux can be written in terms of the concentration of liquid vapors ($c(r,\theta,z)$) as $\overrightarrow{J} = -D\overrightarrow{\nabla}c$, where D is the diffusion coefficient of liquid vapors in the ambient surroundings. Therefore, the rate of mass loss would be, $\Phi_D = -\int_\Omega D\overrightarrow{\nabla}c.d\overrightarrow{S}$. In order to evaluate this integral, we use the equivalence between the electric potential (ψ) and vapor concentration (c), as discussed in Table 2.1.

For an electrical system, we can write charge $Q = -\int \varepsilon\overrightarrow{\nabla}\psi.d\overrightarrow{S} = C_\varepsilon(\psi_s - \psi_\infty)$ where C_ε is the electrical capacitance. Similarly, the diffusion flux of molecules can be written as [138] $\Phi_D = C_D(c_s - c_\infty)$ where c_s is the saturation vapor density of liquid and c_∞ is the vapor density of liquid far away from surface. C_D is the diffusion

Table 2.1.: Equivalence between electrostatics and molecular diffusion system

Electrostatics	**Molecular diffusion**
ψ (Potential)	c (Vapor Density)
ε (Permittivity)	D (Diffusion coefficient)
$\overrightarrow{\nabla}.(\overrightarrow{\varepsilon\nabla}\psi) = 0$	$\overrightarrow{\nabla}.(\overrightarrow{D\nabla}c) = 0$
$\overrightarrow{P} = \varepsilon\overrightarrow{E} = -\varepsilon\overrightarrow{\nabla}\psi$	$\overrightarrow{J} = -D\overrightarrow{\nabla}c$
$Q = \int_\Omega \overrightarrow{P}.d\overrightarrow{S} = -\int_\Omega \varepsilon\overrightarrow{\nabla}\psi.d\overrightarrow{S} = C_\varepsilon(\psi_s - \psi_\infty)$	$\Phi_D = \int_\Omega \overrightarrow{J}.d\overrightarrow{S} = -\int_\Omega D\overrightarrow{\nabla}c.d\overrightarrow{S} = C_D(c_s - c_\infty)$
$C_\varepsilon = f(\varepsilon)$ (Electrostatic Capacitance)	$C_D = f(D)$ (Diffusion Capacitance)

equivalent capacitance of a truncated cylinder with finite length [139] which is given by,

$$C_D = \frac{2\pi D H_z}{\alpha}\left(1 + \frac{0.3069}{\alpha} + \frac{0.2717}{\alpha^2}\right)\frac{\theta}{\pi}, \tag{2.3}$$

where $\alpha = \log(\frac{H_z}{R_s})$ and R_s is the radius of curvature of the droplet. Note, that the diffusion equivalent capacitance of the cylinder with finite length has been appropriately scaled for reduced surface area of the truncated cylinder. If we assume that the density of liquid (P) is constant as the droplet evaporates, the rate of mass loss can be expressed as,

$$\Phi_D = -\frac{dm}{dt} = -P\frac{dV}{dt}, \tag{2.4}$$

where m is the mass of droplet, V is the volume of liquid for a given contact angle and t is time. Therefore,

$$\frac{dV}{dt} = -C_D(c_s - c_\infty). \tag{2.5}$$

For simplicity, we assume that the evaporation occurs at a constant temperature so that c_s is independent of time. If evaporative cooling or natural convection is significant, the model needs to be appropriately generalized [140]. Also, Eq. (2.3)

assumes that the evaporation from the front and back surfaces of the cylinder are negligible, which is justified as long as $H_z \gg r$. Volume, $V(\theta)$ and Radius, $R_s(\theta)$ of droplet can be related to the contact angle θ and contact radius r as follows,

$$V(\theta) = r^2 H_z \left(\frac{\theta}{\sin^2\theta} - \frac{\cos\theta}{\sin\theta} \right), \tag{2.6}$$

$$R_s(\theta) = \frac{r}{\sin(\theta)}. \tag{2.7}$$

The rate of change of contact angle as a function of θ is given by,

$$\frac{d\theta}{dt} = -\frac{D(c_s - c_\infty)}{Pr^2} \frac{(\theta \sin^2\theta)}{1 - \theta\cot\theta} \left(1 + \frac{0.3069}{\alpha} + \frac{0.2717}{\alpha^2} \right) \frac{1}{\alpha} = -\lambda f(\theta, r, H_z). \tag{2.8}$$

where $\lambda = \frac{D(c_s - c_\infty)}{P}$ captures the material parameters of the droplet. This equation is numerically integrated to obtain $\theta(t)$ and $V(t)$. Fig. 2.7 shows the evolution of droplet contact angle (θ) and volume (V) as a function of time(t).

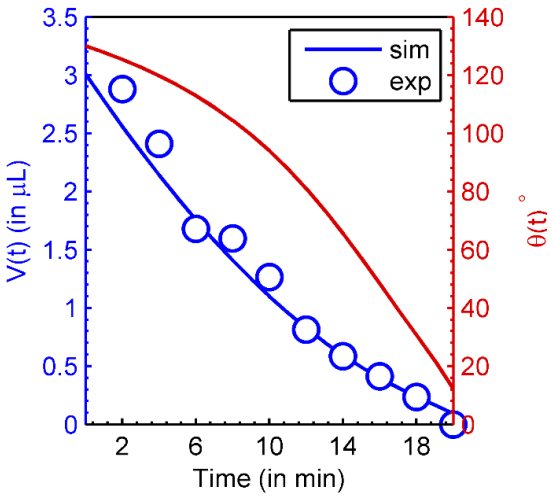

Fig. 2.7.: Evolution of droplet contact angle (θ) (right) and droplet volume (V) (left) as a function of time. The variation of droplet volume as a function of time can analytically be approximated as $V = V_0(1 - \frac{t}{\tau})^n$ [141] with $n = 3/2$ where V_0 is the initial volume of the droplet and τ the total evaporation time. Simulation Parameter: $(c_s - c_\infty)/c_s = 0.88$

Simulation parameters are listed in Table 2.2 and Table 2.3. Interestingly, despite the complexity of the equation, one finds that the volume evolution of the droplet can often be described by a power-law [141],

$$V(t) = V_0 \left(1 - \frac{t}{\tau}\right)^n . \tag{2.9}$$

where τ and n are empirical parameters defined by the shape of the droplet and the mode of the evaporation. We find that the parameters $n = 3/2$ and $\tau = 20$ min fit well the experimental data.

Table 2.2.: Table of physical constants

Parameter	**Value**	**Ref.**
Mobility of Na^+ ions in water	5.1×10^{-4} cm^2/Vs	[142]
Mobility of Cl^- ions in water	7.6×10^{-4} cm^2/Vs	[142]
Mobility of H^+ ions in water	3.0×10^{-3} cm^2/Vs	[142]
Mobility of OH^- ions in water	2.0×10^{-3} cm^2/Vs	[142]
Permittivity in free space	8.85×10^{-14} F/cm	[143]
Relative permittivity of water	78.9	[144]
Density of water	1 g/cm^3	[145]
Saturation vapor density of water in air at room temperature	$\sim 2.1 \times 10^{-5}$ g/cm^3	[136]
Diffusion constant for water vapor in air at room temperature	~ 0.2 cm^2/sec	[136]
Humidity factor, $(c_s - c_\infty)/c_s$	0.60	Fit
Ionic concentration of free H^+/OH^- ions in pure water	10^{-7} M	-
Thickness of stern layer	0.4 nm	[146]

Table 2.3.: Table of geometry parameters

Parameter	**Value**
Electrode width (W)	400 μm
Electrodes separation (L)	20 μm
Length of electrode in contact with solution (H_z)	4 mm
Initial angle of the droplet with the substrate (θ_0)	130°
Droplet contact width (r)	400 μm
Effective area for double layer capacitance (A)	0.21 cm^2

2.5 Time evolution of impedance/conductance

The net impedance of the droplet is given by,

$$Z_{\text{drop}}(\omega, t) = \left(R_{\text{sol}}(t) + \frac{2}{j\omega C_{\text{dl}}(t)} \right) || \left(\frac{1}{j\omega C_{\text{geo}}(t)} \right). \tag{2.10}$$

Given the geometry dependence of the circuit components and time dependence of geometry, we can determine the time dependence of different circuit components as follows:

2.5.1 Solution Resistance decreases and Conductance increases as droplet evaporates

Variation in solution resistance due to evaporation comes from two distinct effects. First, the geometry factor $g(r, \theta)$ evolves with $\theta(t)$, so that $g(t) = g(\theta(t))$, see Fig. 2.4(b) and Fig. 2.7. Second, the concentration of the ions in the solution increases inversely with the volume of the evaporating droplet, $V(t)$. If the electrolyte is fully ionized, we can assume that conductivity is directly proportional to the ionic concentration. Therefore, the conductivity $\sigma(t) = \sigma_0 V_0 / V(t)$ increases as a function of time. At any time, solution resistance is given by,

$$R_{\text{sol}} = \frac{g(t)}{\sigma(t) H_z} = \frac{g(t) V(t)}{\sigma_0 H_z V_0} = R_0 \frac{g(t)}{g_0} \frac{V(t)}{V_0}, \tag{2.11}$$

where R_0 represents the resistance of the solution at time $t = 0$ and $g_0 = g(t = 0)$. Here, V_0 and σ_0 are the initial volume and conductivity of the droplet, respectively. Fig. 2.8(a) shows the evolution of R_{sol} and $G_{\text{sol}} \equiv R_{\text{sol}}^{-1}$ as a function of time.

2.5.2 Double Layer Capacitance increases as droplet evaporates

The increased concentration of the evaporating droplet is also reflected in C_{dl} , as follows: Since, the concentration at any time t is given by $n_i(t) = n_0 V_0/V(t)$, the double layer capacitance would be,

$$C_{\text{dl}}(t) = A\sqrt{\frac{2q^2\varepsilon n_i(t)}{kT}}\cosh\left(\frac{qV_e}{2kT}\right) = C_{DL,0}\sqrt{\frac{V_0}{V(t)}}, \tag{2.12}$$

where $C_{DL,0}$ is the double layer capacitance at $t = 0$. Fig. 2.8(b) shows the evolution of the double layer capacitance as a function of time.

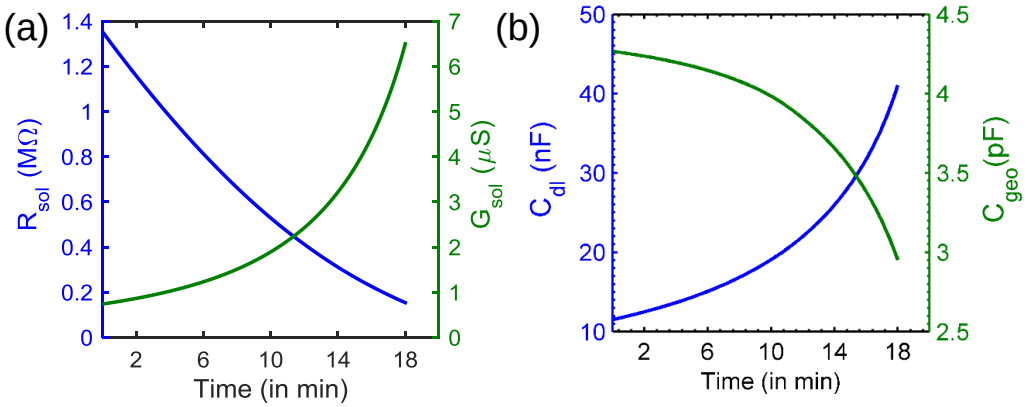

Fig. 2.8.: (a) Time dependence of solution resistance (left) and solution conductance (right) (b) Time evolution of double layer capacitance (left) and Geometry capacitance (right) for $n_0 = 10$ μM and $V_0 = 3$ μL.

2.5.3 Geometry Capacitance decreases as droplet evaporates

The geometry (dielectric) capacitance $C_{\text{geo}} = H_z\frac{\varepsilon}{g(t)}$ is independent of the ion concentration (except indirectly through the permittivity of the solution, ε), but depends

on the geometry of the droplet through $g(t)$. The variation of C_{geo} as a function of time is shown in Fig. 2.8(b). Our numerical simulations show that both $g(\theta)$ and $\theta(t)$ are monotonically decreasing functions of θ (Fig. 2.4 (b)) and t (Fig. 2.7) respectively; therefore $g(t)$ increases monotonically with time t . Therefore, the geometry capacitance decreases with time unlike G_{sol} and C_{dl}.

To summarize, the impedance evolution is specified by two parameters, $g(r, \theta(t))$ and $V(t)/V_0$. Once these two parameters are known either from experiments, or detailed numerical models such as surface evolver [130]; or by approximate analytical/numerical model discussed above, one can compute any electrical characteristics associated with evaporating droplets. In the next section, we will illustrate the concept by analyzing a droplet-based sensor.

2.6 Application of the model to a droplet based sensor

The model described in previous section can be used to characterize the impedance of evaporating droplets as a function of time and frequency. Also, as discussed earlier, an evaporating droplet based biosensor can be used to beat the diffusion limited time response: the shrinking droplet brings the analyte biomolecules close to the sensor surface faster than the diffusion. As a result, the concentration of the biomolecules increases inversely with the volume of the droplet and this increased concentration is reflected in enhanced sensitivity for even attomolar-concentration of biomolecules [27]. In this section, we discuss the application of the model to droplet based biosensors, and determine the relative improvement in sensitivity using the evaporation scheme as compared to the bulk based sensor. Further, we discuss the effect of parasitic impedance in limiting the sensor response.

2.6.1 Frequency-dependent time response of Biosensors

In order to determine the relative improvement in sensitivity of the droplet-based sensor as compared to the bulk sensor, we define sensitivity of the droplet-based

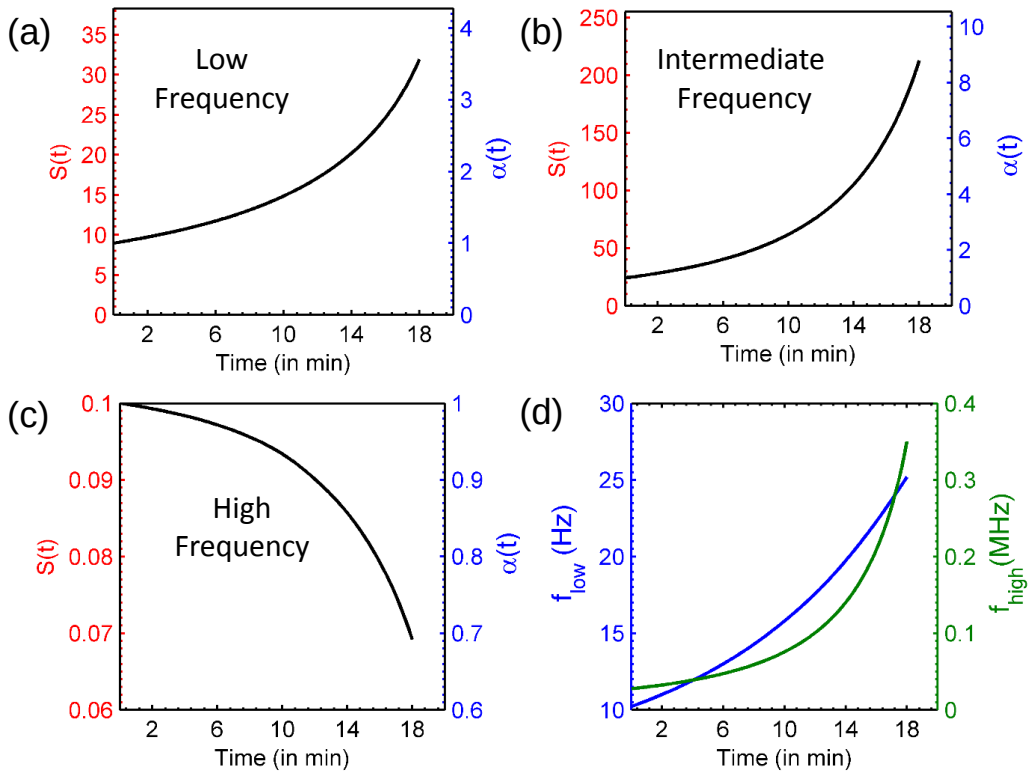

Fig. 2.9.: Sensitivity as a function of evaporation time for (a) low frequency operation (b) intermediate frequency operation (c) high frequency operation (d) Evolution of cut-off frequencies as a function of time for $n_0 = 10$ μ M and $V_0 = 3$ μL.

sensor as normalized change in admittance of droplet containing analyte (Y_ρ) with respect to a reference solution i.e. DI water (Y_{DI}). Therefore,

$$S(t) = |\frac{Y_\rho(t) - Y_{DI}(t)}{Y_{DI}(t=0)}| = \alpha(t) \times |\frac{Y_\rho(t=0) - Y_{DI}(t=0)}{Y_{DI}(t=0)}|. \tag{2.13}$$

Low frequency operation is independent of droplet geometry, but can be used for sensing

In this range of frequency $f \ll f_{\text{low}}(t)$ for all $0 < t < \tau$, the double layer capacitance is the dominant component i.e. $Y(t) \sim j\omega C_{\text{dl}}(t)$. As the droplet shrinks and the concentration increases, the reduction in the double layer thickness is reflected in increasing C_{dl}. The sensitivity of this mode of operation can be defined

as the change in the double layer capacitance upon addition of chemical/biomolecule ($C_{dl,\rho}$) with respect to a reference solution (DI water) ($C_{dl,DI}$). Using Eq. (2.13) with $Y(t) = j\omega C_{\mathrm{dl}}(t)$, the sensitivity is given by,

$$S(t) \sim \frac{C_{dl,\rho}(t) - C_{dl,DI}(t)}{C_{dl,DI}(t=0)} = \frac{\Delta C_{dl,\rho}}{C_{dl,DI}(t=0)}. \tag{2.14}$$

The amplification in sensitivity relative to time $t = 0$ is obtained by inserting Eq. (2.12) in Eq. (2.14), i.e.,

$$\alpha(t) = \sqrt{\frac{V_0}{V(t)}} \approx \frac{1}{(1-\frac{t}{\tau})^{\frac{n}{2}}} \tag{2.15}$$

where we have used the empirical approximation of $V(t)/V_0$ from Eq. (2.9). Note that the amplification factor is independent of the contact angle of the droplet at any time. Fig. 2.9(a) shows the sensitivity and amplification factor for very low frequency mode of operation of a sensor with initial ion concentration $n_0 = 10$ μM.

Intermediate frequency operation is the most sensitive regime

This regime of operation occurs when $f_{\mathrm{low}}(t) \ll f \ll f_{\mathrm{high}}(t)$, and therefore $Y(t) \sim G_{\mathrm{sol}}(t)$. In this regime, the capacitive response of the ions is no longer relevant and the in-phase response of the ions with respect to the applied signal dictates the net impedance.

The sensitivity $S(t)$ in this regime of operation can be defined in terms of the conductance change upon addition of chemical/biomolecule (G_ρ) with reference to DI water (G_{DI}),, i.e.,

$$S(t) = \frac{G_\rho(t) - G_{DI}(t)}{G_{DI}(t=0)} = \alpha(t)\frac{\Delta G_0(t=0)}{G_{DI}(t=0)}, \tag{2.16}$$

where $\Delta G_0 = G_\rho(t=0) - G_{DI}(t=0)$ and the amplification factor,

$$\alpha(t) \approx \frac{g_0}{g(t)} \times \frac{V_0}{V(t)} \sim \frac{1}{(1-\frac{t}{\tau})^n} \tag{2.17}$$

relates the sensitivity enhancement obtained as a function of time. Note that even though, $g(t)$ is monotonically increasing as a function of time, the net amplification factor ($\alpha(t)$) still increases due to considerable reduction in droplet volume $V(t)$. This equation suggests that a very high sensitivity can be achieved if we operate the sensor in a frequency regime where G_{sol} is dominant. Fig. 2.9(b) shows the sensitivity and amplification factor for intermediate frequency mode of operation of a sensor with initial ion concentration $n_0 = 10\ \mu$ M.

High frequency operation is unsuitable for determining droplet composition but good for determining the shape

This regime occurs when $f \gg f_{\text{high}}(t)$, so that $Y(t) \sim j\omega C_{\text{geo}}(t)$. Again the sensitivity of the system can be defined as

$$S(t) = \frac{C_{\text{geo},\rho}(t) - C_{\text{geo},DI}(t)}{C_{\text{geo},DI}(t=0)} = \alpha(t)\frac{\Delta C_{\text{geo},\rho}(t=0)}{C_{\text{geo},DI}(t=0)}, \tag{2.18}$$

where $C_{\text{geo},\rho}$ and $C_{\text{geo},DI}$ are respectively the geometry capacitances for the droplet with chemical/biomolecules and the reference solution (DI water). The amplification in sensitivity relative to time $t = 0$, is given by,

$$\alpha(t) = \frac{g_0}{g(t)}. \tag{2.19}$$

Since $g(t)$ is a monotonically increasing function of time, the sensitivity in this regime of operation degrades with time i.e. $\alpha(t) \leq 1$. Fig. 2.9(c) shows the evolution of sensitivity ($S(t)$) and amplification factor ($\alpha(t)$) as a function of time. It is assumed that the permittivity change of the solution upon addition of chemical/biomolecules is 10%.

Further, for a conductance based sensor (with negligible change in solution permittivity), $\Delta C_{\text{geo},\rho} = 0$ and hence this regime is unsuitable for biomolecule detection. However, if one is interested in characterizing the time-dependent evolution of the ge-

ometry of the droplet (e.g. shape or volume), this frequency regime is ideally suited, since the impedance is independent of salt/analyte concentration and depends exclusively on droplet geometry.

Time-dependence of cut-off frequencies: In general, as the droplet evaporates, the relative importance of a particular circuit component changes as well. This is because the cut-off frequencies, $f_{\text{low}}(t) = \frac{2}{2\pi R_{\text{sol}}(t) C_{\text{dl}}(t)}$ and $f_{\text{high}}(t) = \frac{1}{2\pi R_{\text{sol}}(t) C_{\text{geo}}(t)}$, themselves evolve with time; as the boundaries of the frequency band shift, the circuit may become more resistive/capacitive at a given frequency of operation. Fig. 2.9(d) shows the evolution of lower and upper cutoff frequencies for a droplet containing salt solution with initial concentration $n_0 = 10$ μM. Given the time and frequency dependence as discussed in Section 2.5, one can determine the frequency of operation for which $\Delta Y(t)$ is maximum for a given set of parameters, such as mobility of ions (μ) and applied bias (V_e). For example, in case μ of ions is large, it would be preferable to operate the sensor in resistive regime for optimal sensitivity. For such an operation, a frequency choice, f_{optimal} such that

$$10 \max(f_{\text{low}}) \leq f_{\text{optimal}} \leq \frac{1}{10} \min(f_{\text{high}}). \tag{2.20}$$

would be appropriate, since this will ensure that the resistive component at any time is atleast 10 times larger (dominantly resistive) than the capacitive component. When the applied bias is large, so that double layer capacitance is significant, a frequency of operation $f_{\text{optimal}} \leq \frac{1}{10} \min(f_{\text{low}})$ would ascertain the operation in dominantly capacitive regime. However, a very large applied bias may not be desirable because it would yield unreasonably low frequencies for capacitive operation and lead to faradaic currents [127] that can contaminate results of impedance spectroscopy. For a more realistic case, when substrate parasitic capacitance must be accounted for (discussed in next section), the upper cut-off frequency is given by $f_{\text{high}}(t) = \frac{1}{2\pi R_{\text{sol}}(t)(C_{\text{par}} + C_{\text{geo}}(t))}$. This implies that the upper cut-off frequency can be substantially lower if the parasitic capacitance (C_{par}) is large. If $10 \max(f_{\text{low}}) \geq \frac{1}{10} \min(f_{\text{high}})$, it is impossible to

operate the sensor in dominantly resistive regime and the parasitic capacitance must be suppressed to increase f_{high}.

2.6.2 Implications of parasitic impedance of the substrate, Z_{par}

So far, we have focused exclusively on Z_{drop}, assuming that the parasitic capacitance/resistance of the substrate is negligible. However, in real systems the parasitic capacitance can be a major limitation to the sensitivity of the device and must be accounted for. Parasitic capacitance dominates at intermediate to high frequencies and can limit frequency range of operation of the sensor. It can either be obtained from experiments with droplet-free measurements or through detailed numerical simulation/analytic modeling. Here, we consider numerical/analytic evaluation of parasitic capacitance for two different substrates which are commonly used for impedance-based sensors:

Glass is an ideal substrate for sensing

Due to its low cost, transparency and low dielectric constant, glass is an ideal candidate for use as a substrate for the sensor. The parasitic capacitance is estimated by numerical simulation of the structure shown in Fig. 2.10(a) using Sentaurus, an advanced multidimensional device simulator [132]. A bias V_{dc} is applied between the electrodes and Laplace equation ($\overrightarrow{\nabla}.(\varepsilon_{\text{glass}}\overrightarrow{\nabla}\varphi) = 0$) is solved to determine the potential, φ and electric field, E inside the substrate. Charge Q_{dc} is estimated on the positive electrode by Gauss Law *i.e.* $Q_{\text{dc}} = \int_{\Omega}\overrightarrow{D}.d\overrightarrow{S} = \int_{\Omega}\varepsilon_{\text{glass}}\overrightarrow{E}.d\overrightarrow{S}$. The capacitance of the substrate is then given by $C_{\text{par}} = Q_{\text{dc}}/V_{\text{dc}}$. An analytic expression for capacitance of coplanar electrodes was derived by Wei [147], *i.e.*

$$C_{\text{par}} = \frac{\varepsilon_{\text{glass}} H_E}{2K(k)/K(\sqrt{1-k^2})}. \tag{2.21}$$

where $K(k)$ is the complete elliptical integral of first kind with $k = L/(L+W)$, $\varepsilon_{\text{glass}}$ denotes the permittivity of glass substrate and H_E is the electrode length.

Fig. 2.10(b) and (c) show the simulation (numerical/analytic) of the parasitic capacitance for different electrode separations (width = 900 μm) and for different electrode widths (separation= 20 μm). The capacitance depends weakly on the electrode separation and width. Numerical simulation is in good agreement with the analytic expression. The marginal difference in simulation and analytic estimate comes from the fact that Wei derived Eq. (2.21) by neglecting the fringing fields in the transformed coordinate system.

SOI substrate has huge parasitic contribution

The silicon-on-insulator (SOI) is a popular substrate in the semiconductor industry because it minimizes the leakage currents, radiation-induced photocurrents, latch-up effects, etc. [148] in comparison to conventional bulk substrates. However, the same leads to huge parasitic losses for impedance sensors, as the electrodes can couple to the doped silicon below the top oxide layer which leads to a large parasitic capacitance. Fig. 2.10(e) and (f) shows the numerical simulation results for parasitic capacitance of an SOI substrate (Fig. 2.10(d)) for different electrode separations (with width $W = 700$ μm) and different widths (with separation, $L = 20$ μm) respectively. The parasitic capacitance of SOI structure ($\sim$ 0.1 nF) is nearly 3 orders of magnitude larger than that of the glass substrate ($\sim$ 0.1 pF). Also, the parasitic capacitance for the SOI substrate increases linearly with increase in the width of the electrodes.

A first order estimate of parasitic capacitance can be obtained by assuming the top silicon layer to be metal, so that net capacitance $C = \frac{WH_E\varepsilon_{\text{ox}}}{2t_{\text{ox}}} = 0.97$ nF. However, since the top silicon layer has finite conductivity, the actual capacitance is smaller than the estimate which is observed in the simulation. Regardless, such a large parasitic coupling decreases $f_{\text{high}} \sim \frac{1}{2\pi R_{\text{sol}}(C_{\text{geo}}+C_{\text{par}})}$ and confines the optimum sensor operation close to the low/intermediate frequency regimes [27].

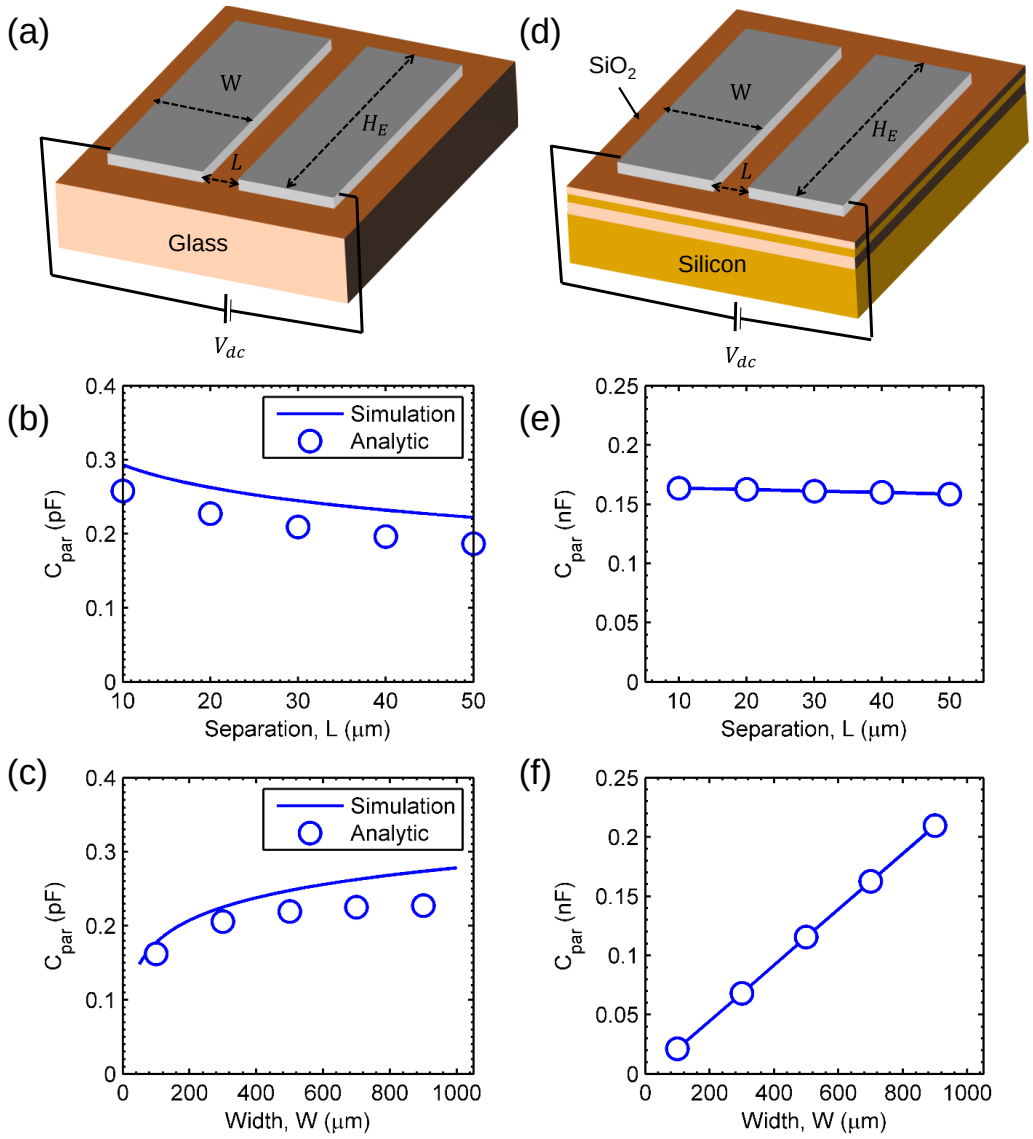

Fig. 2.10.: Simulation of parasitic capacitance for two different substrates. Geometry used for the simulation for glass substrate (a) and SOI substrate (d). Variation of parasitic capacitance as a function of (b) , (e) electrode separation and (c), (f) electrode width for glass and SOI substrate respectively.

If one must perform droplet characterization on SOI substrate at very high frequencies, a parallel plate detection system as described in Sadeghi *et al.* [125] may be used. This will ensures that most of the electric field from the electrode is confined within the droplet resulting in less sensitivity to the substrate contribution.

2.7 Experimental verification

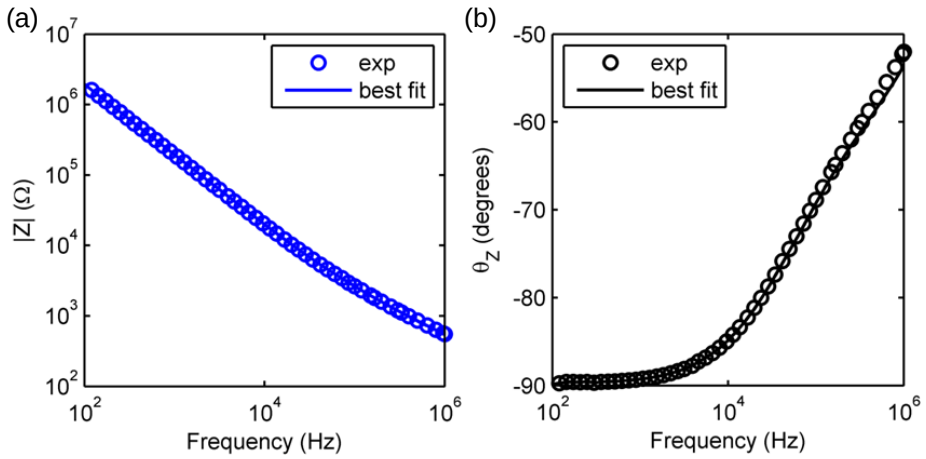

Fig. 2.11.: Experimental data for (a) magnitude and (b) phase of the parasitic impedance as a function of frequency.

In order to validate the model described in the numerical section, both time and frequency response of droplets containing different DNA concentrations were analyzed. The DNA solution (purchased from Fermentas, Inc.) had 850 bp long synthetic molecules in 1xTAE buffer solution. The DNA molecules were precipitated using an isopropanol precipitation method and resuspended in nuclease-free DI water. Additional experimental details are provided in Ebrahimi *et al.* [27].

Frequency response of the system at t =2 min was calibrated with the numerical model (see Eq. (2.2)) to determine the ionic conductivity (σ) for different DNA concentrations (see Fig. 2.12(a)-(f)) [149]. Using this ionic conductivity (σ), the time response of the system was determined using $Z = Z_{\text{drop}}(t)||Z_{\text{par}}$ (see Eq. (2.10), Fig. 2.13 (a),(b)). Z_{par} was obtained from the droplet free measurement on the substrate (see Fig. 2.11). The ionic conduction was assumed to take place due to H^+ and OH^- ions as the experiments were performed using DI water containing DNA molecules.

Since, the concentration of the DNA molecules is small ($<$ nM), we assume the dielectric permittivity of the DNA solution to be same as that of pure water. This

assumption is in agreement with experimental results reported by Takashima *et al.* [150] on DNA solutions at concentration below 1%. However, if the concentration of DNA molecules is large, the frequency dependent dielectric relaxation of DNA

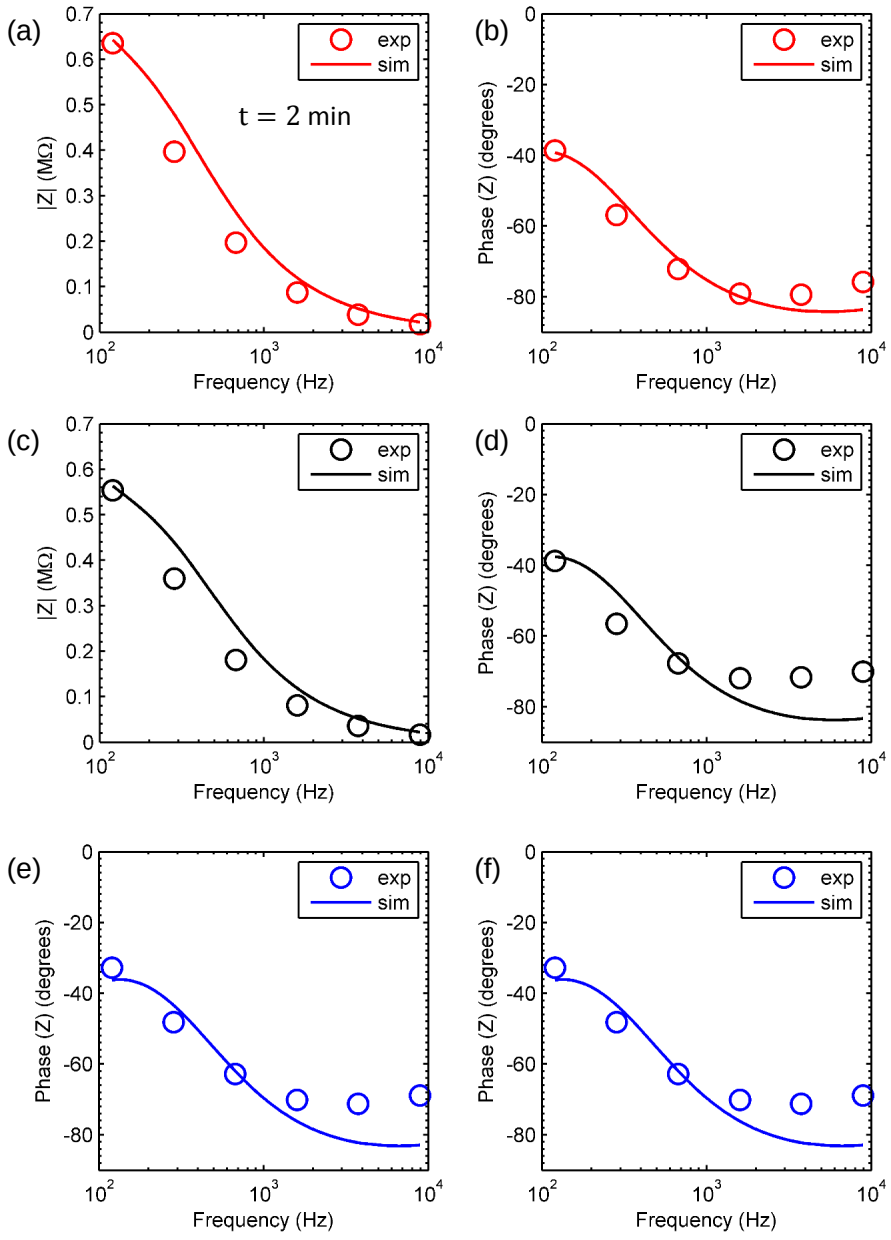

Fig. 2.12.: Impedance Magnitude and Phase vs. Frequency (calibration curves) at $t = 2$ min for different DNA concentration (a),(b) 330 fM; (c),(d) 3.3 pM; and (e), (f) 33 pM.

solution [151] must be accounted for in the geometric capacitance (C_{geo}) discussed in Section 2.3.

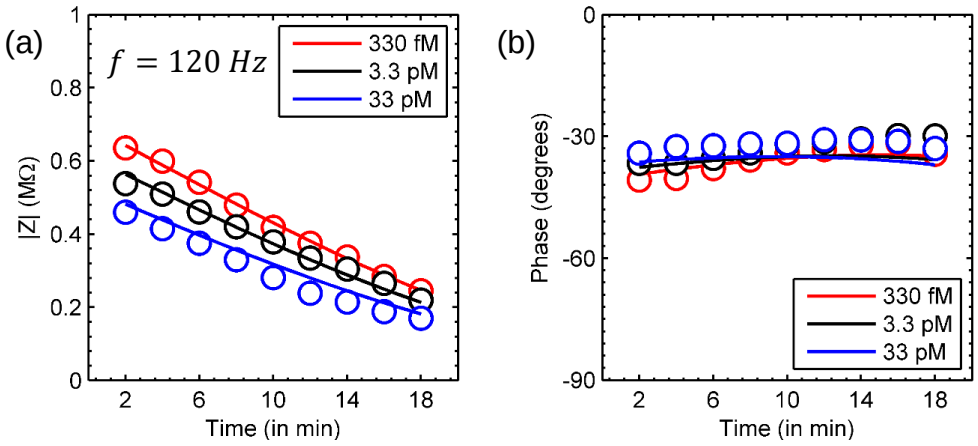

Fig. 2.13.: Impedance Magnitude and Phase vs. Time for different DNA concentration: 330 fM (red), 3.3 pM (black) and 33 pM (blue). Lines and circles represent simulation and experiment respectively.

Inspite of the various simplifying assumptions made in Section 2.2, the model (solid lines) predictions agree with the experimental results (circles) remarkably well. Indeed, apart from fitting the $t = 2$ min conductivity at various analyte concentration, the model describes the time-evolution and frequency dependence of the droplet impedance consistently without any other fitting parameters. The key features of the experiments are reproduced: *First*, the model correctly estimates the frequency response of the system. At low frequency, the impedance is dependent on the composition of droplet (DNA) (compare, Fig. 2.12(a)-(f)). At high frequency, the impedance of the parasitic substrate dominates and yields essentially same impedance for different DNA concentrations, making high frequency regime unsuitable for detection. *Second*, Fig. 2.13(a),(b) shows that the time-evolution of the impedance predicted by the theoretical model correctly reproduces the features observed in the experiments. The impedance of the droplets with different DNA concentrations converge at higher times, due to decrease in droplet volume($\Delta Z(t) \propto V(t)^{\eta}$, where $\eta \approx \frac{1}{2}$ or 1 depending on whether C_{dl} or R_{sol} is dominant (refer Eq. (2.10), Eq. (2.11) and Eq. (2.12)). Due

to large parasitic capacitance, f_{high} varies in range 350 Hz-960 Hz from t= 0 to $t = 18$ min respectively. This limits the operation of the device to sub-KHz range for sensing operation even at larger times.

2.8 Limitations of the impedance model

Although the model described in Section 2.3 is appropriate for non-faradaic systems, it needs to be appropriately generalized for applicability to Faradaic systems. It can be done by including the charge transfer resistance (R_{ct}) and Warburg impedance (Z_{w}) in parallel with the C_{dl} (see Fig. 2.1)(c). If the amplitude of ac signal applied to the electrodes is small, then $R_{\text{ct}} = RT/(nFi_0)$, where R is the universal gas constant, T is the absolute temperature, F is the Faraday's constant, n is the number of electrons involved in the oxidation/reduction reaction ($O + ne^- \leftrightarrows R$) and i_0 is the exchange current which depends on the concentration of the redox species near the electrodes and standard rate constant [127]. Z_{w} depends on the frequency (f), the diffusion coefficient of the oxidant (D_O)/reductant (D_R), and concentrations of oxidant (C_O)/reductant (C_R), and n [127].

2.9 Conclusions

We have developed a comprehensive numerical and compact modeling framework for the impedance of an evaporating droplet. The model is simple, and yet the theoretical framework correctly predicts the complex, time-dependent electrical response of an evaporating droplet containing analyte molecules. Indeed, once the geometry factor $g(t)$ and the volume evolution $V(t)$ are determined, either through experiments or through numerical/analytic modeling, the response of the system is completely specified. As a result, this physics-based model can be used to optimize a variety of droplet-related systems (e.g., the operation of a droplet-based sensor) once the system parameters, such as mobility of ions and applied bias, are specified. The model also highlights the critical importance of the substrate for highly sensitive impedance-

based chem-bio sensing. Specifically, for example, the model suggests that, compared to typical SOI substrate, the reduced parasitic impedance of a glass substrate would improve the overall sensitivity as well as provide a broader bandwidth of operation. Furthermore, higher frequencies can be used to characterize the droplet shape and size, since the impedance in that regime is independent of the droplet composition. If one must use SOI substrate for integration purposes, a comparable level of sensitivity is obtained only if the operating frequency is reduced to an extent that completely eliminates the effects of parasitic impedance on the overall impedance of the system.

3. DROPLET DESALTING FOR BIOLOGICAL APPLICATIONS

Potentiometric biosensors, which can detect the analyte charge directly, allow label-free detection and are easily miniaturized. Since the target molecules conjugate with the probe molecule only in salt-based electrolyte solutions, screening by these ions fundamentally limits the sensitivity of charge-based (potentiometric) biosensors. In Chapter 2, we discussed how a droplet sensor overcomes fundamental diffusion-limited response by monitoring the impedance at regular time-intervals as the droplet evaporates. In this chapter[1], we show that the finite volume of the droplet also makes it possible to electrostatically modulate the ionic concentration locally near the sensor. This control of ionic concentration could pave the way for multiplexed label-free electronic detection in physiological solutions without sacrificing sensitivity. Further, this could open up avenues in bias mediated polymerase chain reaction (PCR), and configurable isoelectric protein separation (ISP).

3.1 Introduction

Advances in improving the transducer: Nanowire-based FET devices [152] have facilitated label-free electronic detection of a range of small biomolecules, including nucleic acids [153–156], proteins [94, 157], viruses [158, 159], etc. Silicon nanowire devices benefits from the scalability of nanofabrication techniques and paved an attractive route towards multiplexed detection with arrays of FETs [157]. While the performance of the transducer has improved significantly, through incorporation of high-k gate dielectrics [154,160] and optimization of device geometry [161,162], relatively lit-

[1] The content of this chapter is adapted/reproduced from Ref. [106], Copyright 2015, AIP Publishing LLC. and from Ref. [108] with permission from IEEE.

tle effort has been dedicated towards overcoming fundamental limited response [126]. On one hand, decades of research on indirect pH-based detection [163, 164] has met with success towards marquee applications such as DNA sequencing with the ISFET [165, 166] and led to recent commercial demonstration of genome sequencing using large scale arrays of CMOS FETs [2]; on the other hand, given the inability for direct electrical detection from physiological samples, a commercially viable solution has been elusive for integrating nanowire FETs within portable-scale diagnostics. In order to overcome this major hurdle, it is necessary to directly address the problem of excess salt ions that interfere with sensing.

Salt ions interfere with biomolecular detection: The background excess of ions in aqueous media greatly complicates the detection of charged species due to heavy shielding of electrode-electrolyte interfaces as well as the target molecules by the electrostatic double layer (EDL) [167–169]. The relevant phenomenological lengthscale is the distance it takes for an electric field induced by a charged molecule to decay down to $1/e$ of its original value, also known as the Debye screening length [127, 170], λ_D:

$$\lambda_D = \sqrt{\frac{\varepsilon k_B T}{2 N_A q^2 n_0}}. \tag{3.1}$$

where ε is the dielectric permittivity, k_B the Boltzmann constant, T the temperature, N_A the Avogadro number, q the fundamental electronic charge and n_0 the ionic strength of the electrolyte. Physiological fluids, such as blood, plasma and serum, are replete with salts with ionic strength values in the range of 135-140mM and, at these concentrations, their Debye length is smaller than 1 nm. In a typical DNA hybridization reaction over a sensor, negative charges are added or an associated change in pH follows when a target DNA strand (1-10 nm) undergoes hybridization with a capture probe functionalized on the sensor surface. Since, the biomolecule (for example, DNA) charge is spread over its length, most of the charge is not mirrored into the transducer but into the solution (the potential induced due to biomolecule

charge decays within the distance on order of debye length). As a result, surface charges residing on the biomolecules cannot actively participate in modulating the charge of the FET [6,171,172]. In order to maximize both signal and sensitivity, it is essential to minimize the ion concentration (n_0) near the surface so that the largest fraction of the molecular charge from the target can be transferred to the device. **Conventional approaches to mitigate screening:** Various approaches have been adopted to mitigate this fundamental screening-limited sensitivity of potentiometric sensors:

1. Commonly used technique includes detection in low-ionic strength electrolytes, either by performing binding-sensing steps at low ionic strength [14] or using a flow-through apparatus that performs the binding and the sensing steps at different ionic strengths [15]. Both the approaches, however, reduce the binding affinity of the target molecule to the immobilized probe, which may degrade selectivity (the ability of a sensor to differentiate between target vs. parasitic molecules).

2. In another approach, Elnathan *et al.* demonstrated a method for direct detection of biomolecules in untreated serum by using fragmented antibody-capturing units. The reduced size of antibody allowed the analytes to bind closer to the sensor surface [17], and hence improved sensitivity.

3. The third approach relies on detection of biomolecular dipoles at high frequency [16]. At high-frequency, the ions do not have sufficient time to form the screening layer, and hence the sensitivity is improved.

Unfortunately, at present, these techniques are neither cost-effective, nor easily integrated into a droplet-based platform.

Droplet based method suppresses screening in a different way: Droplets offer a fundamentally different approach to desalting: Due to finite number of ions in sub-nL droplet, it is possible to temporarily desalt the droplet electrically near

the sensor region to maximize the sensitivity. In Section 3.2, we discuss the concept and operational principle of the desalting device. In Section 3.3, we discuss the numerical and analytical model to determine the desalting efficiency of the system. In Section 3.4, we discuss the design guidelines for ensuring the desalting. In Section 3.5, we discuss the experimental results which confirm the theoretical hypothesis. In Section 3.6, we discuss the application of desalting in a) sensitivity enhancement in FET based charge sensor, b) electrostatic denaturation of DNA for sensor reusability and isothermal DNA amplification, c) isoelectric protein focusing by electrostatic modulation of pH.

3.2 Concept and Operational Principle

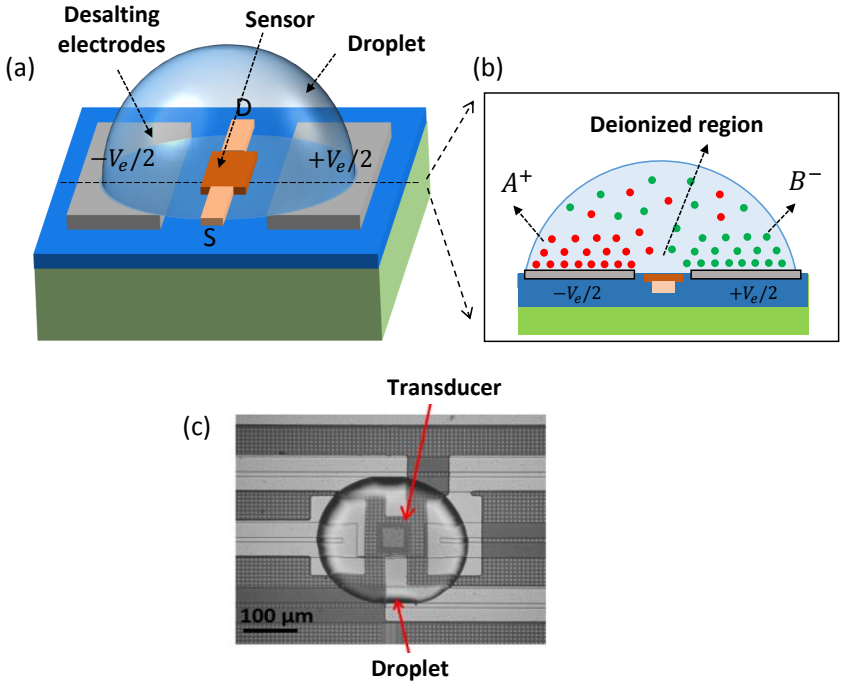

Fig. 3.1.: Schematics (a) and (b) of electronic desalting in microdroplets. (b) By absorbing salt ions in the EDLs of desalting electrodes, the bulk of the droplet can be depleted. (c) Micrograph of two pairs of on-chip desalting electrodes patterned around a transducer and encapsulated within a droplet. The transducer's salt-dependent response can be modulated using this construct.

A schematic for localized electronic desalting is shown in Fig. 3.1 . A desalting voltage, V_e is applied across the on-chip metal electrodes as shown in Fig. 3.1(a) and (b). Fig. 3.1(c) shows an image of a FET sensor surrounded by micro-patterned electrodes (O(100 μm $\times$ 100 μm)) and a microinjected droplet in air within which the desalting-sensing experiment is performed. The microdroplet is stabilized with the incorporation of glycerol, which has been shown to prevent evaporation of sub-nanoliter volumes on transistors during heating experiments [102]. This is because glycerol has a smaller vapor pressure [173] as compared to the water, and hence reduced evaporation rate.

For an unbiased droplet, the concentration of positive ($p(\overrightarrow{r})$) and negative ions ($n(\overrightarrow{r})$) at any spatial position $\overrightarrow{r}$ within the droplet is uniform *i.e.* $n(\overrightarrow{r}) = p(\overrightarrow{r}) = n_0$, where n_0 is the ionic concentration. However, with desalting bias, a large fraction of the positive and negative ions from droplet bulk accumulate within the EDLs over the negative and positive polarity electrodes, respectively. For a sufficiently high applied bias and electrode area, this causes a substantial decrease in n and p from the rest of the droplet. In order to minimize side effects such as redox reactions, gas bubbling and heating [174] that occur under strong forcing fields due to overpotentials, the electrode bias should be small (below the electrolysis limit of the sensing solution).

3.3 Theory of Electrostatic Desalting

In order to determine the degree of desalting in the droplet with ionic concentration n_0, at an arbitrary bias V_e, we need to solve for the potential distribution, ψ and concentration of cations, p and anions, n throughout the volume of the droplet. Guoy-Chapman theory is traditionally used to determine the concentration of the ionic species in bulk solution [127]. The concentration of ionic species can be related to the potential, ψ inside the solution as follows:

$$p = n_0 \exp\left(-\frac{zq\psi}{k_B T}\right) \qquad\qquad n = n_0 \exp\left(\frac{zq\psi}{k_B T}\right). \tag{3.2}$$

where, z is the valency of salt ions. The potential (ψ) and ionic concentrations (p and n) within the solution can be obtained in equilibrium by solution of Poisson-Boltzmann Equation:

$$-\nabla.(\varepsilon\nabla\psi) = zq(p-n). \tag{3.3}$$

However, for large biases, the theory predicts unreasonably large concentration of ions near the electrode interface and the theory must be modified to account for finite size of ions must be used. Kilick *et al.* [175] proposed a modified Poisson-Boltzmann (MPB) theory to account for steric effects due to finite ion size. The concentration of the ionic species can be obtained by solving MPB:

$$\nabla.(\varepsilon\nabla\psi) = -zq(p-n) = -zqn_i\frac{2\sinh(\frac{zq\psi}{k_BT})}{1+2\nu\sinh^2(\frac{zq\psi}{2k_BT})}. \tag{3.4}$$

where, n_i is the bulk ionic concentration away from the electrodes in region of zero electric field. The packing fraction, $\nu = 2n_ia^3$, accounts for the finite size of the molecules, so that the density does not exceed $1/a^3$. For a bulk system, the number of ions in the solution can be considered infinite and the ionic concentration away from electrodes, n_i can be assumed same as the ionic concentration, n_0 of the solution. However, a droplet system involves additional complexity due to finite number of ions, and hence it also must account for ion conservation within the droplet. Therefore, the minimum concentration n_i within the droplet needs to be obtained self-consistently by solution of the MPB equation and the ion conservation equation.

In this section, we present two approaches to determine the degree of desalting for a given applied bias, ionic concentration and droplet volume. First, a numerical approach which solves the equations in a droplet based system self-consistently and second, a semi-analytical approach which determines the degree of desalting by approximating the 2D system to an equivalent 1D system.

3.3.1 Numerical Model

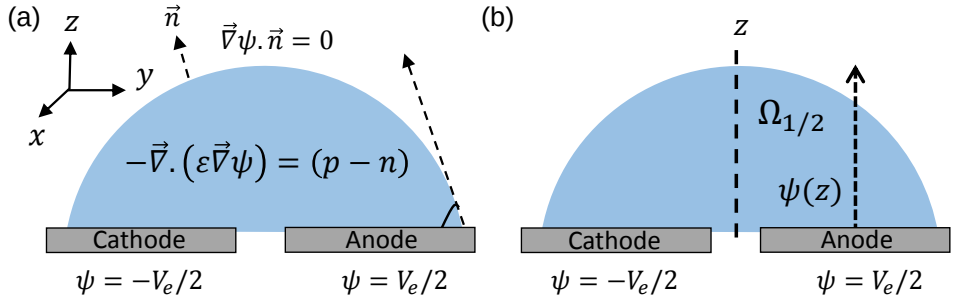

Fig. 3.2.: Domain for (a) Numerical, (b) Analytical Simulation

The numerical model solves Eq. (3.4) for a symmetric 1:1 electrolyte ($z = 1$) and implements the right hand side of equation as two discrete functions (see Eq. (3.5)) in droplet geometry shown in Fig. 3.2(a). An iterative solution of Eq. (3.5) and Eq. (3.6), subject to the boundary condition (Eq. (3.7)), determines ψ.

Degree of desalting reduces with increase in n_0 and decreases in V_e: Fig. 3.3 shows the potential profile (ψ), positive (p) and negative (n) ion density within a 300 pL droplet for 1 μM droplet at two different desalting biases. Ions pile up near the electrodes and, consequently deplete the droplet bulk. As the bias increases from 0.4 V to 1 V, the degree of desalting near the sensor region ($x = 0$) increases. Fig. 3.4 shows the dependence of the ion density on the initial salt concentration for same desalting bias ($V_e = 1$ V). As the ionic concentration of the solution increases, the desalting efficiency (i.e. the modified ionic charge density ($p(x, y)$ or $n(x, y)$) near the sensor relative to n_0) decreases due to partial screening of the electrode bias by the charge that builds up near the electrodes. While a 10 μM droplet can be desalted to a fraction, f less than 10^{-5} of its original value near the sensor at $1V$ bias, the 1 mM droplet can only be desalted to $f \sim 0.5$ at 1 V bias.

Although the numerical model provides the distribution of ions in the droplet, it is computationally intensive, and therefore an analytical model that can provide an

Table 3.1.: Numerical model for calculating ion profiles during desalting

Poisson Equation	$$-\overrightarrow{\nabla}.(\varepsilon\overrightarrow{\nabla}\psi) = (p-n) \quad (3.5)$$
For $p \leq 1/a^3$ or $n \leq 1/a^3$	$p = n_i \exp(\frac{-q\psi}{k_B T})$, $n = n_i \exp(\frac{q\psi}{k_B T})$
For $p > 1/a^3$	$p = 1/a^3, n = 0$
For $n > 1/a^3$	$n = 1/a^3, p = 0$
Ion conservation:	$$\int_\Omega p dV = \int_\Omega n dV = n_0 V \quad (3.6)$$
Boundary Condition: On Electrodes:	$$\psi = \pm V_{desalting}/2 \quad (3.7)$$ (Dirichlet Boundary Condition)
On Outer Boundaries:	$$\overrightarrow{\nabla}\psi.n = 0$$ (Neumann Boundary Condition)

estimate of degree of desalting as a function of the droplet geometry and applied bias would be useful.

3.3.2 Analytical Model

The parallel potential contour lines (specially for higher ionic concentrations of physiological interest) near the electrodes (see Fig. 3.4) suggest that the electric field near the electrodes is essentially perpendicular. Therefore, an analytical analysis based on Kilic *et al.*'s 1-D compact charge model [175] is possible. Based on ionic charge conservation:

$$\int_\Omega n_0 \, dV_\Omega = \int_{\Omega_{1/2}} (n(\overrightarrow{r}) + p(\overrightarrow{r})) \, dV. \quad (3.8)$$

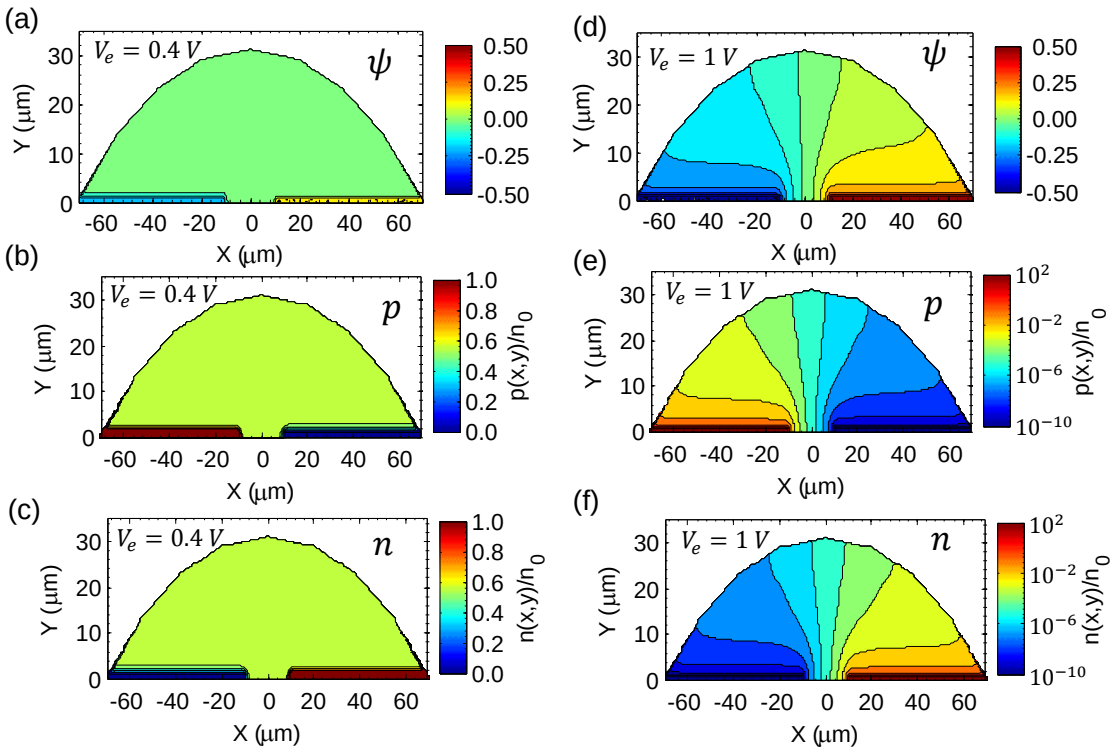

Fig. 3.3.: Numerical calculation of potential (ψ), and positive (p) and negative ion profile (n) in a 300 pL droplet 6100 μm^2 electrode area) for 1 μM concentration at 2 different desalting biases (V_e), i.e., 0.4 V ((a), (b), (d)) and 1.0 V ((d), (e), (f))

where, $n(\overrightarrow{r})$ and $p(\overrightarrow{r})$ represent the negative and positive ion distributions, respectively, and $\Omega_{1/2}$ denotes the region with one-half of the droplet volume as shown in Fig. 3.2.

$$n_0 V_\Omega = \int_{\Omega_{1/2}} (n(\overrightarrow{r}) + p(\overrightarrow{r}) - 2n_i)dV + \int_{\Omega_{1/2}} 2n_i dV. \tag{3.9}$$

The left integral on the right hand side of Eq. (3.9) can be divided into two parts: 1) due to the compact charge layer with thickness, l_c and density $1/a^3$, and 2) due to the double layer charge which exponentially decays. This gives,

$$n_0 V_\Omega \approx \frac{l_c A_e}{a^3} + \int_{\Omega_{1/2}} 2n_i(\cosh(\frac{q\psi}{kT}) - 1)dV + \int_{\Omega_{1/2}} 2n_i dV. \tag{3.10}$$

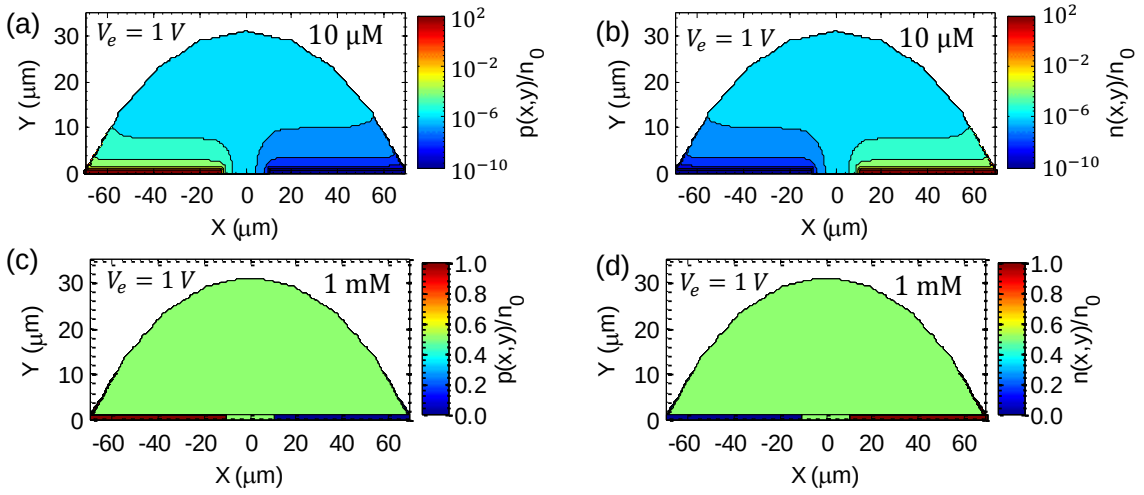

Fig. 3.4.: Numerical calculation of positive (p) and negative (n) ion profile in a 300 pL droplet 6100 μm^2 electrode area) for two different ionic concentrations, i.e., 1 μM ((a) and (b)), and 10 μ M ((c) and (d)) at 1 V desalting bias (V_e).

If we assume that the double layer is thin, $\psi(x, y, z) \approx \psi(z)$. The potential varies as [127]:

$$\psi(z) = 4\,\mathrm{artanh}\left(\tanh(\frac{u_0}{4})\exp(-\frac{z}{\lambda_i})\right). \tag{3.11}$$

where, λ_i is the modified debye length upon application of desalting bias. This gives,

$$n_0 V_\Omega = \frac{l_c A_e}{a^3} + 8 n_i \lambda_i A_e \sinh^2\left(\frac{qV_b}{4kT}\right) + n_i V_\Omega. \tag{3.12}$$

where,

$$V_b = V_c = \frac{kT}{q}\log\left(\frac{1}{n_i a^3}\right), \quad \text{for} \quad V_e > V_c, \tag{3.13a}$$

$$V_b = V_e \quad \text{for} \quad V_e < V_c, \tag{3.13b}$$

and,

$$l_c = \lambda_0\sqrt{2\nu_0}(-1 + \frac{f\nu_0}{2} + \sqrt{(1 - \frac{f\nu_0}{2})^2 + (|\frac{qV_e}{kT}| - \log(\frac{1}{a^3 n_i}))}), \quad \text{for} \quad V_e > V_c, \tag{3.14a}$$

$$l_c = 0, \quad \text{for} \quad V_e \leq V_c. \tag{3.14b}$$

λ_0 is the initial Debye length for the background ionic concentration, and $V_c = \frac{k_B T}{q} \log(\frac{1}{f n_0 a^3})$ is the critical voltage above which ionic charge starts to accumulate in the compact layer, $\nu_0 = 2 n_0 a^3$ and $f = n_i/n_0$ is the ratio of desalted ionic concentration and the initial ionic concentration in the center of the droplet. The potential drop across the double layer, $V_b = \min(V_e, V_c)$. Below the critical voltage, all charge resides within the double layer and, hence, $l_c \to 0$. n_i can be solved using Eq. (3.12) for any ionic concentration, n_0, and applied bias, V_e, for a given electrode area (A_e) and droplet volume (V).

Fig. 3.5 shows the comparison of the numerically obtained potential profile (ψ) and the negative ion density (n) as a function of distance z perpependicular to the positively biased electrodes. Simulation results indicate that the 1D approximation of the potential profile holds remarkably well. Further, the potential and the negative ion density drops off to the bulk value within a few nanometers. This indicates that most of the accumulated charge lies close the electrode interface.

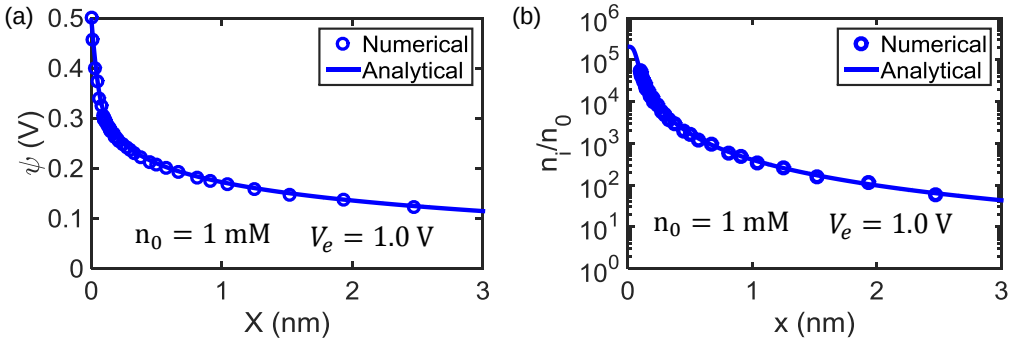

Fig. 3.5.: Numerical calculation of ion profile showing negative ion density in a 300 pL droplet 6100 μm^2 electrode area) at (a) 1 μM and (b) 10 μM background strength under 1 V desalting bias.

The amount of excess surface charge absorbed on the electrodes is given by,

$$Q_e = A_e\sigma_e = \mp \int_{\Omega_{1/2}} q(n-p)dV. \tag{3.15}$$

where, $-$and $+$ signs correspond to positive and negative electrode polarity, respectively. Assuming that the double layer is thin, we get an estimate of the surface charge density, σ_e, absorbed within the EDL over the electrodes i.e.

$$\sigma_e = \mp\frac{ql_c}{a^3} \mp 4qn_0\lambda_0\sqrt{f}\sinh\left(\frac{qV_b}{2k_BT}\right). \tag{3.16}$$

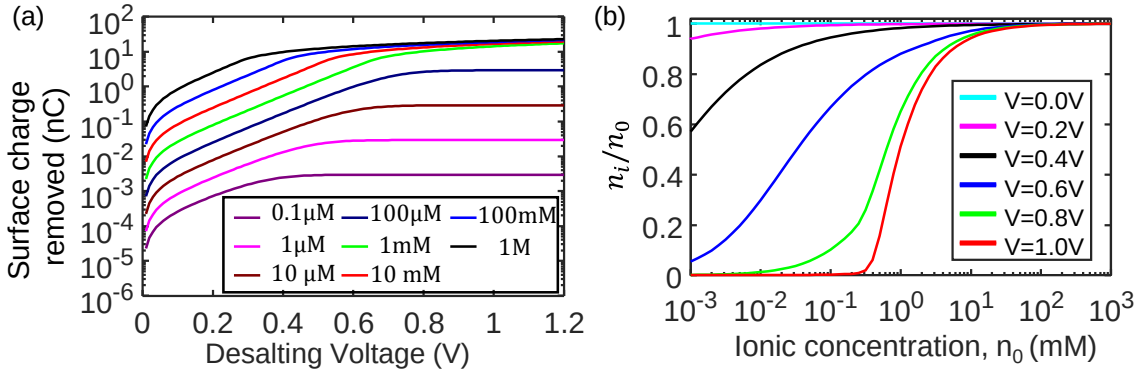

Fig. 3.6.: (a) Maximum surface excess ionic charge that may be absorbed into the EDL over an electrode (10^4 μm^2) from various solutions at non-Faradaic conditions, (b) Ion density at the center of the droplet is plotted as a function of salt concentration for different desalting bias.

Ionic charge absorbed by the on-chip electrodes from the droplet, as a function of the desalting bias, is plotted for various ionic concentrations in Fig. 3.6(a). The accumulated charge density in Boltzmann layer increases as $\exp(\frac{qV_e}{2k_BT})$. However, as the bias exceeds the critical value, charge begins accumulating in the compact layer and $l_c \approx 2\lambda_0\sqrt{n_0a^3\frac{qV_e}{kT}}$. We observe that, in low ionic strength droplets, the surface ionic charge absorbed in the EDL saturates with voltage due to a limited number of available ions. At higher concentrations, steric effects begin to dominate and are responsible for the diminished capacity. Fig. 3.6(b) shows the variation of

bulk ionic concentration (n_i) in the droplet as a function of initial salt concentration. The desalting efficiency of the system increases with the applied bias from 0 to 1.0 V. For small ionic concentrations, the critical voltage is large, hence, the droplet bulk is considerably desalted. For large ionic concentrations (>10 mM), however, we see that the desalting efficiency is drastically reduced due to finite capacity of polarizable electrodes for charge uptake. At these conditions, V_c is very small and charge accumulation is forced to occur within the compact layer while desalting the droplet. Since, the thickness of this compact layer is weakly dependent on the applied bias (i.e. $\sqrt{V_e}$), this leads to substantially lower desalting at high salt concentrations (100 mM).

3.3.3 Comparison between proposed theory and traditional theories

Fig. 3.7 shows the comparison of the double layer (DL) charge density obtained from the Guoy-Chapmann model (without finite size and finite number of ion effects), Modified Poisson-Boltzmann theory (MPB) (with finite size, but without the effect of finite number of ions) and the self-consistent theory (accounting for both finite size and finite number of ions). Following observations can be made:

1. As expected in all three models, the desalting efficiency increases as the applied bias across the electrode increases,

2. The models predict similar DL charge density when the applied bias is small, since the density of ions is still less than the maximum permissible limit defined by its size and the bulk droplet concentration is close to its original value,

3. For low salt concentration, the steric effects are negligible and both the GC model and MPB model predict similar charge density. However, the self-consistent model deviates due to significant bulk depletion of ions,

4. For high salt concentrations, the steric effects are dominant and hence the GC model and MPB model differ from each other. Further, the predictions of the

self-consistent model are closer to the MPB model at higher concentrations due to decrease in desalting efficiency.

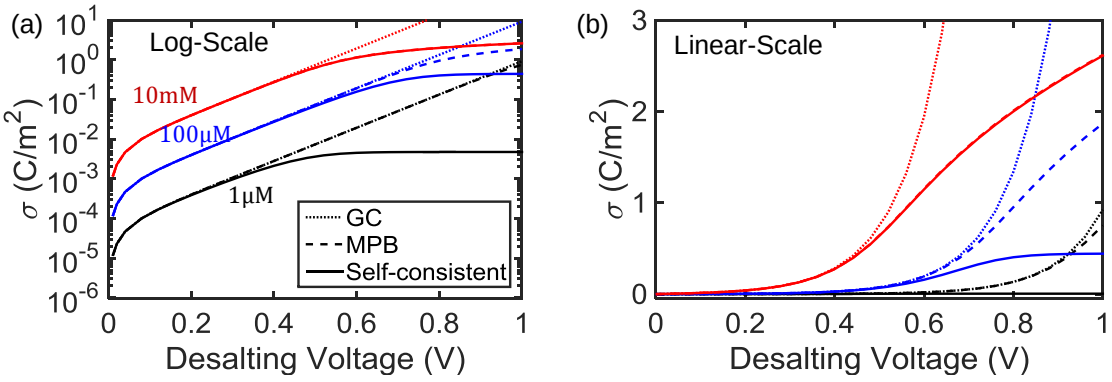

Fig. 3.7.: Comparison between different theories: ionic charge absorption vs. desalting bias

3.4 Design rules for droplet desalting

To relate the degree of desalting to applied bias and salt concentration, we determine the maximum droplet volume V_{max} that can be desalted to a fraction f of the original salt concentration, n_0 for a given electrode area, A_e. By rearranging Eq. (3.12), we get:

$$V_{\max} = A_e \left(\frac{8\sqrt{f}}{1-f} \lambda_0 \sinh^2 \left(\frac{qV_b}{4kT} \right) + \frac{l_c}{n_0 a^3 (1-f)} \right). \tag{3.17}$$

Need small V_Ω/A_e ratio for higher desalting: Fig. 3.8 (a) shows the ratio of droplet volume (V_Ω) to electrode area (A_e) that is required for desalting the droplet of various salt concentrations to a fraction $f = 0.5$. For desalting small ionic concentrations (<1 mM), the droplet volume to electrode area ratio can be considerably large ($> 100\ \mu m$). However, in order to desalt large ionic concentrations (> 100 mM) below the reduction potential, this ratio must be small ($< 1\ \mu m$). For example, with $100\ \mu m \times 100\ \mu m$ electrodes, we require 1 pL droplet volume spread over the

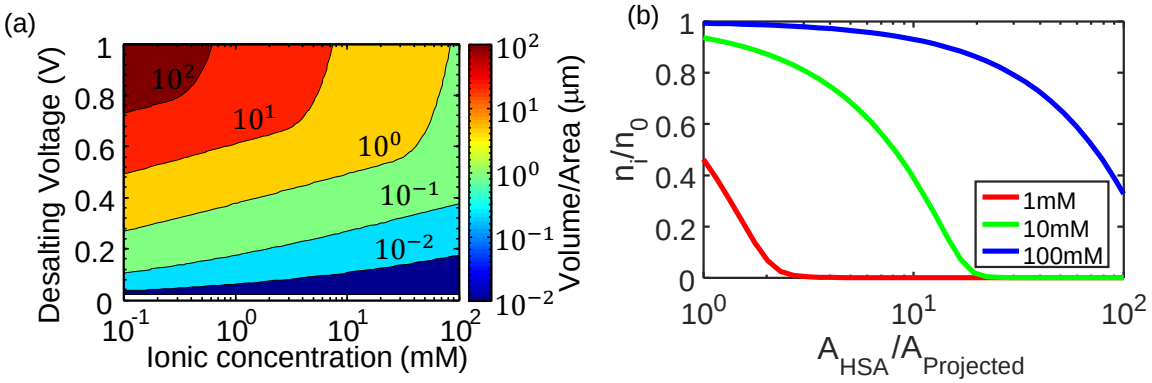

Fig. 3.8.: (a) Ratio of the volume of droplet to the area of the electrode required for desalting the droplet by 50%, as a function of desalting voltage and ionic concentration. Desalting at 100 mM concentration under 1 V desalting bias requires an aspect ratio of 1 μm, (b) n_i/n_0 as a function of enhancement in area ($\eta = A_{fractal}/A_{Projected}$) due to high-surface electrodes for different ionic concentrations

entire electrode area to match the desired ratio. However, this would require a super-hydrophilic surface [176] and such small droplets maybe difficult to stabilize on the electrode surface. Another approach could be to use high surface area (HSA) electrodes to desalt the droplets (will discuss in Section 3.5) which could enable depletion of more addressable droplet volumes ($>$ 100 pL) at 100mM concentration. Fig. 3.8(b) shows the desalting that can be obtained using a high-surface area electrode. n_i/n_0 is plotted as a function of the area enhancement (i.e. the high surface electrode area (A_{HSA}) with respect to the projected electrode area ($A_{Projected} = A_e$)). While desalting is negligible for 100mM with smooth electrodes, the droplet can be desalting to less than 50% of its original value for area enhancement $\sim$ 100X.

3.5 Experimental Demonstration of Desalting by Collaborators at UIUC

All experiments were performed using foundry fabricated CMOS FET devices (TSMC, Taiwan), with an extended gate architecture. On-chip platinum electrodes around the sensor were defined by a 1000 $\mathring{A}$ thick metal-2 layer, with adequate step coverage, through conventional photolithography, evaporation and lift-off. All surface

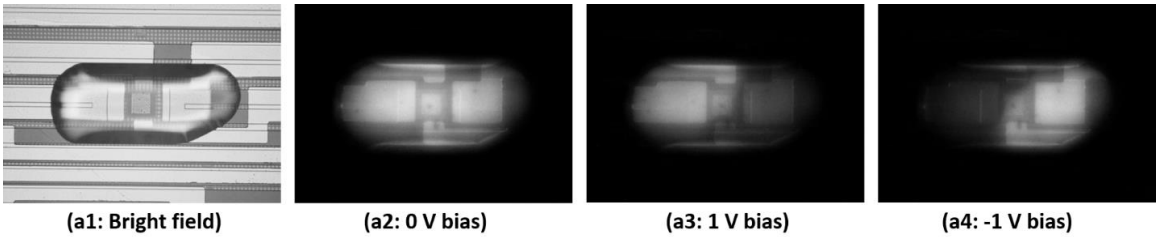

Fig. 3.9.: (a1-a4) Images of desalting in a droplet ([NaCl] = 1.174mM) in 4-electrode configuration, using surface functionalized SNARF-5F dye.

treatment chemicals were purchased from Sigma-Aldrich Corp., MO, USA. During each experiment, prior to electrolyte loading/exchange, chips were degreased and cleaned with oxygen plasma treatment in a diener benchtop RIE system (Thierry Corp., MI USA). For microdroplet experiments, 0.5-1.5 nL size droplets (including 13.5% added glycerol) were spotted using an IM-300 programmable microinjector (Narishige, Japan), with a 7 μm diameter glass needle tip mounted on a X-Y-Z micrometer stage for precise positioning of the droplet.

3.5.1 Imaging surface ionic changes during desalting

In order to demonstrate desalting experimentally, we performed fluorescence measurement on droplet with the surface functionalized with ion/pH sensitive SNARF-5F dye. This dye is known to fluoresce within the 5-8 pH range. The fluoresence response of the dye was measured as a function of desalting bias. Fig. 3.9(a1-a4) shows a device within a microdroplet and its fluorescent response at 1V desalting after 30 seconds, with both forward and reverse bias controls. In this experiment, both the North/West and South/East electrodes were biased to V_{e1} and V_{e2} respectively, leading to a desalting bias, $V_e = V_{e_2} - V_{e_1}$. The figure shows a gradient in fluorescence upon application of desalting bias. As expected the fluorescence image shows a partitioning along the diagnoal line of symmetry.

3.5.2 High-surface area electrodes for enhanced desalting

As discussed in Section 3.4, high-surface area electrodes (HSA) are required to obtain desalting for high salt concentrations. HSA platinum-black electrodes were prepared by known electrodeposition methods [177, 178], using a Gamry Reference 600 Potentiostat (Gamry Instruments, PA, USA). Pt-black was galvanostatically deposited on a seed layer of 100 nm thick Ti/Pt from dihydrogen hexachloroplatinate (0.08mM $H_2PtCl_6.6H_2O$, Sigma Aldrich, with 0.25 g/L of $(CH_3COO)_2Pb$, Alfa Aesar) at -0.08Acm^2 vs. Ag/AgCl. Decreasing the deposition current density helped with better process control for microelectrode tolerances. Fig. 3.10(a) shows micrographs of Pt-black deposited on test electrodes in a circular well (250 μm diameter, 20 μm spacing between electrodes) and on-chip electrodes in a rectangular well (250 μm $\times$ 100 μm) around a transducer. SEM image of these electrodes (Fig. 3.10(b)) confirms a highly branched, dendritic morphology and the critical dimension in the nanostructure is of the order of $\sim$ 50 nm, which should provide the necessary area increase for desalting from high salt conditions.

Examination of surface area enhancement through electrochemical impedance spectroscopy (EIS): We examined the surface area enhancement due to nanostructured HSA electrodes over smooth Pt by EIS [179–181]. Fig. 3.10(c) shows a Bode plots of the impedance of circular test electrodes in bulk 1X PBS. Surface area increase from smooth Pt to Pt-black is reflected in the large decrease in impedance magnitude at 1 Hz, or left-shifting of the phase minima towards lower frequency because of the increase in EDL capacitance. By comparing the ratio of capacitances (imaginary component) at low frequency, we observed that the electrically available increment was ca. 25-fold. The desalting capacity also increased for the test electrodes with the area enhancement, and we measured this within microdroplets at various desalting voltages.

Conditioning by cyclic voltametry (CV) further improves the surface area: Although the physical area was drastically enhanced (Fig. 3.10(c)) and ex-

pected to provide two orders of magnitude improvement, we only observed a limited increase during experiments. This may be attributed to either the incomplete coverage of the surface in contact with the droplet because of the increased surface energy cost of nanostructured surfaces that typically renders them repellant, or exclusion effects from steric issues that possibly come into play for ion absorption over a non-ideal surface as the roughness ($\leq$ 50 nm) approaches the phenomenological lengthscale, λ_D. However, by conditioning the electrode surface through cyclic voltammetry (CV) treatment [182], we can further improve and stabilize the surface characteristics of Pt-black for increased ion absorption during desalting. Test electrodes were cycled 5 times between -0.5 V and +0.9V vs. Ag/AgCl at the rate of 100 mV/s in 1X PBS. From the EIS results (Fig. 3.10(c)), we observed that the impedance at 1 Hz decreased further and the phase minima left-shifted to an even lower frequency. This translated to a 4-fold increase over the as deposited Pt-black so that, with CV treatment, the effective area of the electrodes increased by ca. 100-fold over smooth Pt.

3.5.3 Determination of desalting capacity by ionic current measurement

Table 3.2.: Desalting capacities of various electrodes measured in bulk and microdroplet

n0 (mM)	Smooth in bulk (%)	Smooth in droplet (%)	HSA electrodes in droplet (%)
100	0.0025	1.07	4.73
10.8	0.16	6.85	41.41
1.17	1.5	>99	>99

In order to determine degree of desalting experimentally, we determined the ionic charge accumulation using the experimentally measured transient ionic current at various desalting voltages through the on-chip electrodes. Fig. 3.10(d) shows experimental ionic current in a 10.8 mM microdroplet at 0.5 V and 1 V desaling bias for both smooth and HSA electrodes. As the electrodes absorbed salts in the EDLs through capacitive charging, the ionic current sharply decayed over time and tracked

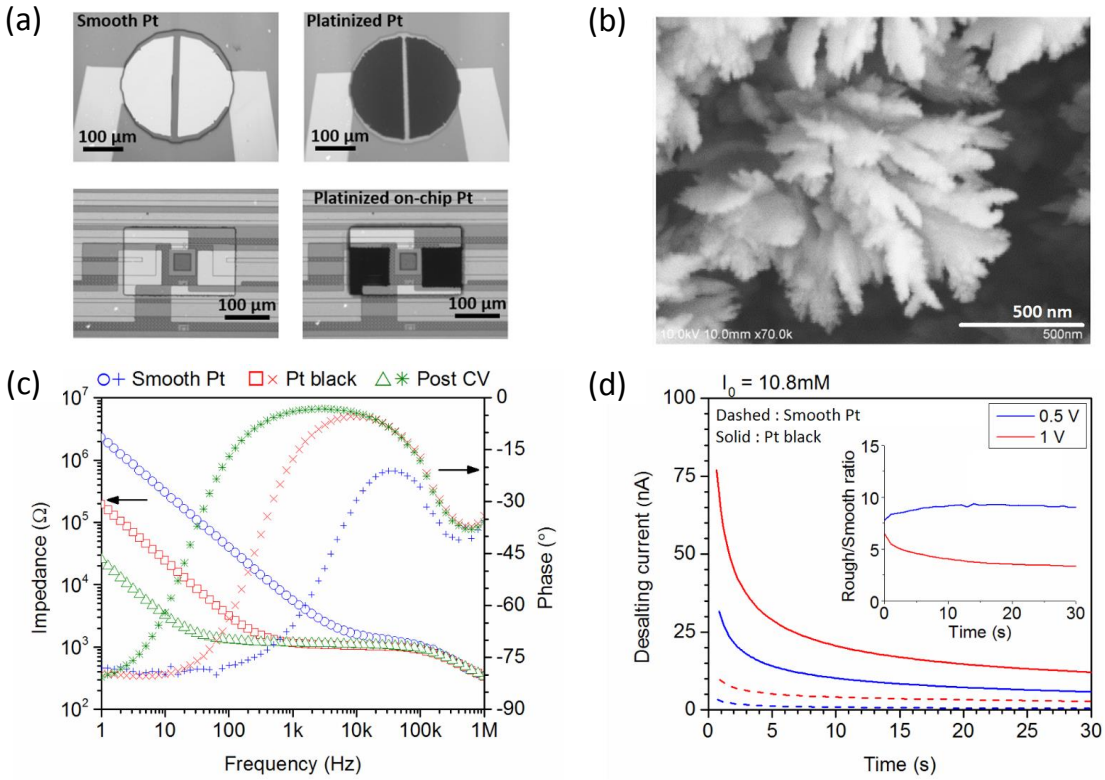

Fig. 3.10.: Imaging of electrode surfaces. (a) Images of Platinum-black (HSA) micro-electrodes patterned in test structures (circular electrodes as well as multi-electrode systems) through controlled electro-deposition process. (b) SEM image at high magnification (70,000X) shows a highly branched, dendritic nanostructure on the surface that leads to high surface area; Electrochemical characterization and performance testing of HSA electrodes. (c) EIS measurements show increased surface area available for desalting due to the nanostructures and subsequent improvement after cyclic voltammetry treatments that enable >100-fold available area increase. (d) Desalting current at 0.5 V and 1 V bias in nano-liter volume droplets show the increased ionic current flow due to the area enhancement of HSA electrodes over smooth electrodes. Inset shows the ratio of rough to smooth electrode transient at each time point.

the flow of ions as they depleted out from the droplet. The current flow between the on-chip electrode pair mirrored each other and we did not observe any leakage current. Total ionic charge separated during this process can be correlated with the predicted desalting capacity at various biasing conditions.

Table 3.2 summarizes the desalting performance of both smooth and HSA electrodes through experimental measurements in bulk (large 0.1 μL volumes) as well as

droplets (500 pL). In the bulk system, with smooth electrodes, we observed negligible salt removal from solutions that contain more than 1 mM of salt. This is in agreement with our calculations (see Fig. 3.8) as V/SA ratios (>>100) were extremely unfavorable for desalting. The capacity improved as we approached the microdroplet scale (V/SA $\sim$ 100), although it was only realistic for depleting at the low end of electrolytes (< 10 mM). The HSA electrodes (V/SA $\sim$ 1), however, demonstrated significant salt removal and we were able to deplete 42% from 10 mM and 5% from 100 mM electrolytes. This translates to ca. 30% increase in Debye length at 10 mM conditions.

3.6 Applications of desalting for biological applications

In this section, we discuss application of desalting to three different but very important applications, a) Improvement in sensitivity of charge-based potentiometric sensor, b) Electrostatic denaturation of DNA, and c) Configuration isoelectric protein seperator.

3.6.1 Improvement in sensitivity of charge-based sensor

As discussed earlier, the sensitivity of a charge-based sensor is fundamentally limited by screening due to counter-ions in the solution. The scheme to locally deplete the ions near the sensor region can be used to improve the sensitivity of the sensor. Nair *et al.* [126] showed that the sensitivity of the charge based FET sensor follows the following dependence on the ionic concentration i.e.

$$S = c_1 \left(\log\left(\rho_0\right) - \frac{\log\left(I_0\right)}{2} + c_2 \right). \tag{3.18}$$

where, c_1 and c_2 are constants [126] depending on the surface density of probes, the probe-target affinity, etc.

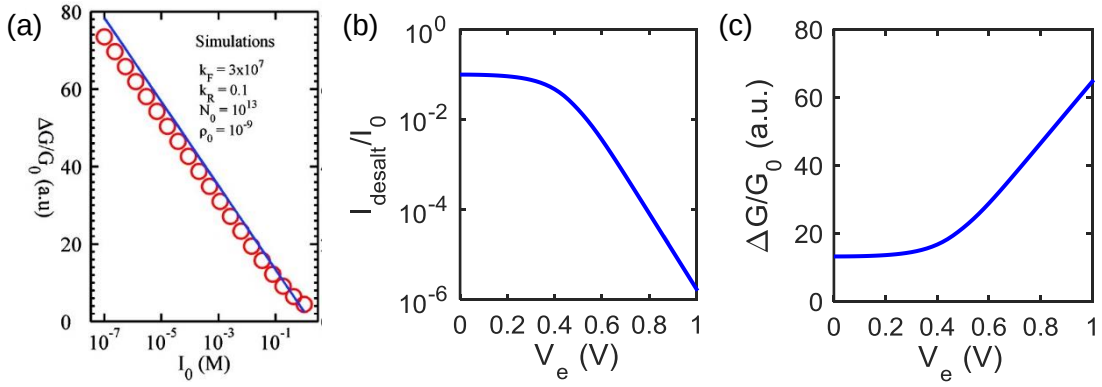

Fig. 3.11.: (a) Dependence of sensitivity on the ionic concentration. Figure reproduced from Nair *et al.* with permission from [126]. Copyright (2008) American Chemical Society, (b) The ionic concentration as a function of desalting bias for a droplet with high surface area electrodes (100X area enhancement), (c) Sensitivity improvement with desalting bias

Fig. 3.11(a) shows the plot of sensitivity ($S = \Delta G/G_0$) reproduced from Nair *et al.* [126]. The sensitivity decays logarithmically as a function of ionic concentration. Fig. 3.11(b) shows the simulation of the salt concentration near the sensor region (center of the droplet) as a function of the desalting bias for a droplet with radius 30 μm and an electrode area enhancement, 100X. The ionic concentration decays by almost 5 orders of magnitude as the desalting bias is increased from 0 to 1V. This results in an increase in sensitivity by almost 3 times as shown in Fig. 3.11(c).

Challenges: The probe-target binding requires a high-salt concentration and therefore, the desalting approach must be implemented as a two-step process: first, the biomolecule conjugation without desalting and next, the sensing step in which desalting is done by a transient voltage pulse to make sure that the conjugation between the probe-target pair is not affected. Further, the charged biomolecules such as proteins, nucleic acids, etc. may themselves be perturbed by the external bias used to desalt the droplet. Additional work must follow to demonstrate the viability of the approach for detection of these biomolecules.

3.6.2 Electrostatic denaturation of DNA

Since, DNA strands are negatively charged, cations are required to stabilize the DNA double helix [183]. For a given ionic concentration, there is a unique temperature at which the helix unfolds. In order to denature the DNA, enough energy must be supplied by increasing the solution temperature. Owxzarzy *et al.* [183] performed melting experiments on a set of DNA duplex oligomers with varied G.C content and length, and developed an empirical equation (see Eq. (3.19)) which fits the experimental data in literature.

$$\frac{1}{T_m\,(2)} = \frac{1}{T_m\,(1)} + (4.29f\,(G.C) - 3.95) \times 10^{-5} \ln\left(\frac{[Na^+]_2}{[Na^+]_1}\right) + 9.40 \times 10^{-6} \times \ln\left(\frac{[Na^+]_2}{[Na^+]_1}\right). \tag{3.19}$$

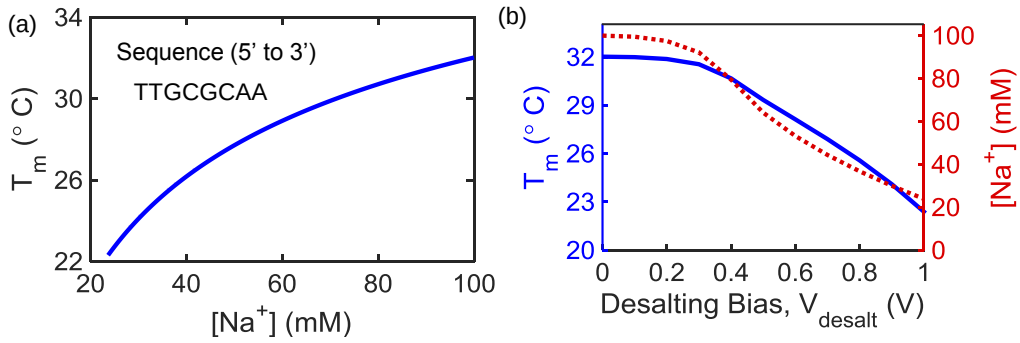

Fig. 3.12.: (a) Dependence of melting temperature (T_m) of the DNA oligomer on the sodium ion concentration ([Na^+]), (b) Bias dependence of [Na^+] in the droplet center (right) for a droplet with 30 μm radius and 30X electrode area enhancement, and T_m variation upon application of desalting bias.

Fig. 3.12 (a) shows the dependence of melting temperature for a DNA oligomer with 5' to 3' sequence (TTGCGCAA) based on Owxzarzy's formula. Our theoretical and experimental demonstration of desalting in small droplets suggests that it is possible to decrease the melting temperature of the DNA oligomers by decreasing the ionic concentration using the bias. Fig. 3.12(b) shows the variation of DNA T_m as a

function of desalting bias for the given DNA sequence. As the desalting bias increases, the bulk concentration is reduced and a reduced T_m is sufficient to unfold the DNA double helix. With appropriate choice of desalting bias, denaturation for the given sequence can be done at room temperature, suggesting the potential for isothermal room temperature PCR. Further, the ability to debind the DNA strands can also allow the reusability of functional probe layer by removal of target strands from the probe. The experimental demonstration of the desalting approach to denature DNA could be a future research direction to work upon.

3.6.3 Protein separation

A protein molecule is positively charged below its isoelectric point and negatively charged above that. Proteins are usually separated from a mixture by use of Isoelectric focusing (IEF). This technique involves adding an ampholyte solution into immobilized pH gradient (IPG) gels. These gels are made up of acrylamide co-polymerized with varying acidic/groups to enable a stable pH gradient. Protein solution is placed in this gel matrix and an electric field is applied across the gel matrix. The positively charged protein migrates towards the negatively charged electrode. As it migrates through a gradient of increasing pH, its charge continuously decreases until it becomes neutral and is no longer affected by the field.

The desalting method can be used to build such a pH gradient in a droplet by modulation of the H^+ ion concentration in a pH solution. Fig. 3.13(a) shows the pH gradient established by the desalting scheme on a solution with pH = 4. Fig. 3.13(b) shows the variation of the pH at the center of the droplet as a function of the desalting bias, and resultant charge of PSA/IgG protein molecules. Since, the isoelectric point (IP) of the proteins are different, these will migrate to different points in the droplet, and can be collected thereafter. The droplet desalting based scheme could provide a versatile tunable replacement of IPG gel to separate proteins electrostatically.

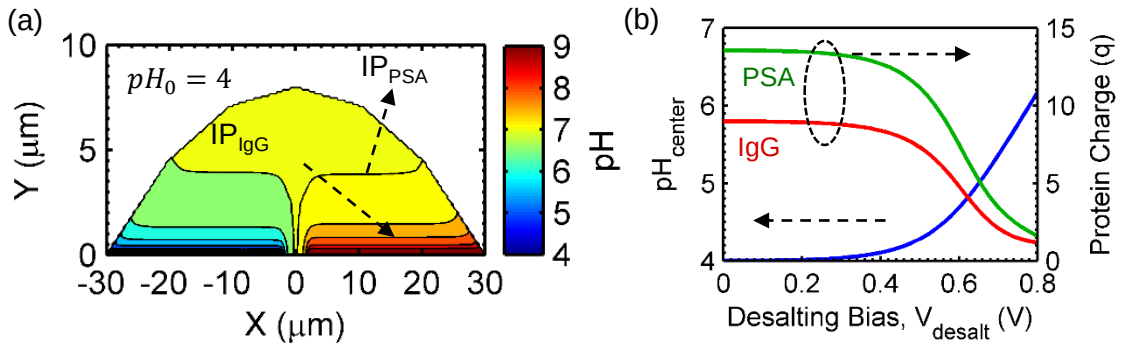

Fig. 3.13.: Application of electrode bias pulls [H^+] ions towards the electrode thereby depleting the droplet bulk of the [H^+]. (a) The pH gradient can potentially be used to separate prostate specific antigen (PSA) from Immunoglogin (IgG) protein. Labeled contours show the Isoelectric point (IP) for the two proteins. The proteins stabilize their position along their respective IP contour lines. (b) The pH in droplet bulk (left) and protein charge (right) as a function of desalting bias.

3.7 Conclusion

Salt plays an important role in many biological processes. For example, salt is essential for conjugation of the DNA strands. Background salt excess in solution is a fundamental limiting factor in the performance of label-free biosensors for molecular detection. In this chapter, we discussed a methodology to locally deplete the ions around a sensor using on-chip electrodes. Volumetric limitation of the desalting capacity adds the requirement of having to do so in a droplet and making this approach more synergistic with digital droplet based assays [184]. While low ionic concentration solutions, can be depleted using smooth electrodes, desalting at higher salt concentrations ($\geq$ 1 mM) efficiently requires use of high-surface area electrodes. This was demonstrated using platinum-black electrodes with a highly dentritic structure. The approach to modulate ionic concentration in droplets could pave way for highly sensitive detection of biomolecular charge. Further, the approach can potentially be useful for isothermal-PCR, and configurable isoelectric protein separation. The experimental demonstration of these applications is an interesting research direction to work upon.

4. DROPLET HEATING FOR BIOLOGICAL APPLICATIONS

In Chapter 2, we discussed an approach to characterize an evaporating droplet using a non-Faradaic sensor and showed how the evaporation helps to reduce the response time and improve sensitivity. In Chapter 3, we discussed an approach to locally deplete the ionic concentration within a droplet and showed that it could be used overcome the fundamental screening limited response of a charge-based FET sensor. In this chapter[1], we will discuss an approach to perform localized heating of individual sub-nanoliter volume droplets. This can allow for new applications including hybridization of low copy number DNA molecules, lysing of single cells, interrogation of ligand-receptor interactions, and rapid temperature cycling for amplification of DNA molecules.

4.1 Introduction

Literature Survey: Previous on-chip, localized heating designs focused on peltier heaters, resistive heaters, or other methods [185–189]. A variation on the resistive heater uses a transistor as a heater whereby adjusting the source-drain current via modulation of the gate voltage can result in heating of the fluid above the device [190]. This approach, however, required a very wide gate region ($\sim$ 700 μm) and is incompatible with the use of picoliter scale droplets. A second approach involving mirowave heating of picoliter droplets in a microfluidic device has been studied [191], but this method does not allow for individualized heating of droplets and also requires mineral oil as an encapsulation layer to minimize evaporation. Finally, optical heating meth-

[1] The content of this chapter is adapted/reproduced from Ref. [102] with permission from Proceedings of National Academy of Sciences.

ods have also been used [192–194], but suffer from setup complexity for individually heating multiple droplets and similarly require an encapsulation layer to minimize evaporation. Earlier, Elibol *et al.* [195], Reddy *et al.* [196], and Jokilaakso *et al.* [197] demonstrated heating via use of individual transistors by applying a voltage bias at 10MHz and 10-25 V_{rms} between the transistor's leads and the bulk substrate of a silicon-on-insulator (SOI) microribbon transistor. This technique focused on characterization of the temperature profile at the surface of a device in a bulk fluid and did not offer control of thermal cross-talk and by-product diffusion between heating elements.

Organization of chapter: In this chapter, we discuss the methodology to locally heat sub-nL droplets without evaporation using on-chip field-effect transistor (FET) based microwave heaters. In Section 4.2, we discuss the device structure and operational principle. In Section 4.3, we discuss the theory of dielectric heating, and discuss the numerical model to determine the temperature rise within these miniaturized droplets. We discuss the size and time dependence of temperature profile within the droplet. In Section 4.4, we discuss the model validation using the experimental results . In Section 4.5, we discuss the application of the localized heating for single-base pair mismatch detection and selective detection of DNA target molecules.

4.2 Device Structure and Operational Principle

Fig. 4.1(a) shows the scheme used to locally heat the droplet. The source/drain terminals are shorted and an high-frequency AC bias is applied between the source/drain and substrate. The droplet of solution is placed onto the device (see Fig. 4.1(b)). The electric field developed due to the AC bias results in dielectric heating of the solution.

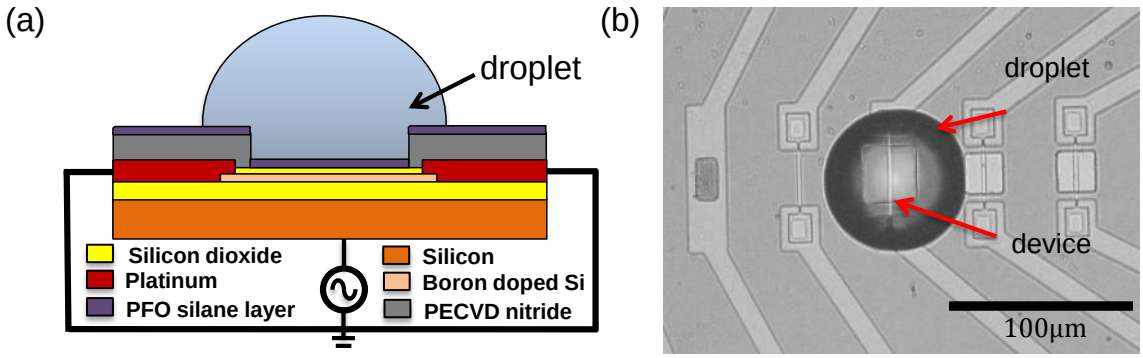

Fig. 4.1.: (a) Cross-section of device showing electrical schematic with an AC voltage applied between the device and the bulk silicon. (b) A top-view of $\sim$ 225pL droplet placed on a heating element. The heating element is 2 μm wide in a 20 μm $\times$ 20 μm release window. Scale bar, 100 μm.

4.3 Theory of dielectric heating and Model System

Dielectric heating is a phenomenon by which a material can be heated with a time-varying electric field. The intrinsic and induced dipole align in direction of the time-varying field. The energy associated with this alignment is dissipated as heat into the surrounding environment. If the medium is electrically conductive, in addition to the dipolar relaxation, additional component arises due to ionic drift of ions which leads to Joule heating. The power density (P) associated with dielectric heating can be related to the frequency (ω) of osciallation of electric field, the loss factor of the material (ε''), vaccum permittivity (ε_0), and the ac electric field (E_{ac}) as follows:

$$P = \frac{1}{2}\sigma E_{ac}^2. \tag{4.1}$$

where, $\sigma = \sigma_i + \sigma_d$, σ_i and σ_d are the conductivities associated with ionic drift and the dipolar relaxation, respectively. The σ_d can be related to ε'' as follows:

$$\sigma_d = \varepsilon_w''\varepsilon_0\omega. \tag{4.2}$$

and the conductivity terms due to the ionic drift in the ionic solution is given by:

$$\sigma_i = q(n_{Na^+}\lambda_{Na^+} + n_{Cl^-}\lambda_{Cl^-}). \tag{4.3}$$

where n_{Na^+} and n_{Cl^-} are the densities of positive and negative salt ions, respectively; and λ_{Na^+} and λ_{Cl^-} are the molar conductivity of the positive and negative salt ions, respectively. As the ionic conductivity increases, the contribution of the joule heating term becomes more dominant and it leads to a marked increase in dielectric heating in the solution. In order to determine the spatial and temporal variation of temperature within the droplet, we first solve for electrical equations to determine the power-dissipation (see Eq. (4.1)) at every point within the droplet, and then solve thermal equations to determine the temperature rise within the droplet.

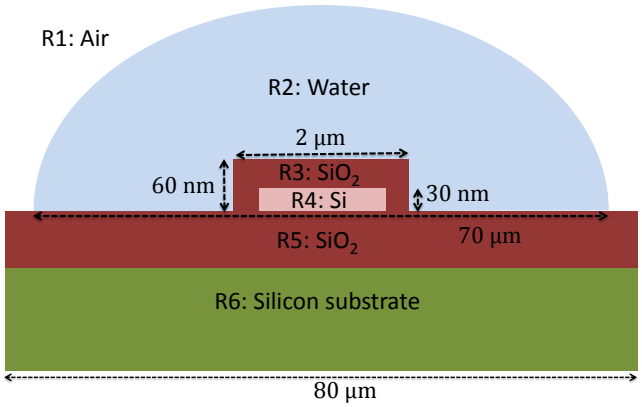

Fig. 4.2.: Structure for electrostatic and thermal simulation.

4.3.1 Electrostatic Simulation Shows Localized Fields

Calculating AC Electric Field, E_{ac}: Dielectric heating depends on the square of E_{ac} (see Eq. (4.1)). The electric field E_{ac} is obtained by solving the Poisson equation (see Table 4.1, Eq. (4.4)) numerically for the simulation domain shown in Fig. 4.2. Due to high frequency of applied ac bias (10 MHz), the electrostatic screening due to the ac field may be neglected [198], hence ρ is set to zero in the RHS of Eq. (4.5) (see

Table 4.1). Finally, the source and drain are grounded i.e. fixed at zero potential; therefore we assume the channel potential to be zero as well (see Table 4.1, Eq. (4.6)). The solution of Eq. (4.5) & Eq. (4.6) (Table 4.1) allows us to calculate E_{ac} throughout the device, including the droplet. Fig. 4.3 shows the electric field profiles in the droplet for different ac biases. Following observations can be made: a) Maximum electric field occurs near edges of the active device due to fringing effects, b) As the applied bias increases, the maximum electric field increases and the fringing field becomes more uniform across the oxide.

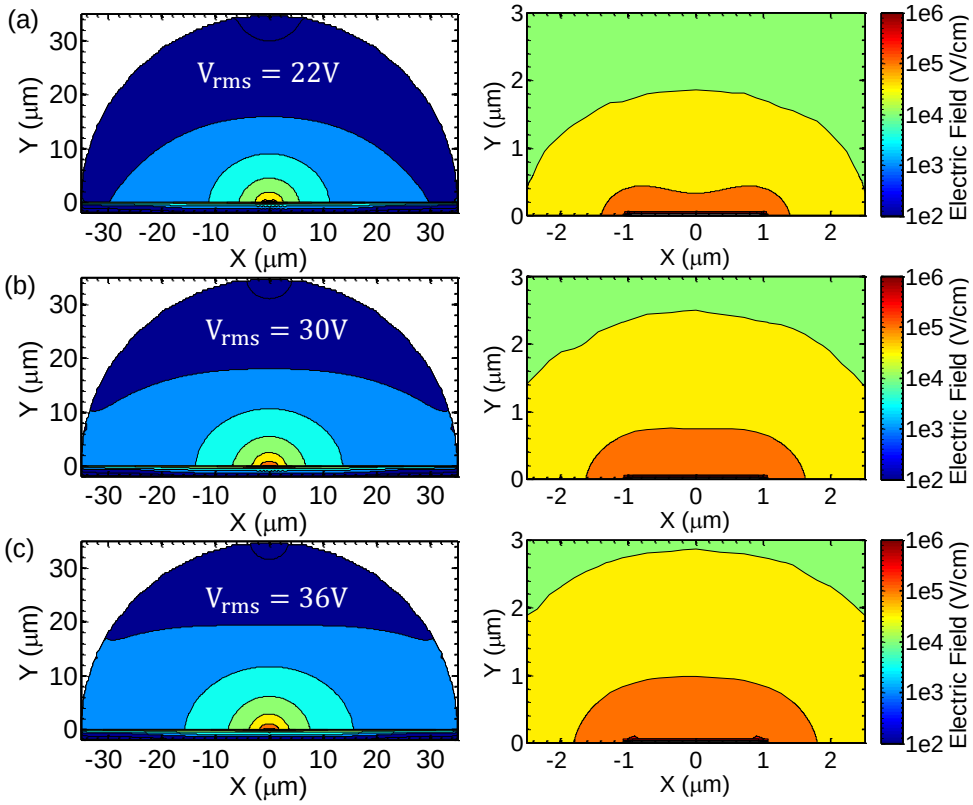

Fig. 4.3.: Electric Field within the droplet for different applied biases. Right hand side figures are the zoomed version of left hand side figures near the core of the droplet.

Calculating ionic conducitivity, σ_i: Next, we determine the density of positive (n_{Na^+}) and negative (n_{Cl^-}) ions within the droplet by solution of DC Poisson Equation (see Eq. (4.7) and Eq. (4.8), Table 4.1). The surface charge, σ_{OH} is calculated by assuming droplet pH = 7 and surface OH group density, $N_s = 5 \times 10^{14}$ cm^{-2} [133].

Table 4.1.: Numerical Equations for Electrostatic Simulation

DC/AC Simulation	
$$-\nabla.(\varepsilon\nabla\varphi) = \rho$$ $$\varphi = \varphi_{ac} + \varphi_{dc}$$	(4.4)
AC Simulations (for obtaining the electric field profile):	
Region: R2-R6 $$-\nabla.(\varepsilon\nabla\varphi_{ac}) = 0$$ $$E_{ac} = -\nabla\varphi_{ac}$$	(4.5)
Boundary Conditions: $$\varphi_{ch} = 0; \quad \varphi_{bulk} = V_{BG}$$	(4.6)
DC Simulations (for obtaining the conductivity):	
Region: R2 $$-\nabla.(\varepsilon\nabla\varphi_{dc}) = q(n_{Na^+} - n_{Cl^-})$$ $$n_{Na^+} = n_0\exp(-q\varphi/k_BT), \qquad n_{Cl^-} = n_0\exp(q\varphi/k_BT)$$	(4.7)
Boundary Condition: $$-\varepsilon_w\nabla\varphi_{dc} = \sigma_{OH}$$ (Region: R2-R3, R2-R5 interface)	(4.8)

σ_i is calculated by assuming it to be proportional to ionic densities (n_{Na^+} and n_{Cl^-}) with an additional proportionality constant (α) (see Eq. (4.10)). Since the potential, V_{dc} due to surface charges (due to formation of double layer) is small ($< 0.1V$), the effective conductivity is essentially identical to that of bulk solution. Regardless, the approach described here is general and should apply to any biasing conditions. Note that the decoupling of the ac and dc Poisson equation (see Eq. (4.2)) is justified because the ac voltage $V_{rms}(22 - 36V) \gg V_{dc}(< 0.1V)$.

Table 4.2.: Description of Symbols

Symbol	Description
φ	Net potential
φ_{ac}	Potential due to applied ac bias
φ_{dc}	Potential due to surface charges
ρ	Density of charges
φ_{ch}	Channel potential
φ_{bulk}	Potential at the bulk contact
V_{BG}	Applied substrate ac bias
σ_{OH}	Surface charge due to ionization of Silanol (SiOH) groups
n_{Na^+}, n_{Cl^-}	Positive and negative ion density within the droplet
T	Temperature
t	Time
σ	Conductivity in the specified region
σ_{ion}	Conductivity due to Na^+ and Cl^- ions
E_{ac}	Field obtained from ac simulation

Table 4.3.: Parameters for electrostatics simulation

Parameter	**Symbol**	**Value**	**Ref**
Permittivity in Free Space	ε_0	8.85×10^{-12} F/m	[143]
Relative Permittivity in Air	ε_a	1	-
Relative Permittivity in Water	ε_w	78.8	[144]
Relative Permittivity in oxide	ε_{ox}	3.9	[199]
Relative Permittivity in silicon	ε_{Si}	11.8	[200]
Electronic Charge	q	1.610^{-19}C	[143]
Boltzmann Constant	k_B	1.3810^{-23} m^2kgs^{-2}	[143]

4.3.2 Thermal Simulation Shows Localized Heating

The temporal and spatial variation of temperature ($T(t, x, y)$) profile within the droplet is determined by solving the time-transient thermal equation:

$$\rho_V C \frac{\partial T}{\partial t} = \nabla.(\kappa \nabla T) + P. \tag{4.9}$$

where ρ is the mass density, C is the specific heat, and κ is the thermal conductivity of the material. The power density (P) is determined from the solution of the ac electric

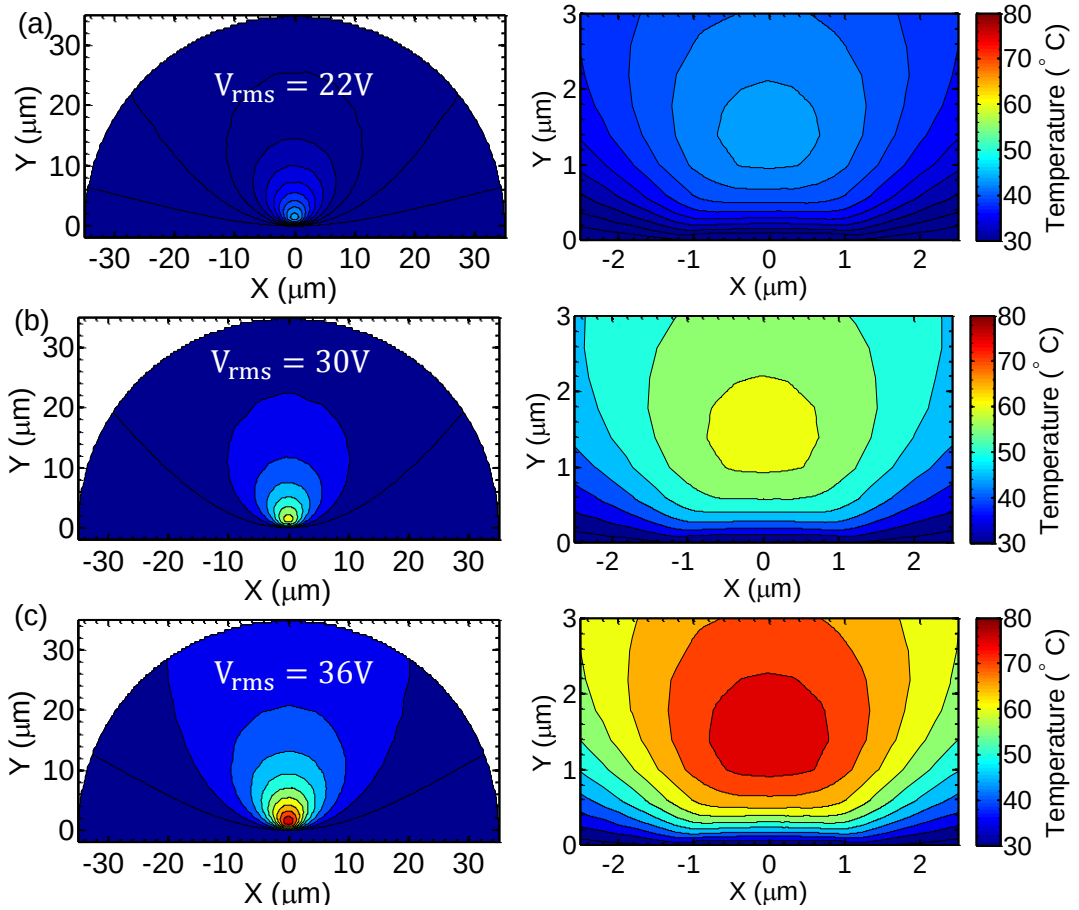

Fig. 4.4.: Temperature within the droplet for different applied biases. Right hand side figures are the zoomed version of left hand side figures near the core of the droplet.

field (E_{ac}) and the ionic conductivity (σ_i) obtained from the electrical simulation as describe earlier. The power density in different regions (see Fig. 4.2) of the device can be determined as follows:

$$
\begin{aligned}
P &= \frac{1}{2}(\sigma_d + \sigma_i)E_{ac}^2, \\
\sigma_i = q\alpha(n_{Na^+}\lambda_{Na^+} + n_{Cl^-}\lambda_{Cl^-}), \quad & \sigma_d = \varepsilon_w^{''}\varepsilon_0\omega \quad \text{(Region: R2)}, \\
\sigma_i = 0, \quad & \sigma_d = \varepsilon_{ox}^{''}\varepsilon_0\omega \quad \text{(Region: R3, R5)}, \\
\sigma_i = 0, \quad & \sigma_d = 0 \quad \text{(Region: R1, R4, R6)}.
\end{aligned}
\tag{4.10}
$$

The heat generation terms include both Joule heating of ions in solution (σ_i) as well as dielectric relaxation in water and oxide (σ_d). Convective transfer of heat from the droplet to the air was approximated by assuming that the droplet is covered by a 5 μm thick boundary layer. Radiative heat transfer, however, was neglected in the simulation. The gate oxide and the bottom oxide are assumed to be free of any trap charges. The physical constants used in the thermal simulation are listed in Table 4.4. Dirichlet boundary condition ($T_b = 300$ K) was applied on all the outer boundaries for the simulation and thermal fluxes were assumed to be continuous across the interfaces.

Fig. 4.4 shows the temperature profile within the droplet for different applied biases. Since the fringing field is maximum close to the active device, the heating is localized localized near the center of the droplet (Fig. 4.3). Further, the temperature at the perimeter of the droplet returns close to the room temperature. This forms a room-temperature encapsulating shell of fluid around the droplet's heated core, which helps minimize evaporation. This is further evident from the temperature cut at the center of the device along the direction perpendicular to oxide surface as shown in Fig. 4.5.

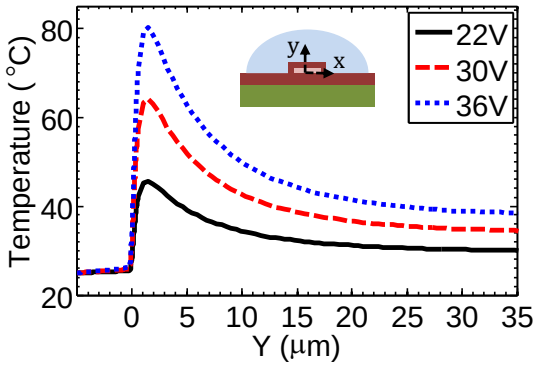

Fig. 4.5.: Temperature within the droplet at X=0 μm for 20, 30 and 36 V.

Table 4.4.: Thermal Simulation Parameters

Parameter	**Symbol**	**Numerical value/units**	**Ref**
Thermal conductivity of Air	k_a	0.024 W/m.K	[201]
Thermal conductivity of Water	k_w	0.58 W/m.K	[202]
Thermal conductivity of oxide	k_{ox}	1.4 W/m.K	[145]
Thermal conductivity of silicon	k_{si}	149 W/m.K	[145]
Mass density of air	ρ_a	1.2 kg/m^3	[201]
Mass density of water	ρ_w	1000 kg/m^3	[145]
Mass density of oxide	ρ_{ox}	2600 kg/m^3	[145]
Mass density of silicon	ρ_{si}	2300 kg/m^3	[145]
Specific Heat Capacity of air	C_a	1000 J/kg.K	[201]
Specific Heat Capacity of water	C_w	4180 J/kg.K	[203]
Specific Heat Capacity of oxide	C_{ox}	1000 J/kg.K	[145]
Specific Heat Capacity of silicon	C_{si}	710 J/kg.K	[145]
Loss factor in oxide at $10MHz$	ε''_{ox}	3.9×10^{-4}	[143]
Loss factor in water at $10MHz$	ε''_w	0.1	[144]
Limiting Molar conductivity of Na^+	λ_{Na^+}	50 S cm^2/mol	[142]
Limiting Molar conductivity of Cl^-	λ_{Cl^-}	76 S cm^2/mol	[142]
Surface Silanol (SiOH) group density	N_s	5×10^{14} cm^2	[133]
Ionic concentration of NaCl	n_0	225 mM	Exp.
pH of buffer solution	pH	7	Exp.
Frequency	ω	10 MHz	Exp.
Calibration parameter	α	0.20	Fit

4.3.3 Maximum droplet temperature does not depend on droplet size

Fig. 4.6 shows the temperature cuts for different droplet sizes at X=0 perpedicular to the oxide surface. The temperature becomes more uniform as the radius of the droplet decreases. Due to significant mismatch in thermal conductivity of the droplet vs. the substrate, the maximum temperature is essentially independent of the droplet size i.e we only observe 4 °C change in temperature for 64 times increase in the volume of the droplet. This relative insensitivity of temperature to the droplet size allows precisely tuning of the droplet temperature regardless the inevitable variation in the droplet size.

The size-independence of maximum tempeature rise could be understood as follows: the maximum temperature of the droplet, $T_{\max}$, is related to the power-dissipated

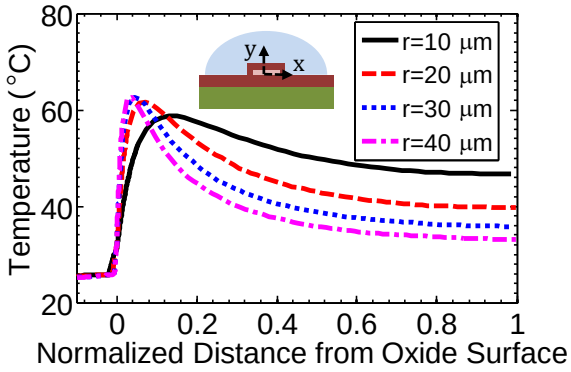

Fig. 4.6.: Temperature within the droplet at X=0 μm for different droplet radius.

within the droplet approximately as $T_{\max} - T_0 \approx P \times R_{net}$, where R_{net} is the net thermal resistance offered to change temperature, P the power generation due to dielectric heating, and T_0 the temperature of the surroundings. The heat loss can occur through either the substrate stack or through the buffer solution. Neglecting the thin bottom oxide layer thickness (0.145 μ m), the ratio of thermal resistance offered by these two processes can be related to the thermal conductivity of the buffer solution (κ_w) and the substrate region (k_{si}), as, $\frac{R_{si}}{R_w} \sim \frac{\kappa_w}{\kappa_{si}}$, where R_{si} is the thermal resistance of the substrate region and R_w is the thermal resistance of the buffer solution. Since, $k_w \ll k_{si}$ (Table 4.4), the substrate region offers a high conduction path for temperature loss to surroundings. Therefore, $T_{\max} - T_0 = P(R_{si}||R_w) \approx PR_{si}$, where $R_{si}||R_w$ represents the parallel combination of resistance due to the two regions. Hence, the maximum temperature attained is mainly determined by the thermal resistance offered by the substrate region (R_{si}) and the temperature of the droplet can be set regardless the inevitable variation in the droplet size. Since, the heat source is localized due to fringing fields, uniformity in the temperature inside droplet increases with decrease in the droplet size

4.3.4 Droplet heats in milli-seconds

Fig. 4.7(a) shows the variation of maximum droplet temperature within the core of the droplet as a function of the time. Steady-state temperature is obtained within few milliseconds of the onset of AC voltage. This is also evident from the temperature cuts perpedicular to the oxide surface for different time points (Fig. 4.7(b)). While the maximum temperature is attained in ∼1 ms, it takes ∼10 ms for the temperature to reach steady state throughout the droplet. Intuitively, the upper limit of time for temperature stabilization can be obtained by assuming the heat flow to be a 1D diffusion process, and the heat loss to occur through both droplet and substrate. Therefore, the time constant, $\tau \sim L_{\text{eff}}^2/(2D_{\text{eff}})$, where L_{eff} and $D_{\text{eff}} = \kappa/(\rho C)$ are effective diffusion length and diffusion coefficient, respectively (see Eq. (4.9)). Considering both the droplet and silicon substrate, we get, $D_{\text{w,eff}} = 1.4 \times 10^{-7}\text{m}^2/\text{sec}$ for droplet and $D_{\text{Si,eff}} = 9.1 \times 10^{-5}\text{m}^2/\text{sec}$ for substrate (see Table 4.4). This implies that the τ is mainly determined by the droplet size, and can be calculated using $L \sim r = 35\ \mu\text{m}$ (radius of the droplet). This gives $\tau \sim 4$ ms which is of the same order as the simulation results. Recently, Issadore *et al.* have reported a similar saturation time due to dielectric heating of water [191]. This method, thus, allows for ultra-fast heating of sub-nL droplets, and could be useful for many applications requiring quick heating.

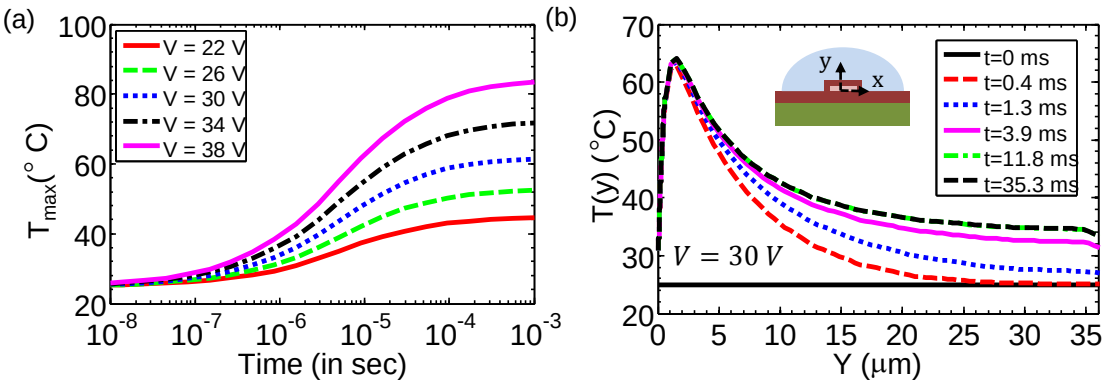

Fig. 4.7.: Time dependence of temperature in the core of the droplet. Temperature saturates to the steady state value within ms.

4.4 Model Validation

In order to determine the temperature rise in the droplet experimentally and relate it to the applied bias, we used a fluorescence measurement[2] on a droplet containing dsDNA modified to form a fluorescence resonance energy transfer (FRET) construct. Briefly, the 5' end of a DNA strand and the 3' end of a complementary DNA strand are modified with fluorescein (FAM) and a black hole quencher (BHQ), respectively [204]. The double-stranded conformation of the DNA sequences results in energy transfer between the FAM and the BHQ, producing a low level of observed fluorescence from the FAM molecule. Upon application of heating bias, the dsDNA denatures. The fluorophores separate, FRET efficiency decreases, resulting in an increase in observed fluorescence from the FAM molecule.

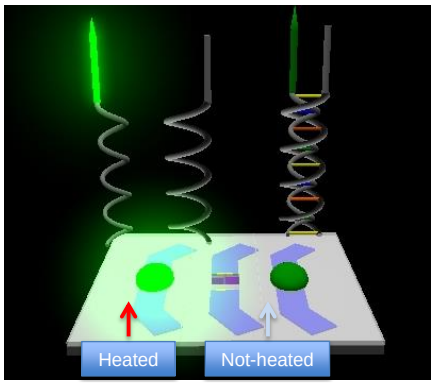

Fig. 4.8.: Graphic depiction of the FRET construct calibration concept. The device on the right is not heated. The DNA molecules in the droplet remain in their double-stranded state. Due to high FRET efficiency, the observed fluorescence is low. The device on the left is heated, resulting in denaturation of the DNA molecules. This causes separation of the FRET acceptor and donor which increases the observed fluorescence.

Experimental Determination of Droplet Temperature by collaborators at UIUC: Three separate FRET constructs were used to determine the bias dependence of the droplet temperature. Fig. 4.9 shows the comparison of fluorescence spectra measured on the fabricated chip and the commercial system. The data shows

[2] Experiments were performed by collaborators at University of Illinois, Urbana Champaign

a sigmoidal curve, and the peak of the sigmoidal curve's first derivative gives the melting temperature (in case of the commercial system) and the melting voltage (in our system) of the dsDNA FRET construct. Since, the melting occurs at a specific temperature for each of these constructs, this provides a mapping of the voltage to the temperature experimentally.

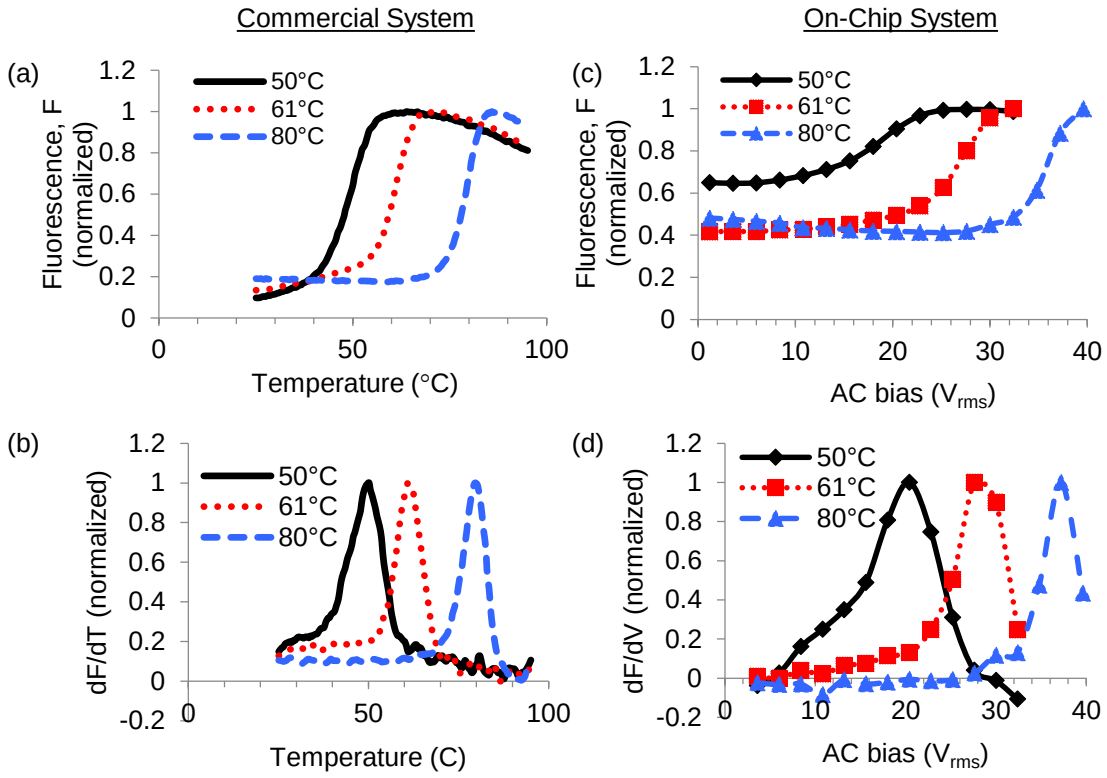

Fig. 4.9.: (a) A melting curve from commercial real-time PCR machine shows an increase in fluorescence as the FRET construct denatures (b) Derivative of (a), the peak of which gives the melting temperature of the FRET construct. (c) On-chip fluorescence data through a voltage sweep from 0-40V_{rms}. (d) Derivative of plot (c) showing the melting voltage of the constructs.

Comparison with Theory: Fig. 4.10 shows the comparison of the simulated temperature rise as a function of the biasing voltage with the experimental data. Temperature scales roughly as the square of applied bias, (i.e. $\Delta T \sim V_{rms}^2$). This could be understood as follows: The maximum temperature rise of the droplet, $T_{\max}$, is related to the power-dissipated within the droplet approximately as $T_{\max} - T_0 \approx$

$P \times R_{net}$. Since, the field (E) in the device is proportional to voltage(V), power scales as, $P = \frac{1}{2}\sigma E^2 \sim V^2$ (see Eq. (4.1)), where σ is the net conductivity associated with ionic drift and the dipolar relaxation (buffer solution/oxide). Therefore, temperature follows the scaling relationship, $T - T_0 \sim V^2$.

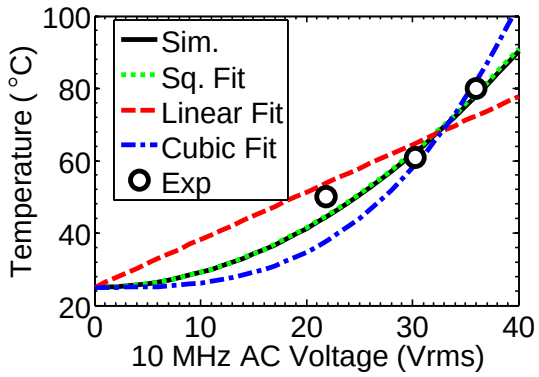

Fig. 4.10.: Bias dependence of temperature in the core of the droplet

By modulating the applied voltage, we can control the temperature profile within the droplet. Thus, at a specific voltage, the dsDNA FRET construct will denature and observed fluorescence will increase (see Fig. 4.9). In next section, we demonstrate how the voltage control of droplet temperature can enable selective detection of DNA.

4.5 Applications of Dielectric-Heating demonstrated by collaborators at UIUC

As discussed earlier, localized heating of droplet can enable a number of applications, such as hybridization of low copy number DNA molecules, lysing of single cells, interrogation of ligand-receptor interactions, and rapid temperature cycling for amplification of DNA molecules. Recently, Ebrahimi *et al.* [205] demonstrated a selective impedance based sensing method which used repeated off-chip heating cycles to change the conformational state and selectively detect the DNA molecules using an on-chip impedance based detection. In this section, we demonstrate the application

of localized heating for a) distinguishing single-base pair mismatch and b) selective detection of DNA by using on-chip heating and off-chip fluorescent based detection.

4.5.1 Distinguishing single-base pair mismatch

The ability to distinguish shifts in melting temperature associated with single base mismatches can be important in medical diagnostics and genetic applications. A single base mismatch results in a decrease in the overall free energy of the double stranded complex, which decreases melting temperature. Fig. 4.11 shows the normalized derivative of fluorescence for a droplet containing three dsDNA: two fully matched dsDNA's (DNA #1 and DNA #2) and a hetroduplex DNA consisting of a single strand from DNA #1 and the opposing single strand from DNA #2. The hetroduplex shows a decrease in melting voltage due to lower denaturation temperature. Heteroduplexes arise from heterozygous PCR amplifications, which are commonly used to determine donor compatibility for organ transplants [206]. This system demonstrates the ability to distinguish a single base mismatch using a DNA melting curve within sub-nanoliter droplets and could be used to identify a non-compatible donor pair.

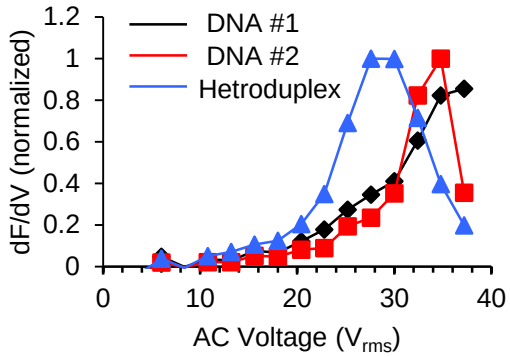

Fig. 4.11.: Derivative of fluorescence w.r.t. voltage for 3 DNA strands, the red and black curves correspond to DNA samples with fully-complementary strands and the blue curve corresponds to a hetroduplex with a single-base pair mismatch. The hetroduplex showed the peak at lower voltage, thereby indicating a base pair mismatch (because of lower melting temperature)

4.5.2 Selective sensing of probe-target hybridization

In order to determine the DNA selectively, we first spot a probe of single stranded DNA on the chip's surface. We then rehydrated the probe DNA with a droplet containing the target DNA to check if the latter was complementary, running an initial melting curve to ensure proper hybridization. As shown in Fig. 4.12, the mismatched DNA shows a zero derivative w.r.t. V_{rms} since the fluorescence spectrum is constant, while the matched DNA shows a distinct peak in derivative of fluorescence spectra because of increase in the fluorescence upon DNA denaturation. This indicates that while mismatched DNA was already in denatured state, the matched DNA was in hybridized state.

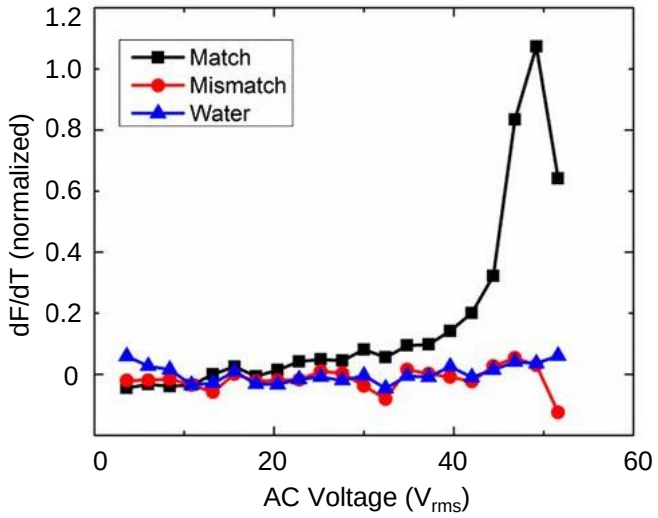

Fig. 4.12.: Probe sequence rehydrated with a complementary sequence, a noncomplementary sequence, or water. A distinct peak in the derivative of fluorescence implies a matching sequence.

This methodology to selectively detect DNA is compatible with current DNA microarray technologies and, in addition, promises to extend the capabilities of current DNA microarrays and DASH platform by including a FRET fluorophore, like cy-5, in the spotted probe DNA; incorporating a heating element under each spot on the array; and utilizing droplets-in-air for individual reaction compartments.

4.6 Conclusion

Integration of various laboratory functions onto microchips has been intensely studied for many years. Lab-on-a-chip technologies are attractive since they require fewer reagents, have higher detection limits, allow for massively parallel analyses, and can have a smaller foot-print. Further advancing these technologies requires the ability to integrate additional elements, such as the miniaturized heating element described here, and the ability to integrate heating elements in a massively parallel format compatible with silicon technology [2]. Notably, our miniaturized heater could also function as dual heater/sensor elements, as these SOI nanowire or nanoribbon structures have been used to detect DNA, proteins, pH and pyrophosphates [18, 160, 207–209].

In summary, by utilizing micro-fabrication techniques and incorporating the novel design of transistor-based heating with individual reaction volumes, 'lab-on-a-chip' technologies can be scaled down to 'lab-on-a-transistor' technologies that exist as sensor/heater hybrids for point-of-care diagnostics. We elucidate a technique to heat sub-nanoliter droplets-in-air for visualization of DNA denaturation with resolution down to single base mismatches with application to current DNA microarray technologies. The theoretical model, developed in this chapter, provides a platform for design of such on-chip heaters and enables a precise control of temperature within minaturized droplets. This methodology to heat droplets can be extended to a variety of other high-throughput screening applications such as high-speed PCR, single cell lysis, single molecule enzymology[3], and interrogation of ligand-receptor interactions in protein melting studies.

[3] The study of enzymes, their kinetics, structure, and function, as well as their relation to each other.

5. FLEXIBLE DEVICES FOR WEARABLE SENSING

5.1 Introduction

In Chapters 2-4, we discussed approaches to address response time, sensitivity and selectivity in portable lab-on-a-chip droplet based sensing platforms. Briefly, in Chapter 2, we discussed a characterization approach to determine the response of an evaporating droplet based sensor, and demonstrated its use in sensitive detection with a fast response time. In Chapter 3, we discussed an approach to locally deplete the ionic concentration within a droplet to address the fundamental screening limited response of the sensor. In Chapter 4, we discussed an approach to locally heat the droplet to do a fluorescence based selective detection. In addition to droplet based portable lab-on-chip sensors, another recent trend over the past decade for biosensors is development of wearable and implantable sensors to enable continuous monitoring of vital health parameters. This could allow round the clock (24 hours) monitoring of the patient's heath enabling the patient to follow a normal life. The key desirable attribute of a wearable biosensor is its flexibility while retaining the device performance to non-bendable state.

2D materials are promising candidates: In this regard, two-dimensional (2D) nanomaterials, such as transition metal dichalcogenide (TMDCs), MX_2: M=Mo, W; X=S, Se, Te, appear promising because of their excellent mechanical flexibility, high mobility (>100 $cm^2V^{-1}s^{-1}$) and wide band gap (E_g >1 eV) [52–55]. For example, while the theoretical yield strain in covalently bonded 2D crystals is $\sim$ 25-30% (at which point brittle fracture occurs), a strain of even 10% causes irreversible plastic deformation in crystalline silicon [46]. These materials can easily be transferred to soft polymeric or plastic substrates [46, 52], such as polyethylene terephthalate (PET) or fabricated on ultra-slim (thickness less than 200 μm) flexible glass sub-

strate [62]. As such, the sensor could adapt to the the curvilinear surfaces of the human body. Furthermore, the channel thickness of the 2D materials can be on the orders of atomic dimensions which is significantly lesser as compared to the 3D materials. This reduced channel thickness allows for an excellent electrostatic control of the channel. In addition, 2D TMD materials, such as phosphorus, have shown mobility as high as 1,000 cm^2 $V^{-1}s^{-1}$, which is significantly higher as compared to traditional flexible electronic devices made of organic, amorphous and metal oxide thin-film transistors [46]. Another advantage of 2D materials, specifically MoS_2, is that it is biocompatible [63, 65, 66, 210], and hence could possibly be implanted for monitoring of tumor cells.

Previous work on MoS_2 biosensor: Previously, Sarkar *et al.* [70] reported detection of streptadavin using MoS_2 biosensor with HfO_2 gate dielectric functionalized with biotin. However, many gate dielectrics including HfO_2 are hydrophilic and have relatively low affinity to biomolecule adsorption. Therefore, in order to monitor the binding events, the oxide surface needs to be treated with additional chemicals, such as APTES (3-aminoproplytriethoysilane) [71]. Most of the sensing experiments take place in ionic media. Treatment with chemicals introduces an extra layer of molecules which further increases the separation between the charged biomolecule layer from the sensor surface. This can considerably deteriorate the device sensitivity due to ionic screening [126].

Limitations and Advantages of MoS_2: MoS_2, like other 2D materials, does not have any dangling bonds, and hence its surface cannot be chemically bonded to the probe layer. Recently, Gaur *et al.* [211] showed that crystalline MoS_2 deposited on oxide surface has hydrophobic nature, and hence it is expected to have a higher affinity to biomolecule adsorption, as compared to non-hydrophobic surfaces such as silicon. Therefore, MoS_2 can serve the dual purpose of surface-adsorption layer as well as sensing layer. While the chemically-bonded probe layer is expected to yield better stability and selectivity, the direct physiosorption of the biomolecules on MoS_2 surface would allow a higher sensitivity due to reduced seperation between the biomolecule

layer and the channel. This remarkable prospect of oxide-free functionalization of MoS_2 biosensors has not been explored yet in the literature.

Our approach and organization of the chapter: In this chapter[1], we describe the implementation of MoS_2 biosensors to electrically detect prostate specific antigen (PSA) in a highly sensitive and label-free manner without the need of a chemically treated gate dielectric. PSA is one of the reliable clinical tools for diagnosing and monitoring prostate cancer. Therefore, the accurate and sensitive detection of PSA at the earliest stage is important for prostate cancer diagnostics and treatment. In Section 5.2, we describe the device schematic and operational principle of the back-gated MoS_2 sensor. In Section 5.3, we describe the experimental details including device fabrication, hydrophobic measurement, demonstration of sensing capability and finally the detection of PSA using anti-PSA/PSA immunoassay. In Section 5.4, we discuss the theoretical model to understand the experimental observations, and estimate the PSA concentration quantitatively. In Section 5.5, we discuss the suggestions for improving the device sensitivity based on the theoretical analysis. Finally, we conclude with Section 5.5 summarizing the essence of the work.

5.2 Device Structure and Operational Principle

Fig. 5.1 illustrates the schematic architecture to detect label-free immunoassay between an anti-PSA modified MoS_2 nanosheet and PSA target. The device configuration of our MoS_2 biosensors is utilized as bottom-gated MoS_2 FETs with higher sensitivity as well as simpler device structure for oxide-free operation. Here, the nature of hydrophobic MoS_2 surface (the contact angle $\sim$ 75.77 °) allows physical adsorption of anti-PSA on the sensing area. PSA (antigen) is then selectively bound to the immobilized antibody. It is well known that the proteins retain their ionization state corresponding to the pH of the aqueous solution (PBS) from which they

[1] The content of this chapter is adapted/reproduced from Ref. [12] with permission from Nature Publishing Group. All the experimental work presented in this chapter (Section 5.3) belongs to the work done by the collaborators at Kyung Hee University, South Korea.

were lyophilized (called " pH memory") [212–214]. Therefore, the surface charge due to lyophilized proteins results in a stable change in the conductance of the transistor (discussed later) without the need of aqueous media for detection. This allows measurement without the use of reference electrode.

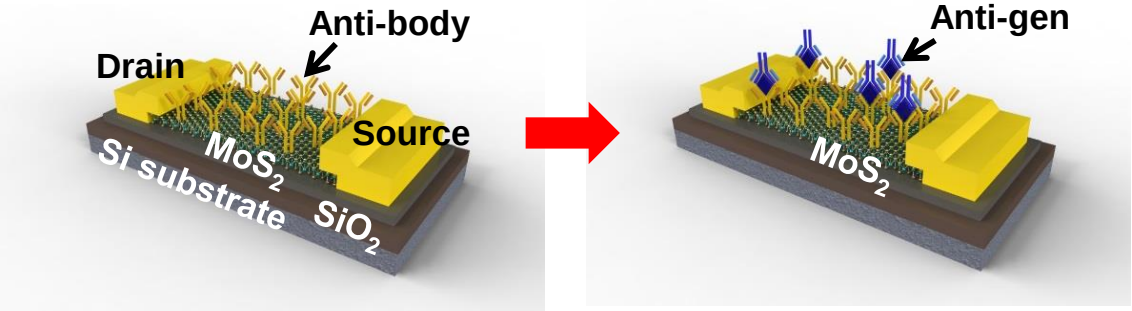

Fig. 5.1.: Schematic of a MoS_2 biosensor configured as PSA detecting label-free immunoassay, illustrating PSA antibody functionalized MoS_2 surface (top) and subsequent binding of PSA antigen with antibody receptors. The MoS_2 nanosheet biosensor consists of a gate insulator of SiO_2(300 nm) and a drain-source metal contact of Ti/Au (15 nm / 300 nm)

5.3 Experimental Work by Collaborators at Kyung Hee University

5.3.1 Device Fabrication by Mechanical Exfoliation

The first step of fabricating transistors is mechanical exfoliation from bulk MoS_2 (SPI Supplies, USA) using scotch tape. Detached thin-film MoS_2 flakes are transferred on highly p-doped Si substrate with SiO_2 (300 nm). Atomic force microscopy (AFM) measurement shows the thickness of MoS_2 flakes is in the range of 20-80 nm. Then silicon wafers with SiO_2 and MoS_2 are cleaned in acetone and IPA for 1 h in order to remove residues. Arrays of 200 $\times$ 200 μm^2 contacts are patterned by conventional photolithography and lift-off process. Metal contacts of Ti/Au (20 nm/300 nm) are subsequently deposited by e-beam evaporation. To reduce contact resistance, samples are annealed at 200C with 100 sccm of Ar gas and 10 sccm of H_2 gas in a thermal vacuum tube.

5.3.2 MoS_2 does not require surface functionalization

As mentioned previously, the hydrophobicity of the MoS_2 surface is a key enabling feature, since hydrophobic surfaces have been well known to yield higher affinity of protein-surface adsorption than hydrophilic surfaces. In order to determine degree of hydrophobicity of MoS_2, we measure contact angles of MoS_2, Au, and SiO_2 surface to explore the potential of protein adsorption on MoS_2 without a specific surface treatment. In Fig. 5.2, the contact angle of MoS_2, Au, and SiO_2 are observed as

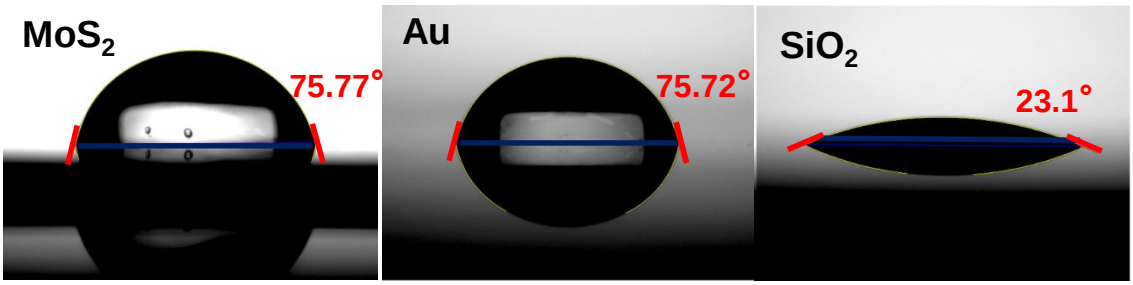

Fig. 5.2.: The water contact angle measurement to confirm hydrophobic characteristic of different substrates: the water contact angle of MoS_2, Au, and SiO_2 substrate are 75.75, 75.72, and 23.1, respectively. The contact angle of MoS_2 surface, which is more hydrophobic than Si-based substrates, is very comparable to that of Au surface. This suggests that MoS_2 nanosheet is an efficient candidate for functionalizing antibody and protein due to its highly hydrophobic surface.

75.77°, 75.72°, and 23.1°, respectively. While SiO_2 surface is hydrophilic with a contact angle of 23.1, MoS_2 and Au surfaces are relatively hydrophobic with contact angles of ∼75°. Due to the extremely low contact angles, SiO_2 is expected to yield low affinity of protein-surface adsorption, and require an additional treatment of APTES coupled with oxygen plasma-cleaned Si-surface to obtain terminal amine groups [215]. Since antibody as well as protein is easily immobilized without the complicated surface treatment on Au, the comparable hydrophobicity of MoS_2 surface with that of Au surface suggests that MoS_2 sensing surface in this study can be functionalized with specific antibody in a non-specific manner.

One may argue that sensor selectivity maybe be degraded due to non-specific binding of parasitic molecules on the MoS_2 layer. However, the selectivitiy can be improved by several methods such as prefilteration steps, such as reported in Stern *et al.* [18], by increasing the incubation time for the adsorption of IgG probe molecules [19] or by the competitive binding of proteins on the (hydrophobic) surface [216, 217].

5.3.3 Biomolecule Physiosorption

For Human IgG measurements, the MoS_2 surface was incubated with different concentrations of human IgG (in phosphate buffer saline (PBS), pH 7.2) for 15 minutes, followed by rinsing with PBS for 1 minute and drying under a nitrogen gas. For preparing an immunoassay for PSA detection, anti-PSA (100 μg/mL in PBS, pH 7.2) was immobilized on the MoS_2 surface for 1 hour. The PSA solution with different PSA concentrations was dispensed for 10 minutes (in PBS, pH 7.78), followed by rinsing using PBS for 1 minute.

5.3.4 Demonstration of biomolecular detection using Human-IgG

As the first step towards the underlying concept of real-time, electrical direct detection of charged biological species without a specific surface treatment, we investigate the sensor response to adsorption variation on 2D MoS_2 crystal as a function of the concentration of charged human Immunoglobulin G (IgG). IgG is the most abundant antibody isotype in human, which has isoelectric point (pI) of $\sim$8.5 (see, Fig. 5.6(a) for a theoretical estimate of 8.1).

Fig. 5.3(a) shows the sensor response to the adsorption of 7 different concentrations of human IgG onto MoS_2 surface. Characteristics of MoS_2 transistors have been shown to be variable with biomolecule adsorption. Here, the on-current (I_{on}) of the MoS_2 transistor shows negligible change with respect to the human IgG concentration, but the off-current (I_{off}) of the MoS_2 transistor significantly changes with human IgG concentration. We will discuss the theoretical model of the sensor in the next section,

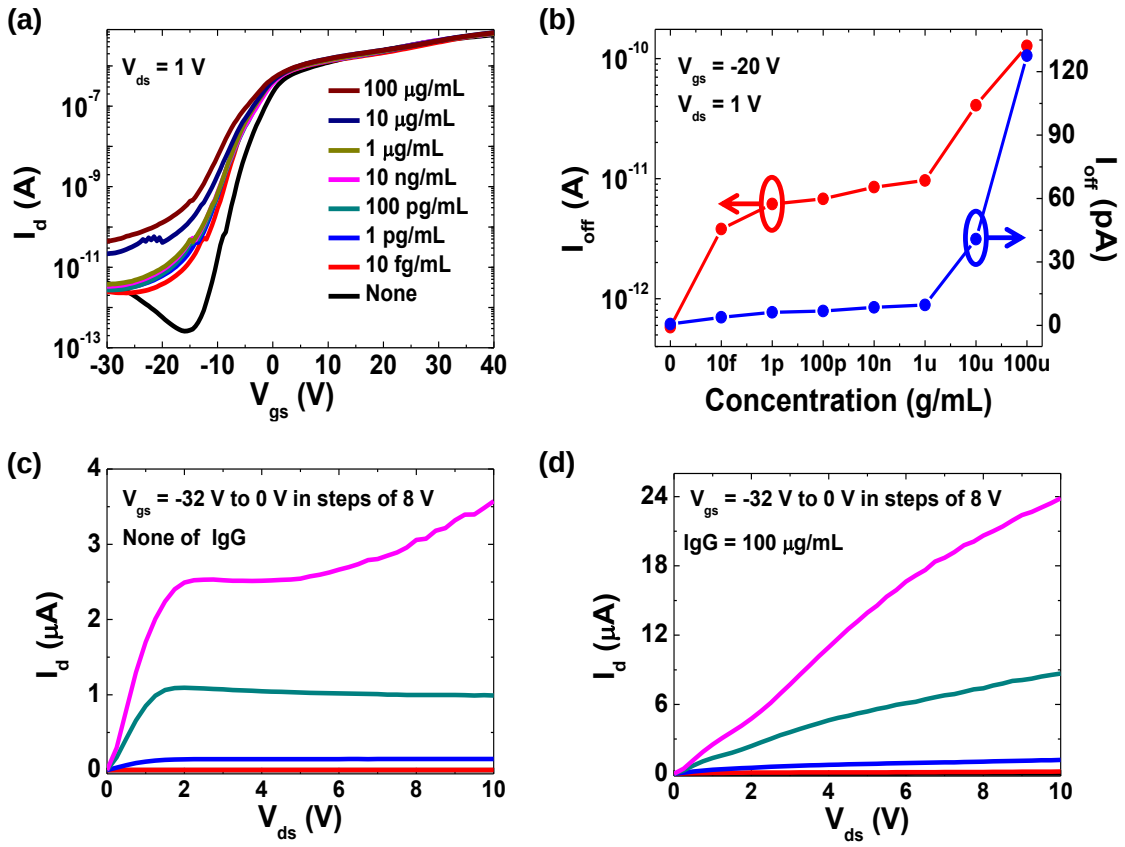

Fig. 5.3.: Adsorption of human IgG onto MoS_2 sensor surface: (a) Transfer characteristics under various concentration of the human IgG from 0 to 100 μg/mL at V_{ds} = 1 V. (b) Plots of off-current versus human IgG concentration show an increase of off-current with increasing concentration of the human-IgG and abrupt increase of off-current at specific concentration of 10 fg/mL for V_{gs} = -20 V and V_{ds} = 1 V. Arrows indicate appropriate axis (red: log-scale, blue: linear-scale). (c), (d) Output characteristics under human IgG conditions of 0 and 100 μg/mL from V_{gs} = -32 V to V_{gs} = 0 V in steps of 8 V, respectively. Following adsorption of human IgG on MoS_2 surface, the drain current exhibits 6-fold increase at a high drain voltage and saturation currents disappear due to the immobile charge of human IgG on the MoS_2 nanosheet.

but the results are easy to understand intuitively: Without a positively charged human IgG, negative gate voltage during off-state depletes electrons in the n-type MoS_2 channel (low off-current, see Fig. 5.3(a) and Fig. 5.8(a) for band diagram). Since human IgG (pI ~8.4-8.5) is positively charged at the measurement condition (pH =

7.2), binding of human IgG to the MoS_2 surface causes an increase in electrons during off-state. However, during on-state, positive gate voltage accumulates electrons in the n-type MoS_2 channel (high on-current) even without human IgG (see Fig. 5.8(b)). Hence, the impact of human IgG bound to MoS_2 surface on the accumulation of electrons is insignificant. As concentration of human IgG increased from 10 pg/mL to 100 μg/mL, the sensor response (I_{off}) also increased, indicating that the amount of the adsorbed human IgG on the MoS_2 sensor surface is approximately proportional to the applied human IgG concentration. Fig. 5.3(c) and Fig. 5.3(d) show the output characteristics of the device without IgG and with IgG concentration of $100\mu g/mL$. Before IgG binding, the sensor shows saturation at high V_{ds} due to channel-pinch off. However, due to positive charge of IgG, the curves become linear reflecting transition from saturation to linear regime. These results provide a potentially important implication that 2D layered MoS_2 can be an attractive candidate for a highly sensitive quantitative detection of biomolecular targets without an additional surface treatment.

5.3.5 PSA Detection

Capture of PSA Molecules by anti-PSA

We next investigate the dependence of sensor response on the applied PSA concentration in an anti-PSA functionalized 2D MoS_2 nanosheet transistor as shown in Fig. 5.1. Fig. 5.4(a) shows the increase of off-state current after anti-PSA (antibody) with a concentration of 100 μg/mL is immobilized to the overall MoS_2 device surface. The extreme increase of off-current in the transistor with anti-PSA physisorbed on the MoS_2 nanosheet surface shows a similar trend from adsorption of human IgG onto MoS_2 sensor surface, which is consistent with binding of positively charged biomolecules. Then, the off-state current decreases as PSA is selectively bound to the immobilized antibody on the MoS_2 surface (Fig. 5.4(b)). Here, the variation of off-current due to the specific binding of negatively charged PSA with the antibodies

allows us to monitor highly sensitive detection of PSA markers from 1 pg/mL to 10 ng/mL, and to compute quantitative bioassay from the binding of a charged biological species. As concentration of PSA increased from 1 pg/mL to 10 ng/mL, the increased sensing response with PSA concentration indicates that the amount of the adsorbed PSA on the anti-PSA immobilized MoS_2 sensor surface is proportional to the PSA concentration. The minimum detectable concentration of PSA (see Fig. 5.4(b)) is 1 pg/mL, which is three orders of magnitude below the clinical cut-off level of 4 ng/mL. Fig. 5.4(c) and (d) shows the output characteristics of the transistor before and after PSA binding. Due to negative charge of PSA, the effective gate voltage on top of MoS_2 surface decreases and this leads to decrease in on-current. This change in on-current is however substantially lower than the change in off-current (compare with Fig. 5.4(b)).

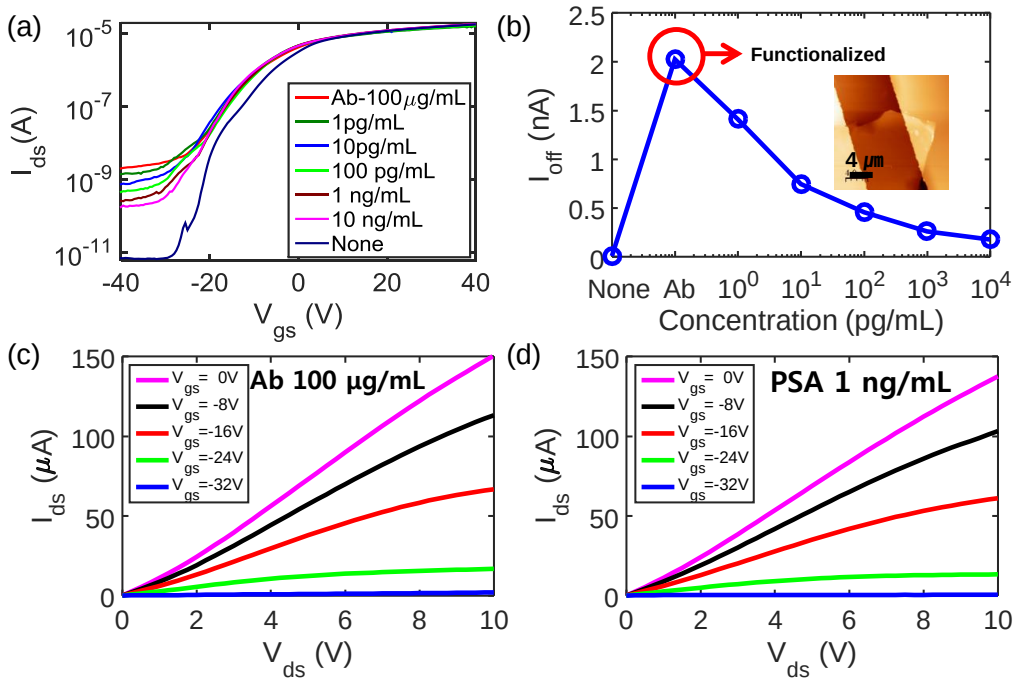

Fig. 5.4.: MoS_2 nanosheet biosensor for PSA detection: (a) Transfer characteristics of MoS_2 transistor biosensor functionalized by anti-PSA (Ab) of 100 μg/mL under various PSA concentrations. "None" refers to device without any biomolecule attachment. (b) Change of the off-current vs. various PSA concentrations for an anti-PSA (Ab) modified n-type MoS_2 transistor at the condition of V_{gs} = - 40 V and V_{ds} = 1 V. Inset shows an AFM image of MoS_2 device with thickness of ~70 nm, width of 12.48 μm and length of 11.64 μm. (c), (d) Output characteristics of MoS_2 nanosheet biosensor with functionalized anti-PSA concentration of 100 μg/mL and PSA concentration of 1 ng/mL from V_{gs} = -32 V to V_{gs} = 0 V in steps of 8 V, respectively.

5.4 Theoretical Analysis

Given the experimental results presented in Section 5.3, the following observations require theoretical interpretation.

1. The current saturates at large-negative biases.

2. The current increases upon binding with anti-PSA and Human IgG, while it decreases upon binding with PSA at pH=7.78.

3. The subthreshold slope of the device is very large (several volts/decade).

4. The subthreshold slope degrades upon anti-PSA (antibody) binding, and improves with increase in PSA concentration.

5. The relative change in off-current is more as compared to the change in on-current upon anti-PSA and PSA binding.

5.4.1 Model

The theory of classical FET-biosensors is well established, but its generalization to double-gated configuration [161], especially in the presence of interface defects and pH dependent biomolecule charge require a careful analysis. A semiclassical approach is appropriate because the carrier transport in a sensor is dominated by scattering that can be addressed adequately by a drift-diffusion formulation. Specifically, in order to interpret the experimental results and to develop a model for MoS_2 biosensors, we solved for both the electrical and chemical equations to determine the biomolecular charge and device characteristics.

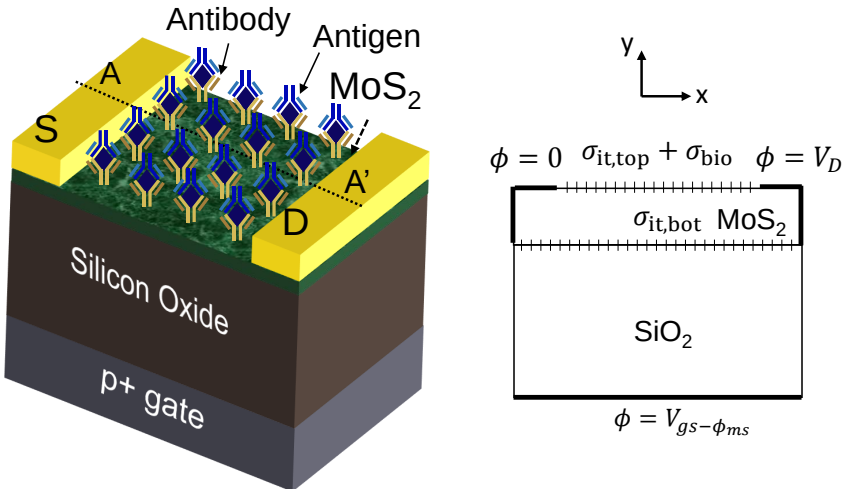

Fig. 5.5.: Schematic of the device used for numerical simulation of device characteristics.

Electrical Model

First, we solved for Poisson and continuity equation self consistently throughout the device in two-dimension (x-y direction, see Fig. 5.5). Table 5.1 shows the numerical model used for determination of device characteristics. Here, ϕ is the electrostatic potential, n and p are electron and hole concentrations in MoS_2 layer, respectively; and μ and D are mobility and diffusion coefficients, respectively. The channel is presumed n-doped with intrinsic doping density, $N_d = 1 \times 10^{16}$ cm^{-3}, which is calibrated with the experimental data for $I_{ds} - V_{gs}$. The intrinsic n-type doping behavior of MoS_2 has been attributed in literature to either sulfur vacancies [218] or due to impurities, such as Rhenium [219]. Similar, doping concentration was also previously reported by Kim *et al.* [220] for multi-layer MoS_2. For simplicity, the biomolecule charge is considered as a uniform surface charge sheet with density (σ_{bio}) at the top MoS_2 surface. This charge is obtained by calibrating the off-current values from the experiment with the simulation. The response due to the biomolecules is compromised by the interface traps at top MoS_2 surface ($\sigma_{\text{it,top}}$) and MoS_2/oxide interface ($\sigma_{\text{it,bottom}}$). The device parameters are summarized in Table 5.2, respectively and the list of the symbols is described in Table 5.3 and Table 5.6.

Table 5.1.: Numerical equations for MoS_2 sensor

Regions 1 & 2 (R1 and R2)	$-\nabla.(\epsilon\nabla\phi) = q(p - n + N_d^+ - N_a^-)$
Region 1 (R1)	$\nabla.(qD_n\nabla n - q\mu_n n\nabla\phi) = 0$ $\nabla.(-qD_p\nabla p - q\mu_p p\nabla\phi) = 0$
Source contact Drain contact Gate contact	$\phi = 0$ $\phi = V_{ds}$ $\phi = V_{gs} - \phi_{\text{ms}}$ where $\phi_{\text{ms}} = \phi_{p+} - \phi_{\text{MoS}_2}$
MoS_2 - SiO_2 interface Top MoS_2 surface	$\epsilon_{\text{MoS}_2}E_{MoS2} - \epsilon_{\text{SiO}_2}E_{\text{SiO}_2} = \sigma_{\text{it,bottom}}$ $-\epsilon_{\text{MoS}_2}E_{\text{MoS}_2} = \sigma_{\text{it,top}} + \sigma_{\text{bio}}$

Table 5.2.: Simulation parameters

Parameter	**Value**	**Ref.**
Multilayer MoS_2 band gap (E_g)	1.3 eV	[220]
Multilayer MoS_2 electron affinity (ξ_{MoS_2})	4.3 eV	[220]
Relative Permittivity in MoS_2 (ε_{r,MoS_2})	4.1	[220]
Relative Permittivity in SiO_2 (ε_{r,SiO_2})	3.9	[199]
Intrinsic doping density (N_d)	1×10^{16} cm^{-3}	[220]
Electron (μ_n)/Hole mobility (μ_p)	50 cm^2/Vs	Fit
Workfunction of $p+$ substrate (ϕ_{p+})	5.17 eV	Cal.
Fixed-charge density at oxide-MoS_2 interface ($N_{it,bot}$)	2.6×10^{11} cm^{-2}	Fit
Uniform donor density at oxide-MoS_2 interface ($D_{it,bot}$)	8×10^{11}eV^{-1}cm^{-2}	Fit
Fixed-charge density at MoS_2-electrolyte interface ($N_{it,top}$)	2.8×10^{11} cm^{-2}	Fit
Series Resistance (R_{ds})	20 KΩ	Fit

Table 5.3.: List of Symbols for charge transport in MoS_2

Parameter Name	**Symbol**
Electrostatic Potential at any point in the device	ϕ
Electron/Hole concentration	n/p
Electron/Hole mobility	μ_n/μ_p
Electron/Hole diffusion coefficient	D_n/D_p
Trap density at MoS_2-electrolyte interface	$\sigma_{it,top}$
Trap density at MoS_2-oxide interface	$\sigma_{it,bottom}$
Drain to source voltage	V_{ds}
Gate to source voltage	V_{gs}
Electronic Charge	q

Determination of Protein charge

While electrical model characterizes the sensor response for a given protein charge (anti-PSA, human IgG or PSA), the protein charge itself is a function of the pH of the sensing solution. Therefore, interpretation of experimental observations requires a model which could relate the protein charge to the solution pH. A protein is composed of basic amine groups and acidic carboxyl groups. The charge on protein, therefore,

depends on the fraction of these groups which are in ionized form at a particular pH. The fraction of base with $pK = -\log_{10}[K_{bi}]$ in ionized form is given by,

$$f_{bi} = \frac{[H^+]}{[H^+] + K_{bi}}. \tag{5.1}$$

and the fraction of acidic groups with $pK = -\log_{10}[K_{ai}]$ in ionized form is given by,

$$f_{ai} = \frac{K_{ai}}{[H^+] + K_{ai}}. \tag{5.2}$$

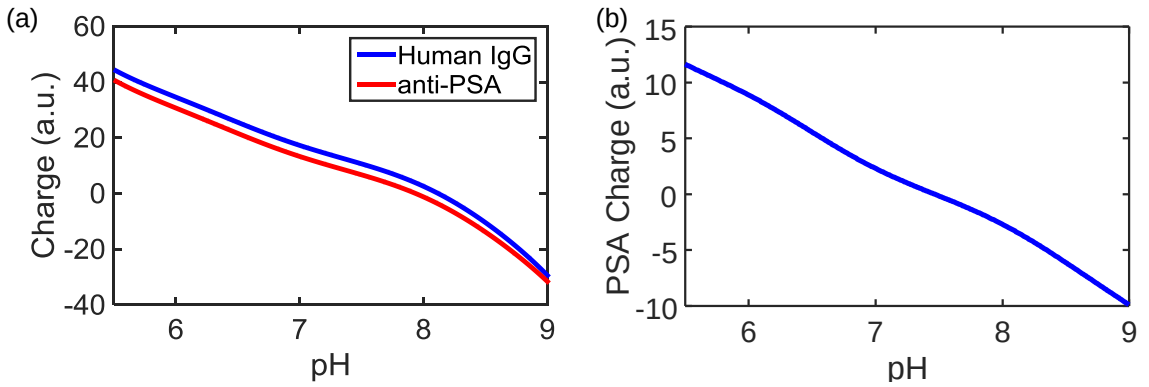

Fig. 5.6.: (a) Human IgG, anti-PSA, and (b) PSA charge as a function of pH. The isoelectric point (IP) of human IgG, anti-PSA and PSA are 8.12, 7.94 and 7.46, respectively.

To determine the protein charge at a given pH, we summed the charge of individual groups over the complete sequence of protein. Charge (q_{protein}) on protein molecule can be expressed as,

$$Q = q(\sum_i i f_{bi} - \sum_j j f_{aj}). \tag{5.3}$$

where i is the number of bases in the protein sequence and j is the number of acids in the protein sequence. Table 5.6 tabulates the sequence for different proteins, and Table 5.4 lists the number of charged amino acids (with their corresponding pK) in protein molecule. Fig. 5.6 shows the plot of protein charge (Human IgG, anti-PSA,

and PSA) as a function of pH. Once the charge on a protein (q_{protein}) at a particular pH is known, the surface charge can be calculated as, $\sigma_s = q_{\text{protein}} N_s$, where N_s is the density of protein molecules on the surface.

Table 5.4.: Number of charged amino acids in human IgG, anti-PSA and PSA and their corresponding pK [221, 222]

Amino Acid	**pK**	**Human IgG**	**anti-PSA**	**PSA**
K (Base) Lysine	10	94	92	12
R (Base) Arginine	12	38	40	10
H (Base) Histidine	6.5	26	26	11
D (Acid) Aspartate	4.4	54	64	11
E (Acid) Glutamate	4.4	66	60	11
C (Acid) Cysteine	8.5	34	34	10
Y (Acid) Tyrosine	10	68	50	4
NH_2 Terminal Group	8	1	1	1
COOH Terminal Group	3.1	1	1	1

5.4.2 Device Characteristics

The electrical model described in previous section is used to determine the device characteristics for different PSA concentrations. Fig. 5.7(a) shows the transfer characteristics of the device (as a function of backgate voltage) for different PSA concentrations. The simulation results explain consistently the key features observed in the experiments (refer Fig. 5.4):

1. **Saturation of current at large negative biases**: The off-current results from the formation of a conduction channel (accumulated electrons) at the top MoS_2 surface in response to the positive charge due to interface traps at the top MoS_2 surface (see Fig. 5.7(a)). While pristine MoS_2 surface is defect-free, these defect are likely due to sulfur vacancies or impurity atoms [218, 219]. Further, when anti-PSA binds to the surface this positive charge increases and leads to further accumulation of electrons. Fig. 5.8 (a) shows the energy band

Table 5.5.: Determination of protein sequence

Segment [**Ref**]: **FASTA Sequence**
1. Human IgG
Fab Light Chain (A) [223]: SDIQMTQSPSSLSASVGDRVTITCRASQSVSSAVAWYQQKPGKAPKLLIYSASSLYS GVPSRFSGSRSGTDFTLTISSLQPEDFATYYCQQYSSYSSLFTFGQGTKVEIKRTVAAPSVFIFPPSDEQLKSGTA SVVCLLNNFYPREAKVQWKVDNALQSGNSQESVTEQDSKDSTYSLSSTLTLSKADYEKHKVYACEVTHQGLSSP VTKSFNRGEC
Fab Heavy Chain (B) [223]: EISEVQLVESGGGLVQPGGSLRLSCAASGFNVKTGLIHWVRQAPGKGLEWVAYI SPYYGSTSYADSVKGRFTISADTSKNTAYLQMNSLRAEDTAVYYCAREYYRWYTAIDYWGQGTLVTVSSASTK GPSVFPLAPSSKSTSGGTAALGCLVKDYFPEPVTVSWNSGALTSGVHTFPAVLQSSGLYSLSSVVTVPSSSLGTQ TYICNVNHKPSNTKVDKKVEPKSCDKTH
Fc Heavy Chain (Hinge, CH_2, CH_3 region) (UniProt [224]): EPKSCDKTHTCPPCPAPELLGGPSVFLFPPKP KDTLMISRTPEVTCVVVDVSHEDPEVKFNWYVDGVEVHNAKTKPREEQYNSTYRVVSVLTVLHQDWLNGKE YKCKVSNKALPAPIEKTISKAKGQPREPQVYTLPPSRDELTKNQVSLTCLVKGFYPSDIAVEWESNGQPENNYK TTPPVLDSDGSFFLYSKLTVDKSRWQQGNVFSCSVMHEALHNHYTQKSLSLSPGK
2. Anti-PSA (IgG_{2a})
Chain C region (UniProt [224]): AKTTAPSVYPLAPVCGDTTGSSVTLGCLVKGYFPEPVTLTWNSGSLSSGVHT FPAVLQSDLYTLSSSVTVTSSTWPSQSITCNVAHPASSTKVDKKIEPRGPTIKPCPPCKCPAPNLLGGPSVFIFPP KIKDVLMISLSPIVTCVVVDVSEDDPDVQISWFVNNVEVHTAQTQTHREDYNSTLRVVSALPIQHQDWMSGKEF KCKVNNKDLPAPIERTISKPKGSVRAPQVYVLPPPEEEMTKKQVTLTCMVTDFMPEDIYVEWTNNGKTELNY KNTEPVLDSDGSYFMYSKLRVEKKNWVERNSYSCSVVHEGLHNHHTTKSFSRTPGK
Heavy chain V region (UniProt [224]): QVQLQQPGAELVRPGSSVKLSCKASGYTFTSYWMDWVKQRPGQGLE WIGNIYPSDSETHYNQKFKDKATLTVDKSSSTAYMQLSSLTSEDSAVYYCAR
Light Chain: DVVMTQSPKTISVTIGQPASISCKSSQRLLNSNGKTFLNWLLQRPGQSPKRLIYLGTKLDSGVPDR FTGSGSGTDFTLKISRVEAEDLGVYYCWQGTHFPYTFGGGTKLEIKRADAAPTVSIFPPSSEQLTSGGASVVCFL NNFYPKDINVKWKIDGSERQNGVLNSWTDQDSKDSTYSMSSTLTLTKDEYERHNSYTCEATHKTSTSPIVKSFN RNEC
3. PSA
Complete Sequence (PDB [223]): IVGGWECEKHSQPWQVLVASRGRAVCGGVLVHPQWVLTAAHCIRNKSVIL LGRHSLFHPEDTGQVFQVSHSFPHPLYDMSLLKNRFLRPGDDSSHDLMLLRLSEPAELTDAVKVMDLPTQEPAL GTTCYASGWGSIEPEEFLTPKKLQCVDLHVISNDVCAQVHPQKVTKFMLCAGRWTGGKSTCSGDSGGPLVCN GVLQGITSWGSEPCALPERPSLYTKVVHYRKWIKDTIVANP

Table 5.6.: List of symbols for protein charge calculation

Parameter	**Symbol**
Hydronium ion concentration in the buffer solution	$[H^+]$
Dissociation constant of j^{th} acidic group in protein	K_{aj}
Association constant of i^{th} base in protein	K_{bi}
Fraction of ionized j^{th} acidic group in protein sequence	f_{aj}
Fraction of ionized i^{th} basic group in protein sequence	f_{bi}
Charge per protein molecule	q_{bio}

diagrams for a device without anti-PSA/PSA binding for different negative gate voltages. The band diagram at the MoS_2-electrolyte interface (x=0.37 μm) hardly changes as the bias decreases from -20V to -40V. This conducting channel at the MoS_2-electrolyte interface which is independent of the gate bias of FET leads to the constant current flow in off-regime.

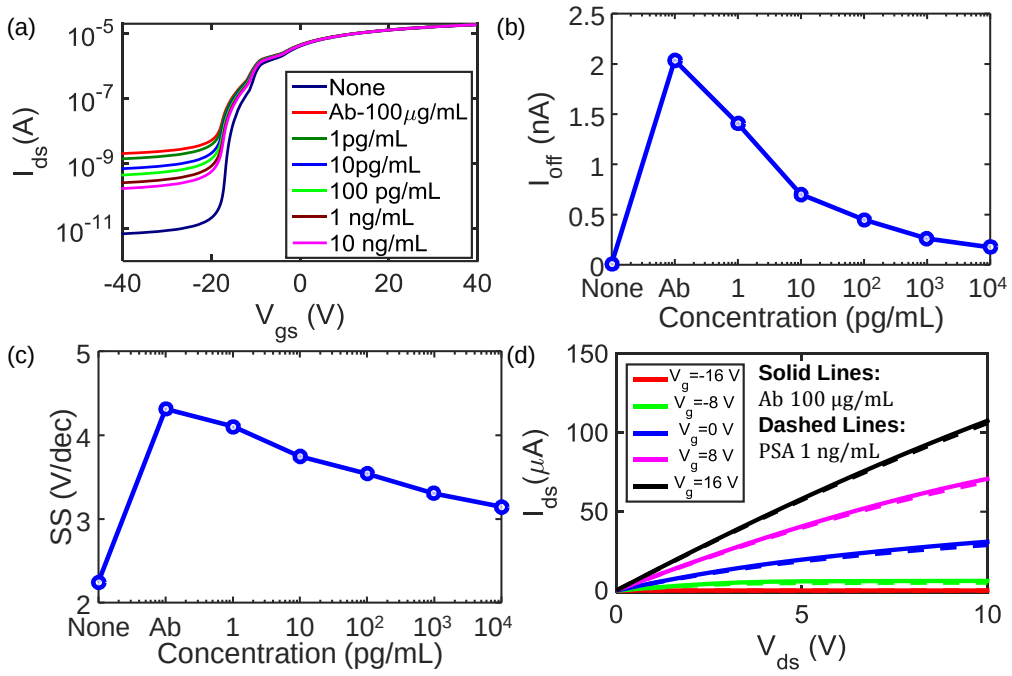

Fig. 5.7.: Simulated MoS_2device characteristics for PSA detection: (a) Transfer characteristics at $V_{ds} = 1$ V; (b) Off-current at $V_{ds} = 1$ V and $V_{gs} = -40$ V as a function of PSA concentration; (c) Average Subthreshold swing (between -10 V and -20 V) as a function of the PSA concentrations; and (d) Output characteristics of MoS_2 sensor with and without PSA on a surface, which has been pre-functionalized with anti-PSA. On-current decreases due to negative charge of PSA.

2. **The increase in current upon anti-PSA (antibody) binding and decrease in current upon binding with PSA**: As discussed in Section 5.4.1, the charge on anti-PSA is positive and the charge on PSA is negative at pH=7.74. The physiosorption of anti-PSA leads to an increase in the positive surface charge (over and above the interface defect charge) at MoS_2-electrolyte interface, and this results in an increase in off-current. The negatively charged PSA neutralizes some of the positive charge, and hence the off-current decreases with increase in PSA concentration (see Fig. 5.7(b)). The on-current also shows a similar trend. Fig. 5.7(d) shows the I_{ds}-V_{ds} characteristics for the device with anti-PSA, and with 1 ng/mL PSA concentration. The on-current of the de-

vice reduces as PSA is added to the solution, consistent with observations in Fig. 5.4(c)-(d).

3. **Large subthreshold-swing**: The large subthreshold-swing of the device can again be attributed to the presence of interface defects both at the MoS_2/electrolyte ($N_{it,top}$) and MoS_2/oxide ($D_{it,bot}$) interface (see Fig. 5.7(b)). In addition to the defects due to vacancies and contamination of MoS_2, the defects at the oxide-MoS_2 interface may arise due to unpassivated bonds at the oxide surface.

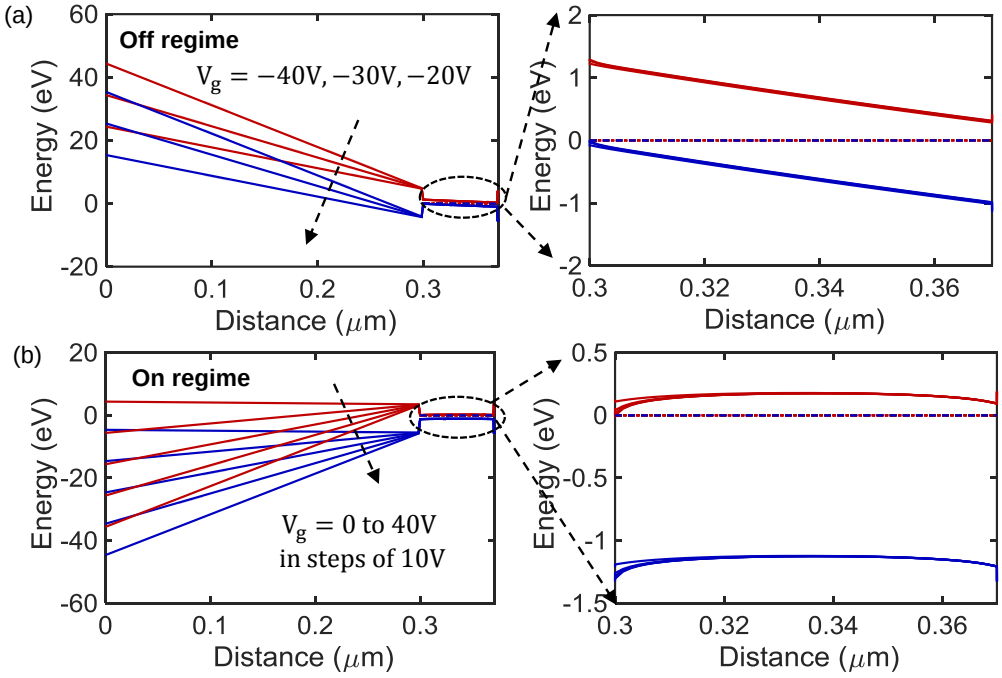

Fig. 5.8.: Band diagram of the MoS_2 channel in different operation regimes (a) Off-current regime, (b) On-current regime

4. **The increase in subthreshold swing upon anti-PSA binding and decrease in sub-threshold slope upon PSA binding**: The average subthreshold swing (SS) of the device increases upon addition of positively charged anti-PSA due to increase in off-current. However, as the concentration of the negatively charged PSA is increased from 1 pg/mL to 10 ng/ml, the off-current decreases tenfold from ~2 nA to 0.2 nA (see Fig. 5.7(b) vs. Fig. 5.4(b), hence

the average subthreshold slope reduces from 4.3V/dec to 3.1V/dec as shown in Fig. 5.7(c).

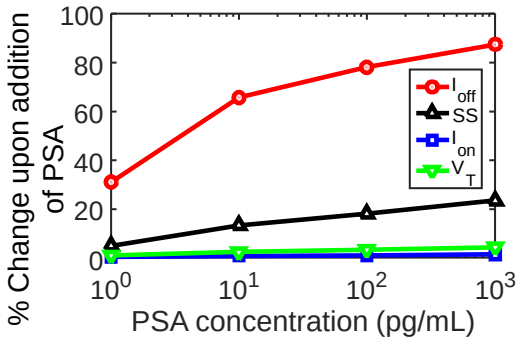

Fig. 5.9.: Comparison of sensitivity based on 4 different device parameters: The base value used is for a MoS_2 surface with anti-PSA bound on its surface. The off-current shows a considerably larger change upon PSA binding as compared to the subthreshold-swing , threshold voltage and on-current.

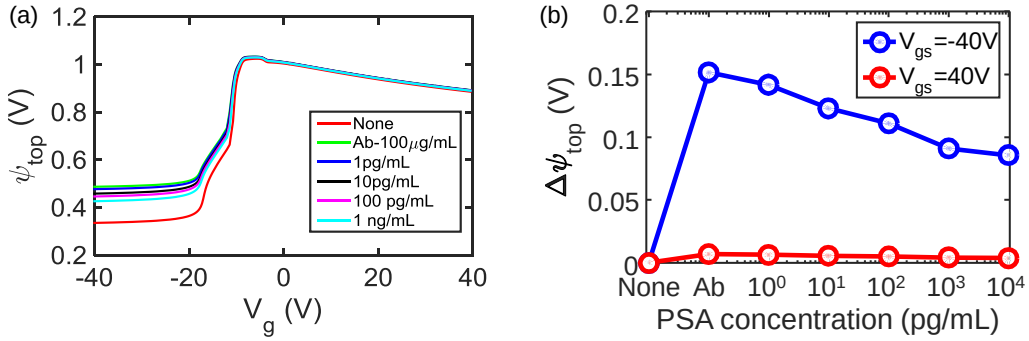

Fig. 5.10.: (a) The surface potential at top (ψ_{top}) surface as a function of gate bias for different biomolecule concentrations at$V_{ds} = 1$ V. (b). Variation of MoS_2 potential at top ($\Delta\psi_{top}$) for $V_g = -40$ V and $V_g = 40$ V as a function of biomolecule concentration. The change in ψ_{top} at high gate bias is negligible leading to a small change in on-current upon PSA binding.

5. **The relative change in off-current is more as compared to the change in on-current upon anti-PSA/PSA binding:** Fig. 5.9 shows the percentage change in device parameters i.e. off-current, I_{off} (at $V_{gs} = -40$ V), average subthreshold-swing, SS (between $-20V$ and $-10V$), linear threshold-voltage, V_T and on-current, $I_{\text{on}}(V_{gs} = 16\text{ V}, V_{ds} = 10\text{ V})$ upon PSA binding. Fig. 5.9

explains why the off-current - more so than any other metric - is such a robust indicator of the capture of biomolecules. Since the MoS_2 device is an accumulation mode device, the relative change in on-current of the transistor is very small. This is because the channel is highly conducting when the device is turned on (see Fig. 5.8(b))and a small change in surface charge due to PSA binding causes a corresponding small change in the drain current. However, when the device is completely off, the channel is off (see Fig. 5.8(a)) and a small change in surface charge due to PSA binding brings relatively larger change in drain current. This is also evident from Fig. 5.10(a)-(b) where change in top MoS_2 surface potential due to PSA binding is considerable when the device is off ($V_{gs} = -40$ V), while it is negligible when the device is turned-on ($V_{gs} = 40$ V). Unlike Lee [225], the capture of PSA does not passivate/create any interface defects, therefore the very small change in V_T and SS reflect, only as a secondary metric, the changes in the off current.

5.4.3 Determination of Surface Densities of Biomolecules

As discussed in Section 5.4.1, the biomolecule charge is considered as a uniform surface charge sheet with density (σ_{bio}) at the top MoS_2 surface, and the surface charge density is obtained by calibrating the off-current values from the experiment with the simulation. The effective surface densities (after accounting for residual ionic screening) of anti-PSA ($N_{\text{anti-PSA}}$) and PSA (N_{PSA}) on MoS_2 surface is estimated theoretically in this section. Briefly, the net charge density on MoS_2 surface for a given pH is given by,

$$\sigma_{\text{surface}}(pH) = q_{\text{anti-PSA}} N_{\text{anti-PSA}} + q_{\text{PSA}} N_{\text{PSA}}. \tag{5.4}$$

Since, the measurements were done at pH=7.78, the charge per anti-PSA molecule is $q_{\text{anti-PSA}}(pH = 7.78) = 2.68\ q$ and the charge per PSA molecule at pH=7.78 is $q_{\text{PSA}}(pH = 7.78) = -1.52\ q$, where q is electronic charge (see Fig. 5.6). Once

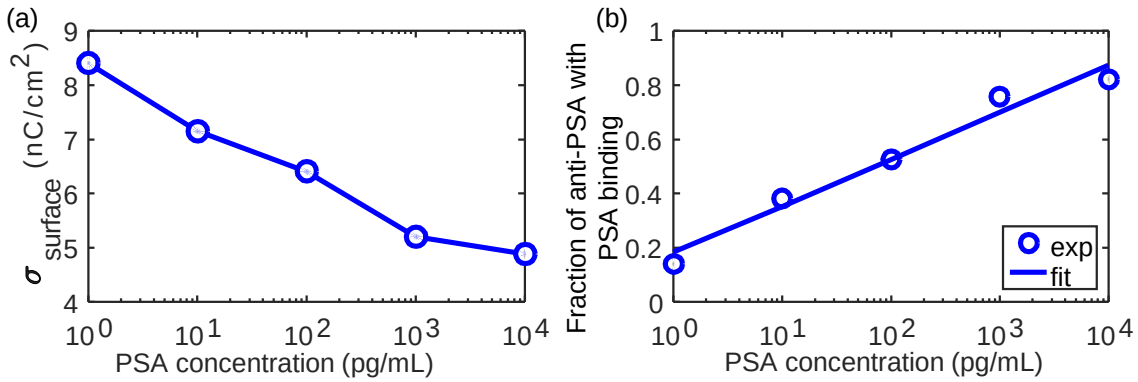

Fig. 5.11.: (a) Calibration curve for surface charge density due to anti-PSA/PSA binding as a function of PSA bulk concentration. (b) The fraction of anti-PSA molecules bound to PSA molecules as a function of PSA concentration. Symbols are values obtained from (a) and fit corresponds to expression $f \sim \zeta \log(\frac{\rho}{\rho_0} + 1)$.

the surface charge density (σ_{surface}) (see Fig. 5.6(a)) is known by calibration with the experimental data, we can find the effective surface density of PSA at different bulk PSA concentrations using Eq. (5.4). Interestingly, the surface charge density of PSA follows a logarithmic trend with respect to its bulk concentration, ρ i.e. $\sigma_{\text{PSA}} = q_{\text{PSA}} N_{\text{PSA}} = q_{\text{PSA}}\ N_{\text{IgG}}\ \zeta \log(\frac{\rho}{\rho_0} + 1)$ where ζ and ρ_0 are fitting parameters. Fig. 5.11 (b) shows the fraction of effective PSA concentration binded to the anti-PSA i.e. $N_{\text{PSA}}/N_{\text{anti-PSA}}$ as a function of bulk PSA concentration (ρ_{PSA}). The symbols represent the values obtained by calibrating simulation with the experimental data and line represents the fit to the expression. Theoretical analysis, thus, provides an estimate for the binding efficiency (i.e. no. of probe molecules bound to the target molecules) as the concentration of the PSA increases, and could be very useful in analysis and optimization of the MoS_2 sensor.

5.5 Device Improvement by reduction of interface traps

The theoretical interpretation of the experimental results suggests opportunity for future optimization. The relatively large subthreshold slope of the MoS_2 ($\sim$ 2.2 V/dec before and $\sim$ 4.3 V/dec after anti-PSA decorates the surface) reflects

relatively high density of interface traps at the top MoS_2 surface and MoS_2/oxide interfaces. Fig. 5.12 suggests that the performance of MoS_2 biosensor would improve approximately 40 times, if surface treatment could reduce the defect density at the top MoS_2 surface by a factor of 5, i.e., from 2×10^{11} # cm^{-2} to 4×10^{10} # cm^{-2}. The reduction of defect density at the MoS_2/oxide interface has even more dramatic consequences: Sensitivity at the same concentration (ρ = 10 ng/mL) improves by almost 4 orders of magnitude as the trap density is reduced from 8×10^{11} eV^{-1} cm^{-2} to 1×10^{10} $eV^{-1}cm^{-2}$. Therefore, while the experimental results already demonstrate considerable potential of MoS_2 based technology in terms of sensitivity, selectivity, fluid stability, and integration on Si-substrate, significant additional improvements are expected with improvement in surface treatment and interface passivation.

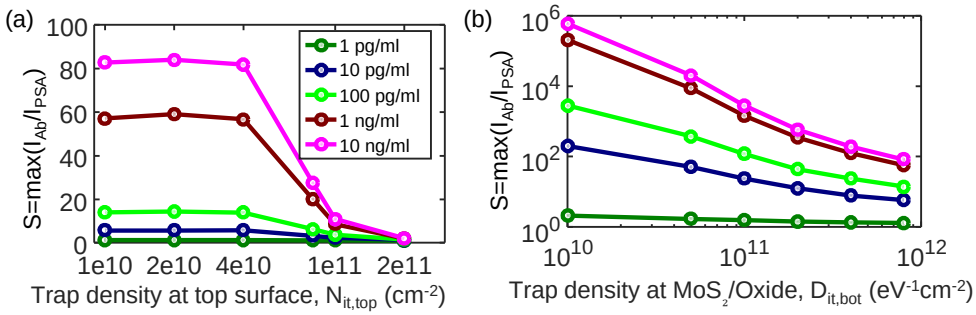

Fig. 5.12.: Improving the sensitivity by interface passivation: (a) Variation of MoS_2 sensitivity as a function of interface trap densities at top surface of MoS_2 for different PSA concentration (with $D_{\text{it,bot}} = 8 \times 10^{11}$ $eV^{-1}cm^{-2}$)) b) Variation of MoS_2 sensitivity as a function of interface trap density at MoS_2-oxide interface (with $N_{\text{it,top}} = 4 \times 10^{10}$ $eV^{-1}cm^{-2}$) for different PSA concentration

5.6 Conclusion

In summary, this chapter describes a comprehensive investigation on the highly sensitive biosensor platform based on multilayer MoS_2 FETs to detect PSA. The results demonstrate the successful use of MoS_2 FET sensor in back-gated scheme without the need of the insulating oxide on the top of channel. The highly hydropho-

bic nature of the MoS_2 surface allows it to serve the dual roles of the transducer and the recognition layer, with considerable improvement in sensitivity and significant simplification of device design. The absence of the oxide layer avoids the additional complexity involved in chemical treatment of the surface, and hence ensures effective coupling of biomolecule charge to the channel. The theoretical model explains the experimental results consistently and indicates that the sensitivity can be further improved through surface treatment and interface passivation. Combined with the rapid advances in large-area synthesis methods of MoS_2 such as CVD, these results deliver a compelling case of potentially using multilayer MoS_2 FETs as flexible biosensors for continuous monitoring of malignant tumors.

6. HYDROGEL BASED IMPLANTABLE BIOCHEMICAL SENSORS

In Chapters 2-4, we discussed approaches to address response time, sensitivity and selectivity in droplet based sensors, which can be used for portable sensors. Briefly, in Chapter 2, we discussed a characterization approach to determine the response of an evaporating droplet based sensor, and demonstrated its use in sensitive detection with a fast response time. In Chapter 3, we discussed an approach to locally deplete the ionic concentration within a droplet to address the fundamental screening limited response of the sensor. In Chapter 4, we discussed an approach to locally heat the droplet to do a fluorescence based selective detection.

As discussed earlier, in addition to droplet based portable lab-on-chip sensors, it is desirable to have wearable and implantable sensors which could continuously monitor the vital heath parameters. In Chapter 5, we discussed the performance of MoS_2, a transition-metal dichalcogenide material, for highly sensitive detection of biomolecules. Such sensors could potentially be used for flexible sensors such as epidermal sensors for tumors. Although, some recent reports suggest that MoS_2 is biocompatible [63,65,66,210], there have not been any extensive studies on long-term stability of these materials in-vivo.

In contrast, hydrogels have been studied extensively [79–83] for their biocompatibility and have shown tremendous potential for implantable biosensing [75, 77, 226]. Their high biocompatibilty orignates from their ability to hold large amount of water and their physiochemical similarity with the native extracellular matrix both compositionally and mechanically [79]. Further, these materials retain their sensing properties within the body [82], and therefore are ideal candidates for continuous in-vivo

monitoring of vital health parameters, such as blood pH. In this chapter[1], we discuss the sensing performance of hydrogel biochemical sensors based on the gel preparation parameters and environment variables.

6.1 Introduction

Decorated with capture probes, stimuli-sensitive hydrogels are three-dimensional cross-linked polymeric materials that swell/shrink depending on analyte (chemical or biomolecule) and environmental conditions such as pH [77, 84–88], ionic concentration [87], temperature [85], glucose [75, 89, 90], antigen [91], etc. These materials have been explored for numerous biomedical applications [227], such as, chemical/biomolecule sensing [75, 77, 84–88, 91, 228], contact lenses [229], drug delivery [79], tissue engineering [230], etc. Biocompatbility of hydrogel has encouraged its recent use in active implantable sensors [75, 77, 226] to continuously monitor vital health parameters.

Operation of Hydrogel sensors: Hydrogel sensors can be operated either in *free swelling* mode (FSM) or *constrained-swelling* mode (CSM). When a FSM sensor is exposed to an analyte solution, the hydrogel volume changes significantly. This change can be monitored by optical [231–233], oscillating [234], or conductimetric [235, 236] sensors. In CSM sensors, on the other hand, the hydrogel is confined between a rigid porous membrane and a semi-rigid deformable membrane [75, 77, 88, 103] (see Fig. 6.1). The rigid porous layer allows the analyte (i.e., proton) to diffuse into the hydrogel. When the analyte concentration changes, hydrogel pressure deforms the deformable membrane below. The magnitude of the pressure (ΔP) depends on several factors, such as the composition of the polymer comprising the hydrogel, the density and affinity of the capture probes to analyte (i.e., protons), and the environmental conditions such as temperature, ionic concentration, etc. The small deflection of the

[1] The content of this chapter is adapted/reproduced from Ref. [104] and Ref. [103] with permission from IEEE.

membrane due to change in pressure can then be read by various transducers such as capacitive sensors [75, 77] and piezoelectric sensors [85, 86, 237].

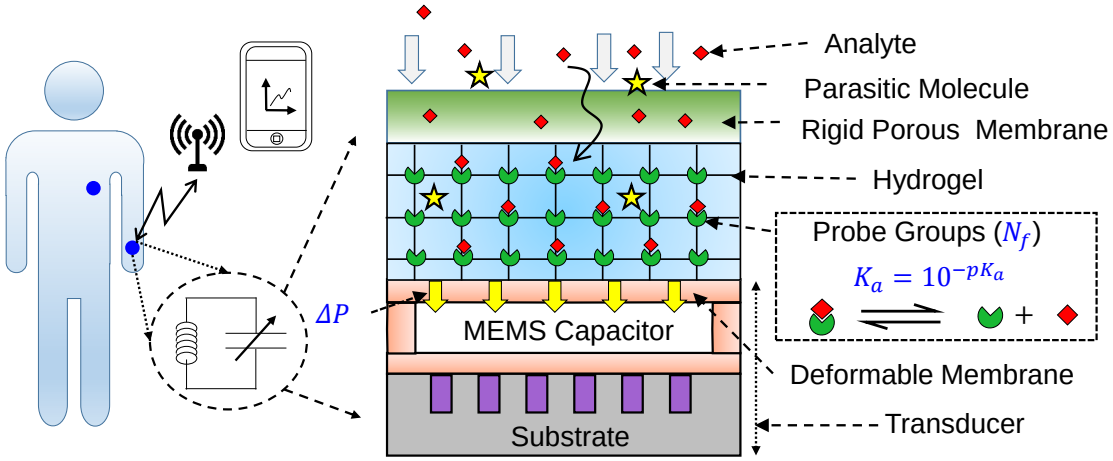

Fig. 6.1.: Schematic of a Hydrogel based Wireless Implantable Biochemical Sensor System: The sensor (blue) is implanted into a human body. The sensor is composed of an LC resonator with a hydrogel sandwiched between a rigid porous membrane and a deformable membrane. The hydrogel is pendent with the ionizable groups (with density, N_f and dissociation constant, K_a) which are responsive to analyte (say, proton) molecules. As the analyte concentration changes, the pressure exerted by hydrogel on deformable membrane changes which can be wirelessly detected.

Studies on FSM sensors: Several groups have reported numerical, analytical and experimental studies regarding the kinetics and steady-state response of *free-swelling* hydrogels. For example, Grimshaw *et al.* [238] and De *et al.* [239, 240] have reported experimental and numerical studies on free swelling kinetics of polyelectrolyte gel (without the porous membrane). Lesho *et al.* [241] reported an analytical formulation supported by experiments to determine swelling kinetics of unconstrained gels. Ballhause *et al.* [242] have numerically investigated the swelling dynamics based upon chemical stimulation due to change in ionic concentration. Kang *et al.* [243] have developed a chemo-electro-mechanical model to investigate pH dependent free-swelling of hydrogels.

Studies on CSM sensors: In contrast, the CSM sensors are relatively new and have not been analyzed as extensively. Herber *et al.* [87] and Lei *et al.* [77]

experimentally studied the pressure generated due to pH. Guenther *et al.* [85, 86, 237] and Trinh *et al.* [244] reported analytical models to determine the response of a gel under constrained conditions. Despite these significant advances both in multi-physics modeling and experiments, the key design trade-offs between the signal (characterized by sensitivity (S) and dynamic range ($\Delta\text{pH}_{\text{range}}$)) and time response (characterized by response time (τ) and symmetry of the response) are not clearly understood. Obviously, it would be difficult to design and optimize a hydrogel sensor unless these tradeoffs are explicitly specified. We will focus on CSM sensors in this chapter.

Important attributes determining sensor response: The two important attributes that govern the sensor response to pH changes are: a) The concentration of ionizable groups (N_f) [87], and b) The affinity of the ionizable group to the protons, which is determined by its acid dissociation constant (K_a). Both these design variables can be changed by using either a different ionizable group (characterized by a different K_a [245]) and/or changing N_f during hydrogel preparation.

Our findings suggest that there are performance trade-offs: An ideal pH sensor should sense the proton density ($c_{\text{H}_0^+}$) with high precision (determined by sensitivity), within a specific period of time (determined by response time), and it should do so over a broad pH range (determined by dynamic range). Also, it is preferable to have a sensor that shows symmetric response for rise and fall in the pH value. However, our findings suggest that these performance parameters are correlated and the improvement of one leads to the degradation of the other. In this chapter, we provide a systematic numerical and analytical framework to interpret and highlight these trade-offs for a gel characterized by (N_f, K_a). Our analysis yields the following important conclusions regarding the trade-off between sensitivity (S)/ dynamic range ($\Delta\text{pH}_{\text{range}}$) and response time ($\tau$)/response symmetry of CSM sensors:

1. Trade-off dictated by density of fixed ionic groups, N_f: While S and $\Delta\text{pH}_{\text{range}}$ of the sensor improve with increasing N_f, τ degrades.

2. Trade-off dictated by dissociation constant, pK_a: While S is highest for choice of $pK_a \sim$ pH (i.e., desired pH range of operation), τ degrades and the sensor response is asymmetric.

Organization of the chapter: The chapter is divided into following sections: In Section 6.2, we discuss the operational principle of the hydrogel based sensors. In Section 6.3, we provide a description of the model system and describe the numerical and analytical model. In Section 6.4, we describe the role of hydrogel preparation parameters in determining the trade-offs between different performance parameters such as signal (sensitivity/dynamic range) and time response (response time/symmetry of response), and discuss the role of environmental variables such as buffer concentration and salt concentration in determining the sensor response. In Section 6.5, we discuss a design strategy to improve dynamic range of the sensor. In Section 6.6, we describe the operation of a glucose sensor and discuss the factors that affect its sensitivity. Finally, we conclude with Section 6.8 by summarizing the essence of the work.

6.2 Device and Operational Principle

A general scheme for use of CSM sensor in detection of analyte concentration [75, 77, 103] is shown in Fig. 6.1. The sensor can be implanted in the body for continuous monitoring of analyte concentration (say, protons). The recognition element is analyte responsive hydrogel pendent with fixed ionizable (anionic/cationic) molecules with a density, N_f and acid dissociation constant, K_a. The hydrogel is constrained between a rigid porous membrane (top) and a transducer (bottom). The porous membrane can be made from a biocompatible material, for example Al_2O_3 [246]. The change in the analyte concentration brings about a change in the capacitance of the micro-electro mechanical system (MEMS) sensor due to the deformation of the flexible membrane. This sensor can be integrated with an inductor to form a LC resonator. The change in resonance frequency reflects the concentration of analyte in the sample, and can be read wirelessly using a receiver (for example, a smartphone).

6.3 Model System

6.3.1 Numerical Framework

A generic hydrogel layer is composed of both anionic groups and cationic groups. The anionic groups are represented as HA, and their deprotonated (anionic, i.e., charged form) is given by A^-. The cationic groups are represented as HB^+ and their deprotonated (neutral form) is given by B. For example, for a cationic group $R{-}NH_2$, $B \equiv R{-}NH_2$ and $HB^+ \equiv R{-}NH_3^+$. The system can be divided into 3 regions: 1) Porous membrane, i.e., region through which the protons enter the hydrogel from the sensing environment (for example, blood); 2) Hydrogel (bio-recognition layer); 3) the pressure transducer. The protons (shown in red diamonds) enter from left into the rigid porous membrane and diffuse into the hydrogel to reach the transducer surface (see Fig. 6.2). Due to change in proton concentration, the ionized state of ionizable groups in the hydrogel changes. This brings a change in concentration of salt ions which leads to osmotic pressure on the transducer.

This can be understood intuitively as follows: When the concentration of salt in two regions of the solution is different, the pressure exerted by water molecules in the region that has lesser salt concentration (more water molecules per unit volume) is larger as compared to the pressure exerted by water molecules in the region that has more salt concentration (less water molecules per unit volume). This difference in pressure results in transport of water molecules from less concentrated region to more concentrated region. However, in case of the setup shown in Fig. 6.2, the hydrogel volume is fixed, and hence the water molecules cannot diffuse into it to equalize the concentration w.r.t. the analyte solution. This results in the pressure being exerted on the transducer.

In order to determine the osmotic pressure, we first must determine the time-dependent spatial concentration of salt ions ($c_i(x,t)$) and protons (c_{H^+}) in the solution. This is determined by self-consistent solution of electrical and chemical equations. In order to simplify analysis, we make the following assumptions:

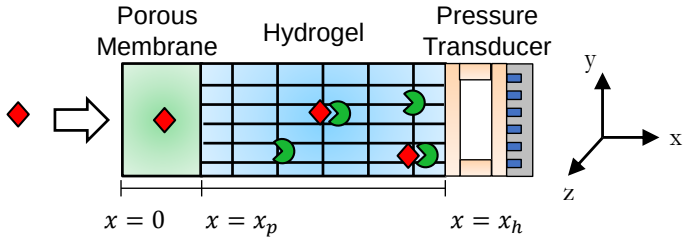

Fig. 6.2.: 1D approximation for simulation of hydrogel sensor. The area of the sensor (y-z plane) is assumed to be much larger than the thickness (x-direction).

1. The area of the sensor (y-z plane) is much larger than the thickness (x-direction), therefore 1D analysis (see, Fig. 6.2) is appropriate.

2. Sensor operates in isochoric conditions, so that the change in the thickness of the hydrogel is negligible,

3. The acid-base reactions are faster compared to the diffusion of protons [238,239], so that chemical equilibrium is established almost instantaneously. Activity factor for all ions is assumed to be 1,

4. Ionic concentration (c_s) is much higher than $c_{H_0^+}$. Therefore, the movement of salt ions is much faster than protons [240].

5. For simplicity, the diffusion coefficient of protons in hydrogel ($D_{\mathrm{H}^+,\mathrm{gel}}$) and porous membrane ($D_{\mathrm{H}^+,\mathrm{por}}$) are assumed to be same as in pure solvent (D_{H^+}). This approximation is true for small polymer volume fraction in hydrogel and large pore size in porous membrane. If pore size is small and/or polymer fraction large, the diffusion constants need to be appropriately modified [247, 248].

6. For simplicity, we assume that internal strains are small (justified in Section 6.7), so that the density of ionizable groups, N_f remains uniform during the sensing operation. If the internal strains are large, our model must be generalized by inclusion of mechanical deformation equations for a more accurate analysis [249].

7. Time response of the pressure transducer is fast as compared to the response of hydrogel.

Fig. 6.2 shows the one-dimensional approximation used for numerical simulation of the device. The proton transport through hydrogel is described by continuity equation including both drift and diffusion components,

$$\begin{gathered}\frac{\partial(c_{\mathrm{H}^+}+c_{\mathrm{HA}}+c_{\mathrm{HB}^+})}{\partial t}=-\frac{\partial}{\partial x}(J_{\mathrm{H}^+})=-\frac{\partial}{\partial x}(J_{\mathrm{H}^+,\mathrm{drift}}+J_{\mathrm{H}^+,\mathrm{diff}}),\\ J_{\mathrm{H}^+,\mathrm{drift}}=-\mu_{\mathrm{H}^+}c_{\mathrm{H}^+}(\frac{\partial\psi}{\partial x}),\qquad J_{\mathrm{H}^+,\mathrm{diff}}=D_{\mathrm{H}^+}(\partial c_{\mathrm{H}^+}/\partial x),\end{gathered}\tag{6.1}$$

with the boundary conditions,

$$c_{\mathrm{H}^+}(x=0,t)=10^{-pH},\qquad\left(\frac{dc_{\mathrm{H}^+}}{dx}\right)_{x=x_h,t}=0.\tag{6.2}$$

Here, c_{H^+} is the proton concentration, c_{HA} and c_{HB^+} are the concentration of protons bound to the anionic ($[A^-]$) and cationic groups ($[B]$) in the hydrogel layer, $J_{\mathrm{H}^+,\mathrm{drift}}$ and $J_{\mathrm{H}^+,\mathrm{diff}}$ are the drift and diffusion components of the proton current density (normalized to the electronic charge), $\psi(x,t)$ is the potential at a position x within the hydrogel or porous membrane layer, and D_{H^+} and μ_{H^+} are the diffusion coefficient and mobility of protons in the hydrogel.

The concentration of the protons bound to the ionizable groups can be described in terms of the chemical equilibrium established between protons and the groups as:

Anionic Groups:

$$\begin{gathered}\mathrm{HA}\overset{K_a}{\leftrightarrows}\ \mathrm{H}^+ + A^-,\qquad K_a=\frac{c_{\mathrm{H}^+}c_{\mathrm{A}^-}}{c_{\mathrm{HA}}},\\ N_a=c_{\mathrm{A}^-}+c_{\mathrm{HA}}.\end{gathered}\tag{6.3}$$

Cationic Groups:

$$HB^{+} \overset{K_b}{\leftrightarrows} \mathrm{H}^{+} + B, \qquad K_b = \frac{c_{\mathrm{H}^+} c_{\mathrm{B}}}{c_{\mathrm{HB}^+}}, \\ N_b = c_{\mathrm{B}} + c_{\mathrm{HB}^+}. \tag{6.4}$$

where, c_{A^-} and c_{B} are the concentrations of deprotonated anionic and cationic groups, respectively. Since the total concentration of the available anionic (N_a) and cationic groups (N_b) is conserved, the concentration of the bound protons can be expressed as:

$$c_{\mathrm{HA}} + c_{\mathrm{HB}^+} = \frac{N_a (c_{\mathrm{H}^+}/K_a)}{1 + c_{\mathrm{H}^+}/K_a} + \frac{N_b (c_{\mathrm{H}^+}/K_b)}{1 + c_{\mathrm{H}^+}/K_b}. \tag{6.5}$$

Using Eq. (6.5) in Eq. (6.1), gives modified continuity equation,

$$\left(1 + \frac{N_a/K_a}{(1 + c_{\mathrm{H}^+}/K_a)^2} + \frac{N_b/K_b}{(1 + c_{\mathrm{H}^+}/K_b)^2}\right) \left(\frac{\partial c_{\mathrm{H}^+}}{\partial t}\right) = -\frac{\partial}{\partial x}(J_{\mathrm{H}^+}). \tag{6.6}$$

Note that, the concentrations of fixed charge groups (N_a, N_b) are zero inside the porous membrane. The potential, $\psi(x,t)$ can be described by the Poisson Equation,

$$-\frac{\partial}{\partial x}\left(\varepsilon(x)\frac{\partial \psi(x,t)}{\partial x}\right) = \rho_{\mathrm{net}}(x,t) = \rho_M(x,t) + \rho_F(x,t). \tag{6.7}$$

where,

$$\rho_M(x,t) = q(c_{\mathrm{Na}^+} - c_{\mathrm{Cl}^-} + c_{\mathrm{H}^+} - c_{\mathrm{OH}^-}), \\ \rho_F(x,t) = q(c_{\mathrm{HB}^+} - c_{\mathrm{A}^-}). \tag{6.8}$$

with the boundary conditions,

$$\psi(x=0,t) = 0, \qquad \left(\frac{d\psi(x,t)}{dx}\right)_{x=x_h} = 0. \tag{6.9}$$

where, $\varepsilon(x)$ is the permittivity within the hydrogel or porous membrane layer, ρ_M and ρ_F are the net mobile and fixed charge concentrations. Since, the salt concentration

is large as compared to the proton concentration, they are in quasi-equilibrium with the potential established due to the proton diffusion into hydrogel. Therefore, their concentration can be expressed as,

$$c_{\mathrm{Na^+}}(x,t) = c_s \exp\left(-\frac{q\psi(x,t)}{kT}\right), \qquad c_{\mathrm{Cl^-}}(x,t) = c_s \exp\left(\frac{q\psi(x,t)}{kT}\right). \tag{6.10}$$

Using Eq. (6.3), Eq. (6.4) and Eq. (6.8), $\rho_F(x,t)$ can be expressed in terms of the anionic and cationic group density as,

$$\rho_F(x,t) = q(c_{\mathrm{HB^+}}(x,t) - c_{\mathrm{A^-}}(x,t)) = q\left(\frac{N_b(c_{\mathrm{H}}/K_b)}{1 + c_{\mathrm{H^+}}/K_b} - \frac{N_a}{1 + c_{\mathrm{H^+}}/K_a}\right). \tag{6.11}$$

In order to determine the time and space dependent concentration of the H^+ ions, we first determine the equilibrium solution at t=0. The concentration of the H^+ ions in equilibrium can be expressed as,

$$c_{\mathrm{H^+}}(x,t) = c_{\mathrm{H_0^+}} \exp\left(-\frac{q\psi(x,t)}{kT}\right). \tag{6.12}$$

The concentration of OH^- ions can be expressed in terms of the H^+ ions and the ionization constant of water (K_w) as, $c_{\mathrm{OH^-}}(x,t) = \frac{\mathrm{K}_w}{c_{\mathrm{H_0^+}}}$. Using Eqs. (6.7)- (6.12), we obtain the concentration of ions in the solution at t=0. Fig. 6.3 shows the equilibrium solution of potential (ψ) and electric field (E), H^+ and OH^- ion concentration, Na^+ and Cl^- ion concentration, and the ionizable group density (N_a) and fixed charge density due to ionization of acidic groups (ρ_F). As expected, the ion density and potential are uniform in both porous membrane and hydrogel. The jump in potential occurs at the interface of the porous membrane and the hydrogel, and this leads to a sharp field across the junction.

Once the equilibrium solution of the concentration of ions is obtained, we next solve Eqs. (6.6)- (6.11) (using the equilibrium solution as initial condition) self-consistently to determine the time and space dependent concentration of ions ($c_i(x,t)$). The pressure inside the hydrogel can be expressed as,

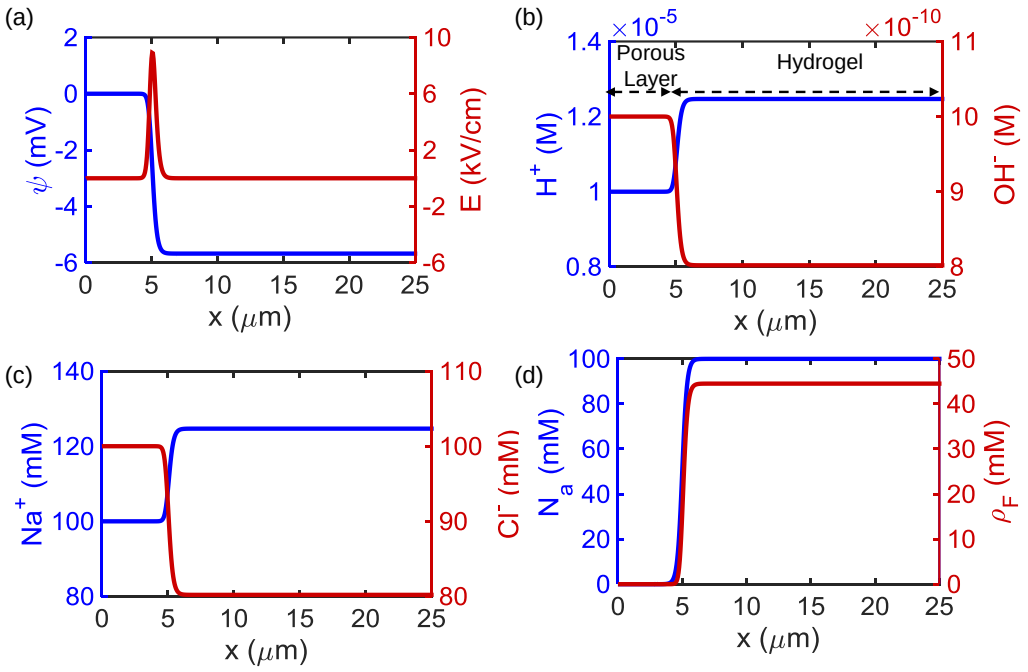

Fig. 6.3.: Equilibrium Solution of the Poisson Equation: a) Potential (ψ) and electric field (E), b) H^+ and OH^- ion concentration, c) The concentration of Na^+ and Cl^- ions, d) Ionizable group density, N_a and fixed charge density, ρ_F. The hydrogel thickness is 20 μm and porous layer thickness is 5 μm. Salt concentration, c_s =100 mM, pH=5.

$$P_{total}(x,t) = P_{\text{mix}} + P_{\text{el}} + P_{\text{ion}}(x,t). \tag{6.13}$$

Since, we assume near isochoric conditions, the contribution of pressure due to polymer-solvent mixing (P_{mix}) and due to gel elongation (P_{el}) is constant and does not result in a change in pressure [87]. Therefore, the net change in pressure that is transduced upon change in pH depends only on the osmotic pressure of ions (P_{ion}), i.e.,

$$P(t) = \Delta P_{\text{total}}(l,t) = RT(c_{\text{gel}} - c_{\text{sol}}). \tag{6.14}$$

where, $c_{\text{gel}} = \sum_i c_i(x = x_h, t)$ and $c_{\text{sol}} = \sum_i c_i(x = 0, t)$ are the net concentration of mobile ions in the hydrogel and the solution respectively, R is universal gas constant, and T is the absolute temperature which is assumed to be uniform.

Subsequently, $P(t)$ is used to evaluate different performance parameters such as *sensitivity (S), dynamic range ($\Delta\text{pH}_{\text{range}}$), response time ($\tau$) and symmetry of response*. The sensitivity is defined as the change in osmotic pressure (ΔP) per unit change in pH. We define the dynamic range as the range of pH for which the sensitivity is greater than 0.5 times its maximal value ($S_{\max}$). And, finally we define the response time of the sensor as the time required for the pressure to reach 90% (rise time, τ_{rise}) of the peak value or time required for the pressure to decrease by 90% (fall time, τ_{fall}) from the peak value. The response is symmetric if $\tau_{\text{rise}} = \tau_{\text{fall}}$.

Experimental Validation: Numerical model presented in this section is validated with the experimental data obtained from Herber *et al.* [87] and Lei *et al.* [77]. Fig. 6.4(a)-(b) show the comparison of the simulated steady state pressure (lines) as a function of pH with the experimental data (symbols) for cationic and anionic gels, respectively. The results are easily explained: The uncharged groups (B) in cationic gels are protonated (HB^+) at low pH values and exert pressure on the deformable membrane. As the pH increases, the amount of the groups that are protonated decrease and hence the pressure decreases. In contrast, anionic gels are neutral (HA) at low pHvalues and they become negatively charged (A^-) as pH is increased. This leads to an increase in repulsive force and hence an increase in pressure.

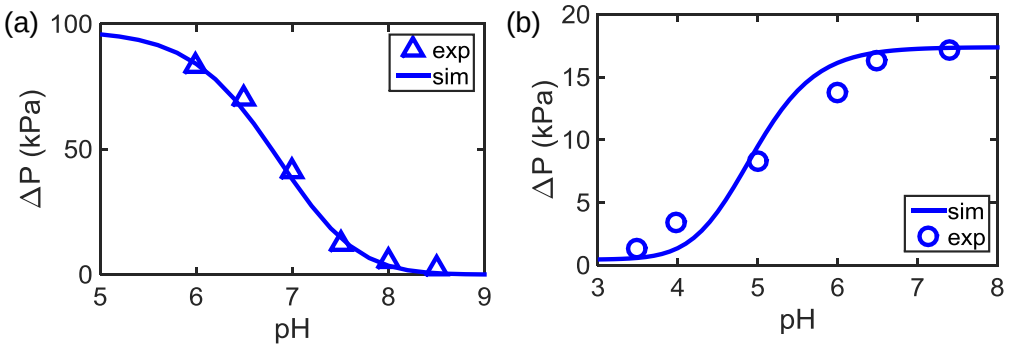

Fig. 6.4.: Experimental validation of static pressure change as a function of pH for (a) cationic and (b) anionic hydrogel. Lines represent the numerical simulation results and circle/polygon represent experimental data obtained from Ref. [87] and [77], respectively.

To summarize, this subsection discussed the numerical framework for relating the gel parameters (N_f, K_a) to the performance parameters. In next subsection, we discuss the analytical framework to relate these gel parameters to S and τ.

6.3.2 Analytical Framework

To understand the essence/origin of the tradeoff, we consider the response of a hydrogel to a small change in pH. First, we determine S in terms of (N_f, K_a) using analytical analysis, and then we relate it to τ to determine the performance trade-off.

To determine S, we relate the pressure change to the gel parameters (N_f, K_a). Invoking the charge neutrality (see Eq. (6.7)) in steady state at the hydrogel/transducer interface (see Fig. 6.2), i.e., $x = x_h$, we get,

$$\rho_{net} = q(c_{\mathrm{Na^+}} - c_{\mathrm{Cl^-}} + c_{\mathrm{H^+}} - c_{\mathrm{OH^-}}) + \rho_F = 0. \tag{6.15}$$

where, c_i are the concentrations of ionic species i and ρ_F is the fixed charge density (see Eq. (6.8)) due to ionizable groups. Since, $\mathrm{H^+}$ and $\mathrm{OH^-}$ concentrations are negligible, Eq. (6.15) becomes,

$$q(c_{\mathrm{Na^+}} - c_{\mathrm{Cl^-}}) + \rho_F = 0. \tag{6.16}$$

The concentration of $\mathrm{Na^+}$ and $\mathrm{Cl^-}$ ions can be related to potential, ψ_d at $x = x_h$ (called Donnan potential) using Eq. (6.10), i.e.,

$$c_{\mathrm{Na^+}} = c_s\lambda, \qquad c_{\mathrm{Cl^-}} = c_s/\lambda. \tag{6.17}$$

where, $\lambda = \exp\left(-\frac{q\psi_d}{k_BT}\right)$ and c_s is the ionic concentration. Similarly, using Eq. (6.12), the concentration of $\mathrm{H^+}$ ions at $x = x_h$ in equilibrium is given by,

$$c_{\mathrm{H^+}} = c_{\mathrm{H_0^+}}\lambda. \tag{6.18}$$

Considering only anionic gels with ionizable density, $N_a = N_f$ and using Eq. (6.3), we get,

$$\rho_F = -qc_{\mathrm{A}^-} = -\frac{qN_f}{(1 + c^+_{\mathrm{H}}/K_a)}. \tag{6.19}$$

Using Eq. (6.16) to Eq. (6.19), we get,

$$\lambda^3 \left(\frac{c_{\mathrm{H}^+_0}}{K_a}\right) + \lambda^2 - \left(\frac{N_f}{c_s} + \frac{c_{\mathrm{H}^+_0}}{K_a}\right) - 1 = 0. \tag{6.20}$$

The concentration of H^+ and OH^- are small compared to salt ions, therefore, we can ignore their contribution to osmotic pressure. The pressure increase at the "transducer/hydrogel interface" is then given by (using Eq. (6.14) & Eq. (6.17)),

$$P \approx RT(\lambda + \frac{1}{\lambda} - 2)c_s. \tag{6.21}$$

Equation (6.20) & Eq. (6.21) can be used to determine the hydrogel pressure (P) as a function of pH, c_s and gel parameters, N_f and K_a. If potential ψ_d is small, $c_{\mathrm{H}^+}(x = x_h) \approx c_{H^+_0}$, and further simplifications can be made. Using Eq. (6.16), Eq. (6.17) and Eq. (6.19), we get,

$$\lambda^2 - \alpha\lambda - 1 = 0. \tag{6.22}$$

where, $\alpha = \frac{(N_f/c_s)}{\frac{c_{H^+_0}}{(1+\frac{H^+_0}{K_a})}}$. Using Eq. (6.21) & Eq. (6.22), we get

$$P \approx RTc_s(\sqrt{\alpha.^2 + 4} - 2) \tag{6.23}$$

The sensitivity, S is given by,

$$S = \frac{dP}{dpH} \approx \alpha \frac{N_f^2}{\sqrt{N_f^2 + \beta^2}}. \tag{6.24}$$

where, $\alpha = 2.3RT\frac{\eta}{(1+\eta)^2}$, $\eta = 10^{-pH+\mathrm{pK_a}}$ and $\beta = 2c_s(1+\eta)$. Eq. (6.24) suggests that as N_f increases, S also increases. This is because with increase in N_f, ρ_F (see Eq. (6.19)) increases, and hence the concentration of ions which exert osmotic pressure increases.

Now that we know S as a function of gel parameters (N_f, $\mathrm{pK_a}$), we relate response time (τ) to the parameters (N_f, $\mathrm{pK_a}$). If the diffusion through the top rigid porous membrane is fast as compared to diffusion through hydrogel, τ is limited only due to transport in hydrogel. Therefore, τ can be expressed as [238, 241],

$$\tau = \gamma\frac{4l^2}{\pi^2 D_{\mathrm{eff}}}, \qquad D_{\mathrm{eff}} = D_{\mathrm{H^+}}/(1+\frac{N_f K_a}{(K_a + c_{\mathrm{H^+}})^2}). \tag{6.25}$$

where, l is the hydrogel thickness (see Fig. 6.2) and $D_{\mathrm{H^+}}$ is the diffusion constant of protons ($c_{\mathrm{H^+}}$) in the hydrogel membrane, and γ is a proportionality constant. The protons moving through the hydrogel membrane are slowed due to instantaneous quasi-equilibrium established between the protons and the ionizable groups (see, Ref [250] for more information), this results in reduced effective diffusion constant (D_{eff}) and an increased τ.

Equation (6.25) suggests that τ scales as l^2, the thickness of the hydrogel. However, for a sensor to work, there must be sufficient strain at the transducer, and this ultimately puts a minimum limit to the hydrogel thickness. For a given l, τ decreases as N_f decreases or as K_a shifts away from $c_{\mathrm{H^+}}$.

Neglecting 1 in Eq. (6.25) and rearranging, we get $N_f = k\tau$ where $k = \frac{\pi^2 D_{\mathrm{H^+}}}{4\gamma l^2}\frac{(K_a + c_{\mathrm{H^+}})^2}{K_a}$. Therefore, by substituting $N_f = k\tau$ in Eq. (6.24), we get S vs. τ trade-off equation,

$$S = \frac{a\tau^2}{\sqrt{\tau^2 + \tau_0^2}}. \tag{6.26}$$

where, $a = 2.3RTk\frac{\eta}{1+\eta}$ and $\tau_0 = 2(1+\eta)c_s/k$.

Trade-off highlighted by Eq. (6.26) is one of the *key conclusions* of the this work. It suggests that an increase in S is correlated to an increase in τ. Therefore, a compromise must be made between the two performance parameters for CSM sensors.

Limitations of analytical analysis: Although the analytical analysis provides some intuition into the trade-off, a numerical model (as discussed earlier) is essential to:

1. Include the effect of Donnan potential, ψ_d (see Fig. 6.5),
2. Account for diffusion through the porous membrane (see Fig. 6.6),
3. Interpret the asymmetry in time response for large pH changes (discussed later),
4. Explain the effect of ionic concentration on the response time (discussed later).

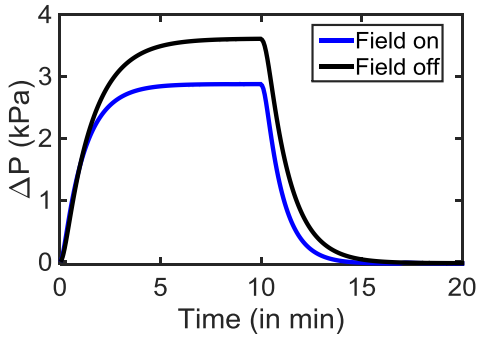

Fig. 6.5.: Effect of drift term on S and τ: Numerically simulated pressure change (ΔP) upon increase in pH, with and without drift term included.

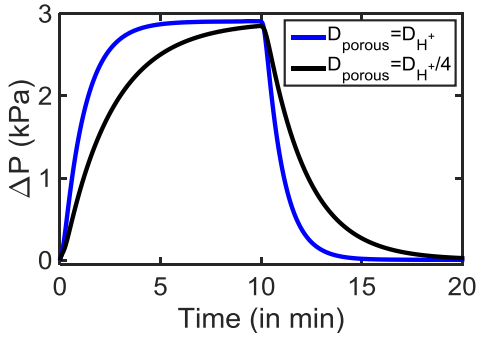

Fig. 6.6.: Effect of slow diffusion in porous membrane: Numerically simulated pressure change upon increase in pH, with different diffusion coefficients for H^+ in porous membrane.

6.4 Results and Discussions

In this section, we use numerical model to determine the response of the sensor on gel parameters ($N_f, \mathrm{pK_a}$), and use analytical model to interpret the trade-offs between the performance parameters. We suggest ways to improve the signal and time response and show that the improvement of one performance parameter (such as sensitivity/dynamic range) leads to degradation of the other (response time/symmetry in response). Therefore, a trade-off must be considered between performance parameters for optimal design of the sensor.

6.4.1 Role of Ionizable Group Density (N_f)

N_f is a design variable that can be changed during hydrogel preparation. As discussed in Section 6.3, N_f not only affects the response time but also sensitivity. In addition, N_f affects the dynamic range and apparent $\mathrm{pK_a}$ (point of maximal sensitivity). In this subsection, we will discuss the role of N_f in dictating these performance parameters and associated trade-offs between them.

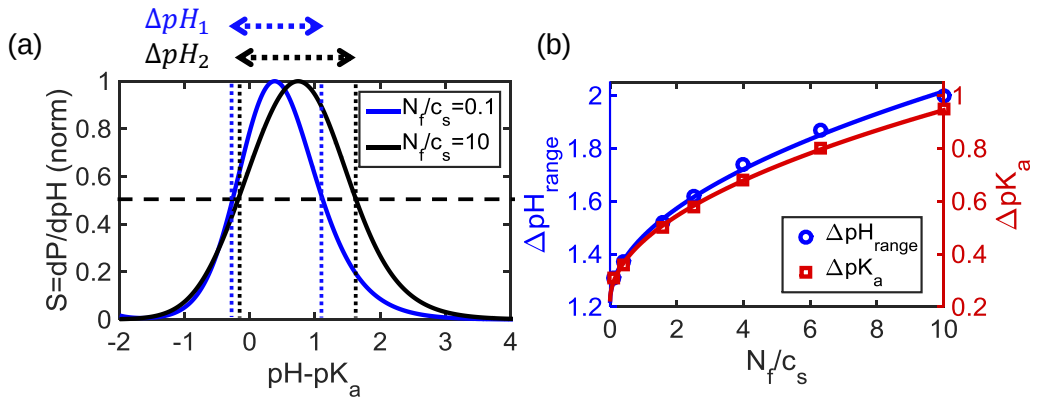

Fig. 6.7.: (a) Normalized change in pressure as a function of pH for two different ratios of anionic density (N_f) to salt concentrations (c_s). The sensitivity is maximum near the $\mathrm{pK_a}$ (i.e., apparent $\mathrm{pK_a}$) of the anionic groups. (b) Change of dynamic range ($\Delta\mathrm{pH_{range}}$) and the difference between the apparent $\mathrm{pK_a}$ and real $\mathrm{pK_a}$ ($\Delta\mathrm{pK_a}$) as a function of the N_f/c_s ratio. As the ratio increases, the dynamic range of the sensor increases. Symbols are the numerical simulation results and the lines are guide to eye.

Large N_f ensures high-dynamic range: Fig. 6.7(a) shows the numerical simulation of normalized sensitivity as a function of $\mathrm{pH} - \mathrm{pK_a}$ for two different ratios of anionic group densities (N_f) to the salt concentration (c_s). Two observations can be made: First, as N_f increases, the maximal sensitivity point, i.e., apparent $\mathrm{pK_a}$ ($\mathrm{pK_{app}}$) shifts to right. The shift in $\mathrm{pK_{app}}$ point reflects the change in Donnan potential due to ionized fixed charges. Second, the dynamic range ($\Delta\mathrm{pH_{range}}$) increases from $\Delta\mathrm{pH_1}$ to $\Delta\mathrm{pH_2}$. Fig. 6.7(b) shows the dependence of $\Delta\mathrm{pH_{range}}$and $\Delta\mathrm{pK_a} = \mathrm{pK_{app}} - \mathrm{pK_a}$ on N_f/c_s ratio. The $\Delta\mathrm{pH_{range}}$ increases by almost 0.7 pH units as N_f/c_s ratio increases from 0.1 to 10. Further, $\mathrm{pK_{app}}$ deviates from the real $\mathrm{pK_a}$ by almost 1 unit for very large anionic density (N_f =1 M for c_s =100 mM). To summarize, if N_f is large, the dynamic range is high and pH at which sensor is most sensitive ($\mathrm{pK_{app}}$) shifts away from $\mathrm{pK_a}$.

While S improves with increasing N_f, τ degrades: Fig. 6.8(a) shows the numerically simulated pressure change as a function of time for a small change in pH (from 5 to 5.1, with $\mathrm{pK_a} = 5$) for two different densities of the anionic group, i.e., 25 mM and 100 mM respectively. While the pressure change (ΔP) increases as N_f changes from 25 mM to 100 mM, it takes longer to reach the saturation pressure value. Fig. 6.8(b) and (c) show the fit of analytical expression for S (see Eq. (6.24)) and τ (see Eq. (6.25)) as a function of N_f to the numerically simulated result, respectively. Excellent agreement of analytical expression with the numerical result justifies our assumptions in deriving the analytical expressions. Fig. 6.8(d) shows the trade-off between sensitivity ($S = \Delta P/\Delta pH$) and response time (τ) as N_f is varied. While S increases with N_f, τ increases as well leading to a slower sensor response. This trend is in agreement with the experiments by Herber et. al. [87] where they increased the relative composition of monomer dimethylaminoethyl methacrylate (DMAEMA) in their hydrogel preparation. Therefore, a compromise must be made between S and τ.

Comparison with analytical model: The analytical result (line) for S vs. τ trade-off in Fig. 6.8(d) matches the numerical result (symbols) quite well with

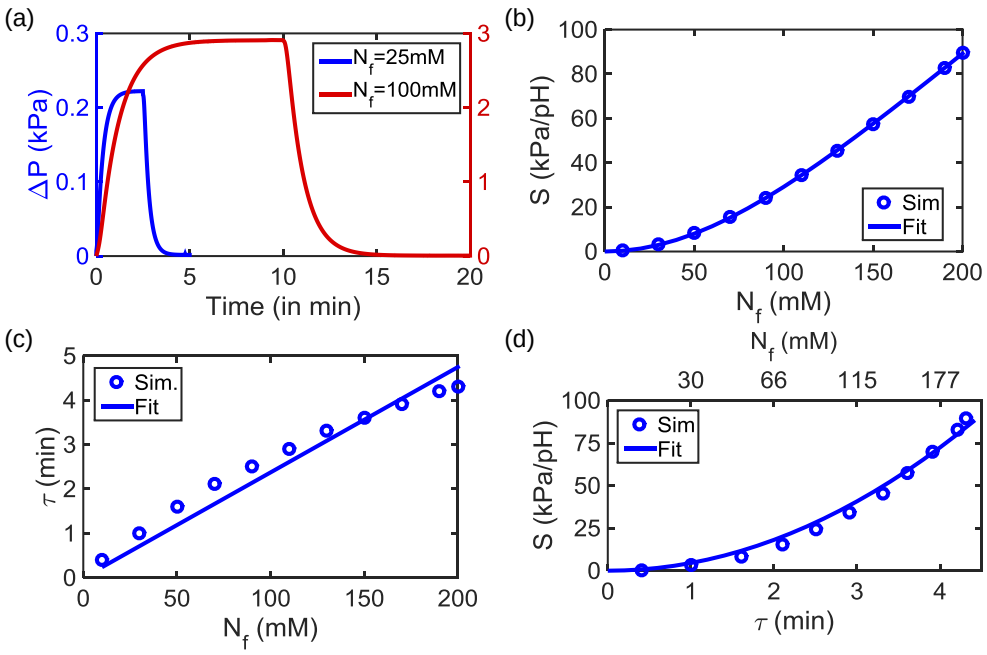

Fig. 6.8.: (a) Change in pressure as a function of time for two different anionic densities upon pH step from 5 to 5.1 ($pK_a = 5$), (b) Fit of analytical expression for S vs. N_f (line) in Eq. (6.24) to numerical simulation (symbols). S increases with increases in N_f, (c) Fit of analytical expression, $N_f = k\tau$ (line) to the numerical simulation (symbols). τ degrades with increase in N_f, (d) Tradeoff between sensitivity and response time: As the sensitivity increases, the response time also increases. Symbols represent numerical simulation and line represents fit using Eq. (6.26). Hydrogel thickness is 20 μm, Porous membrane thickness is 5 μm.

Table 6.1.: List of fitting parameters for match of analytical expressions to numerical model

Fig., Plot	Fitting Parameters
Fig. 6.8(b), S vs. N_f	$\alpha = 0.6$ kPa/mM, $\beta = 180.4$ mM
Fig. 6.8(c), τ vs. N_f	$k = 42$ mM/min
Fig. 6.8(d), S vs. τ	$a = 16420$ kPa min^{-1}, $\tau_0 = 3629$ min
Fig. 6.9(b), τ_s vs. pK_a	$a = 9.5 \times 10^{-2}$ min mM
Fig. 6.10(c), τ_{rise} vs. pK_a	$a = 7.24 \times 10^{-2}$ min mM, $c_{H^+,eff} = 10^{-3}$ mM
Fig. 6.10(d), τ_{fall} vs. pK_a	$a = 5.83 \times 10^{-2}$ min mM, $c_{H^+,eff} = 4.5 \times 10^{-3}$ mM

appropriate fitting parameters a and τ_0 (see Table 6.1), which further justifies our assumptions in derivation of Eq. (6.26). Numerical simulations show that neglecting

Donnan potential overestimates sensitivity by ∼25% and response time by ∼30% (see Fig. 6.5). Also, while Eq. (6.25) suggests that τ is independent of salt concentration (c_s), detailed numerical simulations (discussed later) show that τ can vary by almost 2-3 times as c_s changes from 20 mM to 200 mM. Finally, the porous membrane itself can lead to a slowdown in the sensor response (see Fig. 6.6). Therefore, although all the qualitative trends and trade-offs as a function of various sensor parameters are explained by analytical analysis, a numerical simulation is essential for accurate prediction of the response time and sensitivity.

To summarize, Fig. 6.7(b) and Fig. 6.8(d) highlight the importance of N_f in dictating the trade-off between different performance parameters. While S and $\Delta\text{pH}_{\text{range}}$ both improve as N_f increases, τ degrades. The requirement to have a reasonable τ puts a maximum limit on N_f.

6.4.2 Role of dissociation constant (pK_a) of ionizable groups

The choice of anionic/cationic ionizable group (characterized by a pK_a) can significantly affect S and τ. In this subsection, we consider the choice of ionizable group for a pH sensor designed to operate near pH=5 (as an illustrative example). However, the implications are general and the same analysis follows for other pH values.

Time response for small pH changes ($\Delta\text{pH} \ll \log_{10}(e)$)

Fig. 6.9(a) shows the numerically simulated change in pressure as a function of time for three different anionic groups for the pH change, ΔpH by 0.1 unit at base pH = 5 (i.e., desired pH operation). Two observations can be made: First, the response of the sensor is symmetric (rise time is same as fall time). Second, τ is maximum for anionic group with pK_a close to the desired range of operation of the device (pH=5).

Fig. 6.9(b) shows the numerically simulated (symbols) response time and pressure change as a function of pK_a of the ionizable group. Analytical expression for response

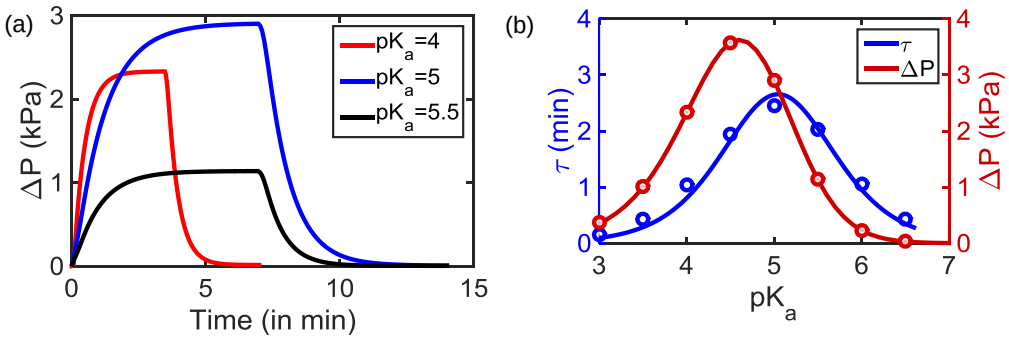

Fig. 6.9.: (a) Change in pressure as a function of time for a pH change from 5 $\rightarrow$ 5.1 $\rightarrow$ 5 for anionic groups with different pK_a values, (b) The change in response time (τ) and pressure change (ΔP) as a function of pK_a. While S is high for pK_a close to the desired pH range, τ is also high. Blue and red symbols represent numerical simulation result, and blue line represent fit using Eq. (6.25) . Red line is a guide to eye. Hydrogel thickness is 20 μm, Porous membrane thickness is 5 μm, N_f =100 mM.

time, $\tau \approx aK_a/(K_a + c_{H^+})^2$ (see Eq. (6.25)) (line) fits the numerical result quite well with appropriate fitting parameter a (see Table 6.1), and average c_{H^+}. The figure illustrates that while sensitivity ($S \sim \Delta P$) is maximum when $pK_a \sim$ pH, the response of the sensor is slowest. Therefore, a trade-off must be considered between S and τ for appropriate design of the sensor.

Time response for large pH changes (ΔpH $\geq \log_{10}(e)$)

Fig. 6.10(a) shows the simulated response of the sensor for a pH change from 4 $\rightarrow$ 5 $\rightarrow$ 4 for anionic groups with different pK_a. Two observations can be made: *a)* The sensitivity is higher when pK_a is close to the base pH value, *b)* The sensor response is asymmetric, i.e., $\tau_{rise} \neq \tau_{fall}$.

Fig. 6.10(b), (c) and (d) shows the numerically simulated (symbols) τ_{rise}, τ_{fall} and sensitivity ($S \sim \Delta P$) as a function of the pK_a, respectively. Analytical expression for response time, $\tau \approx aK_a/(K_a + c_{H^+,eff})^2$ (see Eq. (6.25)) fits the numerical result for both τ_{rise} and τ_{fall} quite well with appropriate fitting parameters (see Table 6.1). Note, that we use effective proton concentration $c_{H^+,eff}$ (obtained from fit) instead of

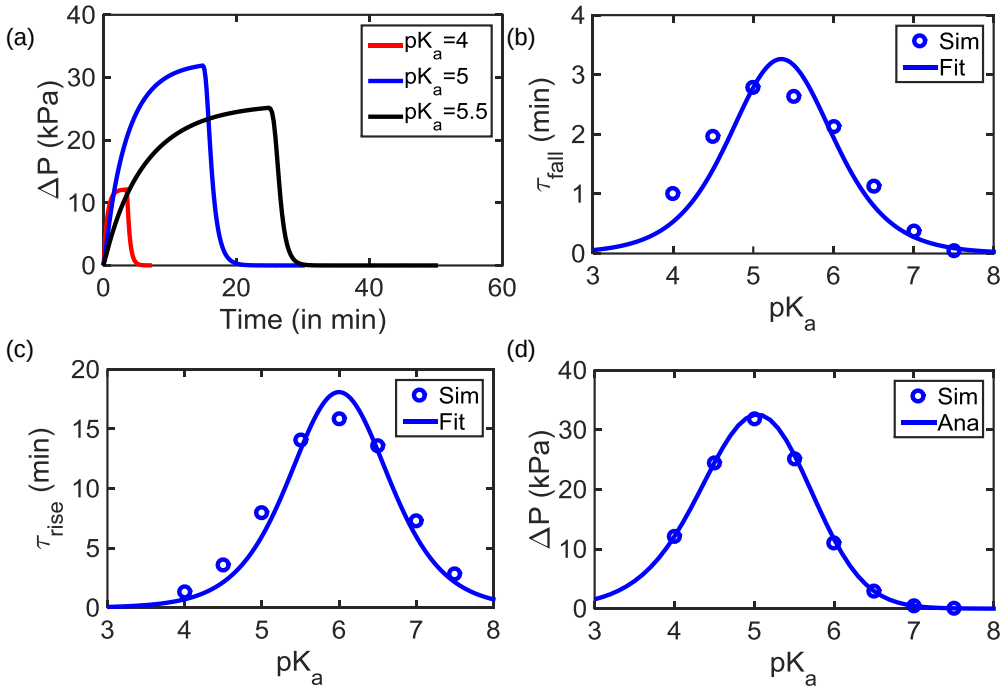

Fig. 6.10.: (a)Change in pressure as a function of time for large changes in pH values (from $pH = 4 \rightarrow 5 \rightarrow 4$) for different choice of anionic groups (i.e., different $\mathrm{pK}_a's$), (b) The rise (τ_{rise}) and (c) fall (τ_{fall}) time and (d) the change in pressure as a function of the pK_a. While the sensor is most sensitivity for pK_a close to the base pH value (i.e., $pH = 5$), the response time is also high. Further, the asymmetry (i.e., $\tau_{\mathrm{rise}} \neq \tau_{\mathrm{fall}}$) is high when pK_a is close to the desired pH range. The symbols show numerical simulation and smooth lines show the fit to the analytical expression (see Eq. (6.25)) for τ_{rise} and τ_{fall}.

c_{H^+}, since the concentration of protons (c_{H^+}) increase/decreases by a factor of 10 as the pH change is large. The figure illustrates that the sensor response is symmetric and faster only for choice of anionic groups whose pK_a is far off from the base pH value. However, S degrades in such a scenario, and therefore a trade-off must be considered.

To summarize, Fig. 6.9(b) and Fig. 6.10(b),(c),(d) highlight the importance of ionizable group (i.e., pK_a) in dictating the trade-off between S and τ, for sensors with both small and large pH variations. While S is maximized if $\mathrm{pK}_a \sim \mathrm{pH}$, τ degrades and the asymmetry (for large pH changes) increases. Therefore, a compromise must

be made between S and τ or symmetry of response for appropriate design of the sensor.

6.4.3 Effect of environment variables

In Section 6.4.1 and Section 6.4.2, we discussed the importance of hydrogel preparation parameters in determining the trade-off between S and τ. In addition to the hydrogel preparation parameters, the environmental variables such as salt concentration (c_s) and buffer ion concentration (N_{buff}) can also affect S and τ. In this section, we discuss the effect of these environmental variables on the performance parameters, S and τ of the sensor.

Ionic concentration (c_s)

S degrades with increasing c_s: Fig. 6.11(a) and (c) show S as a function of c_s for small change in pH around pK_a <pH and pK_a >pH, respectively. S decreases as the c_s increases. This is because as c_s increases the amount of excess salt (proportional to the generated pressure) required to neutralize the anionic charged group decreases.

τ improves with increasing c_s only for pK_a <pH: The time response of the sensor w.r.t. change in ionic concentration shows an interesting trend. For pK_a <pH of anionic groups, the sensor responds faster as the salt concentration increases (see Fig. 6.11(b)). However, for pK_a >pH of the anionic groups, the sensor responds slower as c_s increases (see Fig. 6.11(d)). This interesting trend can be explained as follows: The response time is given by $\tau \sim \frac{N_f K_a}{c_{\text{H}^+}^2}$ (see Eq. (6.25)). For pK_a <<pH, $\tau \sim 10^{\text{pK}_\text{app}}$. Since, pK_app decreases with increase in c_s (see Fig. 6.7(b)), τ decreases. For pK_a >>pH, $\tau \sim 10^{-\text{pK}_\text{app}}$. Therefore, τ increases with increase in c_s. To summarise, a diluted solution shows a higher sensitivitiy and faster/slower response time depending on the pH and pK_a of the ionizable groups.

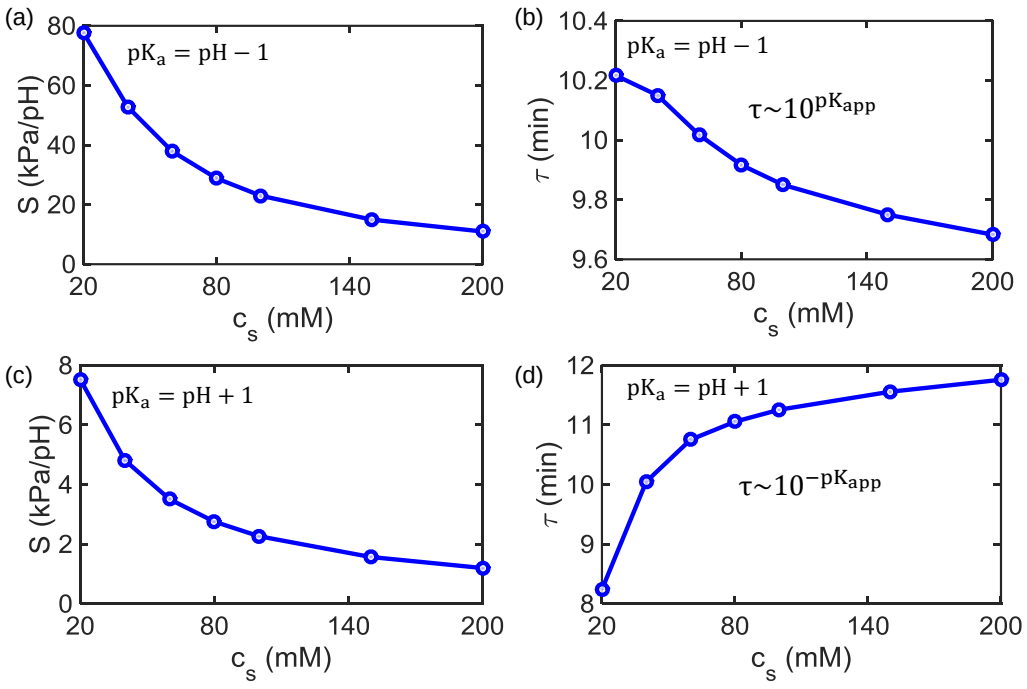

Fig. 6.11.: Effect of salt concentration (c_s) on the sensor response: S decreases with increase in c_s for both (a) pK$_a$ <pH and (c) pK$_a$ >pH. (b),(d) τ decreases with increase in c_s for pK$_a$ <pH, and increases with increase in c_s for pK$_a$ >pH.

Buffer ions improve time response ($N_{\mathbf{buff}}$)

Equation (6.1) assumes that the transport of proton occurs directly without any buffer mediated diffusion. In case, buffer ions are present the equation needs to be modified as follows:

$$\begin{aligned} \frac{\partial(c_{\mathrm{H^+}} + c_{\mathrm{HA}} + c_{\mathrm{HB^+}} + c_{\mathrm{H,buff}})}{\partial t} &= -\frac{\partial}{\partial x}(J_{\mathrm{H^+}} + J_{\mathrm{H,buff}}), \\ J_{H,\mathrm{buff}} = -D_{H,\mathrm{buff}}\frac{\partial c_{H,\mathrm{buff}}}{\partial x} &+ \alpha_{\mathrm{buff}}\ \mu_{H,\mathrm{buff}} c_{H,\mathrm{buff}}\frac{\partial \psi}{\partial x}. \end{aligned} \tag{6.27}$$

where, $c_{H,,\mathrm{buff}}$ is the concentration of the protons bound to the buffer ions, $J_{H,\mathrm{buff}}$ is the total drift/diffusion current due to the buffer ions, $D_{H,\mathrm{buff}}$ and $\mu_{H,\mathrm{buff}}$ are the diffusivity and mobility of protonated buffer ions in the hydrogel, and α_{buff} is the charge on the protonated buffer ion, i.e., 0 for acidic buffer ([HA′]) and +1 for basic

buffer ([HB'$^+$]). Further, similar to the affixed cationic and anionic groups in the gel (see Eq. (6.3) & Eq. (6.4)), the protonated and deprotonated form of the mobile cationic and anionic buffer ions can be expressed in terms of the buffer concentration (N_{buff}). Buffer ions mediate the transfer of protons from the solution to the hydrogel and this leads to a faster response as the buffer ion concentration increases (as shown in Fig. 6.12).

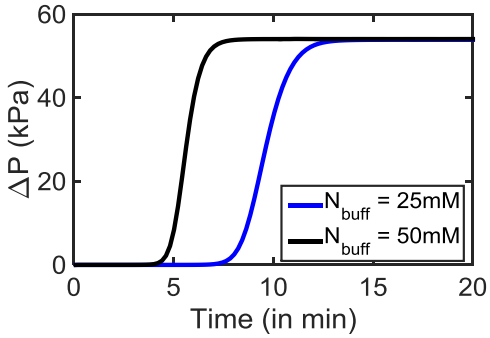

Fig. 6.12.: Effect of buffer ion concentration on the sensor response. While the sensitivity remains same, the response of the sensor becomes faster as the buffer concentration increases. Simulation conditions: pH is stepped from 9 to 6 for a cationic gel with N_f = 100 mM and pK_a =7.4 and buffer, $\text{pK}_{\text{buff}} = 4$

6.5 Design strategy to improve dynamic range

Fig. 6.7(a) shows that the hydrogel is responsive only in a narrow bandwidth around pK_a of the ionizable groups used for the hydrogel preparation. The dynamic range ($\Delta\text{pH}_{\text{range}}$) could be improved by increasing the number density of ionizable groups, but as explained earlier it leads to a slower sensor response. The high sensitivity near pK_a of the ionizable group suggests that the dynamic range can also be improved by using hydrogels prepared with more than one type of ionizable group, i.e., using multiple ionizable monomer units having different pK_a values (say, pK_{a1} and pK_{a2}) and different densities (N_{f1} and N_{f2}). Although hydrogels with multiple ionizable groups have been prepared/characterized by other research groups, the ap-

propriate choice of the ionizable groups to extend the dynamic range, and its resultant impact on the response time has not been studied previously in context of hydrogel.

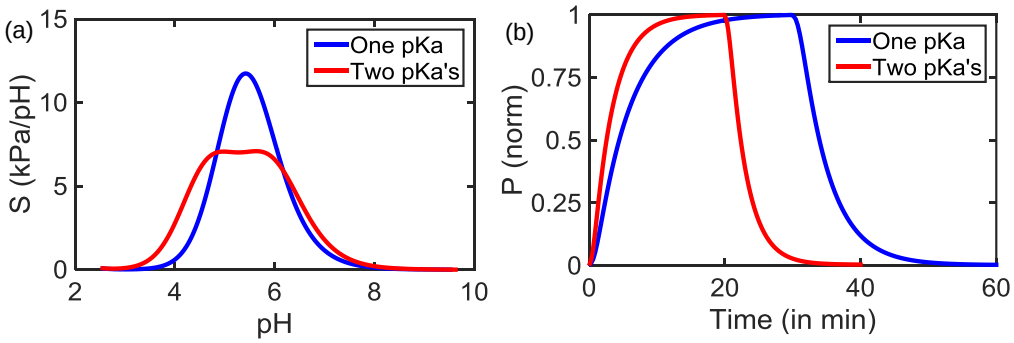

Fig. 6.13.: (a) Comparison of sensitivity of mono-ionic gel (only one type of ionizable monomer) with poly-ionic gel (two different ionizable monomers) as a function of pH. pK_a and N_f for mono-ionic gel were chosen to be 5.0 and 100 mM respectively, and the pK_a's and N_f values for poly-ionic gel were pK_{a1}=4.3, pK_{a2}=5.7, N_{f1}=68 mM, N_{f2}=32 mM. (b) Normalized response of the sensor as a function of time. The response of the poly-ionic gel is faster than that of mono-ionic gel.

Multiple pK_a improves ΔpH_{range}, linearity and τ: Fig. 6.13(a) shows the sensitivity of the sensor as a function of pH for a hydrogel composed of two different type of anionic ionizable groups. The dynamic range of this sensor is larger ($\Delta pH_{range} = 2.5$) than the gel with only one type of ionizable group ($\Delta pH_{range} = 1.4$) hydrogel system. Further, the sensor shows a more linear operation (same sensitivity over extended range) as compared to the sensor with just one type of ionizable group. However, the peak sensitivity of the gel with two type of ionizable groups is smaller than the gel having only one type of ionizable group (as the net ionizable group density is same). Interestingly, the response of the gel with two type of ionizable groups is faster than the response of hydrogel with only one type of ionizable group as shown in Fig. 6.13(b). This is because the effective N_f which plays a role in slowing down the proton diffusion at a particular pH value is less than the total ionizable group density (as can be observed from the decrease in sensitivity).

6.6 Glucose Sensor

Untill now, we have discussed the operation of hydrogel based pH sensor and the importance of gel parameters and environmental variables in determining the sensor response. A hydrogel based non-enzymatic glucose sensor works in a similar way, although it involves a two step reaction. First, the H^+ ions dissociate from the weak acid, HA (for example, phenyl boronic acid (PBA)) to form A^-:

$$\mathrm{HA} \overset{K_a}{\leftrightarrows} \mathrm{H}^+ + A^-, \qquad K_a = \frac{c_{\mathrm{H}^+} c_{\mathrm{A}^-}}{c_{\mathrm{HA}}}. \tag{6.28}$$

Next, the glucose molecules attach to the acidic groups to form a GA^- complex:

$$A^- + G \overset{K_g}{\leftrightarrows} GA^-, \qquad K_g = \frac{c_{GA^-}}{c_{A^-} c_{HA}}. \tag{6.29}$$

The net concentration of the acidic groups is conserved. Therefore, we have,

$$N_a = c_{GA^-} + c_{A^-} + c_{HA}. \tag{6.30}$$

Using Eqs. (6.28)- (6.30), the concentration of fixed charges in the hydrogel can be expressed in terms of c_{H^+} and c_{G} as:

$$\rho_F = q\left(c_{\mathrm{GA}^-} + c_{\mathrm{A}^-}\right) = q \frac{1}{\left(1 + \frac{c_{\mathrm{H}^+}}{K_{\mathrm{eff}}}\right)} N_f. \tag{6.31}$$

where, $K_{\mathrm{eff}} = K_a\left(1 + \frac{c_{\mathrm{G}}}{K_g}\right)$ is a function of glucose concentration, c_{G}. Therefore, the analytical model developed for the sensitivity analysis of the pH sensor is valid for glucose sensor with the understanding that pK_a in Eq. (6.20) needs to be replaced by $\mathrm{pK}_{\mathrm{eff}} = -\log_{10}(K_{\mathrm{eff}})$. Fig. 6.14(a) shows the match of experimental data using the analytical equation. The results are easy to understand: As the concentration of the glucose increases, the ionized (A^-) react with glucose molecules to form GA^- complex. The decrease in A^- is compensated by the increase in ionization of the

acidic groups. As a result, the net fixed charge density inside the hydrogel increases, leading to an increase in osmotic pressure.

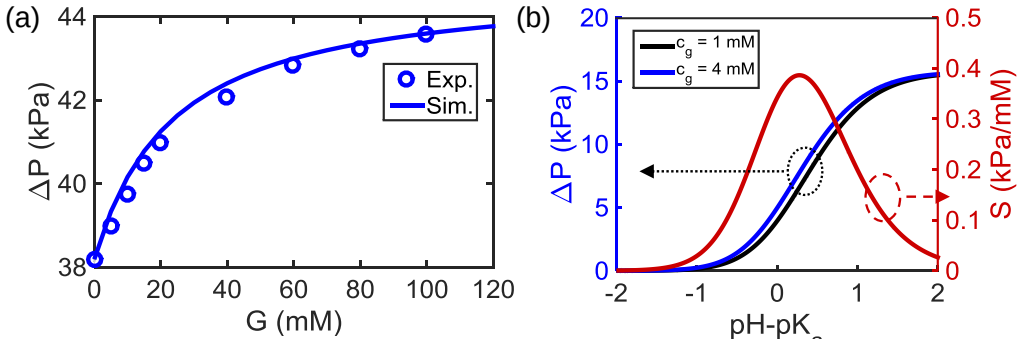

Fig. 6.14.: (a) ΔP as a function of glucose concentration (G). Experimental data obtained from Lei *et al.* [75]. (b) The pressure for two different glucose concentrations, i.e., 2 mM (black) and 4 mM (blue) as a function of pH-pK_a. The sensitivity is maximum close to the pK_h $\sim$ pH of the acidic groups. Parameters: N_f = 50 mM, c_s = 100 mM.

Fig. 6.14(b) shows the pressure change as a function of pH$-$pK_a for different concentration of glucose, i.e., 1 mM and 4 mM. The sensitivity, $S = dP/dc_{\mathrm{G}}$ shows a maximum close pK_a=pH. This result is similar to our analysis on pH sensor, where the sensitivity is maximized with a pK_a close to the pH range of operation. Similar to the pH sensor, the sensitivity of the glucose sensor can be considerably enhanced by embedding A^- with higher association constant (A_1 to A_3) with glucose, decreasing c_s and increasing N_f (see Fig. 6.15).

To summarize, our analysis suggests that the operation of the non-enzymatic glucose sensor can be described in a similar way as compared to pH sensor, and S can be maximized by using pK_a close to the desired pH range or using a probe molecule with higher affinity to the glucose.

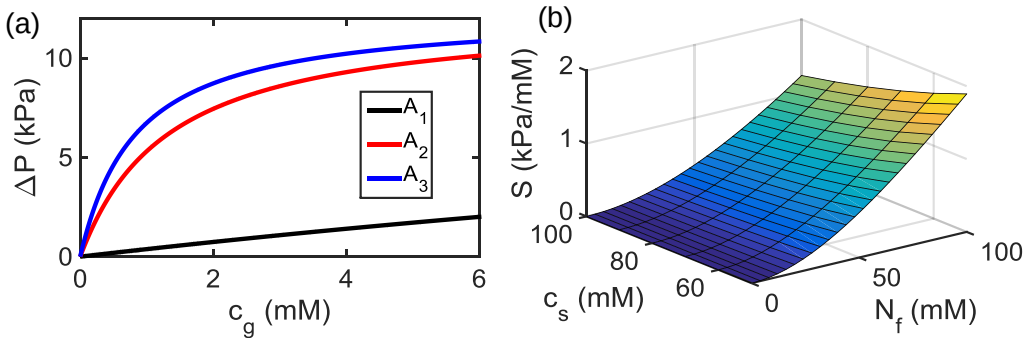

Fig. 6.15.: (a) Effect of the affinity constant $(1/K_g)$ of acidic group with the glucose. A_1 (PBA), A_2 (A pyridinium Derivative) and A_3 (A diboronic acid) are three different acids (HA) with increasing association constants [251].

6.7 Mechanical Deformation of Hydrogel

In Section 6.3, we assumed that the internal strain in the hydrogel is small enough so that we can assume a fixed density of ionizable groups (N_f). Such an assumption, however, requires a careful analysis as follows. The mechanical deformation of the hydrogel in one-dimension can be described by the equation of motion for the displacement (u) of a point in hydrogel (see Fig. 6.16) from its equilibrium value [252], namely,

$$\rho\frac{\partial^2 u}{\partial x^2} + f\frac{\partial u}{\partial t} = \frac{\partial \sigma}{\partial x} + \rho b, \tag{6.32}$$

where ρ is the mass density, f is the parameter for the mechanical damping, σ is the stress, and b is the sum total of all the body forces (i.e., the volume forces which act throughout the body, for example, gravity).

The swelling process is slow, therefore, we can neglect the effect of inertia i.e. the first term in Eq. (6.32) containing the second derivative of displacement in time [253]. simplifies to,

$$f\frac{\partial u}{\partial t} = \frac{\partial \sigma}{\partial x} + \rho b. \tag{6.33}$$

Furthermore, in absence of any body forces in x-direction, we can write,

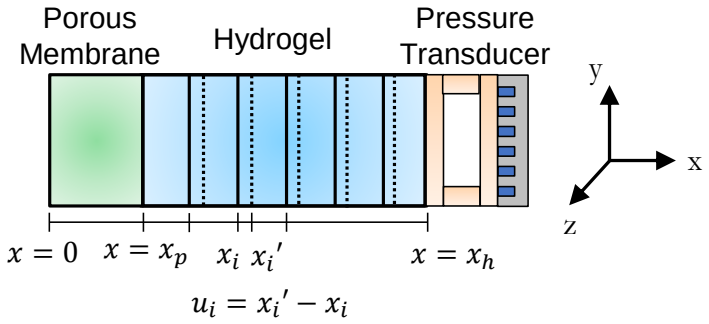

Fig. 6.16.: Mechanical deformation of hydrogel. The dashed line shows the displaced grid within the hydrogel. u is the displacement of the ith grid point from its equilibrium position.

$$f\frac{\partial u}{\partial t} = \frac{\partial \sigma}{\partial x}. \tag{6.34}$$

Now, σ depends on difference between two parameters: mechanical strain, $\varepsilon = \partial u/\partial x$ and the swelling strain (ε_P) (due to osmotic pressure, P) and is given by,

$$\sigma = E(\varepsilon - \varepsilon_P), \tag{6.35}$$

where E is the modulus of elasticity. The swelling strain, ε_P is given by [242,253,254],

$$\varepsilon_P = k(P(x,t) - P_0), \tag{6.36}$$

where P is osmotic pressure at a given time and position, P_0 is the initial osmotic pressure, and k is the swelling coefficient which depends on type of the gel and the absolute temperature. The time constant associated with mechanical relaxation is given by,

$$\tau_{\text{mech}} = l^2/\pi^2 D_{\text{mech}}, \tag{6.37}$$

where l is the characteristic length, and $D_{\text{mech}} = E/f$ is the effective mechanical diffusion coefficient corresponding to the mechanical relaxation. For the hydrogel

thickness considered in this analysis ($l = 20$ μm), $\tau_{\text{mech}} = 0.2$ min with $D_{\text{mech}} = 3.2 \times 10^{-11}$ m^2/sec [255]. In contrast, as discussed in Section 6.4, the effective time for proton diffusion (τ_P) is several minutes. Since, $\tau_P >> \tau_{\text{mech}}$, the stress relaxation can be assumed instantaneous, and the left hand side of the Eq. (6.34) reduces to zero, so that

$$\frac{d\sigma}{dx} = 0. \tag{6.38}$$

Integrating Eq. (6.38) and using Eq. (6.36), we get,

$$\sigma = E(\varepsilon - \varepsilon_P) = \sigma_0, \tag{6.39}$$

where σ_0 is the integral constant. This gives,

$$\varepsilon(x,t) = \frac{\sigma_0}{E} + k(P(x,t) - P_0). \tag{6.40}$$

Without loss of generality, we can assume that the strain is zero under equilibrium conditions, i.e., for $P = P_0$. This gives,

$$\varepsilon(x,t) = k(P(x,t) - P_0). \tag{6.41}$$

as the strain induced due to the osmotic pressure. For the analysis done in this work, $\Delta P \leq 5$ kPa for small changes in pH (~ 0.1) and $\Delta P \leq 35$ kPa for large pH changes (~ 1) (see Fig. 6.9 and Fig. 6.10), therefore, the strain $\varepsilon \sim 0.008$ for small pH changes and $\varepsilon \sim 0.056$ (with $k = 1.64 \times 10^{-6}$ Pa [254]). Hence, the maximum strain is less than 1% for small pH change and less than 6% for larger pH changes. Therefore, the assumption of the constant N_f is fully justified. Our results are in agreement with analysis done by Wallmersperger *et al.* [254] where they report strain <5% for their samples. If the pH change is very large (few units) and/or N_f is very large (few molars), then the strain would become large ($> 10\%$), and the model would need to be generalized by inclusion of mechanical deformation equations and solving the system self-consistently.

6.8 Conclusions

Biocompatibility of hydrogel encourages its use in implantable biochemical sensors, however, the design of the hydrogel based sensors is non-trivial and requires a careful theoretical analysis for optimizing different performance parameters such as signal (sensitivity/dynamic range) and time response (response time/symmetry of sensor response). Our analysis demonstrates that there is a fundamental trade-off between performance parameters of a CSM hydrogel sensor. Specifically,

1. If a high sensitivity and a high dynamic range are desirable (for applications where sluggishness of the response is not a primary concern), the density of ionizable group (N_f) should be high and the ionizable group should be selected such that its pK_a is close to the desired pH range.

2. On the other hand, if fast response time and symmetry are essential prerequisites, N_f should be low and ionizable group should be selected such that its pK_a is shifted away from the desired pH range.

Our analysis suggests suggests that the dynamic range can be improved by using hydrogels prepared with more than one type of ionizable group. The technical feasibility of this approach would be fruitful future research direction for hydrogel sensors.

Table 6.2.: Description of Symbols

Symbol	Quantity
τ	Response time
τ_{rise} or τ_{fall}	Time required for pressure to reach 90% of the peak pressure value or decrease by 90% of the peak value.
S	Sensitivity of the sensor
$\Delta\text{pH}_{\text{range}}$	Dynamic range of the sensor
l	Thickness of hydrogel membrane
B, A^-	Deprotonated form of cationic and anionic groups, respectively. Example: B$\equiv$ R-NH_2, $\text{A}^- \equiv$ R-COO^-
HB^+, HA	Protonated form of cationic and anionic groups, respectively.
$c_{\text{H}^+}, c_{\text{OH}^-}$, c_{Na^+},c_{Cl^-}	Concentration of proton, hydroxyl, sodium and chloride ions at position x and time t, respectively.
$c_{\text{H}_0^+}$	Concentration of protons to be detected in sample solution
c_s	Ionic concentration of the solution
ρ_{M}	Mobile ion charge density
ρ_{F}	Fixed charge density due to protonation/deprotonation of the ionizable groups in hydrogel
K_a, K_b	Acid dissociation constant for anionic and cationic groups, respectively in hydrogel
K_w	The ionization constant of water at absolute temperature T
pK_a, pK_b	$\text{pK}_\text{a} = -\log_{10}(K_a)$, $\text{pK}_\text{b} = -\log_{10}(K_b)$
N_a, N_b	The density of ionizable anionic and cationic groups, respectively
N_f	The density of the ionizable groups (anionic or cationic)
D_{eff}	Effective diffusion coefficient of protons in hydrogel after accounting for reaction with ionizable groups
ψ_d	Donnan Potential, i.e., potential at $x = x_h$ in steady state

7. COMPACT MODELING FOR SYSTEM INTEGRATION OF FET BASED SENSORS

So far, we discussed strategies to address response time (Chapter 2), sensitivity (Chapter 3) and selectivity (Chapter 4) of droplet-based lab-on-a-chip systems for portable applications. In Chapter 5, we discussed the performance potential of MoS_2, a transition metal dichalcogenide, for detection of cancer biomarkers. These materials are promising candidates for flexible sensors and can be used in wearable sensors for frequent monitoring of vital health parameters. In Chapter 6, we discussed the design trade-offs in hydrogel based biochemical sensors for implantable continuous monitoring devices.

In order to develop an integrated sensing system composed of individual components working in tandem, it is important to capture the behavior of these components in a simple language that is understandable by circuit simulator. Verilog-A, derived from hardware description language (Verilog-HDL), is such an industry standard modeling language. It can be used to describe the behavior of electrical components, such as diodes, resistors and field-effect transistors, as well as non-electrical components, such as a micro-electro mechanical system (MEMS) sensor. Further, the language provides a higher level of abstraction as compared to SPICE and therefore, the models defined in Verilog-A can be easily generalized to more include more sophisticated elements. As an illustrative example, in this chapter, we discuss a physics-based (Verilog-A) compact model to simulate DC, transient, small-signal and noise performance of FET based pH sensors. The illustration should, however, serve as a general guideline for compact modeling of other components, such as droplet-based sensors.

7.1 Introduction

Importance of high-pH resolution: Measuring pH at a high resolution is important for food, pharmaceutical, agriculture, biomedical industry and environmental monitoring. For example, intracellular pH plays an important role in cell metabolism. A deviation in tissue pH can be an indicator of a malignant tumor [256]. Further, the blood pH of a healthy adult varies from 7.35 to 7.45 units. Any chronic deviation may an indicator of certain diseases such as acidosis, etc. which can be fatal in extreme cases [257]. The solubility, stability and permeability of a drug through biological membrane also depends on pH [258], and therefore a precise measurement using a miniaturized sensor can be very useful. Further, the solubility of heavy metals, like lead, zinc and copper, in soil is also dependent on the pH [259], and hence pH measurement is also important for environment.

ISFETs are promising candidates: Ion-sensitive field-effect transistors (ISFETs) [164] have garnered considerable attention due to their compactness, low-cost and ease of fabrication. Recently, pH-FETs have also been used for human genome sequencing [2,165,260]. Several commercially available pH-FET achieve pH resolution of 0.01 units (for example, MiniLab H137 ISFET pH Meter [261]). The resolution of a pH-FET is technology and geometry specific, and as such it is desirable to have a compact model that anticipates the optimum operation of the sensor not only for arbitrary time-dependent fluidic environment, but also in complex analog circuits where biasing configuration may change over time. The sensor resolution is dictated by sensitivity as well as the noise. Rajan *et al.* [262] experimentally demonstrate that signal-to-noise-ratio (SNR) of silicon nanowire (Si-NW) biochemical sensors is maximized in the linear regime, close to the point of peak transconductance. Theoretical analysis by Go *et al.* shows that the SNR of double-gated FET (DGFET) pH sensor is highest in depletion regime [11], and predicted that, in principle, a pH resolution of 0.001 is achievable. Deen *et al.* performed numerical simulations of

planar FET biosensor to show that the noise is minimum in sub-threshold region of operation [263].

Need for compact models for FET pH sensors: In this regard, it is desirable to have compact models that can evaluate the performance of the sensor in terms of its SNR at arbitrary operating conditions and device geometry. Indeed, there are several reports of compact modeling for analysis of DC operation of FET based pH sensors. For example, Massobrio *et al.* [95], Grattarola *et al.* [96] and Martinoia *et al.* [97] developed physical models for DC analysis of planar ISFETs and incorporated them into SPICE to predict response of different oxides to pH sensing and analyze non-ideal effects in ISFETs. Later, Martinoia *et al.* [264] incorporated the model as a behavioral macromodel in HSPICE. Fernandes *et al.* [98] extended the DC model for incorporation of biomolecule charge as an ion-permiable charged membrane, and implemented in HSPICE. Livi *et al.* [99] proposed a Verilog-A model for DC analysis of silicon nanowire pH Sensor. These early works are certainly useful, however, the utility of the existing model will broaden significantly if we can improve the DC model by accounting for the bias dependencies of interface/electrolyte capacitances and generalize the model to calculate transient and small-signal responses, so that the one may predict signal-to-noise performance of the sensor, integrated within a complex signal processing environment.

Our contribution: Therefore, in this work, we develop a physics-based compact model for DC, transient, small-signal and noise-analysis of field-effect transistor (FET) based pH sensors, implemented in Verilog-A. Compared to a SPICE-based sub-circuit, a Verilog-A implementation has several advantages: (i) Verilog-A models are described at higher levels of abstraction, so that future improvements/generalization are easily implemented. (ii) It allows the use of limiting functions [265], such as limitexp, which improves the convergence of the simulator running the model. (iii) One can integrate non-electrical components, such as a micro-electro mechanical system (MEMS) sensor [266], in Verilog-A. Therefore, a Verilog-A implementation can be used for system integration of different lab-on-a-chip components. The model pre-

sented here is versatile and can describe the pH sensing operation of different classes of FET sensors (see Fig. 7.1(a)) such as single-gated and double-gated FET.

The model is utilized to:

1. Determine DC, transient and small-signal characteristics of ion sensitive FET and electrolyte-insulator system.

2. Determine the dominant noise mechanism for the sensor, and find the optimal operating point for improving the sensor resolution.

3. Demonstrate circuit simulation of a low-power sensor interface.

Organization of the chapter: The chapter is organized as follows: In Section 7.2, we discuss the model system and the compact models for DC, AC, and transient and noise analysis of the FET pH sensors. We validate the model with available experimental data in literature. In Section 7.3, we use the model to determine the noise associated with electrolyte and the FET. Further, we determine the pH resolution as a function of the gate bias, and show that the minimum resolution is dictated by an interplay of noise due to both FET and electrolyte. Next, we show that for sensors operating in subthreshold-regime, length should be decreased and width increased for minimizing noise (improving pH resolution), and for sensors operating in inversion-regime, both length and width should be increased. We extend the model to analyze the sensitivity and noise of extended-gate FET pH sensors. Finally, in Section 7.4, we demonstrate the use of compact model in determining the sensitivity of a sensor interface to the pH changes.

7.2 Model System

Fig. 7.1(b) describes the operation of an example pH-FET sensor. The solution is exposed directly to the gate oxide, and the protons in the solution react with the surface (-OH) groups to make the surface positively/negatively charged. The response of the sensor is described by the site-binding model, which relates the surface charges

due to protonation/de-protonation of surface groups to the pH. The sensor is modeled as two decoupled circuit elements, each describing the operation of the electrolyte and the FET transducer, respectively. This decoupling allows the model to describe the operation of a range of FET pH sensors as shown in Fig. 7.1(a).

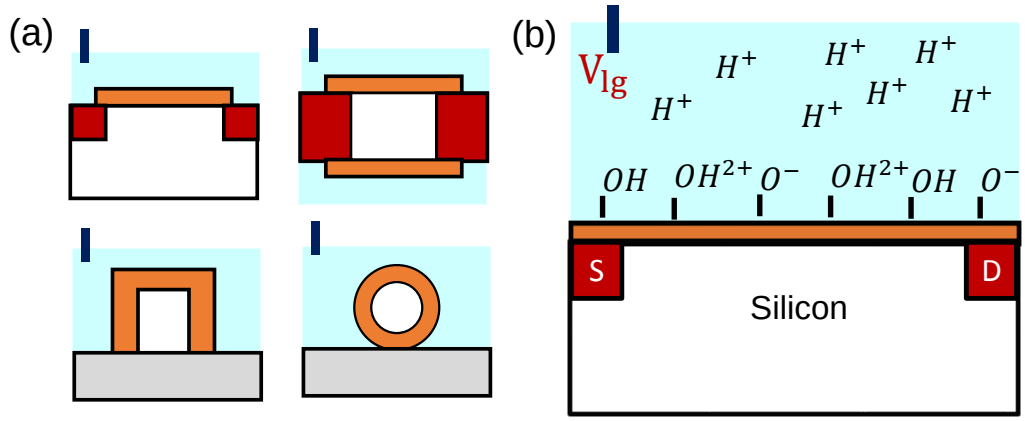

Fig. 7.1.: (a) Sketch of different MOSFETs used for pH sensing, (b) Operation of an pH-FET sensor: The (-OH) groups protonate/deprotonate to give a net surface charge density. This leads to a shift in threshold voltage of the device.

The sensitivity (S) of the sensor can be defined in terms of the change in the threshold voltage of pH-FET per unit change in pH, i.e.,

$$S = \left| \frac{\Delta V_{TH}}{\Delta \text{pH}} \right|. \tag{7.1}$$

The resolution ($\Delta \text{pH}_{\text{resolution}}$) with which a signal can be reliably differentiated from noise is given by,

$$\Delta \text{pH}_{\text{resolution}} = 3 \times \frac{\delta V_{\text{noise}}}{S}. \tag{7.2}$$

where, δV_{noise} is the noise. In order to determine the pH resolution, we need to determine both the signal (S) and the noise (δV_{noise}). In this section, we discuss the DC, AC, transient and noise model for FET pH sensors.

7.2.1 DC Compact Model

Fig. 7.3(a) shows the DC model for the ISFET. The electrolyte is modeled as a non-linear voltage source (ψ_e(pH)) (see Fig. 7.2 and Fig. 7.3(a)) whose voltage is dependent on pH, ionic concentration, i_0, the number density of the surface ionizable groups (N_{OH} for the [-OH] groups and $N_{\mathrm{NH_2}}$ for the [-NH_2] groups), and their associated dissociation/association constants. The potential (ψ_e), i.e., the difference between the potential at electrolyte/insulator interface (ψ_g) and liquid gate voltage V_{lg} is a function of the pH.

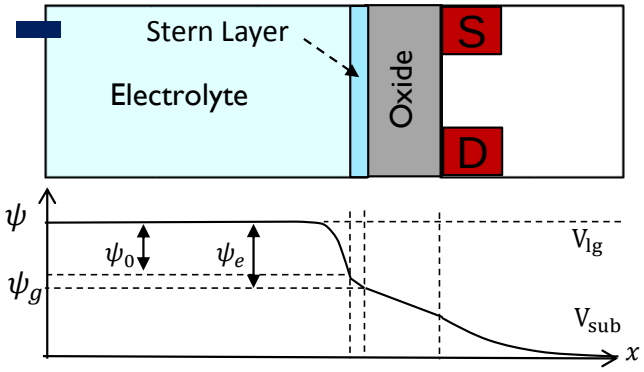

Fig. 7.2.: Sketch of pH-FET and depiction of different voltages

In order to determine the pH dependence of ψ_e, we need to solve the charge neutrality equation in Verilog-A,

$$Q_{\mathrm{dl}}(\psi_0) + Q_{\mathrm{sensor}}(\psi_e) + Q_{\mathrm{mos}}(\psi_g) + Q_{\mathrm{par}}(V_{\mathrm{sub}}, \psi_g) = 0. \tag{7.3}$$

where, Q_{dl} is the charge due to accumulation of ions near the electrolyte-oxide interface, Q_{sensor} is the charge at the sensor surface due to protonation/deprotonation of the proton responsive groups (-OH or -NH_2 groups), and Q_{par} is the charge due to any parasitic capacitance. The potential difference between the electrolyte/oxide interface and the liquid gate can be expressed as,

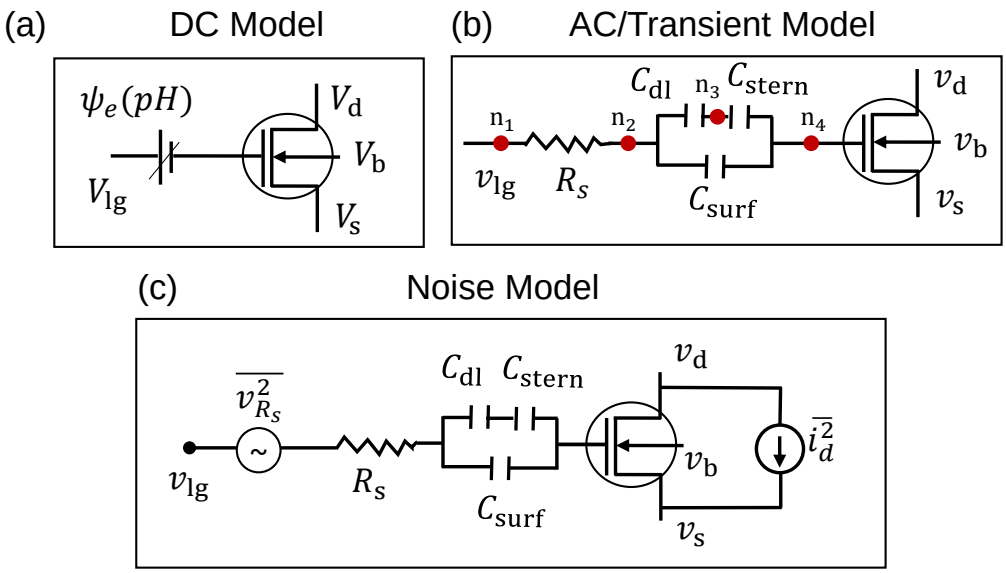

Fig. 7.3.: Compact model for (a) DC, (b) AC/Transient, and (c) Noise analysis of FET pH sensors.

$$\psi_e = \psi_g - V_{lg}. \tag{7.4}$$

where, ψ_g is the effective gate voltage, i.e., the potential at the electrolyte/oxide interface. The potential, ψ_0 can be expressed in terms of ψ_e as,

$$\psi_0 = \psi_e + \frac{Q_{\text{dl}}}{A_{\text{sensor}} C_{\text{stern}}}. \tag{7.5}$$

where, C'_{stern} is the stern-layer capacitance per unit area and A_{sensor} is the area of the sensor surface. The different charges can be evaluated as follows:

Double layer charge: The electrolyte double layer charge (Q_{dl}) can be expressed in terms of the potential (ψ_0) at the outer Helmholtz plane using the classical Grahame's equation:

$$Q_{\text{dl}}(\psi_0) = -A_{\text{sensor}} \sqrt{8kT\epsilon_w n_0} \sinh\left(\frac{q\psi_0}{2kT}\right). \tag{7.6}$$

where ε_w is the permittivity in the electrolyte, n_0 is the number concentration of ions in the bulk electrolyte.

Surface Charge: Surface charge at the top of the oxide surface is due to the protonation and deprotonation of the hydroxyl groups (-OH) and amine groups (-NH_2). We use the site-binding model [133] to determine the surface charge. The protonation and deprotation of the surface charge due to (-OH) groups and (-NH_2) groups can be described by following equilibrium equations,

$$\mathrm{AOH_2^+} \overset{K_a}{\leftrightarrows} \mathrm{AOH + H_s^+}, \qquad K_a = \frac{[\mathrm{AOH}][\mathrm{H_s^+}]}{[\mathrm{AOH^{2+}}]}, \tag{7.7}$$

$$\mathrm{AO}H \overset{K_b}{\leftrightarrows} \mathrm{AO^- + H_s^+}, \qquad K_b = \frac{[\mathrm{AO^-}][\mathrm{H_s^+}]}{[\mathrm{AOH}]}, \tag{7.8}$$

$$\mathrm{BNH_3^+} \overset{K_n}{\leftrightarrows} \mathrm{BNH_2 + H_s^+}, \qquad K_n = \frac{[\mathrm{BNH_2}][\mathrm{H_s^+}]}{[\mathrm{BNH^{3+}}]}. \tag{7.9}$$

where, $[\mathrm{H_s^+}]$ indicates the concentrations of protons at the electrolyte-oxide interface, and can be expressed in terms of the bulk concentration of protons, $[\mathrm{H_b^+}]$ as,

$$[\mathrm{H_s^+}] = [\mathrm{H_b^+}] \exp(-q\psi_e/k_B T). \tag{7.10}$$

The total density of the surface (-OH) groups is given by,

$$N_{\mathrm{OH}} = [\mathrm{AOH^{2+}}] + [\mathrm{AOH}] + [\mathrm{AO^-}]. \tag{7.11}$$

Similarly, the total density of the surface (-NH_2) groups is given by,

$$N_{\mathrm{NH_2}} = [\mathrm{NH^{3+}}] + [\mathrm{NH_2}]. \tag{7.12}$$

The net surface charge is given by,

$$Q_{\mathrm{sensor}} = qA_{\mathrm{sensor}} \left([\mathrm{AOH_2^+}] - [\mathrm{AO^-}] + [\mathrm{BNH_3^+}] \right). \tag{7.13}$$

Using Eqs. (7.7)- (7.13), we get the surface charge density due to (-OH) groups as,

$$\sigma_{\mathrm{OH}}(\psi_e) = -2qN_{\mathrm{OH}} \left(\frac{\tanh(q\psi_e/kT + 2.3(\mathrm{pH} - (\mathrm{pK}_a + \mathrm{pK}_b)/2)}{10^{\frac{\mathrm{pK}_b - \mathrm{pK}_a}{2}} \mathrm{sech}(q\psi_e/kT + 2.3(\mathrm{pH} - (\mathrm{pK}_a + \mathrm{pK}_b)/2)) + 2} \right). \tag{7.14}$$

and due to (-NH_2) groups as,

$$\sigma_{\mathrm{NH_2}}(\psi_e) = \frac{qN_{\mathrm{NH_2}}}{2} \left(1 - \tanh(q\psi_e/kT + 2.3(\mathrm{pH} - pK_n))\right). \tag{7.15}$$

where,

$$\mathrm{pK}_a = -\log_{10}(K_a), \qquad \mathrm{pK}_b = -\log_{10}(K_b),$$
$$pK_n = -\log_{10}(K_n), \qquad \mathrm{pH} = -\log_{10}(\mathrm{H}_b^+).$$

The net surface charge is given by,

$$Q_{\mathrm{sensor}}(\psi_e) = A_{\mathrm{sensor}}\ \sigma_{\mathrm{OH}}(\psi_e) + A_{\mathrm{sensor}}\ \sigma_{\mathrm{NH_2}}(\psi_e). \tag{7.16}$$

MOSFET charge and Charge to due parasitics: The MOSFET charge (Q_{mos}) is technology and geometry dependent and assumed to be negligible compared to the electrolyte (Q_{dl}) and surface (Q_{sensor}) charges. Further, we assume that the any parasitic contributions to charge (Q_{par}) are small enough to be neglected as compared to Q_{dl} and Q_{sensor}. Neglecting Q_{mos} and Q_{par}, the charge neutrality equation becomes,

$$Q_{\mathrm{dl}}(\psi_0) + Q_{\mathrm{sensor}}(\psi_e) = 0. \tag{7.17}$$

Using Eq. (7.5), Eq. (7.6) and Eq. (7.17), we can express ψ_e in terms of surface ionization parameters (pK_a, pK_b and pK_n), densities (N_{OH} and $N_{\mathrm{NH_2}}$) as follows:

$$\psi_e = \frac{2kT}{q} \mathrm{asinh}\left(\frac{\sigma_{\mathrm{sensor}}(\psi_e)}{\sqrt{8kT\epsilon_w n_0}} \right) + \frac{\sigma_{\mathrm{sensor}}(\psi_e)}{C_{\mathrm{stern}}}. \tag{7.18}$$

Equation (7.18) represents a non-linear equation in ψ_e and is implemented as a self-voltage dependent voltage source in Verilog-A. Unlike previous DC models for ISFET sensors [95–97,99,264], Eq. (7.18) incorporates the bias dependence of the double layer charge (see Eq. (7.6)). We implement the *sinh* function in terms of *limexp* function (an advantage of Verilog-A as compared to SPICE) which restricts numerical overshoot and improves convergence. Although the bias dependence of the double layer charge causes negligible change in ψ_e at high ionic concentrations, numerical results (not shown) show that it can result in almost 6% error in ψ_e at low ionic concentrations.

The FET part of the model can be represented by any compact model supported by the circuit-simulator, namely single-gated MOSFET, a multi-gated FET or more generally, an externally defined Verilog-A FET model.

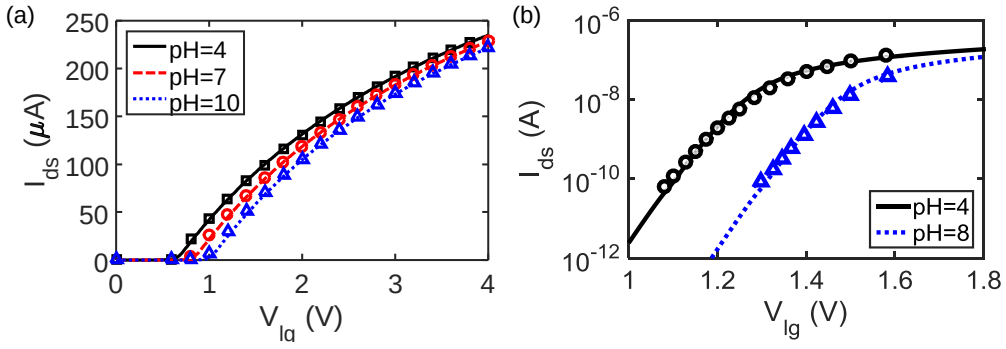

Fig. 7.4.: DC Model Validation: Match of experimental data (symbols) with compact model: (a) I-V characteristics obtained from Martinoia *et al.* [264]. Parameters: $\mathrm{pK}_a = -2$, $\mathrm{pK}_b = 6$, $pK_n = 10$, $N_{\mathrm{OH}} = 2 \times 10^{14}$ cm^{-2}, $N_{\mathrm{NH_2}} = 4 \times 10^{14}$ cm^{-2}, (b) I-V characteristics obtained from Go *et al.* [11]. Parameters: $\mathrm{pK}_a = 6$ $\mathrm{pK}_b = 10$ $N_s = 8 \times 10^{14}$ cm^{-2} [133]

Fig. 7.4 (a) and (b)[1] show the validation of the DC model with experimental data reported in Martinoia *et al.* [264] and Go *et al.* [11], respectively. Despite of the assumption that the MOSFET charge is negligible, the model predicts the experimental data remarkably well in all regions of operation.

[1] Adapted from Ref. [107] with permission from IEEE.

7.2.2 Transient Model

Fig. 7.3(b) shows the transient model for the ISFET. Again, this model is comprised of two decoupled elements, one for the electrolyte and electrolyte/insulator interface and other for FET (or insulator). For simplicity, we assume quasi-steady state, i.e., we assume that ions respond to the pH and bias changes very quickly. However, for analog applications that involve charge-storage circuits, such as switched analog circuits, the model must be generalized [267, 268]. The quasi-static assumption allows the transient model of the electrolyte and electrolyte/insulator interface to be described in terms of 3 capacitors and 1 resistor: (a) The double layer capacitance (C_{dl}), (b) Stern Capacitance (C_{stern}), and (c) The capacitance due to the charging/discharging of the surface ionizable groups (C_{sensor}), and (d) Electrolyte resistance, R_s originating from the finite conductivity of ions present in the solution. Typically, reference electrodes are large as compared to the sensor area, and therefore the electrolyte resistance can be as,

$$R_s = \frac{1}{\kappa}\sqrt{\frac{\pi}{A_{\text{sensor}}}}. \tag{7.19}$$

where, $\kappa = q(\mu_n + \mu_p)n_0$ is the electrolyte conductivity. We assume that the reference electrode is an ideal faradaic electrode, i.e., it does not have any resistance to charge transfer (charge transfer resistance, $R_{ct} \rightarrow 0$) and the mass transfer impedance is negligible ($Z_w \rightarrow 0$) [100] . Therefore, there is no potential drop at the electrode-electrolyte interface.

Yang *et al.* showed that if the capacitors are non-linear functions of bias, the formulation of transient currents in terms of capacitors instead of charges leads to an error in calculated nodal voltages/currents [269]. Therefore, the transient current through the electrolyte is defined directly in terms of the charges, since the electrolyte and the surface charges are non-linear functions of bias. The nodal current-voltage and current-charge relationship are,

$$
\begin{aligned}
V(n_1, n_2) &= I(n_1, n_2) R_s, \\
I_u(n_2, n_4) &= A_{\text{sensor}} \frac{d\sigma_{\text{dl}}}{dt}, \\
I_l(n_2, n_4) &= A_{\text{sensor}} \frac{d\sigma_{\text{sensor}}}{dt}, \\
I(n_3, n_4) &= A_{\text{sensor}} \frac{d}{dt}(C_{\text{stern}} V(n_3, n_4)).
\end{aligned}
\tag{7.20}
$$

where, I_u, I_l and I are the transient currents through the upper branch, lower branch and total current flowing across nodes, $n_1 - n_4$ in transient state (see Fig. 7.3(b)), and $V(n_i, n_j)$ denote the voltage across the nodes i and j.

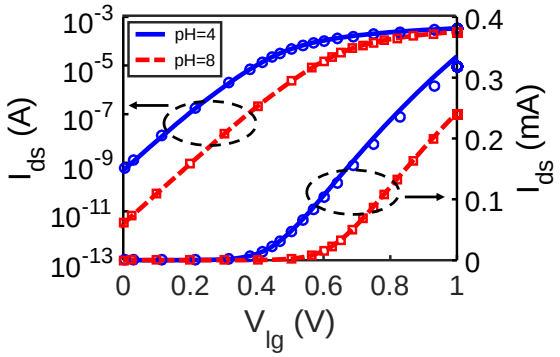

Fig. 7.5.: Comparison between the transient model and the dc model for a gate voltage sweep. Excellent agreement between the DC (solid lines) and transient model (Symbols) shows that MOSFET charge can be assumed negligible, especially for pH values farther away from point of zero charge (pH_{pzc}=2)

Unlike the DC model, where the MOSFET charge is assumed negligible, the transient model solves the system self-consistently and appropriately sets the voltage at the gate oxide/electrolyte interface. Fig. 7.5 (a) shows the comparison of the I-V characteristics obtained from a DC sweep (lines) and a transient gate voltage sweep (symbols) of ISFET for a 130 nm bulk MOSFET technology. Despite the simplifying assumption in the DC model that the electrolyte and the FET part can be decoupled, both the models match remarkably well, particularly for higher pH values (when the

surface charge is relatively large) indicating that MOSFET charge can be assumed negligible.

7.2.3 Small-signal Compact Model

For small-signal (AC) analysis using a DC operating point, the small signal currents across nodes $n_2 - n_4$ are expressed directly in terms of the capacitors:

$$i_{ac}(n_2, n_4) = C_{24}\frac{d(v_{ac}(n_2, n_4))}{dt}. \tag{7.21}$$

where, $C_{24} = \frac{C_{\rm dl}C_{\rm stern}}{C_{\rm dl}+C_{\rm stern}} + C_{\rm sensor}$ is the net capacitance between nodes, n_2 and n_4 (see Fig. 7.3). Both, double layer capacitance, $C_{\rm dl}$ and capacitance due to surface ionizable charges ($C_{\rm sensor}$) are non-linear functions of the DC potentials ψ_0 and $\psi_{\rm dl}$ and are evaluated using Eq. (7.6), Eq. (7.14) and Eq. (7.15) as,

$$\begin{aligned}
C_{\rm dl} &= -A_{\rm sensor}\frac{d\sigma_{\rm dl}}{d\psi_0} = A_{\rm sensor}\sqrt{\frac{2q^2\varepsilon_w n_0}{kT}}\cosh\left(\frac{q\psi_0}{2kT}\right), \\
C_{\rm sensor} &= -A_{\rm sensor}\frac{d\sigma_{\rm sensor}}{d\psi_e} \\
&= A_{\rm sensor}\left(\frac{2q^2N_{\rm OH}}{kT}\frac{(10^{({\rm pK}_b-{\rm pK}_a)/2}\cosh({\rm pH}-({\rm pK}_a+{\rm pK}_b)/2))+2)}{(10^{({\rm pK}_b-{\rm pK}_a)/2}+2.0\cosh({\rm pH}-({\rm pK}_a+{\rm pK}_b)/2))^2}\right) \\
&+ A_{\rm sensor}\left(\frac{q^2N_{\rm NH_2}{\rm sech}^2({\rm pH}-pK_n)}{4kT}\right).
\end{aligned} \tag{7.22}$$

$C_{\rm Stern} = A_{\rm Sensor}C'_{\rm Stern}$ is the stern capacitance. Bousse *et al.* [270] showed that there is an additional term due to Warburg impedance in series with $C_{\rm sensor}$, corresponding to the variation in surface pH due to applied signal. However, at low frequencies, this component is not important and can be neglected. Note that as is conventional for circuit simulation, we use a very high resistance (not shown in Fig. 7.3) in parallel to the capacitors (i.e., between nodes $n_2 - n_4$ to make sure that all nodes have a dc path to ground. The transient operating point is obtained by ramping both the pH and $V_{\rm lg}$ as a function of time to the values at which the small-signal analysis is done. The obtained operating point is used to evaluate the small-signal response.

Such a functionality to run small-signal analysis after a transient analysis is available in many circuit simulators like HSPICE. For small-signal analysis using transient operating point, the currents are defined directly in terms of charges Eq. (7.20). The small-signal analysis using transient operating point is more accurate (due to inherent self-consistency in calculation of ψ_e and ψ_0) as compared to dc operating point. However, the latter is computationally less intensive and yields same results.

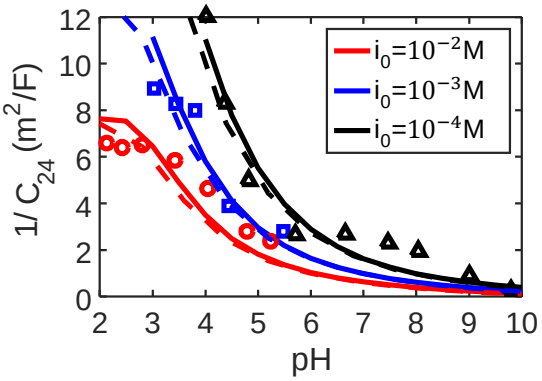

Fig. 7.6.: Small-signal model validation: Inverse capacitance vs. pH for different ionic concentration for a metal-oxide-electrolyte system. Exp. data (symbols) is obtained from Bousse *et al.* [133]. Solid lines: DC operating point, Dashed lines: Transient operating point

Fig. 7.6 shows the validation of the AC model for a metal-oxide-electrolyte system using both dc (solid lines) and transient operating point (dashed lines). The model shows an excellent agreement with the experimental data obtained from Bousse *et al.* [270], confirming that both dc and transient models can be used for small-signal analysis.

7.2.4 Noise Compact Model

Fig. 7.3(c) shows the noise model for the ISFET sensor. The reference electrode is assumed to be ideal so that its noise is negligible. The electrolyte thermal noise is modeled as a thermal voltage source (S_{V,R_s}) due to the electrolyte resistance, R_s (see Eq. (7.23)). The electrolyte noise is inversely proportional to the conductivity of the

solution (see Eq. (7.19)). The lower the electrolyte concentration, higher the thermal resistance and higher the electrolyte noise.

The drain current noise ($\bar{i_d}^2$) due to the FET is sum of the channel thermal noise ($S_{I,\text{Thermal}}$) and flicker noise ($S_{I,\text{Flicker}}$). For HSPICE simulations, we use BSIM thermal noise model (see Eq. (7.24)) and unified flicker noise model (see Eq. (7.26)) which is valid in all regimes of operation, including subthreshold-region and the inversion region. In addition, we use a simplified thermal noise model (see Eq. (7.25)) and $\Delta n - \Delta\mu$ flicker noise model (see Eq. (7.27)) to understand the results intuitively.

Briefly, BSIM thermal noise model can be expressed in terms of the inversion charge (Q_{inv}), the effective carrier mobility (μ_{eff}) and an additional noise parameter, NTNOI which can be used to account for short-channel effects in MOSFET.

The BSIM flicker noise is described using Eq. (7.26), where $S_{I,\text{inv}}$ and $S_{I,\text{sub}}$ are the flicker noises for the inversion and subthreshold regime, respectively. The flicker noise is a function of the oxide-trap density (N_t) and the mobility scattering coefficient (α) through parameters (NA, NB, NC), and the device length and width, either explicitly or implicitly through the drain current (I_{ds}).

The net-input referred noise voltage (δV_{noise}) can be expressed as the sum of the electrolyte noise and the MOSFET channel and thermal noise (see Eq. (7.28)), where G is the gain from the liquid-gate terminal (v_{lg}) to the MOSFET drain terminal (v_d) (see Fig. 7.5(c)). The upper limit of the noise-bandwidth (f_{high}) depends on the measurement frequency, and the lower limit of the noise-bandwidth ($f_{\text{low}} \sim 1/\tau$) depends on the time (τ) for which the measurement is carried out.

Table 7.1.: Noise Model for ISFET

Electrolyte Noise Model:

$$S_{V,R_s} = 4kTR_s \tag{7.23}$$

BSIM FET Thermal Noise Model:

$$S_{I,\text{Thermal}} = \frac{4k_BT\mu_{\text{eff}}|Q_{\text{inv}}|}{L_{\text{eff}}^2}NTNOI \tag{7.24}$$

Simplified Thermal Noise Model:

$$S_{I,\text{Thermal}} = \gamma\frac{8}{3}k_BTg_m \tag{7.25}$$

BSIM FET Flicker Noise Model:

$$\begin{aligned} S_{I,\text{Flicker}} &= \frac{1}{f^{EF}}\frac{S_{I,\text{inv}} \times S_{I,\text{sub}}}{S_{I,\text{inv}} + S_{I,\text{sub}}} \\ S_{I,\text{inv}_1} &= \frac{\lambda k_BTq^2\mu_{\text{eff}}I_{ds}}{aC_{oxe}L_{\text{eff}}}(NA \times F_1 + NB \times F_2 + NC \times F_3) \\ S_{I,\text{inv}_2} &= \frac{k_BTI_{ds}^2\Delta L_{clm}\lambda}{W_{\text{eff}}L_{\text{eff}}^2}(NA + NB \times F_4 + NC \times F_5) \\ S_{I,\text{sub}}(f) &= \frac{NA \times k_BTI_{ds}^2\lambda}{W_{\text{eff}}L_{\text{eff}}N^2} \\ S_{I,\text{inv}} &= S_{I,\text{inv}_1} + S_{I,\text{inv}_2} \end{aligned} \tag{7.26}$$

$\Delta n - \Delta\mu$ Flicker Noise Model:

$$\begin{aligned} S_{V_G} &= S_{VFB}\left(1 + \left(\alpha\mu_{\text{eff}}C_{\text{eff}}\frac{I_D}{g_m}\right)\right)^2 \\ S_{VFB} &= \frac{q^2k_BTN_t\lambda}{fWLC_{ox}^2} \end{aligned} \tag{7.27}$$

Net Input-Referred Noise Model:

$$\begin{aligned} S_V &= S_{V,R_s}\Delta f + \frac{S_{I,\text{Thermal}}\Delta f + S_{I,\text{Flicker}}\log(f_{\text{high}}/f_{\text{low}})}{G^2} \\ \delta V_{\text{noise}} &= \sqrt{S_V}, \qquad \Delta f = f_{\text{high}} - f_{\text{low}}, \qquad G = \left|\frac{v_d}{v_{lg}}\right| \end{aligned} \tag{7.28}$$

7.3 Results And Discussions

7.3.1 Sensitivity of pH sensor is independent of the device operating point

As discussed earlier, pH resolution of the FET sensor is dictated by both the sensitivity and the noise due to FET and electrolyte. The sensitivity of the sensor depends on pH and the surface parameters (surface ionizable group density and equilibrium constants). Fig. 7.8(a) and (b) show the surface potential change ($|\psi_e|$) and the sensitivity ($S = |d\psi_e/d\text{pH}|$) as a function of the pH of the solution for a SiO_2 sensing surface, respectively. HSPICE simulations were done with parameters corresponding to 130 nm process technology (see Fig. 7.7 for device characteristics and Ref. [271] for model parameters). The figure illustrates that the sensitivity is maximum away from the pH_{pzc} of the surface. However, the surface potential (ψ_e) is independent of the operating regime of the MOSFET (see Eq. (7.18)). Therefore, the sensitivity of a planar ISFET sensor is independent of the bias regime of the operation and the bias dependence of pH resolution in planar ISFET comes solely due to noise and not due to the sensitivity.

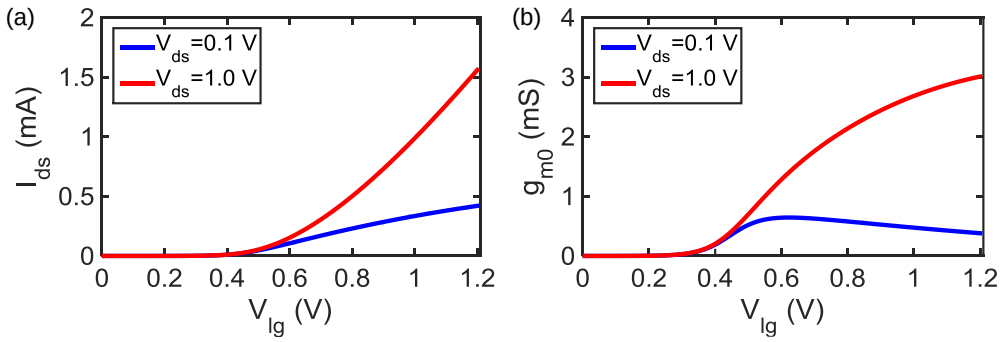

Fig. 7.7.: (a) Transfer characteristics of 130 nm process with L=10 μm and W=100 μm, (b) Transconductance (g_m) as a function of gate bias for 130 nm bulk CMOS with L=10 μm and W=100 μm

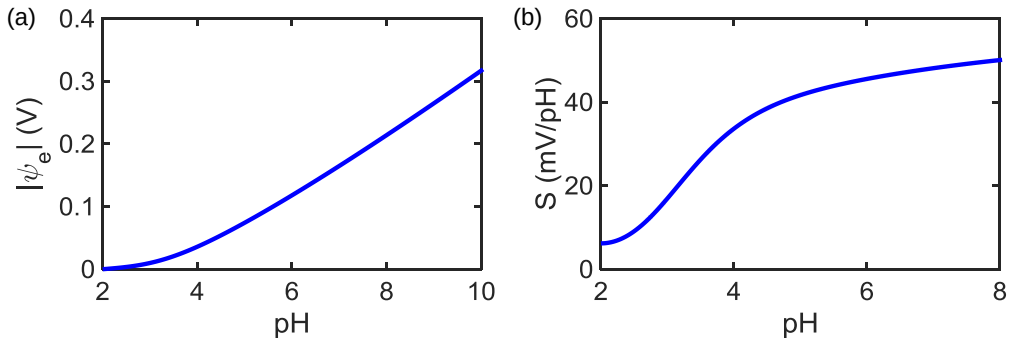

Fig. 7.8.: (a) Absolute change in surface potential as a function of pH, and (b) Sensitivity as a function of pH

7.3.2 Noise due to Different Sources in ISFET

Thermal Noise due to electrolyte is independent of the FET operational regime

Fig. 7.9 shows the plot of noise spectral density (S_{R_s}) obtained from HSPICE simulations due to electrolyte thermal noise as a function of ionic concentration for different gate area. Although the simulations were done on a 130 nm bulk MOSFET technology [271] (see Fig. 7.7 for device characteristics) with different gate areas, the electrolyte noise is independent of operating point and technology node of the FET as long as the area of the sensor remains the same. S_{R_s} varies inversely with both the ionic conductivity and the square root of the area (see Eq. (7.19) & Eq. (7.23)). Therefore, $\delta V_{R_s,noise}$ varies as, $\delta V_{\text{noise}} \sim i_0^{-1/2} A^{-1/4} f_{\text{high}}^{1/2}$ (see Eq. (7.19), Eq. (7.23) and Eq. (7.28)), since $f_{\text{high}} \gg f_{\text{low}}$ for typical measurement conditions (we use $f_{\text{high}} = 1$ KHz and $f_{\text{low}} = 0.1$ Hz). The smaller the ionic concentration, sensor area or larger the measurement frequency, the higher is the noise due to the electrolyte. Although, the conclusions are similar to the theoretical analysis by Go *et al.* [11] and Deen *et al.* [263], the implementation of electrolyte noise in Verilog-A would allow to determine the impact of device level noise in complex signal processing circuits.

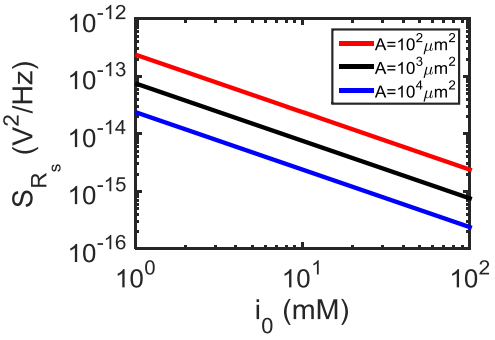

Fig. 7.9.: Input Referred Electrolyte Thermal Noise Spectral density. Electrolyte noise decreases with increase in ionic concentration and increase in gate area

FET Thermal Noise dominates in sub-threshold regime

Fig. 7.10 shows the dependence of FET thermal noise on the gate bias for a 130 nm bulk MOSFET technology (see Fig. 7.7 for device characteristics) with $L = 10\ \mu m$ and $W = 100\ \mu m$. The solid lines refer to the HSPICE simulations using the BSIM model and the dashed lines represent the simulation using the simplified thermal noise model. The results can be understood intuitively using simplified model as follows: At low gate bias, the channel resistance is very high (g_m is small) as there are very few charge carriers in the channel. This leads to a very large input-referred channel thermal noise spectral density ($S_{V,\text{Thermal}} \sim S_{I,\text{Thermal}}/g_m^2$, refer Eq. (7.27)). As the gate bias increases, g_m increases (see Fig. 7.7(b)) leading to a decrease in the thermal noise. Finally, the thermal noise voltage increases again due to reduction in g_m because of mobility degradation. A larger drain bias results in an increased g_m, and hence the input-referred noise voltage is lower at higher drain bias.

FET Flicker Noise dominates in inversion regime

The BSIM flicker noise model accounts for the noise due to oxide-trap-induced carrier number as well as correlated surface mobility fluctuation mechanisms. Fig. 7.11 shows the HSPICE simulation for flicker noise spectral density (solid lines) at $f = 1$

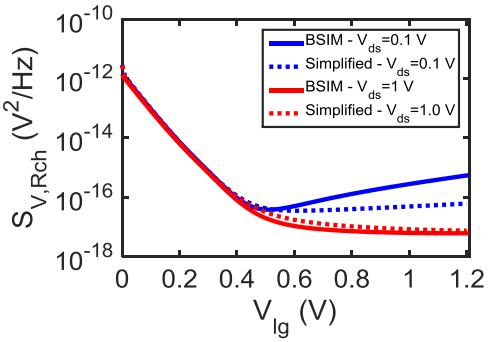

Fig. 7.10.: Input Referred Thermal Noise Spectral density for different drain biases

Hz using BSIM noise model for different drain biases. In order to interpret the results, we match the BSIM flicker noise model result with the $\Delta n - \Delta\mu$ model. The results can be understood as follows: At low gate bias, the input-referred noise spectral density, $S_{V,\text{Flicker}} \approx S_{VFB}$ (see Eq. (7.27)). As the gate bias increases, the transconductance efficiency, $\eta = g_m/I_{ds}$ decreases and hence, flicker noise, $S_{V,\text{Flicker}} \sim 1/\eta^2$ increases. For a larger drain bias, the device is in saturation and hence η is larger. Therefore, the noise is smaller for larger drain bias.

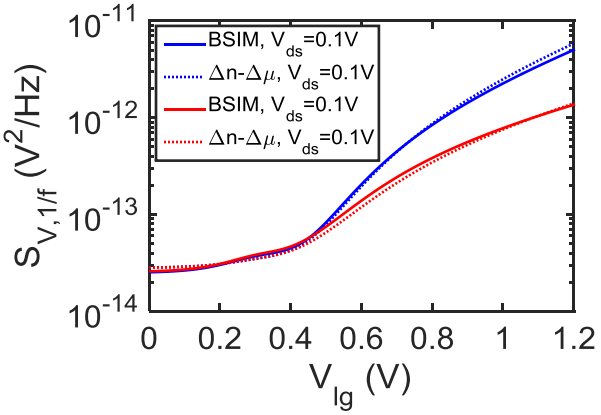

Fig. 7.11.: Input referred flicker noise spectral density. The sold lines show the results obtained from HSPICE simulation, while the dashed lines show the match to the simplified model (for thermal noise) and Δn-$\Delta\mu$ model (for flicker noise)

7.3.3 Point of minimum pH resolution occurs near on-set of inversion

Fig. 7.12 shows the comparison of the input referred noise voltage (δV_{noise}) due to different noise sources. The figure shows that the point of minimum noise is dictated by an interplay of FET thermal and flicker noise as well as electrolyte noise. While thermal noise dominates at low gate bias, flicker noise is dominant noise source at large gate bias. Near the onset of inversion, the electrolyte noise is the dominant noise source. Fig. 7.13 shows that the pH resolution of the device follows the input-referred noise voltage, since the signal (i.e. pH sensitivity) is constant w.r.t. the bias voltages. The pH resolution is minimum close to the onset of inversion. Also, as expected, the noise analysis using both the dc and transient model give the same result. While Rajan *et al.* [262] attributed the minimum noise for their biochemical sensors to the bias dependent trap-density in flicker noise, Go *et al.* [11] incorrectly attributed it to rise in flicker noise at low-gate bias. In contrast, our analysis indicates that the noise minimum can occur due to the increase in thermal noise as the bias voltage decreases.

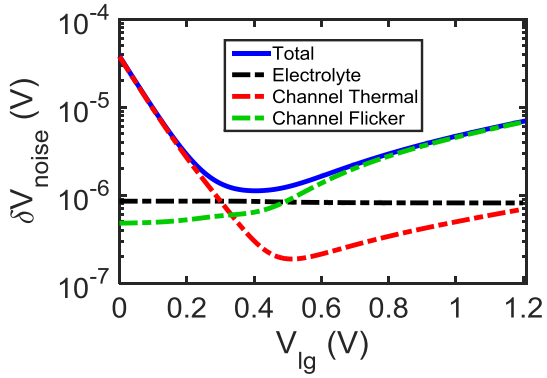

Fig. 7.12.: Input referred noise voltage as a function of gate bias. FET thermal noise dominates below subthreshold, while FET flicker noise dominates above threshold. Electrolyte thermal noise remains constant

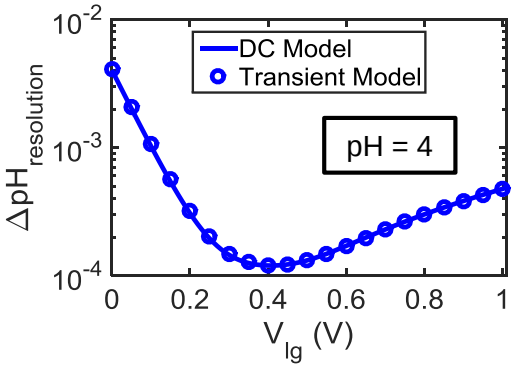

Fig. 7.13.: pH resolution as a function of gate bias. Minimum pH resolution occurs near onset of inversion. Solid line and Symbol shows simulation using dc and transient operating point, respectively.

Table 7.2.: Parameter values for noise simulation

No.	Parameter Name	Value
1	Equivalent Oxide Thickness (EOT)	2.35 nm
2	Capacitance of Stern Layer (C_{stern})	20 μF/cm^2
3	Low-field effective mobility (μ_{eff})	452 cm^2/Vs
4	Oxide-trap density (N_t)	2.8×10^{16} eV^{-1} cm^{-3}
5	Coulomb Scattering Coefficient (α)	3.4×10^4 Vs/C
6	Tunneling parameter (λ)	0.1 nm
7	Frequency Bandwidth	0.1 Hz-1 KHz

7.3.4 Impact of MOSFET Scaling

Over the past 30 years, the electronic industry has seen an exponential decrease in the transistor size for smaller footprint, higher speed and lower-power consumption. However, we show that for pH-FET sensors, the transistors scaling need not be an appropriate choice.

Fig. 7.14 shows the impact of channel length (L) scaling on the noise performance of the sensor. While the input-referred FET thermal noise increases with increase in L, both flicker noise and electrolyte thermal noise decrease with L. Fig. 7.15 shows the impact of channel width (W) scaling on the noise performance of the sensor. Both

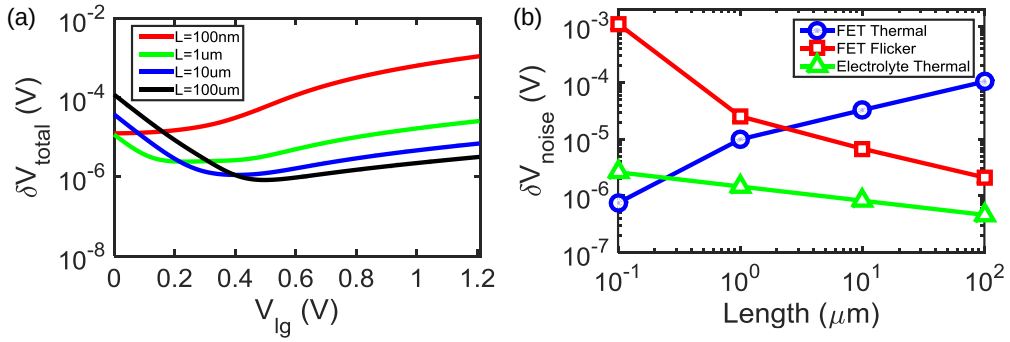

Fig. 7.14.: (a) Scaling dependence of the sensor noise: Total input referred noise voltage as a function of the gate bias for different channel lengths (b) FET flicker (at V_{lg} =1 V) , FET thermal (V_{lg} = 0 V) and electrolyte thermal noise as a function of channel length for fixed gate width (W=100 μm)

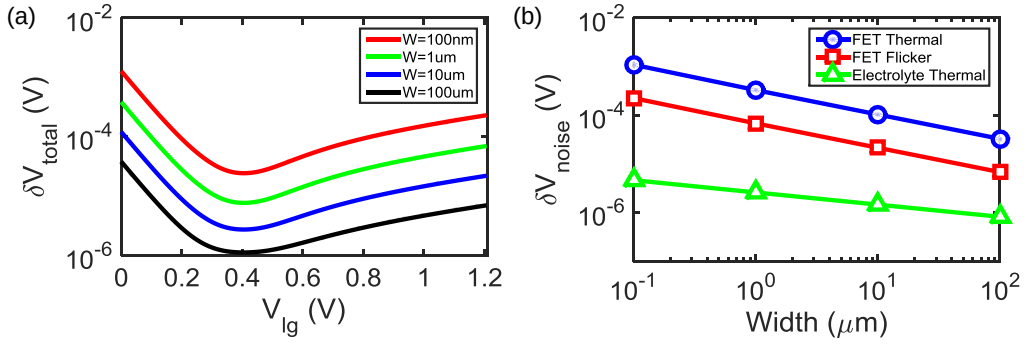

Fig. 7.15.: (a) Scaling dependence of the sensor noise: Total input referred noise voltage as a function of the gate bias for different channel widths, (b) FET flicker (at V_{lg} = 1 V) , FET thermal (V_{lg} = 0 V) and electrolyte thermal noise as a function of channel width for fixed channel length (L=10 μm).

FET thermal and flicker noise voltage scale as $W^{-1/2}$, while electrolyte thermal noise scales as $W^{-1/4}$.

To summarize, if the sensor operation is desired at low gate biases (sub-threshold regime), gate length should be reduced and width increased. However, if sensor operation is desired at high gate biases (in inversion regime), both length and width of the sensor should be increased. The scaling considerations for the pH-FET sensor require a careful investigation of noise. The compact model allows to investigate the impact of sensor scaling on the noise (and therefore pH resolution) very easily.

7.3.5 Scaling considerations for Extended-Gate FET pH sensors

Advantages of EGFET over ISFET: In Section 7.2, we discussed a Verilog-A model for pH-FET sensor with solution directly exposed to the sensing area. As such, the ions in the electrolyte can penetrate the gate insulator causing instability in device characteristics. To tackle this problem, extended gate field-effect transistor (EGFET) can be used to separate the sensing region from the active device. Fig. 7.16 shows the structure of a typical EGFET sensor in which the extended gate and FET device are fabricated into the same chip. The system consists of an extended metal gate connected to the active device and exposed to the sensing environment. Further, it offers numerous other advantages over traditional ISFETs such as insensitivity to light [272] and temperature, lower cost of fabrication, simple passivation and packaging and flexibility in shape of the sensing membrane.

For a MOSFET device, the gate bias is directly proportional to the surface charge on the gate in linear operation regime. Similarly, one might intuitively (but incorrectly) attribute another advantage to EGFET, i.e., increased sensitivity due to larger sensing area. But, such a simple consideration neglects the effect of enhanced electrolyte screening and increased parasitic capacitance due to scaling. In this section, we provide a comprehensive understanding of the sensitivity of EGFET sensor and compare it with pH-FET sensor with solution directly exposed to the sensing area (which we refer henceforth as ISFET).

In order to determine the impact of scaling of the sensor area (A_{sensor}) and the parasitic area (A_{par}) on the sensitivity, we start with the charge neutrality condition given in Eq. (7.3). Unlike ISFET, the parasitic contributions can be significant for the EGFET sensor. Rewriting the charge neutrality condition in terms of surface charge density, we get.

$$A_{\text{sensor}}\sigma_{\text{sensor}}(\psi_e) + A_{\text{sensor}}\sigma_{\text{dl}}(\psi_0) + A_{\text{par}}\sigma_{\text{par}}(\psi_g, V_{\text{sub}}) + A_{\text{ox}}\sigma_{\text{Si}} = 0. \tag{7.29}$$

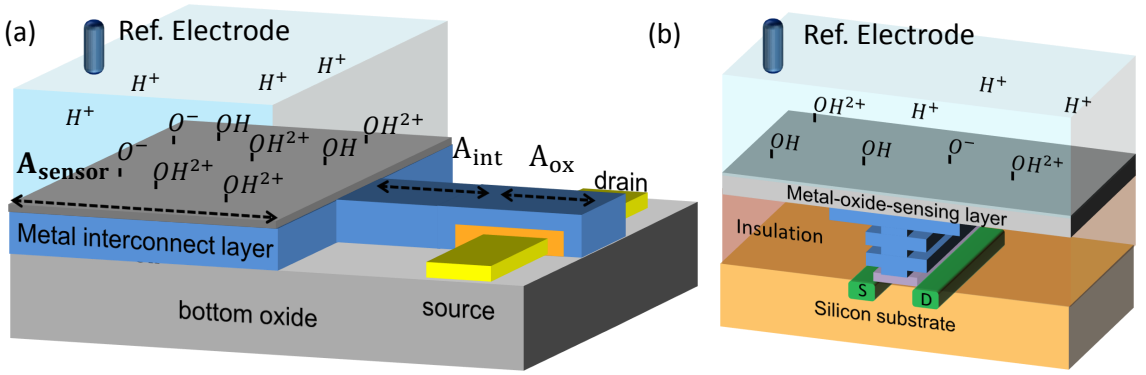

Fig. 7.16.: (a) Sketch of Extended Gate ion-sensitive FET (Not to scale). The design is more reliable since the gate oxide is not directly exposed to the fluid. Labeled are area of the sensing layer (A_{sensor}), active device area (A_{ox}) and the interconnect area (A_{int}). The area of the parasitic capacitance is $A_{\text{par}} = A_{\text{int}} + A_{\text{sensor}}$. (b) Ion-Torrent extended gate pH sensor design.

where, $A_{\text{par}} = A_{\text{int}} + A_{\text{sensor}}$, the parasitic capacitance area is sum total of the interconnect area (A_{int}) and the sensor area (A_{sensor}) (see Fig. 7.16) and V_{sub} is the substrate bias. The parasitic contribution, σ_{par}, can be expressed as,

$$Q_{\text{par}} = C_{\text{par}} \left(V_{\text{sub}} - \psi_g \right). \tag{7.30}$$

where, $C_{\text{par}} = \varepsilon_{ox}/t_{\text{par}}$ is the capacitance per unit area of the parasitic oxide, and t_{par} is the thickness of the parasitic oxide.

In order to determine the sensitivity (S), we need to determine the absolute shift in the surface potential (ψ_g) upon change in pH, i.e.,

$$S = \left| \frac{\delta \psi_g}{\delta \text{pH}} \right|. \tag{7.31}$$

Using Eq. (7.4), the change in ψ_g at a fixed liquid gate bias can be expressed in terms of the change in ψ_e as,

$$\delta \psi_g = \delta \psi_e. \tag{7.32}$$

Rearranging Eq. (7.29) and using Eq. (7.30) we get,

$$\sigma_{\text{sensor}} = -\sigma_{\text{dl}}(\psi_0) - \frac{\eta}{Z} C_{\text{par}}(V_{\text{sub}} - \psi_g) - \frac{1}{Z}\sigma_{si}(\psi_g). \tag{7.33}$$

where, we define, $\eta = (A_{\text{par}}/A_{\text{ox}})$ and $Z = (A_{sensor}/A_{\text{ox}})$ as the scaling factor. Taking a derivative of Eq. (7.33) with respect to ψ_e, we get,

$$\frac{\delta\sigma_{\text{sensor}}}{\delta\psi_e} = C_{\text{diff}} + \left(\frac{\eta}{Z}\right) C_{\text{par}} + \left(\frac{1}{Z}\right) C_g. \tag{7.34}$$

where, $C_{\text{dif}} = -\frac{\delta\sigma_{\text{dl}}}{\delta\psi_e}$ is the differential capacitance of the electrolyte, and $C_g = \frac{\delta\sigma_g}{\delta\psi_g}$ is the gate capacitance. Using Eq. (7.10), the local pH (pH_s) at sensor surface can be expressed in terms of the bulk pH (pH_B) as,

$$\text{pH}_s = \text{pH}_B + \frac{q\psi_0}{kT}. \tag{7.35}$$

This gives,

$$\frac{\delta\sigma_{\text{sensor}}}{\delta\text{pH}_s} = -q\beta_{\text{sensor}}. \tag{7.36}$$

where, β_{sensor} is defined as the intrinsic buffer capacity for the protonation/deprotonation of the surface groups. Therefore, the differential change in ψ_e with change in pH_s is given by,

$$\frac{\delta\psi_e}{\delta\text{pH}_s} = \frac{\delta\psi_e}{\delta\sigma_{\text{sensor}}}\frac{\delta\sigma_{\text{sensor}}}{\delta\text{pH}_s} = -\frac{q\beta_{\text{sensor}}}{C_{\text{dif}} + \left(\frac{\eta}{Z}\right) C_{\text{par}} + \left(\frac{1}{Z}\right) C_g}. \tag{7.37}$$

Using Eq. (7.35), we get,

$$\frac{\delta\psi_e}{\delta(\text{pH}_B + \frac{q\psi_0}{2.3kT})} = -\frac{\beta_{\text{sensor}}}{C_{dif} + \left(\frac{\eta}{Z}\right) C_{\text{par}} + \left(\frac{1}{Z}\right) C_g}. \tag{7.38}$$

Rearrangement of Eq. (7.38) gives,

$$S = \left|\frac{\delta\psi_g}{\delta\text{pH}_B}\right| = \left|\frac{\delta\psi_e}{\delta(\text{pH}_B)}\right| = 2.3\frac{kT}{q}\alpha. \tag{7.39}$$

where,

$$\alpha = \frac{1}{\frac{1}{C_{\text{sensor}}}\left(C_{\text{dif}} + \frac{\eta C_{\text{par}} + C_g}{Z}\right) + 1}. \tag{7.40}$$

is the modified sensitivity parameter, and $C_{\text{sensor}} = \frac{q^2 \beta_{\text{sensor}}}{2.3kT}$. This can be rewritten as,

$$S = \frac{2.3\ kT/q}{1 + a + b/Z}. \tag{7.41}$$

where, $a = C_{\text{diff}}/C_{\text{sensor}}$ and $b = \frac{\eta C_{\text{par}} + C_g}{C_{\text{int}}}$. Typically, η itself scales as Z scales (see Fig. 7.16). In that case, η can be expressed in terms of the interconnect area and the sensor area as, $\eta = (A_{\text{int}} + A_{\text{sensor}})/A_{\text{ox}}$. This gives, $a = (C_{\text{diff}} + C_{\text{par}})/C_{\text{int}}$ and $b = \frac{\eta_{\text{int}} C_{\text{par}} + C_g}{C_{\text{int}}}$ with $\eta_{\text{int}} = A_{\text{int}}/A_{ox}$. Equation (7.41) captures the essence of scaling of the sensor area by a factor of Z. As the sensor area is increased (Z increases), the sensitivity approaches a maximum value independent of the MOSFET type.

Model explains experimental results: Fig. 7.17 shows the match of experimental data in Yin *et al.* [273] with the analytical expression[2]. The analytical result matches the experimental data remarkably well showing that the sensitivity of the EGFET sensor can be very well described by this simple equation. In order to do

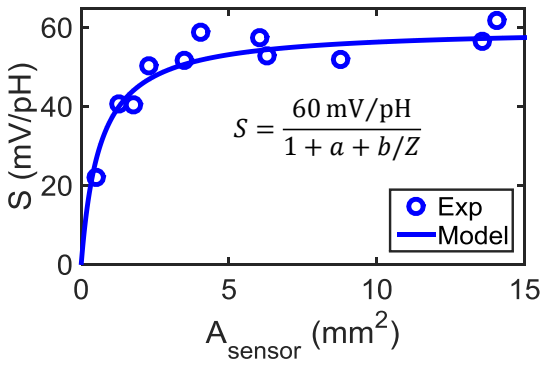

Fig. 7.17.: Matching of experimental data [273] with Eq. (7.41). When the sensor area is small, the parasitic capacitances degrade the device sensitivity. As the sensor area becomes large, irrespective of the parasitic capacitances the device sensitivity reaches its maximum value.

[2] Adapted from Ref. [109] with permission from IEEE.

HSPICE simulation of the EGFET sensor, we generalize Eq. (7.18) by incorporating the effect of the parasitic capacitance. Equation (7.18) then becomes,

$$\psi_e = \frac{2kT}{q}\text{asinh}\left(\frac{A_{\text{sensor}}\sigma_{\text{sensor}}(\psi_e) + A_{\text{par}}C_{\text{par}}(\psi_g - V_{\text{lg}})}{A_{\text{sensor}}\sqrt{8kT\epsilon_w n_0}}\right) + \frac{\sigma_{\text{sensor}}(\psi_e)}{C_{\text{stern}}}. \quad (7.42)$$

For $A_{\text{sensor}} > A_{\text{ox}}$, $S_{\text{EGFET}} = S_{\text{ISFET}}$ regardless of interconnect penalty: Fig. 7.18(a) shows the HSPICE simulation of shift in threshold voltage of an EGFET sensor as a function of pH with different scaling factors and a constant interconnect size ($A_{\text{int}} >> A_{\text{ox}}$). As the sensor area approaches the FET area, the change in threshold voltage saturates. This is also evident from plot of the EGFET sensitivity as a function of the scaling factor as shown in Fig. 7.18(b). For $A_{\text{int}} = 0$, the sensitivity of the EGFET sensor is same as that of ISFET irrespective of the sensor area (as there are negligible parasitic losses).

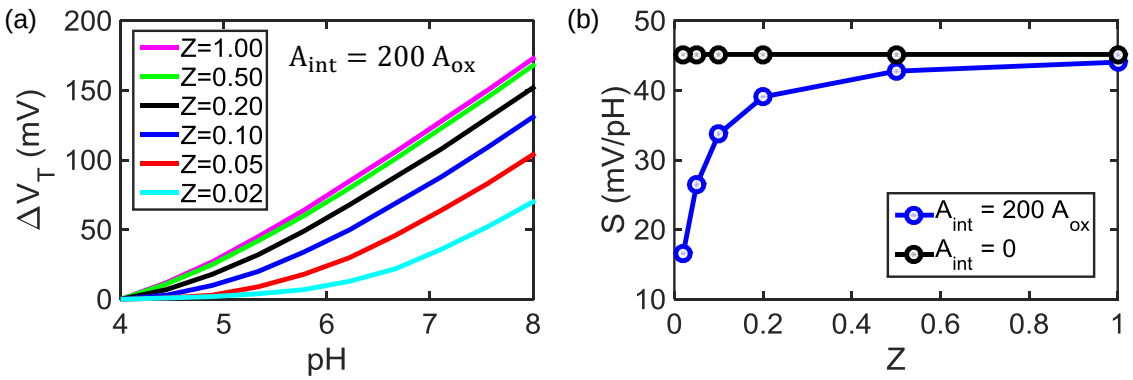

Fig. 7.18.: (a) HSPICE simulation of pH sensitivity for an EGFET as a function of Z for $A_{\text{int}} \gg A_{ox}$, (b) Sensitivity as a function of scaling factor, Z for two scenarios (i) For negligible A_{int}, S remains constant with Z. (ii) For $A_{\text{int}} \gg A_{ox}$, S scales with Z (shown in the inset) in $Z \ll 1$regime and saturates to the ISFET response at $Z \gg 1$

Noise of EGFET sensor is essentially same as ISFET:

The noise contributions from the FET thermal and FET flicker noise for the EGFET sensor are same as ISFET sensor. However, since the sensor area (A_{sensor}) is different as compared to the FET area (A_{ox}), the noise due to the electrolyte resistance in EGFET is $(A_{\text{sensor}}/A_{\text{ox}})^{-1/4}$ times as compared to ISFET (see Eq. (7.19), Eq. (7.23) and Eq. (7.28)). Fig. 7.19(a) shows a comparison of total input-referred noise for EGFET with $A_{\text{sensor}} = 50A_{\text{ox}}$ and ISFET. As expected, the noise in subthreshold and inversion region are same as compared to ISFET, since FET noise dominates in these two regions. The noise of the EGFET sensor at the onset of inversion ($V_{\text{lg}} \sim 0.4V$) is roughly $(50)^{1/4}$ smaller as compared to the ISFET. Therefore, the pH resolution (see Fig. 7.19(b)) is $(50)^{1/4} \sim 2.7$ smaller for EGFET at the onset of inversion as compared to ISFET.

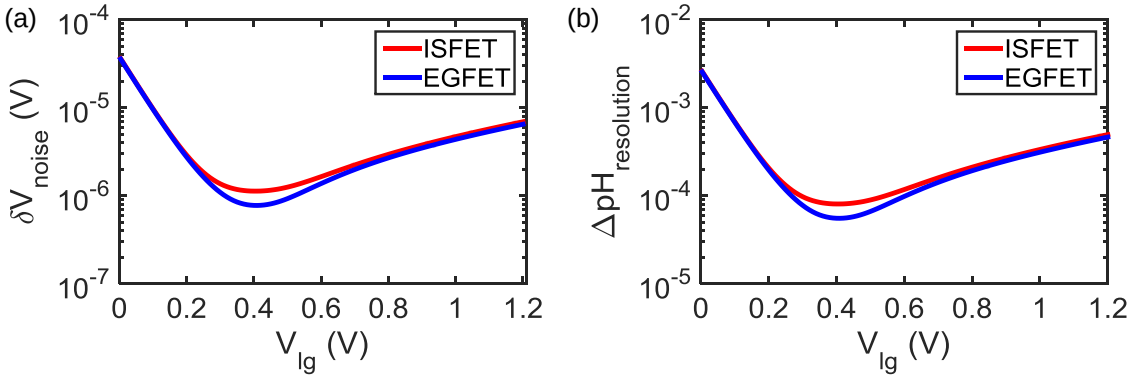

Fig. 7.19.: Comparison of (a) noise and (b) pH resolution of EGFET with ISFET.

To summarize, in this section, we presented a comprehensive analysis of sensitivity of the EGFET sensor as the sensor area is scaled. Our analysis shows that regardless of the interconnect penalty, $S_{\text{EGFET}} = S_{\text{ISFET}}$ with $A_{\text{sensor}} > A_{\text{ox}}$. The pH resolution of the EGFET sensor is marginally better than that of ISFET sensor if the device is operated at onset of the inversion. Though, the extended-gate device doesn't give any enhancement in sensitivity, various other advantages such as long term stability, etc still make it a good choice for pH sensing/bio-sensing application.

7.4 Circuit Demonstration by Collaborators at Purdue

The ultimate goal of any compact model is to be able to determine the operation of a circuit for a given set of parameters. Therefore, in order to demonstrate the capability and robustness of the compact model, we performed circuit simulation using Spectre on a sensor interface shown in Fig. 7.20 [274].

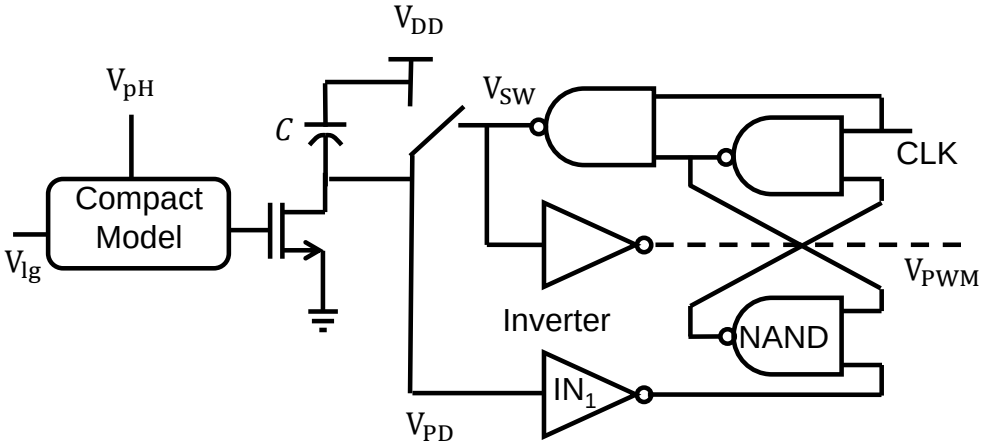

Fig. 7.20.: Block diagram for the sensor interface

The interface consists of three NAND gates, two inverters, one analog switch, and one capacitor. Fig. 7.21 shows the time response of the interface at different operational stages. First, the active-high V_{SW} signal changes from HIGH to LOW at the rising edge of the CLK signal. This initiates the discharging of the node V_{PD} and the V_{PD} signal starts to decrease. Once the V_{PD} signal reaches the inverter IN_1 threshold voltage, the output pushes the V_{SW} signal to HIGH, leading to the capacitor discharging. The V_{PWM} is the inverse of the V_{SW} signal. The pulse width can be related to the current through the pH sensitive transistor as follows:

$$T_{PW} = \frac{CV_{TH}}{I_{ISFET}}. \tag{7.43}$$

Fig. 7.22 shows the pulse width signal as a function of the pH. As the pH increases, the current through the ISFET decreases leading to an increase in the pulse width

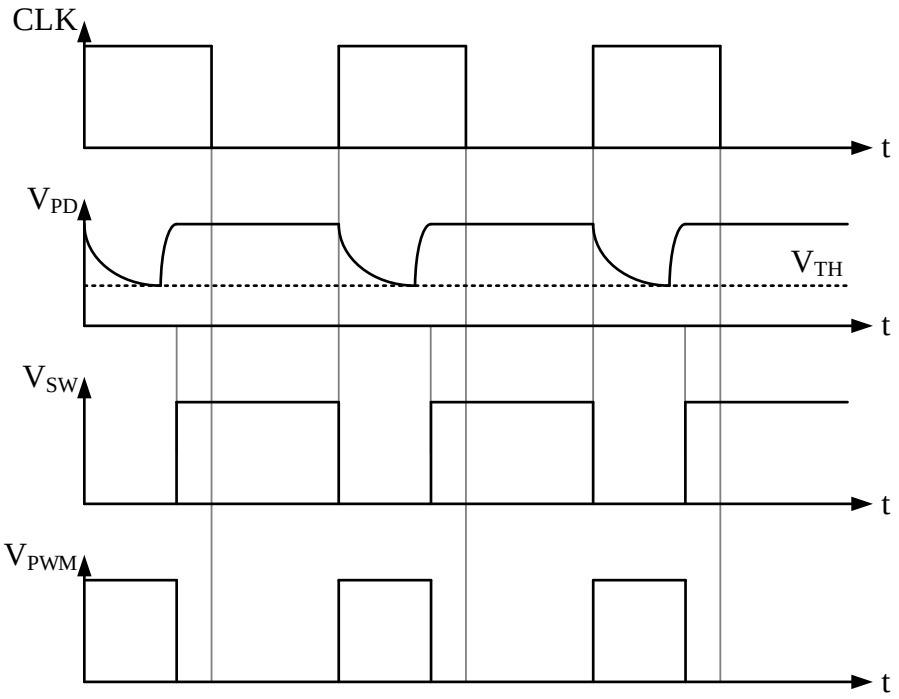

Fig. 7.21.: Timing diagram for the sensor interface

(see Eq. (7.43)). The non-linearity with respect to the pH comes due to non-linear nature of surface-potential (see Fig. 7.8) and inverse relationship of pulse width w.r.t. the current. This sensor interface is expected to be less sensitive to the supply voltage noise and also more power efficient than typical transimpedance amplifier based design [274]. Also, since the output signal is in the time domain, i.e., pulse width, rather than the voltage or current domain, it is expected to have a wide dynamic range.

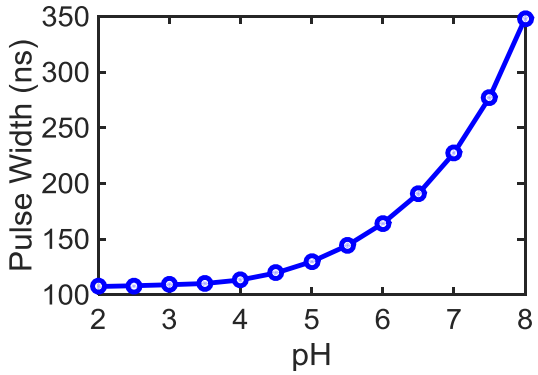

Fig. 7.22.: Simulated pulse width versus pH.

7.5 Conclusions

We have developed a physics-based compact model to characterize the dc, ac, transient and noise response of FET based pH sensors. The physics of surface charging due to change in solution pH is captured in terms of a simplified pH dependent voltage source for the dc model and bias-dependent capacitive components for the transient model. AC model is formulated in terms of both DC and transient operating point. The noise for the electrolyte resistor is modeled and compared with FET noise. Simulations show that while FET thermal noise dominates at low gate biases, flicker noise dominates at high gate biases. The sensitivity is maximized near the onset of inversion and the minimum noise is dictated by all three noise components. Length scaling reduces the flicker noise and electrolyte noise, while it increases the channel thermal noise. Width scaling reduces all three noise sources. The analysis for the EGFET sensor shows that regardless of the interconnect penalty, $S_{\text{EGFET}} = S_{\text{ISFET}}$ with $A_{\text{sensor}} > A_{\text{ox}}$, and the pH resolution of EGFET is marginally better as compared to the ISFET if operated at onset of inversion. The demonstrative use of compact model in sensor interface shows its robustness for optimization of a range of circuits such as pH based genome-sequencers, etc. An implementation of DC model in Verilog-A is available at *nanohub.org* [105].

8. SUMMARY AND FUTURE WORK

8.1 Summary of the thesis and key contributions

In this thesis, we provided a comprehensive design framework for portable, wearable, and implantable (PWI) biosensors. Our specific contributions are as follows:

8.1.1 Lab-on-a-chip droplet based portable biosensors

1. **Characterization framework for evaporating droplets:** We developed a comprehensive numerical and analytical modeling framework for impedance characterization of an evaporating droplet with the following features:

   (a) The theoretical framework correctly predicts the complex, time-dependent electrical response of an evaporating droplet containing analyte molecules.

   (b) The model suggests that intermediate frequency regime, where the solution resistance is dominant, is the most optimum frequency regime for sensor operation. If only droplet shape needs to be determined and not the composition, high-frequency regime of operation is most suitable.

   (c) Further, the work highlights critical importance of the substrate in determining the impedance response of the system. Specifically, the model suggests that compared to typical SOI substrate, the reduced parasitic impedance of a glass substrate would improve the overall response as well as provide a broader bandwidth of operation.

   The model and the approach presented is very general and can be applied to a variety of droplet-related systems (e.g., the operation of a droplet-based sensor).

2. **Electrostatic control of ionic concentration in droplets:** We developed a comprehensive understanding of desalination in small droplets using a numerical and analytical model.

   (a) We generalized the Modified Poisson-Boltzmann model to account for a finite number of ions in a droplet. Our model predicts the maximum volume of a droplet that can be desalted for the given electrode area, electrode voltage, and ionic concentration.

   (b) We proposed and demonstrated an approach to deionize the solution with high ionic concentrations by using high surface area electrodes.

   (c) Theoretical results suggest that desalination in small droplets can be used to: i) Overcome the screening limited response of the charge-based sensors, ii) Perform bias dependent DNA denaturation for isothermal-PCR or sensor reusability, and iii) Do a configurable isoelectric protein separation.

   The model is very general and can be applied to a variety of systems where the analyte volume is very small.

3. **FET-based dielectric heating in droplets:** We developed a theoretical model to determine the spatial and temporal heating profile in sub-nL droplet by dielectric heating using an on-chip FET.

   (a) The model provides a means to precisely control the temperature within the droplet.

   (b) The model suggests that the temperature within the droplet is localized close to the heat source, regardless of the droplet size.

   (c) The model suggests that the droplet temperature reaches steady state within few ms.

   The technique was demonstrated to selectively recognize the probe-target binding as well as single-base mismatch between DNA strands. This ability to heat

a droplet on a chip can be used for a variety of high-throughput screening applications, such high-speed PCR, single cell lysis, single molecule enzymology, and interrogation of ligand-receptor interactions in protein melting studies.

8.1.2 Wearable Sensors

Performance Potential of Multi-layer MoS_2 for development of flexible wearable biosensors: We performed a comprehensive investigation of the performance potential of multilayer MoS_2 FETs to detect biomolecules (specifically, the cancer biomarker PSA). The results demonstrate the successful use of MoS_2 FET sensor in back-gated scheme without the need of the insulating oxide on the top of channel. The highly hydrophobic nature of the MoS_2 surface allows it to serve the dual roles of the transducer and the recognition layer, with considerable improvement in sensitivity and significant simplification of device design.

1. The theoretical model consistently explains the experimental puzzles, i.e., saturation of off-current, high subthreshold-slope; and decrease in off-current and subthreshold-slope upon PSA binding.

2. The results indicate that the sensitivity can be further improved through surface treatment and interface passivation.

3. Further, the model is used to determine the binding efficiency of the sensor and can thus be used to optimize the sensor.

Combined with the rapid advances in large-area synthesis methods of MoS_2 such as CVD, our results deliver a compelling case of potentially using multilayer MoS_2 FETs as flexible wearable/implantable biosensors for continuous monitoring of vital health parameters.

8.1.3 Implantable Sensors

Performance trade-offs in hydrogel based implantable biochemical sensors: We developed a numerical and analytical framework to determine the performance parameters i.e. sensitivity, response time and dynamic range of hydrogel-based implantable biochemical sensors based on gel preparation parameters, such as the ionizable group density (N_f) and its dissociation constant (K_a). Our analysis demonstrates that there is a fundamental trade-off between these parameters. Specifically,

1. If a high sensitivity and a high dynamic range is desirable (for applications where sluggishness of the response is not a primary concern), the density of ionizable group (N_f) should be high and the ionizable group should be selected such that its pK_a is close to the desired pH range.

2. On the other hand, if fast response time and symmetry is an essential prerequisite, N_f should be low and ionizable group should be selected such that its pK_a is shifted away from the desired pH range.

Our analysis suggests that the dynamic range can be improved by using hydrogels prepared with more than one type of ionizable group. The model is very versatile and can be used to predict the response of many biochemical sensors where hydrogel is actively considered as a sensor or encapsulation material.

8.1.4 System Integration

An illustrative Verilog-A compact model for pH-FET sensors: We developed a physics-based compact model to characterize the DC, AC, transient and noise response of FET based pH sensors. The physics of surface charging due to change in solution pH is captured in terms of a simplified pH dependent voltage source for the DC model and bias-dependent capacitive components for the transient model. AC model is formulated in terms of both DC and transient operating point. The noise

for the electrolyte resistor is modeled and compared with FET noise. Our analysis suggests:

1. FET thermal noise dominates in subthreshold-regime, flicker noise dominates in inversion. The sensitivity is maximized near the onset of inversion and the minimum noise is dictated by all three noise components.

2. Length scaling reduces the flicker noise and electrolyte noise, while it increases the channel thermal noise. Width scaling reduces all three noise sources.

3. Regardless of the interconnect penalty, $S_{\mathrm{EGFET}} = S_{\mathrm{ISFET}}$ with $A_{\mathrm{sensor}} > A_{\mathrm{ox}}$, and the pH resolution of EGFET is marginally better as compared to the ISFET if operated at onset of inversion.

The demonstrative use of compact model in sensor interface shows its robustness for optimization of range of circuits such as pH based genome-sequencers, etc. Further, the modeling approach highlighted can be used to model non-electrical elements for system integration of lab-on-a-chip components.

8.2 Future work

While the contributions of this thesis are significant, the prototype devices analyzed should be viewed as building blocks for a system-level analysis. Furthermore, the understanding developed through this thesis could be used for design of more advanced devices, such as transient electronic devices and electroceuticals. Below, we describe possible extensions of the work presented in this thesis.

8.2.1 System integration of Sensors

The rapid advances in digital microfluidics for massively parallel handling, manipulation, amplification, and analysis of millions of droplets pave the way for realization of high-throughput, label-free electrical screening of biological entities for applications

in fast drug screening, personal proteomics, etc. As discussed in this thesis, droplet-based biosensors can be used to overcome some of the fundamental limitations of the classical sensors, such as diffusion limited time response and screening-limited sensitivity. One research direction is experimental demonstration of enhanced sensitivity using the desalting scheme described in this thesis. Furthermore, novel theoretical concepts such as bias-dependent DNA denaturation can be experimentally demonstrated and explored for applications in isothermal PCR and sensor reusability.

Another interesting area of research is system integration of droplet sensors. The functioning of a truely lab-on-a-chip portable device requires integration of different steps, such as, sample collection, sample treatment, analyte-specific reaction, signal generation and detection on a single platform [275]. For example, we demonstrated that droplet heating can be used to modulate the conformation of the DNA strands (denatured vs. hybridized) and optically analyze DNA denaturation for selective detection. However, optical systems are often bulky and not amenable to minaturization. On other hand, we demonstrated a method to characterize a droplet containing analyte molecules. Addressing selectivity in such a impedance based sensor requires either pre-filteration or several off-chip heating cycles [205]. Therefore, one possible research direction could be to integrate these two schemes onto a fully functional lab-on-a-chip platform. Finally, the component design and fabrication procedures must evolve to ensure that different modules are compatible with each other, and are able to function together.

8.2.2 Electroceuticals

Electroceuticals are a range of biomedical implantable actuation devices (see Fig. 8.1) which deliver electrical impulses to the neurons for regulating the functionality of body's organs. It is an emerging area of research and it has tremendous potential to restore the lost functionality of body's organs [276, 277]. For example, these electrical impulses can be used to stimulate pancreas for regulating blood sugar

levels in diabetic patients, or these can stimulate the blood vessels to reduce hypertension. The advantage of electrical stimulation in comparison to drugs is that when used with precise control, this can be used to specifically target certain disorders without inducing side effects.

Fig. 8.1.: Illustration of an electroceutical implant: Neurons are stimulated using an implanted electrical device to treat an array of conditions. Adapted by permission from Macmillan Publishers Ltd: Nature [276], copyright (2013)

The traditional approach to mapping of neural networks relies on recording the electrical activity of a large set of neurons at a time. However, the neurons function at nanoscale, and therefore the sensors to study the interaction between these neurons must operate at this scale [277]. Therefore, as a first step, minaturized sensors can be used to record the electrical activity of the neural network with nanoscale precision. The models developed in this thesis (for example, impedance characterization model, the model for diffusion of ions in hydrogel or compact model for FET H^+ ion sensor) can be used to enable co-design and optimization of these sensors. These model can be calibrated with in-vivo experiments, and be used to model the neural circuits, and establish a correlation between different body functions and the associated network. Once the correlation is well-established, nano-actuators can be utilized for closed-

loop control of the brain by manipulating the activities of chosen set of neurons for restoring the lost functionality of body's organs in patients.

8.2.3 Transient Electronics

Transient electronics refers to electronic devices that can be programmed to completely dissolved within a certain period of time. Upon dissolution, these devices disintegrate into biologically or environmentally benign products. This ability to disappear after a programmed use can be very useful for bio-degradable diagnostic and therapeutic implants.

One possible future direction for research could be development and optimization of transient electronic biosensors. Recently, Hwang *et al.* demonstrated dissolvable circuits made up of silicon nanomembranes (see Fig. 8.2 [278]). The dissolution of silicon occurs through hydrolysis, and the transience time can be controlled by changing the critical dimensions of the device. The theoretical model developed for reaction and diffusion of ionic species (for hydrogel sensors) can be generalized to estimate the dissolution and operation of the devices. Park *et al.* showed that these transient electronic devices can be thermally triggered to degrade faster [279]. Therefore, another interesting research direction could be to extend the thermal model developed in this thesis and utilize it for analysis and optimization of thermally triggered (and maybe self-destructive) transient electronic devices. Finally, the compact models developed for the sensors can be integrated with the result from the transient analysis to describe the time-transient operation of sensors.

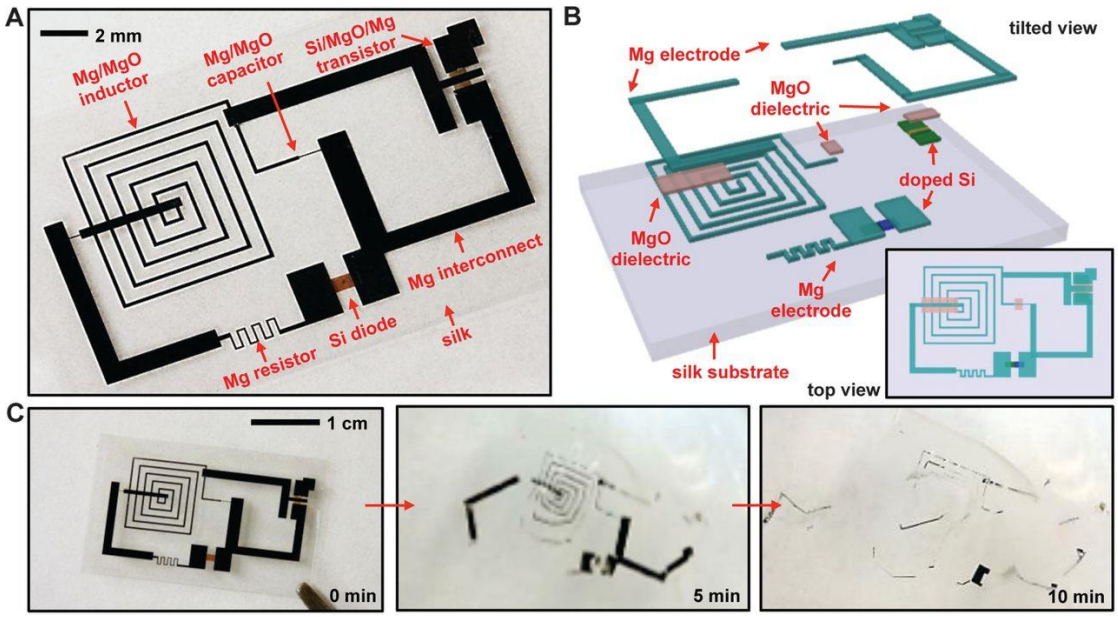

Fig. 8.2.: Illustration of transient electronic devices: (a) Devices include transitors, diodes, inductors, capacitors, and resistors, with interconnects, all on silk substrate, (b) Schematic illustration in 3D, (c) Images showing time sequence of dissolution in water. From Hwang *et al.* [278]. Reprinted with permission from AAAS.

8.3 Concluding Remarks

We stand at the edge of a technological revolution that will fundamentally alter the way we live and interact with the surrounding environment. A revolution whose scale, scope and complexity will be unlike anything that human being has ever seen before. First came the agricultural revolution, next industrial and finally digital revolution which changed the way information was stored and communicated.

The incipient healthcare revolution will bring a patient centric healthcare system where miniaturized sensing and actuation elements will work in tandem with the electronic communication devices to enable automated timely medical diagnosis, prognosis and treatment. We are delving into an era where treatment will begin before the symptoms of a disease start to appear, an era where the medication will be personalized and the gene sequence could be modified to suit the individuals needs.

The enabling technologies for this revolution are already in place: nanoelectronic components with feature size about 400 times smaller than neurons (4 μm - 100 μm) and digital microfluidic components with capability to process fluidic volumes about 10^{-19} times smaller than the volume of water in an adult human body. However, what is necessary is a joint effort by experimentalists and theoreticians from multi-disciplinary fields, including electronics, biology, chemistry and information system, to not only understand the most complex machine, human brain, but to develop systems which could use that understanding to manipulate body functions. The industries must work with universities to refine innovative ideas in medicare and bring it to masses.

REFERENCES

REFERENCES

[1] "Noncommunicable diseases country profiles 2014," World Health Organization, Tech. Rep., 2014. [Online]. Available: http://www.who.int/nmh/publications/ncd-profiles-2014/en/

[2] J. M. Rothberg, W. Hinz, T. M. Rearick, J. Schultz, W. Mileski, M. Davey, J. H. Leamon, K. Johnson, M. J. Milgrew, M. Edwards, J. Hoon, J. F. Simons, D. Marran, J. W. Myers, J. F. Davidson, A. Branting, J. R. Nobile, B. P. Puc, D. Light, T. a. Clark, M. Huber, J. T. Branciforte, I. B. Stoner, S. E. Cawley, M. Lyons, Y. Fu, N. Homer, M. Sedova, X. Miao, B. Reed, J. Sabina, E. Feierstein, M. Schorn, M. Alanjary, E. Dimalanta, D. Dressman, R. Kasinskas, T. Sokolsky, J. a. Fidanza, E. Namsaraev, K. J. McKernan, A. Williams, G. T. Roth, and J. Bustillo, "An integrated semiconductor device enabling non-optical genome sequencing," Nature, vol. 475, no. 7356, pp. 348–352, jul 2011. [Online]. Available: http://www.nature.com/doifinder/10.1038/nature10242

[3] R. C. Webb, A. P. Bonifas, A. Behnaz, Y. Zhang, K. J. Yu, H. Cheng, M. Shi, Z. Bian, Z. Liu, Y.-S. Kim, W.-H. Yeo, J. S. Park, J. Song, Y. Li, Y. Huang, A. M. Gorbach, and J. A. Rogers, "Ultrathin conformal devices for precise and continuous thermal characterization of human skin," Nature Materials, vol. 12, no. 10, pp. 938–944, sep 2013. [Online]. Available: http://www.nature.com/doifinder/10.1038/nmat3755

[4] H. Yao, C. Marcheselli, A. Afanasiev, I. Lahdesmaki, and B. A. Parviz, "A soft hydrogel contact lens with an encapsulated sensor for tear glucose monitoring," in 2012 IEEE 25th International Conference on Micro Electro Mechanical Systems (MEMS), no. February. IEEE, jan 2012, pp. 769–772. [Online]. Available: http://ieeexplore.ieee.org/lpdocs/epic03/wrapper.htm?arnumber=6170299

[5] P. Dak, A. Ebrahimi, V. Swaminathan, C. Duarte-Guevara, R. Bashir, and M. Alam, "Droplet-based Biosensing for Lab-on-a-Chip, Open Microfluidics Platforms," Biosensors, vol. 6, no. 2, p. 14, apr 2016. [Online]. Available: http://www.mdpi.com/2079-6374/6/2/14

[6] P. R. Nair and M. A. Alam, "Performance limits of nanobiosensors," Applied Physics Letters, vol. 88, no. 23, p. 233120, 2006. [Online]. Available: http://link.aip.org/link/APPLAB/v88/i23/p233120/s1{&}Agg=doi

[7] F. Gao, Z. Zhu, J. Lei, Y. Geng, and H. Ju, "Sub-femtomolar electrochemical detection of DNA using surface circular strand-replacement polymerization and gold nanoparticle catalyzed silver deposition for signal amplification," Biosensors and Bioelectronics, vol. 39, no. 1, pp. 199–203, jan 2013. [Online]. Available: http://linkinghub.elsevier.com/retrieve/pii/S0956566312004770

[8] E. D. Goluch, J.-M. Nam, D. G. Georganopoulou, T. N. Chiesl, K. a. Shaikh, K. S. Ryu, A. E. Barron, C. a. Mirkin, and C. Liu, "A bio-barcode assay for on-chip attomolar-sensitivity protein detection," Lab on a Chip, vol. 6, no. 10, p. 1293, oct 2006. [Online]. Available: http://xlink.rsc.org/?DOI=b606294f

[9] H. D. Hill and C. A. Mirkin, "The bio-barcode assay for the detection of protein and nucleic acid targets using DTT-induced ligand exchange," Nature Protocols, vol. 1, no. 1, pp. 324–336, jun 2006. [Online]. Available: http://www.nature.com/doifinder/10.1038/nprot.2006.51

[10] P. Bergveld, "Development, Operation, and Application of the Ion-Sensitive Field-Effect Transistor as a Tool for Electrophysiology," IEEE Transactions on Biomedical Engineering, vol. BME-19, no. 5, pp. 342–351, sep 1972. [Online]. Available: http://ieeexplore.ieee.org/lpdocs/epic03/wrapper.htm?arnumber=4120550

[11] J. Go, P. R. Nair, and M. A. Alam, "Theory of signal and noise in double-gated nanoscale electronic pH sensors," Journal of Applied Physics, vol. 112, no. 3, p. 034516, aug 2012. [Online]. Available: http://scitation.aip.org/content/aip/journal/jap/112/3/10.1063/1.4737604

[12] J. Lee, P. Dak, Y. Lee, H. Park, W. Choi, M. A. Alam, and S. Kim, "Two-dimensional Layered MoS2 Biosensors Enable Highly Sensitive Detection of Biomolecules," Scientific Reports, vol. 4, p. 7352, dec 2014. [Online]. Available: http://www.nature.com/srep/2014/141217/srep07352/full/srep07352.html

[13] C. Toumazou and P. Georgiou, "Piet Bergveld - 40 years of ISFET technology: From neuronal sensing to DNA sequencing," Electronics Letters, vol. 47, no. 26, p. S7, 2011. [Online]. Available: http://link.aip.org/link/ELLEAK/v47/i26/pS7/s1{&}Agg=doi

[14] E. Stern, R. Wagner, F. J. Sigworth, R. Breaker, T. M. Fahmy, and M. a. Reed, "Importance of the Debye Screening Length on Nanowire Field Effect Transistor Sensors," Nano Letters, vol. 7, no. 11, pp. 3405–3409, nov 2007. [Online]. Available: http://pubs.acs.org/doi/abs/10.1021/nl071792z

[15] A. Kim, C. S. Ah, C. W. Park, J.-H. Yang, T. Kim, C.-G. Ahn, S. H. Park, and G. Y. Sung, "Direct label-free electrical immunodetection in human serum using a flow-through-apparatus approach with integrated field-effect transistors," Biosensors and Bioelectronics, vol. 25, no. 7, pp. 1767–1773, mar 2010. [Online]. Available: http://linkinghub.elsevier.com/retrieve/pii/S0956566309007040

[16] G. S. Kulkarni and Z. Zhong, "Detection beyond the Debye Screening Length in a High-Frequency Nanoelectronic Biosensor," Nano Letters, vol. 12, no. 2, pp. 719–723, feb 2012. [Online]. Available: http://pubs.acs.org/doi/abs/10.1021/nl203666a

[17] R. Elnathan, M. Kwiat, A. Pevzner, Y. Engel, L. Burstein, A. Khatchtourints, A. Lichtenstein, R. Kantaev, and F. Patolsky, "Biorecognition Layer Engineering: Overcoming Screening Limitations of Nanowire-Based FET Devices," Nano Letters, vol. 12, no. 10, pp. 5245–5254, oct 2012. [Online]. Available: http://pubs.acs.org/doi/abs/10.1021/nl302434w

[18] E. Stern, A. Vacic, N. K. Rajan, J. M. Criscione, J. Park, B. R. Ilic, D. J. Mooney, M. a. Reed, and T. M. Fahmy, "Label-free biomarker detection from whole blood," Nature Nanotechnology, vol. 5, no. 2, pp. 138–142, feb 2010. [Online]. Available: http://www.nature.com/doifinder/10.1038/nnano.2009.353

[19] P. R. Nair and M. A. Alam, "Theory of "Selectivity" of label-free nanobiosensors: A geometro-physical perspective," Journal of Applied Physics, vol. 107, no. 6, p. 064701, mar 2010. [Online]. Available: http://scitation.aip.org/content/aip/journal/jap/107/6/10.1063/1.3310531

[20] L. Malic, D. Brassard, T. Veres, and M. Tabrizian, "Integration and detection of biochemical assays in digital microfluidic LOC devices," Lab Chip, vol. 10, no. 4, pp. 418–431, feb 2010. [Online]. Available: http://xlink.rsc.org/?DOI=B917668C

[21] E. K. Sackmann, A. L. Fulton, and D. J. Beebe, "The present and future role of microfluidics in biomedical research," Nature, vol. 507, no. 7491, pp. 181–189, mar 2014. [Online]. Available: http://www.nature.com/doifinder/10.1038/nature13118

[22] J. Suehiro, A. Ohtsubo, T. Hatano, and M. Hara, "Selective detection of bacteria by a dielectrophoretic impedance measurement method using an antibody-immobilized electrode chip," Sensors and Actuators B: Chemical, vol. 119, no. 1, pp. 319–326, nov 2006. [Online]. Available: http://linkinghub.elsevier.com/retrieve/pii/S0925400505009901

[23] L. Yang, P. P. Banada, M. R. Chatni, K. Seop Lim, A. K. Bhunia, M. Ladisch, and R. Bashir, "A multifunctional micro-fluidic system for dielectrophoretic concentration coupled with immuno-capture of low numbers of Listeria monocytogenes," Lab on a Chip, vol. 6, no. 7, p. 896, jul 2006. [Online]. Available: http://xlink.rsc.org/?DOI=b607061m

[24] K. Choi, A. H. Ng, R. Fobel, and A. R. Wheeler, "Digital Microfluidics," Annual Review of Analytical Chemistry, vol. 5, no. 1, pp. 413–440, jul 2012. [Online]. Available: http://www.annualreviews.org/doi/abs/10.1146/annurev-anchem-062011-143028

[25] S.-Y. Teh, R. Lin, L.-H. Hung, and A. P. Lee, "Droplet microfluidics," Lab on a Chip, vol. 8, no. 2, p. 198, feb 2008. [Online]. Available: http://xlink.rsc.org/?DOI=b715524g

[26] F. De Angelis, F. Gentile, F. Mecarini, G. Das, M. Moretti, P. Candeloro, M. L. Coluccio, G. Cojoc, A. Accardo, C. Liberale, R. P. Zaccaria, G. Perozziello, L. Tirinato, A. Toma, G. Cuda, R. Cingolani, and E. Di Fabrizio, "Breaking the diffusion limit with super-hydrophobic delivery of molecules to plasmonic nanofocusing SERS structures," Nature Photonics, vol. 5, no. 11, pp. 682–687, sep 2011. [Online]. Available: http://www.nature.com/doifinder/10.1038/nphoton.2011.222

[27] A. Ebrahimi, P. Dak, E. Salm, S. Dash, S. V. Garimella, R. Bashir, and M. A. Alam, "Nanotextured superhydrophobic electrodes enable detection of attomolar-scale DNA concentration within a droplet by non-faradaic impedance spectroscopy," Lab on a Chip, vol. 13, no. 21, p. 4248, nov 2013. [Online]. Available: http://xlink.rsc.org/?DOI=c3lc50517k

[28] E. W. M. Kemna, L. I. Segerink, F. Wolbers, I. Vermes, and A. van den Berg, "Label-free, high-throughput, electrical detection of cells in droplets," The Analyst, vol. 138, no. 16, p. 4585, aug 2013. [Online]. Available: http://xlink.rsc.org/?DOI=c3an00569k

[29] A. W. Martinez, S. T. Phillips, M. J. Butte, and G. M. Whitesides, "Patterned Paper as a Platform for Inexpensive, Low-Volume, Portable Bioassays," Angewandte Chemie International Edition, vol. 46, no. 8, pp. 1318–1320, feb 2007. [Online]. Available: http://doi.wiley.com/10.1002/anie.200603817

[30] M. Melli, G. Scoles, and M. Lazzarino, "Fast Detection of Biomolecules in Diffusion-Limited Regime Using Micromechanical Pillars," ACS Nano, vol. 5, no. 10, pp. 7928–7935, oct 2011. [Online]. Available: http://pubs.acs.org/doi/abs/10.1021/nn202224g

[31] H. Song, D. L. Chen, and R. F. Ismagilov, "Reactions in Droplets in Microfluidic Channels," Angewandte Chemie International Edition, vol. 45, no. 44, pp. 7336–7356, nov 2006. [Online]. Available: http://doi.wiley.com/10.1002/anie.200601554

[32] W. Wang and T. B. Jones, "Moving droplets between closed and open microfluidic systems," Lab Chip, vol. 15, no. 10, pp. 2201–2212, 2015. [Online]. Available: http://xlink.rsc.org/?DOI=C5LC00014A

[33] I. Barbulovic-Nad, S. H. Au, and A. R. Wheeler, "A microfluidic platform for complete mammalian cell culture," Lab on a Chip, vol. 10, no. 12, p. 1536, 2010. [Online]. Available: http://xlink.rsc.org/?DOI=c002147d

[34] N. R. Beer, B. J. Hindson, E. K. Wheeler, S. B. Hall, K. A. Rose, I. M. Kennedy, and B. W. Colston, "On-Chip, Real-Time, Single-Copy Polymerase Chain Reaction in Picoliter Droplets," Analytical Chemistry, vol. 79, no. 22, pp. 8471–8475, nov 2007. [Online]. Available: http://pubs.acs.org/doi/abs/10.1021/ac701809w

[35] H. Li, R. Luo, and K. Lam, "Modeling of ionic transport in electric-stimulus-responsive hydrogels," Journal of Membrane Science, vol. 289, no. 1-2, pp. 284–296, feb 2007. [Online]. Available: http://linkinghub.elsevier.com/retrieve/pii/S0376738806008349

[36] H. Moon, A. R. Wheeler, R. L. Garrell, J. A. Loo, and C.-J. C. Kim, "An integrated digital microfluidic chip for multiplexed proteomic sample preparation and analysis by MALDI-MS," Lab on a Chip, vol. 6, no. 9, p. 1213, sep 2006. [Online]. Available: http://xlink.rsc.org/?DOI=b601954d

[37] J. Zhang, H. P. Lang, F. Huber, A. Bietsch, W. Grange, U. Certa, R. Mckendry, H.-J. Güntherodt, M. Hegner, and C. Gerber, "Rapid and label-free nanomechanical detection of biomarker transcripts in human RNA," Nature Nanotechnology, vol. 1, no. 3, pp. 214–220, dec 2006. [Online]. Available: http://www.nature.com/doifinder/10.1038/nnano.2006.134

[38] V. Srinivasan, V. K. Pamula, and R. B. Fair, "An integrated digital microfluidic lab-on-a-chip for clinical diagnostics on human physiological fluids," Lab on a Chip, vol. 4, no. 4, p. 310, aug 2004. [Online]. Available: http://xlink.rsc.org/?DOI=b403341h

[39] X. Xiang, L. Chen, C. Zhang, M. Luo, X. Ji, and Z. He, "A fluorescence-based colorimetric droplet platform for biosensor application to the detection of α-fetoprotein," The Analyst, vol. 137, no. 23, p. 5586, 2012. [Online]. Available: http://xlink.rsc.org/?DOI=c2an36111f

[40] P. Dubois, G. Marchand, Y. Fouillet, J. Berthier, T. Douki, F. Hassine, S. Gmouh, and M. Vaultier, "Ionic Liquid Droplet as e-Microreactor," Analytical Chemistry, vol. 78, no. 14, pp. 4909–4917, jul 2006. [Online]. Available: http://pubs.acs.org/doi/abs/10.1021/ac060481q

[41] C. E. Sims and N. L. Allbritton, "Analysis of single mammalian cells on-chip," Lab on a Chip, vol. 7, no. 4, p. 423, may 2007. [Online]. Available: http://xlink.rsc.org/?DOI=b615235j

[42] S. Patel, H. Park, P. Bonato, L. Chan, and M. Rodgers, "A review of wearable sensors and systems with application in rehabilitation," Journal of NeuroEngineering and Rehabilitation, vol. 9, no. 1, p. 21, 2012. [Online]. Available: http://www.jneuroengrehab.com/content/9/1/21

[43] S.-j. Yeh, "Monitoring Blood Glucose Changes in Cutaneous Tissue by Temperature-modulated Localized Reflectance Measurements," Clinical Chemistry, vol. 49, no. 6, pp. 924–934, jun 2003. [Online]. Available: http://www.clinchem.org/content/49/6/924

[44] K. Maruo, M. Tsurugi, T. Ota, H. Arimoto, Y. Yamada, M. Tamura, M. Ishii, and Y. Ozaki, "Noninvasive blood glucose assay using a newly developed near-infrared system," IEEE Journal of Selected Topics in Quantum Electronics, vol. 9, no. 2, pp. 322–330, mar 2003. [Online]. Available: http://ieeexplore.ieee.org/lpdocs/epic03/wrapper.htm?arnumber=1238997

[45] B. D. Cameron and G. L. Cóte, "Noninvasive glucose sensing utilizing a digital closed-loop polarimetric approach." IEEE transactions on bio-medical engineering, vol. 44, no. 12, pp. 1221–7, dec 1997. [Online]. Available: http://www.ncbi.nlm.nih.gov/pubmed/9401221

[46] D. Akinwande, N. Petrone, and J. Hone, "Two-dimensional flexible nanoelectronics," Nature Communications, vol. 5, p. 5678, dec 2014. [Online]. Available: http://www.nature.com/doifinder/10.1038/ncomms6678

[47] W. S. Wong and A. Salleo, Eds., Flexible Electronics, ser. Electronic Materials: Science & Technology. Boston, MA: Springer US, 2009, vol. 11. [Online]. Available: http://link.springer.com/10.1007/978-0-387-74363-9

[48] M. X. Chu, K. Miyajima, D. Takahashi, T. Arakawa, K. Sano, S.-i. Sawada, H. Kudo, Y. Iwasaki, K. Akiyoshi, and M. Mochizuki, "Soft contact lens biosensor for in situ monitoring of tear glucose as non-invasive blood sugar assessment," Talanta, vol. 83, no. 3, pp. 960–965, jan 2011. [Online]. Available: http://linkinghub.elsevier.com/retrieve/pii/S0039914010008519

[49] Y.-t. Liao, H. Yao, A. Lingley, B. Parviz, and B. P. Otis, "A 3-uW CMOS Glucose Sensor for Wireless Contact-Lens Tear Glucose Monitoring," IEEE Journal of Solid-State Circuits, vol. 47, no. 1, pp. 335–344, jan 2012. [Online]. Available: http://ieeexplore.ieee.org/lpdocs/epic03/wrapper.htm?arnumber=6071020

[50] H. Yao, A. Afanasiev, I. Lahdesmaki, and B. Parviz, "A dual microscale glucose sensor on a contact lens, tested in conditions mimicking the eye," in 2011 IEEE 24th International Conference on Micro Electro Mechanical Systems, vol. 1. IEEE, jan 2011, pp. 25–28. [Online]. Available: http://ieeexplore.ieee.org/lpdocs/epic03/wrapper.htm?arnumber=5734353

[51] S. L. Swisher, M. C. Lin, A. Liao, E. J. Leeflang, Y. Khan, F. J. Pavinatto, K. Mann, A. Naujokas, D. Young, S. Roy, M. R. Harrison, A. C. Arias, V. Subramanian, and M. M. Maharbiz, "Impedance sensing device enables early detection of pressure ulcers in vivo." Nature communications, vol. 6, p. 6575, 2015. [Online]. Available: http://www.nature.com/ncomms/2015/150317/ncomms7575/full/ncomms7575.html?WT.ec{_}id=NCOMMS-20150318

[52] J. Yoon, W. Park, G.-Y. Bae, Y. Kim, H. S. Jang, Y. Hyun, S. K. Lim, Y. H. Kahng, W.-K. Hong, B. H. Lee, and H. C. Ko, "Highly Flexible and Transparent Multilayer MoS 2 Transistors with Graphene Electrodes," Small, vol. 9, no. 19, pp. n/a–n/a, feb 2013. [Online]. Available: http://doi.wiley.com/10.1002/smll.201300134

[53] H. Kwon, W. Choi, D. Lee, Y. Lee, J. Kwon, B. Yoo, C. P. Grigoropoulos, and S. Kim, "Selective and localized laser annealing effect for high-performance flexible multilayer MoS2 thin-film transistors," Nano Research, vol. 7, no. 8, pp. 1137–1145, aug 2014. [Online]. Available: http://link.springer.com/10.1007/s12274-014-0476-1

[54] J.-s. Rhyee, J. Kwon, P. Dak, J. H. Kim, S. M. Kim, J. Park, Y. K. Hong, W. G. Song, I. Omkaram, M. A. Alam, and S. Kim, "High-Mobility Transistors Based on Large-Area and Highly Crystalline CVD-Grown MoSe 2 Films on Insulating Substrates," Advanced Materials, vol. 28, no. 12, pp. 2316–2321, mar 2016. [Online]. Available: http://doi.wiley.com/10.1002/adma.201504789

[55] Y. S. Rim, S.-H. Bae, H. Chen, N. De Marco, and Y. Yang, "Recent Progress in Materials and Devices toward Printable and Flexible Sensors," Advanced Materials, pp. n/a–n/a, feb 2016. [Online]. Available: http://doi.wiley.com/10.1002/adma.201505118

[56] A. K. Geim and K. S. Novoselov, "The rise of graphene," Nature Materials, vol. 6, no. 3, pp. 183–191, mar 2007. [Online]. Available: http://www.nature.com/doifinder/10.1038/nmat1849

[57] Y.-M. Lin, A. Valdes-Garcia, S.-J. Han, D. B. Farmer, I. Meric, Y. Sun, Y. Wu, C. Dimitrakopoulos, A. Grill, P. Avouris, and K. a. Jenkins, "Wafer-scale graphene integrated circuit." Science (New York, N.Y.), vol. 332, no. 6035, pp. 1294–7, jun 2011. [Online]. Available: http://www.ncbi.nlm.nih.gov/pubmed/21659599

[58] B. Radisavljevic, a. Radenovic, J. Brivio, V. Giacometti, and a. Kis, "Single-layer MoS2 transistors." Nature nanotechnology, vol. 6, no. 3, pp. 147–50, mar 2011. [Online]. Available: http://www.ncbi.nlm.nih.gov/pubmed/21278752

[59] H. Wang, L. Yu, Y.-h. Lee, Y. Shi, A. Hsu, M. L. Chin, L.-j. Li, M. Dubey, J. Kong, and T. Palacios, "Integrated circuits based on bilayer MoS2 transistors." Nano letters, vol. 12, no. 9, pp. 4674–80, sep 2012. [Online]. Available: http://www.ncbi.nlm.nih.gov/pubmed/22862813

[60] Z. Wang, M. Shaygan, M. Otto, D. Schall, and D. Neumaier, "Flexible Hall sensors based on graphene," Nanoscale, vol. 8, no. 14, pp. 7683–7687, 2016. [Online]. Available: http://xlink.rsc.org/?DOI=C5NR08729E

[61] S. J. Kim, K. Choi, B. Lee, Y. Kim, and B. H. Hong, "Materials for Flexible, Stretchable Electronics: Graphene and 2D Materials," Annual Review of Materials Research, vol. 45, no. 1, pp. 63–84, jul 2015. [Online]. Available: http://www.annualreviews.org/doi/abs/10.1146/annurev-matsci-070214-020901

[62] S. Garner, G. Merz, J. Tosch, C. Chang, D. Marshall, X. Li, J. Lin, C. Kuo, S. Lewis, R. Kohler, J. Matusick, C. Kang, G.-S. Huang, Y.-C. Shih, and C.-Y. Shih, "Flexible glass substrate for roll-to-roll manufacturing," 2011. [Online]. Available: http://www.aimcal.org/uploads/4/6/6/9/46695933/garner{_}abstract.pdf

[63] P. Shah, T. N. Narayanan, C.-Z. Li, and S. Alwarappan, "Probing the biocompatibility of MoS2 nanosheets by cytotoxicity assay and electrical impedance spectroscopy." Nanotechnology, vol. 26, no. 31, p. 315102, 2015. [Online]. Available: http://iopscience.iop.org/article/10.1088/0957-4484/26/31/315102

[64] B. Yu, N. Long, Y. Moussy, and F. Moussy, "A long-term flexible minimally-invasive implantable glucose biosensor based on an epoxy-enhanced polyurethane membrane," Biosensors and Bioelectronics, vol. 21, no. 12, pp. 2275–2282, jun 2006. [Online]. Available: http://linkinghub.elsevier.com/retrieve/pii/S0956566305003544

[65] J. H. Appel, D. O. Li, J. D. Podlevsky, A. Debnath, A. A. Green, Q. H. Wang, and J. Chae, "Low Cytotoxicity and Genotoxicity of Two-Dimensional MoS 2 and WS 2," ACS Biomaterials Science & Engineering, vol. 2, no. 3, pp. 361–367, mar 2016. [Online]. Available: http://pubs.acs.org/doi/abs/10.1021/acsbiomaterials.5b00467

[66] H. Wu, R. Yang, B. Song, Q. Han, J. Li, Y. Zhang, Y. Fang, R. Tenne, and C. Wang, "Biocompatible Inorganic Fullerene-Like Molybdenum Disulfide Nanoparticles Produced by Pulsed Laser Ablation in Water," ACS Nano, vol. 5, no. 2, pp. 1276–1281, feb 2011. [Online]. Available: http://pubs.acs.org/doi/abs/10.1021/nn102941b

[67] M. Pumera, "Graphene in biosensing," Materials Today, vol. 14, no. 7-8, pp. 308–315, jul 2011. [Online]. Available: http://linkinghub.elsevier.com/retrieve/pii/S1369702111701602

[68] Y. H. Kwak, D. S. Choi, Y. N. Kim, H. Kim, D. H. Yoon, S.-S. Ahn, J.-W. Yang, W. S. Yang, and S. Seo, "Flexible glucose sensor using CVD-grown graphene-based field effect transistor," Biosensors and Bioelectronics, vol. 37, no. 1, pp. 82–87, aug 2012. [Online]. Available: http://linkinghub.elsevier.com/retrieve/pii/S0956566312002710

[69] X. Dong, Y. Shi, W. Huang, P. Chen, and L.-J. Li, "Electrical detection of DNA hybridization with single-base specificity using transistors based on CVD-grown graphene sheets." Advanced materials (Deerfield Beach, Fla.), vol. 22, no. 14, pp. 1649–53, may 2010. [Online]. Available: http://www.ncbi.nlm.nih.gov/pubmed/20496398

[70] D. Sarkar, W. Liu, X. Xie, A. C. Anselmo, S. Mitragotri, and K. Banerjee, "MoS 2 Field-Effect Transistor for Next-Generation Label-Free Biosensors," ACS Nano, vol. 8, no. 4, pp. 3992–4003, apr 2014. [Online]. Available: http://pubs.acs.org/doi/abs/10.1021/nn5009148

[71] L. Wang, Y. Wang, J. I. Wong, T. Palacios, J. Kong, and H. Y. Yang, "Functionalized MoS2 Nanosheet-Based Field-Effect Biosensor for Label-Free Sensitive Detection of Cancer Marker Proteins in Solution," Small, vol. 10, no. 6, pp. 1101–1105, mar 2014. [Online]. Available: http://doi.wiley.com/10.1002/smll.201302081

[72] S. Furman, "Implantable cardiac pacemakers: Status report and resource guideline," The American Journal of Cardiology, vol. 34, no. 4, pp. 487–500, oct 1974. [Online]. Available: http://linkinghub.elsevier.com/retrieve/pii/000291497490023X

[73] F. G. Zeng, S. Rebscher, W. Harrison, X. Sun, and H. Feng, "Cochlear implants: system design, integration, and evaluation." IEEE reviews in biomedical engineering, vol. 1, no. dc, pp. 115–142, 2008.

[74] H. Neves, "Materials for implantable systems," in Implantable Sensor Systems for Medical Applications. Elsevier, 2013, pp. 3–38. [Online]. Available: http://linkinghub.elsevier.com/retrieve/pii/B9781845699871500016

[75] M. Lei, A. Baldi, E. Nuxoll, R. A. Siegel, and B. Ziaie, "A Hydrogel-Based Implantable Micromachined Transponder for Wireless Glucose Measurement," Diabetes Technology & Therapeutics, vol. 8, no. 1, pp. 112–122, feb 2006. [Online]. Available: http://online.liebertpub.com/doi/abs/10.1089/dia.2006.8.112

[76] B. Yu, C. Wang, Y. M. Ju, L. West, J. Harmon, Y. Moussy, and F. Moussy, "Use of hydrogel coating to improve the performance of implanted glucose sensors," Biosensors and Bioelectronics, vol. 23, no. 8, pp. 1278–1284, mar 2008. [Online]. Available: http://linkinghub.elsevier.com/retrieve/pii/S0956566307004800

[77] M. Lei, A. Baldi, E. Nuxoll, R. A. Siegel, and B. Ziaie, "Hydrogel-based microsensors for wireless chemical monitoring," Biomedical Microdevices, vol. 11, no. 3, pp. 529–538, jun 2009. [Online]. Available: http://link.springer.com/10.1007/s10544-008-9168-5

[78] Y. M. Ju, B. Yu, L. West, Y. Moussy, and F. Moussy, "A novel porous collagen scaffold around an implantable biosensor for improving biocompatibility. II. Long-term in vitro / in vivo sensitivity characteristics of sensors with NDGA- or GA-crosslinked collagen scaffolds," Journal of Biomedical Materials Research Part A, vol. 9999A, no. 2, pp. NA–NA, 2009. [Online]. Available: http://doi.wiley.com/10.1002/jbm.a.32400

[79] T. R. Hoare and D. S. Kohane, "Hydrogels in drug delivery: Progress and challenges," Polymer, vol. 49, no. 8, pp. 1993–2007, apr 2008. [Online]. Available: http://www.sciencedirect.com/science/article/pii/S0032386108000487

[80] S. P. Nichols, A. Koh, W. L. Storm, J. H. Shin, and M. H. Schoenfisch, "Biocompatible Materials for Continuous Glucose Monitoring Devices," Chemical Reviews, vol. 113, no. 4, pp. 2528–2549, apr 2013. [Online]. Available: http://pubs.acs.org/doi/abs/10.1021/cr300387j

[81] E. Caló and V. V. Khutoryanskiy, "Biomedical applications of hydrogels: A review of patents and commercial products," European Polymer Journal, vol. 65, pp. 252–267, apr 2015. [Online]. Available: http://linkinghub.elsevier.com/retrieve/pii/S0014305714004091

[82] Y. J. Heo, H. Shibata, T. Okitsu, T. Kawanishi, and S. Takeuchi, "Long-term in vivo glucose monitoring using fluorescent hydrogel fibers," Proceedings of the National Academy of Sciences, vol. 108, no. 33, pp. 13 399–13 403, aug 2011. [Online]. Available: http://www.pnas.org/cgi/doi/10.1073/pnas.1104954108

[83] K. Deligkaris, T. S. Tadele, W. Olthuis, and A. van den Berg, "Hydrogel based devices for biomedical applications," Sensors and Actuators B: Chemical, vol. 147, no. 2, pp. 765–774, jun 2010. [Online]. Available: http://linkinghub.elsevier.com/retrieve/pii/S0925400510003096

[84] G. Gerlach, M. Guenther, J. Sorber, G. Suchaneck, K.-F. Arndt, and A. Richter, "Chemical and pH sensors based on the swelling behavior of hydrogels," Sensors and Actuators B: Chemical, vol. 111-112, pp. 555–561, nov 2005. [Online]. Available: http://linkinghub.elsevier.com/retrieve/pii/S092540050500328X

[85] M. Guenther, G. Gerlach, and T. Wallmersperger, "Non-linear Effects in Hydrogel-based Chemical Sensors: Experiment and Modeling," Journal of Intelligent Material Systems and Structures, vol. 20, no. 8, pp. 949–961, may 2009. [Online]. Available: http://jim.sagepub.com/cgi/doi/10.1177/1045389X08101562

[86] M. Guenther, D. Kuckling, C. Corten, G. Gerlach, J. Sorber, G. Suchaneck, and K. Arndt, "Chemical sensors based on multiresponsive block copolymer hydrogels," Sensors and Actuators B: Chemical, vol. 126, no. 1, pp. 97–106, sep 2007. [Online]. Available: http://linkinghub.elsevier.com/retrieve/pii/S092540050600743X

[87] S. Herber, J. Eijkel, W. Olthuis, P. Bergveld, and A. van den Berg, "Study of chemically induced pressure generation of hydrogels under isochoric conditions using a microfabricated device," The Journal of Chemical Physics, vol. 121, no. 6, p. 2746, 2004. [Online]. Available: http://scitation.aip.org/content/aip/journal/jcp/121/6/10.1063/1.1773153

[88] M. Lei, A. Baldi, T. Pan, Y. Gu, R. Siegel, and B. Ziaie, "A hydrogel-based wireless chemical sensor," in 17th IEEE International Conference on Micro Electro Mechanical Systems. Maastricht MEMS 2004 Technical Digest. IEEE, 2004, pp. 391–394. [Online]. Available: http://ieeexplore.ieee.org/lpdocs/epic03/wrapper.htm?arnumber=1290604

[89] C. Zhang, G. G. Cano, and P. V. Braun, "Linear and fast hydrogel glucose sensor materials enabled by volume resetting agents." Advanced materials (Deerfield Beach, Fla.), vol. 26, no. 32, pp. 5678–83, aug 2014. [Online]. Available: http://www.ncbi.nlm.nih.gov/pubmed/25042106

[90] C. Zhang, M. D. Losego, and P. V. Braun, "Hydrogel-Based Glucose Sensors: Effects of Phenylboronic Acid Chemical Structure on Response," Chemistry of Materials, vol. 25, no. 15, pp. 3239–3250, aug 2013. [Online]. Available: http://pubs.acs.org/doi/abs/10.1021/cm401738p

[91] T. Miyata, N. Asami, and T. Uragami, "A reversibly antigen-responsive hydrogel." Nature, vol. 399, no. 6738, pp. 766–9, jun 1999. [Online]. Available: http://dx.doi.org/10.1038/21619

[92] M. S. Makowski and A. Ivanisevic, "Molecular analysis of blood with micro-/nanoscale field-effect-transistor biosensors." Small (Weinheim an der Bergstrasse, Germany), vol. 7, no. 14, pp. 1863–75, jul 2011. [Online]. Available: http://www.pubmedcentral.nih.gov/articlerender.fcgi?artid=3876889{&}tool=pmcentrez{&}rendertype=abstract

[93] D. Sarkar and K. Banerjee, "Proposal for tunnel-field-effect-transistor as ultra-sensitive and label-free biosensors," Applied Physics Letters, vol. 100, no. 14, p. 143108, 2012. [Online]. Available: http://link.aip.org/link/APPLAB/v100/i14/p143108/s1{&}Agg=doi

[94] E. Stern, J. F. Klemic, D. a. Routenberg, P. N. Wyrembak, D. B. Turner-Evans, A. D. Hamilton, D. a. LaVan, T. M. Fahmy, and M. a. Reed, "Label-free immunodetection with CMOS-compatible semiconducting nanowires," Nature, vol. 445, no. 7127, pp. 519–522, feb 2007. [Online]. Available: http://www.nature.com/doifinder/10.1038/nature05498

[95] G. Massobrio, S. Martinoia, and M. Grattarola, "Ion Sensitive Field Effect Transistor (ISFET) Model Implemented in SPICE," Simulation of Semiconductor Devices and Processes, vol. 4, 1991. [Online]. Available: http://in4.iue.tuwien.ac.at/pdfs/sisdep1991/pdfs/Massobrio{_}62.pdf

[96] M. Grattarola, G. Massobrio, and S. Martinoia, "Modeling H+ - sensitive FETs with SPICE," IEEE Transactions on Electron Devices, vol. 39, no. 4, pp. 813–819, apr 1992. [Online]. Available: http://ieeexplore.ieee.org/lpdocs/epic03/wrapper.htm?arnumber=127470

[97] S. Martinoia, M. Grattarola, and G. Massobrio, "Modelling non-ideal behaviours in H+-sensitive FETs with SPICE," Sensors and Actuators B: Chemical, vol. 7, no. 1-3, pp. 561–564, mar 1992. [Online]. Available: http://linkinghub.elsevier.com/retrieve/pii/0925400592803644

[98] P. G. Fernandes, H. J. Stiegler, M. Zhao, K. D. Cantley, B. Obradovic, R. a. Chapman, H.-C. Wen, G. Mahmud, and E. M. Vogel, "SPICE macromodel of silicon-on-insulator-field-effect-transistor-based biological sensors," Sensors and Actuators B: Chemical, vol. 161, no. 1, pp. 163–170, jan 2012. [Online]. Available: http://linkinghub.elsevier.com/retrieve/pii/S092540051100894X

[99] P. Livi, K. Bedner, A. Tarasov, M. Wipf, Y. Chen, C. Schönenberger, and A. Hierlemann, "A Verilog-A model for silicon nanowire biosensors: From theory to verification," Sensors and Actuators B: Chemical, vol. 179, pp. 293–300, mar 2013. [Online]. Available: http://linkinghub.elsevier.com/retrieve/pii/S0925400512009380

[100] P. Dak, A. Ebrahimi, and M. A. Alam, "Non-faradaic impedance characterization of an evaporating droplet for microfluidic and biosensing applications," Lab Chip, vol. 14, no. 14, pp. 2469–2479, jul 2014. [Online]. Available: http://xlink.rsc.org/?DOI=C4LC00193A

[101] V. V. Swaminathan, P. Dak, B. Reddy Jr., E. Salm, C. D. Guevara, Y. Zhong, J. C. Huang, J. H. Hang, Y.-S. Liu, A. Fischer, M. A. Alam, and R. Bashir, "Localized Electronic Desalting Around Field-Effect Sensors for Molecular Detection In Droplets With Enhanced Sensitivity," in IEEE Engineering in Medicine and Biology Society, 2014. [Online]. Available: http://emb.citengine.com/event/embc-2014/paper-details?pdID=1083

[102] E. Salm, C. D. Guevara, P. Dak, B. R. Dorvel, B. Reddy, M. A. Alam, and R. Bashir, "Ultralocalized thermal reactions in subnanoliter droplets-in-air," Proceedings of the National Academy of Sciences, vol. 110, no. 9, pp. 3310–3315, feb 2013. [Online]. Available: http://www.pubmedcentral.nih.gov/articlerender.fcgi?artid=3587226{&}tool=pmcentrez{&}rendertype=abstracthttp://www.pnas.org/lookup/doi/10.1073/pnas.1219639110

[103] P. Dak and M. A. Alam, "Predictive model for hydrogel based wireless implantable bio-chemical sensors," in 2015 73rd Annual Device Research Conference (DRC). IEEE, jun 2015, pp. 229–230. [Online]. Available: http://ieeexplore.ieee.org/lpdocs/epic03/wrapper.htm?arnumber=7175650

[104] P. Dak and M. A. Alam, "Numerical and Analytical Modeling to Determine Performance Tradeoffs in Hydrogel-Based pH Sensors," IEEE Transactions on Electron Devices, vol. 63, no. 6, pp. 2524–2530, 2016. [Online]. Available: http://ieeexplore.ieee.org/stamp/stamp.jsp?arnumber=7466865

[105] P. Dak and M. A. Alam, "FET pH Sensor Model 1.0.1," 2014. [Online]. Available: https://nanohub.org/publications/11/1

[106] V. V. Swaminathan, P. Dak, B. Reddy, E. Salm, C. Duarte-Guevara, Y. Zhong, A. Fischer, Y.-S. Liu, M. A. Alam, and R. Bashir, "Electronic desalting for controlling the ionic environment in droplet-based biosensing platforms," Applied Physics Letters, vol. 106, no. 5, p. 053105, feb 2015. [Online]. Available: http://scitation.aip.org/content/aip/journal/apl/106/5/10.1063/1.4907351

[107] M. A. Alam, P. Dak, M. A. Wahab, and X. Sun, "Physics-based compact models for insulated-gate field-effect biosensors, landau-transistors, and thin-film solar cells," in 2015 IEEE Custom Integrated Circuits Conference (CICC). IEEE, sep 2015, pp. 1–8. [Online]. Available: http://ieeexplore.ieee.org/lpdocs/epic03/wrapper.htm?arnumber=7338406

[108] P. Dak and M. A. Alam, "Electrostatic desalting of micro-droplets to enable novel chemical/biosensing applications," in 72nd Device Research Conference, vol. 232, no. 2. IEEE, jun 2014, pp. 275–276. [Online]. Available: http://ieeexplore.ieee.org/lpdocs/epic03/wrapper.htm?arnumber=6872404

[109] P. Dak, P. Nair, J. Go, and M. A. Alam, "Extended-gate biosensors achieve fluid stability with no loss in charge sensitivity," in 71st Device Research Conference, vol. 20, no. 2003. IEEE, jun 2013, pp. 105–106. [Online]. Available: http://ieeexplore.ieee.org/lpdocs/epic03/wrapper.htm?arnumber=6633815

[110] P. Dak and M. A. Alam, "Non-Faradaic Impedance Model 1.0.0," 2015. [Online]. Available: https://nanohub.org/publications/81/1

[111] P. R. Nair, J. Go, G. J. Landells, T. R. Pandit, M. A. Alam, X. Jin, P. Dak, and A. Jain, "BioSensorLab," 2014. [Online]. Available: https://nanohub.org/resources/senstran

[112] A. Marmur, "The Lotus Effect: Superhydrophobicity and Metastability," Langmuir, vol. 20, no. 9, pp. 3517–3519, apr 2004. [Online]. Available: http://pubs.acs.org/doi/abs/10.1021/la036369u

[113] R. D. Deegan, O. Bakajin, T. F. Dupont, G. Huber, S. R. Nagel, and T. A. Witten, "No Title," Nature, vol. 389, no. 6653, pp. 827–829, oct 1997. [Online]. Available: http://www.nature.com/doifinder/10.1038/39827

[114] R. D. Deegan, "Pattern formation in drying drops," Physical Review E, vol. 61, no. 1, pp. 475–485, jan 2000. [Online]. Available: http://link.aps.org/doi/10.1103/PhysRevE.61.475

[115] P. J. Yunker, T. Still, M. A. Lohr, and A. G. Yodh, "Suppression of the coffee-ring effect by shape-dependent capillary interactions," Nature, vol. 476, no. 7360, pp. 308–311, aug 2011. [Online]. Available: http://www.nature.com/doifinder/10.1038/nature10344

[116] A. U. Chen and O. a. Basaran, "A new method for significantly reducing drop radius without reducing nozzle radius in drop-on-demand drop production," Physics of Fluids, vol. 14, no. 1, p. L1, 2002. [Online]. Available: http://link.aip.org/link/PHFLE6/v14/i1/pL1/s1{&}Agg=doi

[117] J. Berná, D. A. Leigh, M. Lubomska, S. M. Mendoza, E. M. Pérez, P. Rudolf, G. Teobaldi, and F. Zerbetto, "Macroscopic transport by synthetic molecular machines." Nature materials, vol. 4, no. 9, pp. 704–10, sep 2005. [Online]. Available: http://www.ncbi.nlm.nih.gov/pubmed/16127455

[118] L. Mazutis, J. Gilbert, W. L. Ung, D. a. Weitz, A. D. Griffiths, and J. a. Heyman, "Single-cell analysis and sorting using droplet-based microfluidics." Nature protocols, vol. 8, no. 5, pp. 870–91, may 2013. [Online]. Available: http://www.ncbi.nlm.nih.gov/pubmed/23558786

[119] J. Jing, J. Reed, J. Huang, X. Hu, V. Clarke, J. Edington, D. Housman, T. S. Anantharaman, E. J. Huff, B. Mishra, B. Porter, A. Shenker, E. Wolfson, C. Hiort, R. Kantor, C. Aston, and D. C. Schwartz, "Automated high resolution optical mapping using arrayed, fluid-fixed DNA molecules." Proceedings of the National Academy of Sciences of the United States of America, vol. 95, no. 14, pp. 8046–51, jul 1998. [Online]. Available: http://www.pubmedcentral.nih.gov/articlerender.fcgi?artid=20926{&}tool=pmcentrez{&}rendertype=abstract

[120] S. Thoroddsen, T. Etoh, and K. Takehara, "High-Speed Imaging of Drops and Bubbles," Annual Review of Fluid Mechanics, vol. 40, no. 1, pp. 257–285, jan 2008. [Online]. Available: http://www.annualreviews.org/doi/abs/10.1146/annurev.fluid.40.111406.102215

[121] S. Ghosh, S. Chattoraj, T. Mondal, and K. Bhattacharyya, "Dynamics in cytoplasm, nucleus, and lipid droplet of a live CHO cell: time-resolved confocal microscopy." Langmuir : the ACS journal of surfaces and colloids, vol. 29, no. 25, pp. 7975–82, jun 2013. [Online]. Available: http://www.ncbi.nlm.nih.gov/pubmed/23705762

[122] G. Chen, M. Mohiuddin Mazumder, R. K. Chang, J. Christian Swindal, and W. P. Acker, "Laser diagnostics for droplet characterization: Application of morphology dependent resonances," Progress in Energy and Combustion Science, vol. 22, no. 2, pp. 163–188, jan 1996. [Online]. Available: http://linkinghub.elsevier.com/retrieve/pii/0360128596000032

[123] a. R. Glover, S. M. Skippon, and R. D. Boyle, "Interferometric laser imaging for droplet sizing: a method for droplet-size measurement in sparse spray systems." Applied optics, vol. 34, no. 36, pp. 8409–21, dec 1995. [Online]. Available: http://www.ncbi.nlm.nih.gov/pubmed/21068962

[124] J.-G. Guan, Y.-Q. Miao, and Q.-J. Zhang, "Impedimetric biosensors." Journal of bioscience and bioengineering, vol. 97, no. 4, pp. 219–26, jan 2004. [Online]. Available: http://www.ncbi.nlm.nih.gov/pubmed/16233619

[125] S. Sadeghi, H. Ding, G. J. Shah, S. Chen, P. Y. Keng, C.-J. Kim, and R. M. van Dam, "On chip droplet characterization: a practical, high-sensitivity measurement of droplet impedance in digital microfluidics." Analytical chemistry, vol. 84, no. 4, pp. 1915–23, feb 2012. [Online]. Available: http://www.ncbi.nlm.nih.gov/pubmed/22248060

[126] P. R. Nair and M. A. Alam, "Screening-Limited Response of NanoBiosensors," Nano Letters, vol. 8, no. 5, pp. 1281–1285, may 2008. [Online]. Available: http://pubs.acs.org/doi/abs/10.1021/nl072593i

[127] A. J. Bard and L. R. Faulkner, Electrochemical Methods: Fundamentals and Applications. John Wiley & Sons, 2001. [Online]. Available: http://www.loc.gov/catdir/description/wiley031/00038210.html

[128] Y. Chen, B. He, J. Lee, and N. a. Patankar, "Anisotropy in the wetting of rough surfaces." Journal of colloid and interface science, vol. 281, no. 2, pp. 458–64, jan 2005. [Online]. Available: http://www.ncbi.nlm.nih.gov/pubmed/15571703

[129] L. J. Lin, S. Y., Chuang, Y. C., Yang, Y. J., Chen, "Evaporation of a Liquid Drop Deposited On a Chemically Heterogeneous Striped Surface," in AIChE, 2013 Annual Meeting, 2013. [Online]. Available: http://www3.aiche.org/proceedings/Abstract.aspx?PaperID=333505

[130] K. Brakke, "Surface Evolver," http://www.susqu.edu/brakke/evolver/evolver.html, pp. Surface Evolver, version 2.70, Susquehanna Univers. [Online]. Available: http://www.susqu.edu/brakke/evolver/evolver.html

[131] J. E. B. Randles, "Kinetics of rapid electrode reactions," Discussions of the Faraday Society, vol. 1, p. 11, 1947. [Online]. Available: http://xlink.rsc.org/?DOI=df9470100011

[132] "Sentaurus, version H-2013.03," pp. Sentaurus, version H–2013.03, United States, 2013. [Online]. Available: http://www.synopsys.com/Tools/TCAD/DeviceSimulation/Pages/SentaurusDevice.aspx

[133] R. van Hal, J. Eijkel, and P. Bergveld, "A general model to describe the electrostatic potential at electrolyte oxide interfaces," Advances in Colloid and Interface Science, vol. 69, no. 1-3, pp. 31–62, dec 1996. [Online]. Available: http://linkinghub.elsevier.com/retrieve/pii/S0001868696003077

[134] D. C. Grahame, "The Electrical Double Layer and the Theory of Electrocapillarity." Chemical Reviews, vol. 41, no. 3, pp. 441–501, dec 1947. [Online]. Available: http://pubs.acs.org/doi/abs/10.1021/cr60130a002

[135] J. Hong, D. S. Yoon, S. K. Kim, T. S. Kim, S. Kim, E. Y. Pak, and K. No, "AC frequency characteristics of coplanar impedance sensors as design parameters." Lab on a chip, vol. 5, no. 3, pp. 270–9, mar 2005. [Online]. Available: http://www.ncbi.nlm.nih.gov/pubmed/15726203

[136] S. M. Rowan, M. I. Newton, and G. McHale, "Evaporation of Microdroplets and the Wetting of Solid Surfaces," The Journal of Physical Chemistry, vol. 99, no. 35, pp. 13 268–13 271, aug 1995. [Online]. Available: http://pubs.acs.org/doi/abs/10.1021/j100035a034

[137] K. S. Birdi, D. T. Vu, and A. Winter, "A study of the evaporation rates of small water drops placed on a solid surface," The Journal of Physical Chemistry, vol. 93, no. 9, pp. 3702–3703, may 1989. [Online]. Available: http://pubs.acs.org/doi/abs/10.1021/j100346a065

[138] R. Picknett and R. Bexon, "The evaporation of sessile or pendant drops in still air," Journal of Colloid and Interface Science, vol. 61, no. 2, pp. 336–350, sep 1977. [Online]. Available: http://linkinghub.elsevier.com/retrieve/pii/0021979777903964

[139] J. D. Jackson, "Charge density on thin straight wire, revisited," American Journal of Physics, vol. 68, no. 9, p. 789, 2000. [Online]. Available: http://link.aip.org/link/AJPIAS/v68/i9/p789/s1{&}Agg=doi

[140] Z. Pan, J. A. Weibel, and S. V. Garimella, "Influence of Surface Wettability on Transport Mechanisms Governing Water Droplet Evaporation," Langmuir, vol. 30, no. 32, pp. 9726–9730, aug 2014. [Online]. Available: http://pubs.acs.org/doi/abs/10.1021/la501931x

[141] S. Dash and S. V. Garimella, "Droplet evaporation dynamics on a superhydrophobic surface with negligible hysteresis." Langmuir : the ACS journal of surfaces and colloids, vol. 29, no. 34, pp. 10 785–95, aug 2013. [Online]. Available: http://www.ncbi.nlm.nih.gov/pubmed/23952149

[142] L. Coury, "Conductance Measurements Part 1 : Theory," Current Separations, vol. 18, no. 3, 1999. [Online]. Available: http://www.currentseparations.com/issues/18-3/cs18-3c.pdf

[143] S. Ramo, J. R. Whinnery, and T. V. Duzer, Fields and Waves in Communication Electronics. Wiley, 1994, vol. 2. [Online]. Available: http://www.loc.gov/catdir/description/wiley032/93034415.html

[144] C. Gabriel, S. Gabriel, E. H. Grant, E. H. Grant, B. S. J. Halstead, and D. Michael P. Mingos, "Dielectric parameters relevant to microwave dielectric heating," Chemical Society Reviews, vol. 27, no. 3, p. 213, 1998. [Online]. Available: http://xlink.rsc.org/?DOI=a827213z

[145] J. L. Sang-Joon and N. Sundararajan, Microfabrication for Microfluidics, 2010th ed. Artech house, 2010. [Online]. Available: http://www.artechhouse.com/Main/Books/Microfabrication-for-Microfluidics-1509.aspx

[146] T. Hiemstra and W. Van Riemsdijk, "Physical chemical interpretation of primary charging behaviour of metal (hydr) oxides," Colloids and Surfaces, vol. 59, pp. 7–25, nov 1991. [Online]. Available: http://linkinghub.elsevier.com/retrieve/pii/016666229180233E

[147] J. Wei, "Distributed capacitance of planar electrodes in optic and acoustic surface wave devices," IEEE Journal of Quantum Electronics, vol. 13, no. 4, pp. 152–158, apr 1977. [Online]. Available: http://ieeexplore.ieee.org/lpdocs/epic03/wrapper.htm?arnumber=1069319

[148] G. K. Celler and S. Cristoloveanu, "Frontiers of silicon-on-insulator," Journal of Applied Physics, vol. 93, no. 9, p. 4955, 2003. [Online]. Available: http://link.aip.org/link/JAPIAU/v93/i9/p4955/s1{&}Agg=doi

[149] Y.-S. Liu, P. P. Banada, S. Bhattacharya, A. K. Bhunia, and R. Bashir, "Electrical characterization of DNA molecules in solution using impedance measurements," Applied Physics Letters, vol. 92, no. 14, p. 143902, 2008. [Online]. Available: http://link.aip.org/link/APPLAB/v92/i14/p143902/s1{&}Agg=doi

[150] S. Takashima, C. Gabriel, R. Sheppard, and E. Grant, "Dielectric behavior of DNA solution at radio and microwave frequencies (at 20 degrees C)," Biophysical Journal, vol. 46, no. 1, pp. 29–34, jul 1984. [Online]. Available: http://linkinghub.elsevier.com/retrieve/pii/S0006349584839958

[151] S. Tomić, S. D. Babić, T. Vuletić, S. Krča, D. Ivanković, L. Griparić, and R. Podgornik, "Dielectric relaxation of DNA aqueous solutions," Physical Review E - Statistical, Nonlinear, and Soft Matter Physics, vol. 75, no. 2, pp. 1–13, 2007.

[152] Y. Cui, "Nanowire Nanosensors for Highly Sensitive and Selective Detection of Biological and Chemical Species," Science, vol. 293, no. 5533, pp. 1289–1292, aug 2001. [Online]. Available: http://www.sciencemag.org/cgi/doi/10.1126/science.1062711

[153] Y. L. Bunimovich, Y. S. Shin, W.-S. Yeo, M. Amori, G. Kwong, and J. R. Heath, "Quantitative Real-Time Measurements of DNA Hybridization with Alkylated Nonoxidized Silicon Nanowires in Electrolyte Solution," Journal of the American Chemical Society, vol. 128, no. 50, pp. 16 323–16 331, dec 2006. [Online]. Available: http://www.ncbi.nlm.nih.gov/pubmed/17165787http://pubs.acs.org/doi/abs/10.1021/ja065923u

[154] B. R. Dorvel, B. Reddy, J. Go, C. Duarte Guevara, E. Salm, M. A. Alam, and R. Bashir, "Silicon Nanowires with High-k Hafnium Oxide Dielectrics for Sensitive Detection of Small Nucleic Acid Oligomers," ACS Nano, vol. 6, no. 7, pp. 6150–6164, jul 2012. [Online]. Available: http://pubs.acs.org/doi/abs/10.1021/nn301495k

[155] A. Gao, N. Lu, Y. Wang, P. Dai, T. Li, X. Gao, Y. Wang, and C. Fan, "Enhanced Sensing of Nucleic Acids with Silicon Nanowire Field Effect Transistor Biosensors," Nano Letters, vol. 12, no. 10, pp. 5262–5268, oct 2012. [Online]. Available: http://pubs.acs.org/doi/abs/10.1021/nl302476h

[156] G.-J. Zhang, J. H. Chua, R.-E. Chee, A. Agarwal, and S. M. Wong, "Label-free direct detection of MiRNAs with silicon nanowire biosensors," Biosensors and Bioelectronics, vol. 24, no. 8, pp. 2504–2508, apr 2009. [Online]. Available: http://linkinghub.elsevier.com/retrieve/pii/S0956566308006933

[157] G. Zheng, F. Patolsky, Y. Cui, W. U. Wang, and C. M. Lieber, "Multiplexed electrical detection of cancer markers with nanowire sensor arrays," Nature Biotechnology, vol. 23, no. 10, pp. 1294–1301, oct 2005. [Online]. Available: http://www.nature.com/doifinder/10.1038/nbt1138

[158] F. N. Ishikawa, H.-K. Chang, M. Curreli, H.-I. Liao, C. A. Olson, P.-C. Chen, R. Zhang, R. W. Roberts, R. Sun, R. J. Cote, M. E. Thompson, and C. Zhou, "Label-Free, Electrical Detection of the SARS Virus N-Protein with Nanowire Biosensors Utilizing Antibody Mimics as Capture Probes," ACS Nano, vol. 3, no. 5, pp. 1219–1224, may 2009. [Online]. Available: http://pubs.acs.org/doi/abs/10.1021/nn900086c

[159] F. Patolsky, G. Zheng, O. Hayden, M. Lakadamyali, X. Zhuang, and C. M. Lieber, "Electrical detection of single viruses," Proceedings of the National Academy of Sciences, vol. 101, no. 39, pp. 14 017–14 022, sep 2004. [Online]. Available: http://www.pnas.org/cgi/doi/10.1073/pnas.0406159101

[160] B. Reddy, B. R. Dorvel, J. Go, P. R. Nair, O. H. Elibol, G. M. Credo, J. S. Daniels, E. K. C. Chow, X. Su, M. Varma, M. A. Alam, and R. Bashir, "High-K dielectric Al2O3 nanowire and nanoplate field effect sensors for improved pH sensing," Biomedical Microdevices, vol. 13, no. 2, pp. 335–344, apr 2011. [Online]. Available: http://link.springer.com/10.1007/s10544-010-9497-z

[161] J.-H. Ahn, S.-J. Choi, J.-W. Han, T. J. Park, S. Y. Lee, and Y.-K. Choi, "Double-gate nanowire field effect transistor for a biosensor." Nano letters, vol. 10, no. 8, pp. 2934–8, aug 2010. [Online]. Available: http://www.ncbi.nlm.nih.gov/pubmed/20698606

[162] J.-H. Ahn, J.-Y. Kim, M.-L. Seol, D. J. Baek, Z. Guo, C.-H. Kim, S.-J. Choi, and Y.-K. Choi, "A pH sensor with a double-gate silicon nanowire field-effect transistor," Applied Physics Letters, vol. 102, no. 8, p. 083701, 2013. [Online]. Available: http://scitation.aip.org/content/aip/journal/apl/102/8/10.1063/1.4793655

[163] P. Bergveld, "The development and application of FET-based biosensors," Biosensors, vol. 2, no. 1, pp. 15–33, jan 1986. [Online]. Available: http://linkinghub.elsevier.com/retrieve/pii/0265928X86850106

[164] P. Bergveld, "Thirty years of ISFETOLOGY," Sensors and Actuators B: Chemical, vol. 88, no. 1, pp. 1–20, jan 2003. [Online]. Available: http://linkinghub.elsevier.com/retrieve/pii/S0925400502003015

[165] J. Go and M. a. Alam, "The future scalability of pH-based genome sequencers: A theoretical perspective," Journal of Applied Physics, vol. 114, no. 16, p. 164311, 2013. [Online]. Available: http://scitation.aip.org/content/aip/journal/jap/114/16/10.1063/1.4825119

[166] S. Purushothaman, C. Toumazou, and C.-P. Ou, "Protons and single nucleotide polymorphism detection: A simple use for the Ion Sensitive Field Effect Transistor," Sensors and Actuators B: Chemical, vol. 114, no. 2, pp. 964–968, apr 2006. [Online]. Available: http://linkinghub.elsevier.com/retrieve/pii/S0925400505007409

[167] D. L. Chapman, "LI. A contribution to the theory of electrocapillarity," Philosophical Magazine Series 6, vol. 25, no. 148, pp. 475–481, apr 1913. [Online]. Available: http://www.tandfonline.com/doi/abs/10.1080/14786440408634187

[168] A. V. Delgado, F. González-Caballero, R. J. Hunter, L. K. Koopal, and J. Lyklema, "Measurement and Interpretation of Electrokinetic Phenomena (IUPAC Technical Report)," Pure and Applied Chemistry, vol. 77, no. 10, pp. 1753–1805, jan 2005. [Online]. Available: http://www.degruyter.com/view/j/pac.2005.77.issue-10/pac200577101753/pac200577101753.xml

[169] M. Gouy, "Sur la constitution de la charge électrique à la surface d'un électrolyte," Journal de Physique Théorique et Appliquée, vol. 9, no. 1, pp. 457–468, 1910. [Online]. Available: http://www.edpsciences.org/10.1051/jphystap:019100090045700

[170] P. Debye and E. Hückel, "Zur Theorie der Elektrolyte. I. Gefrierpunktserniedrigung und verwandte Erscheinungen," Physikalische Zeitschrift, vol. 24, no. 9, pp. 185–206, 1923.

[171] P. R. Nair and M. A. Alam, "Design Considerations of Silicon Nanowire Biosensors," IEEE Transactions on Electron Devices, vol. 54, no. 12, pp. 3400–3408, 2007. [Online]. Available: http://ieeexplore.ieee.org/lpdocs/epic03/wrapper.htm?arnumber=4383044

[172] M. H. Sorensen, N. A. Mortensen, and M. Brandbyge, "Screening model for nanowire surface-charge sensors in liquid," Applied Physics Letters, vol. 91, no. 10, p. 102105, 2007. [Online]. Available: http://scitation.aip.org/content/aip/journal/apl/91/10/10.1063/1.2779930

[173] H. K. Cammenga, F. W. Schulze, and W. Theuerl, "Vapor pressure and evaporation coefficient of glycerol," Journal of Chemical & Engineering Data, vol. 22, no. 2, pp. 131–134, apr 1977. [Online]. Available: http://pubs.acs.org/doi/abs/10.1021/je60073a004

[174] J.-H. Lee, W.-S. Bae, and J.-H. Choi, "Electrode reactions and adsorption/desorption performance related to the applied potential in a capacitive deionization process," Desalination, vol. 258, no. 1-3, pp. 159–163, aug 2010. [Online]. Available: http://linkinghub.elsevier.com/retrieve/pii/S0011916410001554

[175] M. S. Kilic, M. Z. Bazant, and A. Ajdari, "Steric effects in the dynamics of electrolytes at large applied voltages. I. Double-layer charging," Physical Review E, vol. 75, no. 2, p. 021502, feb 2007. [Online]. Available: http://link.aps.org/doi/10.1103/PhysRevE.75.021502

[176] J. Drelich, E. Chibowski, D. D. Meng, and K. Terpilowski, "Hydrophilic and superhydrophilic surfaces and materials," Soft Matter, vol. 7, no. 21, p. 9804, 2011. [Online]. Available: http://xlink.rsc.org/?DOI=c1sm05849e

[177] R. Jayashree, J. Spendelow, J. Yeom, C. Rastogi, M. Shannon, and P. Kenis, "Characterization and application of electrodeposited Pt, Pt/Pd, and Pd catalyst structures for direct formic acid micro fuel cells," Electrochimica Acta, vol. 50, no. 24, pp. 4674–4682, aug 2005. [Online]. Available: http://linkinghub.elsevier.com/retrieve/pii/S0013468605001957

[178] L. Zhu, N. Kroodsma, J. Yeom, J. L. Haan, M. A. Shannon, and D. D. Meng, "An on-demand microfluidic hydrogen generator with self-regulated gas generation and self-circulated reactant exchange with a rechargeable reservoir," Microfluidics and Nanofluidics, vol. 11, no. 5, pp. 569–578, nov 2011. [Online]. Available: http://link.springer.com/10.1007/s10404-011-0822-5

[179] E. Barsoukov and J. R. Macdonald, Eds., Impedance spectroscopy: theory, experiment, and applications, 2nd ed. Hoboken: Wiley-Interscience, 2005.

[180] F. Heer, W. Franks, A. Blau, S. Taschini, C. Ziegler, A. Hierlemann, and H. Baltes, "CMOS microelectrode array for the monitoring of electrogenic cells," Biosensors and Bioelectronics, vol. 20, no. 2, pp. 358–366, sep 2004. [Online]. Available: http://linkinghub.elsevier.com/retrieve/pii/S0956566304000806

[181] J. Kang, J. Wen, S. H. Jayaram, A. Yu, and X. Wang, "Development of an equivalent circuit model for electrochemical double layer capacitors (EDLCs) with distinct electrolytes," Electrochimica Acta, vol. 115, pp. 587–598, jan 2014. [Online]. Available: http://linkinghub.elsevier.com/retrieve/pii/S0013468613021890

[182] L. Qiang, S. Vaddiraju, J. F. Rusling, and F. Papadimitrakopoulos, "Highly sensitive and reusable Pt-black microfluidic electrodes for long-term electrochemical sensing," Biosensors and Bioelectronics, vol. 26, no. 2, pp. 682–688, oct 2010. [Online]. Available: http://linkinghub.elsevier.com/retrieve/pii/S0956566310003659

[183] R. Owczarzy, Y. You, B. G. Moreira, J. a. Manthey, L. Huang, M. a. Behlke, and J. a. Walder, "Effects of Sodium Ions on DNA Duplex Oligomers: Improved Predictions of Melting Temperatures," Biochemistry, vol. 43, no. 12, pp. 3537–3554, mar 2004. [Online]. Available: http://pubs.acs.org/doi/abs/10.1021/bi034621r

[184] B. J. Hindson, K. D. Ness, D. a. Masquelier, P. Belgrader, N. J. Heredia, A. J. Makarewicz, I. J. Bright, M. Y. Lucero, A. L. Hiddessen, T. C. Legler, T. K. Kitano, M. R. Hodel, J. F. Petersen, P. W. Wyatt, E. R. Steenblock, P. H. Shah, L. J. Bousse, C. B. Troup, J. C. Mellen, D. K. Wittmann, N. G. Erndt, T. H. Cauley, R. T. Koehler, A. P. So, S. Dube, K. a. Rose, L. Montesclaros, S. Wang, D. P. Stumbo, S. P. Hodges, S. Romine, F. P. Milanovich, H. E. White, J. F. Regan, G. a. Karlin-Neumann, C. M. Hindson, S. Saxonov, and B. W. Colston, "High-Throughput Droplet Digital PCR System for Absolute Quantitation of DNA Copy Number," Analytical Chemistry, vol. 83, no. 22, pp. 8604–8610, nov 2011. [Online]. Available: http://pubs.acs.org/doi/abs/10.1021/ac202028g

[185] G. Maltezos, M. Johnston, and A. Scherer, "Thermal management in microfluidics using micro-Peltier junctions," Applied Physics Letters, vol. 87, no. 15, p. 154105, 2005. [Online]. Available: http://link.aip.org/link/APPLAB/v87/i15/p154105/s1{&}Agg=doi

[186] I. Park, Z. Li, A. P. Pisano, and R. S. Williams, "Selective Surface Functionalization of Silicon Nanowires via Nanoscale Joule Heating," Nano Letters, vol. 7, no. 10, pp. 3106–3111, oct 2007. [Online]. Available: http://www.ncbi.nlm.nih.gov/pubmed/17894518http://pubs.acs.org/doi/abs/10.1021/nl071637k

[187] C.-Y. Lee, G.-B. Lee, J.-L. Lin, F.-C. Huang, and C.-S. Liao, "Integrated microfluidic systems for cell lysis, mixing/pumping and DNA amplification," Journal of Micromechanics and Microengineering, vol. 15, no. 6, pp. 1215–1223, jun 2005. [Online]. Available: http://stacks.iop.org/0960-1317/15/i=6/a=011?key=crossref.fb6eb8deb5a8333c2aacc8ff148d6812

[188] B. Giordano, J. Ferrance, S. Swedberg, A. Hühmer, and J. Landers, "Polymerase Chain Reaction in Polymeric Microchips: DNA Amplification in Less Than 240 Seconds," Analytical Biochemistry, vol. 291, no. 1, pp. 124–132, apr 2001. [Online]. Available: http://www.ncbi.nlm.nih.gov/pubmed/11262165http://linkinghub.elsevier.com/retrieve/pii/S0003269700949741

[189] J. J. Shah, S. G. Sundaresan, J. Geist, D. R. Reyes, J. C. Booth, M. V. Rao, and M. Gaitan, "Microwave dielectric heating of fluids in an integrated microfluidic device," Journal of Micromechanics and Microengineering, vol. 17, no. 11, pp. 2224–2230, nov 2007. [Online]. Available: http://stacks.iop.org/0960-1317/17/i=11/a=008?key=crossref.ec7e1984c0781d1db17919f779da1f2a

[190] M. Graf, U. Frey, S. Taschini, and a. Hierlemann, "Micro hot plate-based sensor array system for the detection of environmentally relevant gases." Analytical chemistry, vol. 78, no. 19, pp. 6801–8, oct 2006. [Online]. Available: http://www.ncbi.nlm.nih.gov/pubmed/17007499

[191] D. Issadore, K. J. Humphry, K. a. Brown, L. Sandberg, D. a. Weitz, and R. M. Westervelt, "Microwave dielectric heating of drops in microfluidic devices." Lab on a chip, vol. 9, no. 12, pp. 1701–6, jun 2009. [Online]. Available: http://www.pubmedcentral.nih.gov/articlerender.fcgi?artid=2892413{&}tool=pmcentrez{&}rendertype=abstract

[192] H. Kim, S. Dixit, C. J. Green, and G. W. Faris, "Nanodroplet real-time PCR system with laser assisted heating," Optics Express, vol. 17, no. 1, p. 218, jan 2009. [Online]. Available: https://www.osapublishing.org/oe/abstract.cfm?uri=oe-17-1-218

[193] H. Kim, S. Vishniakou, and G. W. Faris, "Petri dish PCR: laser-heated reactions in nanoliter droplet arrays," Lab on a Chip, vol. 9, no. 9, p. 1230, may 2009. [Online]. Available: http://xlink.rsc.org/?DOI=b817288a

[194] H. Terazono, A. Hattori, H. Takei, K. Takeda, and K. Yasuda, "Development of 1480 nm Photothermal High-Speed Real-Time Polymerase Chain Reaction System for Rapid Nucleotide Recognition," Japanese Journal of Applied Physics, vol. 47, no. 6, pp. 5212–5216, jun 2008. [Online]. Available: http://stacks.iop.org/1347-4065/47/5212

[195] O. H. Elibol, B. Reddy Jr., P. R. Nair, B. Dorvel, F. Butler, Z. S. Ahsan, D. E. Bergstrom, M. A. Alam, and R. Bashir, "Localized heating on silicon field effect transistors: Device fabrication and temperature measurements in fluid," Lab on a Chip, vol. 9, no. 19, p. 2789, oct 2009. [Online]. Available: http://xlink.rsc.org/?DOI=b906048k

[196] B. Reddy, O. H. Elibol, P. R. Nair, B. R. Dorvel, F. Butler, Z. Ahsan, D. E. Bergstrom, M. A. Alam, and R. Bashir, "Silicon Field Effect Transistors as Dual-Use Sensor-Heater Hybrids," Analytical Chemistry, vol. 83, no. 3, pp. 888–895, feb 2011. [Online]. Available: http://pubs.acs.org/doi/abs/10.1021/ac102566f

[197] N. Jokilaakso, E. Salm, A. Chen, L. Millet, C. D. Guevara, B. Dorvel, B. Reddy, A. E. Karlstrom, Y. Chen, H. Ji, R. Sooryakumar, and R. Bashir, "Ultra-localized single cell electroporation using silicon nanowires." Lab on a chip, vol. 13, no. 3, pp. 336–9, 2013. [Online]. Available: http://www.pubmedcentral.nih.gov/articlerender.fcgi?artid=3535553{&}tool=pmcentrez{&}rendertype=abstract

[198] T. M. SQUIRES and M. Z. BAZANT, "Induced-charge electro-osmosis," Journal of Fluid Mechanics, vol. 509, pp. 217–252, jun 2004. [Online]. Available: http://www.journals.cambridge.org/abstract{_}S0022112004009309

[199] R. F. Pierret, Advanced Semiconductor Fundamentals Second Edition, 2nd ed. Pearson, 2003.

[200] R. Hull, Properties of Crystalline Silicon, R. Hull, Ed. Institution of Engineering and Technology, 1999. [Online]. Available: http://app.knovel.com/hotlink/toc/id:kpPCS00005/properties-crystalline/properties-crystalline

[201] R. B. Montgomery, "Viscocity and thermal conductivity of air and diffusitivity of water vapor in air," Journal of Meteorology, vol. 4, no. 6, pp. 193–196, dec 1947. [Online]. Available: http://journals.ametsoc.org/doi/abs/10.1175/1520-0469(1947)004⟨0193:VATCOA2⟩.0.CO;2

[202] M. L. V. Ramires, C. a. Nieto de Castro, Y. Nagasaka, A. Nagashima, M. J. Assael, and W. a. Wakeham, "Standard Reference Data for the Thermal Conductivity of Water," Journal of Physical and Chemical Reference Data, vol. 24, no. 3, p. 1377, 1995. [Online]. Available: http://scitation.aip.org/content/aip/journal/jpcrd/24/3/10.1063/1.555963

[203] D. R. Kimbrough, "Heat Capacity, Body Temperature, and Hypothermia," Journal of Chemical Education, vol. 75, no. 1, p. 48, jan 1998. [Online]. Available: http://pubs.acs.org/doi/abs/10.1021/ed075p48

[204] M. Murphy, I. Rasnik, W. Cheng, T. M. Lohman, and T. Ha, "Probing Single-Stranded DNA Conformational Flexibility Using Fluorescence Spectroscopy," Biophysical Journal, vol. 86, no. 4, pp. 2530–2537, 2004. [Online]. Available: http://linkinghub.elsevier.com/retrieve/pii/S0006349504743088

[205] A. Ebrahimi and M. A. Alam, "Time-resolved PCA of "droplet impedance" identifies DNA hybridization at nM concentration," Sensors and Actuators B: Chemical, vol. 215, pp. 215–224, aug 2015. [Online]. Available: http://www.sciencedirect.com/science/article/pii/S0925400515003731

[206] G. H. Reed, J. O. Kent, and C. T. Wittwer, "High-resolution DNA melting analysis for simple and efficient molecular diagnostics," Pharmacogenomics, vol. 8, no. 6, pp. 597–608, jun 2007. [Online]. Available: http://www.futuremedicine.com/doi/abs/10.2217/14622416.8.6.597

[207] J. Fritz, E. B. Cooper, S. Gaudet, P. K. Sorger, and S. R. Manalis, "Electronic detection of DNA by its intrinsic molecular charge." Proceedings of the National Academy of Sciences of the United States of America, vol. 99, no. 22, pp. 14 142–6, oct 2002. [Online]. Available: http://www.pubmedcentral.nih.gov/articlerender.fcgi?artid=137851{&}tool=pmcentrez{&}rendertype=abstract

[208] O. H. Elibol, B. Reddy, and R. Bashir, "Nanoscale thickness double-gated field effect silicon sensors for sensitive pH detection in fluid," Applied Physics Letters, vol. 92, no. 19, p. 193904, 2008. [Online]. Available: http://link.aip.org/link/APPLAB/v92/i19/p193904/s1{&}Agg=doi

[209] D. J. Liu, G. M. Credo, X. Su, K. Wu, H. C. Lim, O. H. Elibol, R. Bashir, and M. Varma, "Surface immobilizable chelator for label-free electrical detection of pyrophosphate." Chemical communications (Cambridge, England), vol. 47, no. 29, pp. 8310–2, 2011. [Online]. Available: http://www.pubmedcentral.nih.gov/articlerender.fcgi?artid=3361515{&}tool=pmcentrez{&}rendertype=abstract

[210] S. Wang, K. Li, Y. Chen, H. Chen, M. Ma, J. Feng, Q. Zhao, and J. Shi, "Biocompatible PEGylated MoS2 nanosheets: Controllable bottom-up synthesis and highly efficient photothermal regression of tumor," Biomaterials, vol. 39, pp. 206–217, jan 2015. [Online]. Available: http://linkinghub.elsevier.com/retrieve/pii/S014296121401165X

[211] A. P. S. Gaur, S. Sahoo, M. Ahmadi, S. P. Dash, M. J.-F. Guinel, and R. S. Katiyar, "Surface Energy Engineering for Tunable Wettability through Controlled Synthesis of MoS 2," Nano Letters, vol. 14, no. 8, pp. 4314–4321, aug 2014. [Online]. Available: http://pubs.acs.org/doi/abs/10.1021/nl501106v

[212] H. R. Costantino, K. Griebenow, R. Langer, and A. M. Klibanov, "On the pH memory of lyophilized compounds containing protein functional groups." Biotechnology and bioengineering, vol. 53, no. 3, pp. 345–8, feb 1997. [Online]. Available: http://www.ncbi.nlm.nih.gov/pubmed/18633990

[213] R. A. Meyers, Molecular Biology And Biotechnology. New York: Wiley, 1995. [Online]. Available: http://www.wiley.com/WileyCDA/WileyTitle/productCd-047118571X.html

[214] A. Zaks and A. M. Klibanov, "Enzyme-catalyzed processes in organic solvents." Proceedings of the National Academy of Sciences, vol. 82, no. 10, pp. 3192–3196, may 1985. [Online]. Available: http://www.pnas.org/cgi/doi/10.1073/pnas.82.10.3192

[215] Z.-H. Wang and G. Jin, "Covalent immobilization of proteins for the biosensor based on imaging ellipsometry." Journal of immunological methods, vol. 285, no. 2, pp. 237–43, feb 2004. [Online]. Available: http://www.ncbi.nlm.nih.gov/pubmed/14980437

[216] S. Choi and J. Chae, "A Physisorbed Interface Design of Biomolecules for Selective and Sensitive Protein Detection," Journal of the Association for Laboratory Automation, vol. 15, no. 3, pp. 172–178, jun 2010. [Online]. Available: http://jla.sagepub.com/lookup/doi/10.1016/j.jala.2009.09.002

[217] S. Choi, R. Wang, A. Lajevardi-Khosh, and J. Chae, "Using competitive protein adsorption to measure fibrinogen in undiluted human serum," Applied Physics Letters, vol. 97, no. 25, p. 253701, 2010. [Online]. Available: http://scitation.aip.org/content/aip/journal/apl/97/25/10.1063/1.3529445

[218] S. McDonnell, R. Addou, C. Buie, R. M. Wallace, and C. L. Hinkle, "Defect-Dominated Doping and Contact Resistance in MoS2," ACS Nano, vol. 8, no. 3, pp. 2880–2888, mar 2014. [Online]. Available: http://pubs.acs.org/doi/abs/10.1021/nn500044q

[219] R. Addou, L. Colombo, and R. M. Wallace, "Surface Defects on Natural MoS2," ACS Applied Materials & Interfaces, vol. 7, no. 22, pp. 11 921–11 929, jun 2015. [Online]. Available: http://pubs.acs.org/doi/abs/10.1021/acsami.5b01778

[220] S. Kim, A. Konar, W.-S. Hwang, J. H. Lee, J. Lee, J. Yang, C. Jung, H. Kim, J.-B. Yoo, J.-Y. Choi, Y. W. Jin, S. Y. Lee, D. Jena, W. Choi, and K. Kim, "High-mobility and low-power thin-film transistors based on multilayer MoS2 crystals," Nature Communications, vol. 3, p. 1011, aug 2012. [Online]. Available: http://www.nature.com/doifinder/10.1038/ncomms2018

[221] G. R. Grimsley, J. M. Scholtz, and C. N. Pace, "A summary of the measured p K values of the ionizable groups in folded proteins," Protein Science, vol. 18, no. 1, pp. NA–NA, 2008. [Online]. Available: http://doi.wiley.com/10.1002/pro.19

[222] L. P. Kozlowski, "Protein Isoelectric Point Calculator." [Online]. Available: http://isoelectric.ovh.org/files/isoelectric-point-theory.html

[223] R. P. D. Bank, "RCSB Protein Data Bank." [Online]. Available: www.rcsb.org

[224] "UniProt." [Online]. Available: http://www.uniprot.org/

[225] K. Lee, P. R. Nair, A. Scott, M. a. Alam, and D. B. Janes, "Device considerations for development of conductance-based biosensors," Journal of Applied Physics, vol. 105, no. 10, p. 102046, may 2009. [Online]. Available: http://scitation.aip.org/content/aip/journal/jap/105/10/10.1063/1.3116630

[226] T. Tokuda, M. Takahashi, K. Uejima, K. Masuda, T. Kawamura, Y. Ohta, M. Motoyama, T. Noda, K. Sasagawa, T. Okitsu, S. Takeuchi, and J. Ohta, "CMOS image sensor-based implantable glucose sensor using glucose-responsive fluorescent hydrogel." Biomedical optics express, vol. 5, no. 11, pp. 3859–70, nov 2014. [Online]. Available: http://www.pubmedcentral.nih.gov/articlerender.fcgi?artid=4242023{&}tool=pmcentrez{&}rendertype=abstract

[227] A. S. Hoffman, "Hydrogels for biomedical applications," Advanced Drug Delivery Reviews, vol. 54, no. 1, pp. 3–12, jan 2002. [Online]. Available: http://linkinghub.elsevier.com/retrieve/pii/S0169409X01002393

[228] N. A. Peppas and C. D. Bures, "Glucose-Responsive Hydrogels," pp. 1163–1173, 2008.

[229] P. C. Nicolson and J. Vogt, "Soft contact lens polymers: an evolution," Biomaterials, vol. 22, no. 24, pp. 3273–3283, dec 2001. [Online]. Available: http://www.sciencedirect.com/science/article/pii/S014296120100165X

[230] K. Y. Lee and D. J. Mooney, "Hydrogels for Tissue Engineering," Chemical Reviews, vol. 101, no. 7, pp. 1869–1880, jul 2001. [Online]. Available: http://dx.doi.org/10.1021/cr000108x

[231] M. McCurley, "An optical biosensor using a fluorescent, swelling sensing element," Biosensors and Bioelectronics, vol. 9, no. 7, pp. 527–533, jan 1994. [Online]. Available: http://www.sciencedirect.com/science/article/pii/0956566394900159

[232] M. T. V. Rooney and W. Rudolf Seitz, "An optically sensitive membrane for pH based on swellable polymer microspheres in a hydrogel," Analytical Communications, vol. 36, no. 7, pp. 267–270, jan 1999. [Online]. Available: http://pubs.rsc.org/en/content/articlehtml/1999/ac/a902183c

[233] Z. Shakhsher, W. R. Seitz, and K. D. Legg, "Single Fiber-Optic pH Sensor Based on Changes in Reflection Accompanying Polymer Swelling," Analytical Chemistry, vol. 66, no. 10, pp. 1731–1735, may 1994. [Online]. Available: http://dx.doi.org/10.1021/ac00082a021

[234] A. Richter, A. Bund, M. Keller, and K.-F. Arndt, "Characterization of a microgravimetric sensor based on pH sensitive hydrogels," Sensors and Actuators B: Chemical, vol. 99, no. 2-3, pp. 579–585, may 2004. [Online]. Available: http://www.sciencedirect.com/science/article/pii/S0925400504000292

[235] N. F. Sheppard Jr., M. J. Lesho, P. McNally, and A. Shaun Francomacaro, "Microfabricated conductimetric pH sensor," Sensors and Actuators B: Chemical, vol. 28, no. 2, pp. 95–102, aug 1995. [Online]. Available: http://www.sciencedirect.com/science/article/pii/092540059401542Phttp://linkinghub.elsevier.com/retrieve/pii/092540059401542P

[236] N. F. Sheppard, R. C. Tucker, and S. Salehi-Had, "Design of a conductimetric pH microsensor based on reversibly swelling hydrogels," Sensors and Actuators B: Chemical, vol. 10, no. 2, pp. 73–77, jan 1993. [Online]. Available: http://www.sciencedirect.com/science/article/pii/092540059380028A

[237] M. Guenther, G. Gerlach, and T. Wallmersperger, "Piezoresistive biochemical sensors based on hydrogels," Microsystem Technologies, vol. 16, no. 5, pp. 703–715, may 2010. [Online]. Available: http://link.springer.com/10.1007/s00542-009-0978-z

[238] P. E. Grimshaw, J. H. Nussbaum, A. J. Grodzinsky, and M. L. Yarmush, "Kinetics of electrically and chemically induced swelling in polyelectrolyte gels," The Journal of Chemical Physics, vol. 93, no. 6, p. 4462, 1990. [Online]. Available: http://scitation.aip.org/content/aip/journal/jcp/93/6/10.1063/1.458729

[239] S. De, N. Aluru, B. Johnson, W. Crone, D. Beebe, and J. Moore, "Equilibrium swelling and kinetics of pH-responsive hydrogels: models, experiments, and simulations," Journal of Microelectromechanical Systems, vol. 11, no. 5, pp. 544–555, oct 2002. [Online]. Available: http://ieeexplore.ieee.org/lpdocs/epic03/wrapper.htm?arnumber=1038850

[240] S. K. De and N. Aluru, "A chemo-electro-mechanical mathematical model for simulation of pH sensitive hydrogels," Mechanics of Materials, vol. 36, no. 5-6, pp. 395–410, may 2004. [Online]. Available: http://linkinghub.elsevier.com/retrieve/pii/S016766360300067X

[241] M. J. Lesho and N. F. Sheppard, "A method for studying swelling kinetics based on measurement of electrical conductivity," Polym Gels Netw, vol. 5, no. 6, pp. 503–523, 1998. [Online]. Available: http://linkinghub.elsevier.com/retrieve/pii/S0966782297000245

[242] D. Ballhause and T. Wallmersperger, "Coupled chemo-electro-mechanical finite element simulation of hydrogels: I. Chemical stimulation," Smart Materials and Structures, vol. 17, no. 4, p. 045011, aug 2008. [Online]. Available: http://stacks.iop.org/0964-1726/17/i=4/a=045011?key=crossref.80c345f81020b6d56b41b27db2594d9a

[243] B. Kang, Y.-d. Dai, X.-h. Shen, and D. Chen, "Dynamical modeling and experimental evidence on the swelling/deswelling behaviors of pH sensitive hydrogels," Materials Letters, vol. 62, no. 19, pp. 3444–3446, jul 2008. [Online]. Available: http://linkinghub.elsevier.com/retrieve/pii/S0167577X08002528

[244] Q. Thong Trinh, G. Gerlach, J. Sorber, and K.-F. Arndt, "Hydrogel-based piezoresistive pH sensors: Design, simulation and output characteristics," Sensors and Actuators B: Chemical, vol. 117, no. 1, pp. 17–26, sep 2006. [Online]. Available: http://linkinghub.elsevier.com/retrieve/pii/S0925400505008683

[245] D. D. Perrin, B. Dempsey, and E. P. Serjeant, pKa prediction for organic acids and bases. Chapman and Hall, 1981. [Online]. Available: https://books.google.com/books/about/pKa{_}prediction{_}for{_}organic{_}acids{_}and{_}bas.html?id=aqwPAQAAMAAJ{&}pgis=1

[246] D. S. Finch, T. Oreskovic, K. Ramadurai, C. F. Herrmann, S. M. George, and R. L. Mahajan, "Biocompatibility of atomic layer-deposited alumina thin films." Journal of biomedical materials research. Part A, vol. 87, no. 1, pp. 100–6, oct 2008. [Online]. Available: http://www.ncbi.nlm.nih.gov/pubmed/18085647

[247] B. Amsden, "Solute Diffusion within Hydrogels. Mechanisms and Models," Macromolecules, vol. 31, no. 23, pp. 8382–8395, nov 1998. [Online]. Available: http://pubs.acs.org/doi/abs/10.1021/ma980765f

[248] L. Pisani, "Simple Expression for the Tortuosity of Porous Media," Transport in Porous Media, vol. 88, no. 2, pp. 193–203, feb 2011. [Online]. Available: http://link.springer.com/10.1007/s11242-011-9734-9

[249] S. R. Eisenberg and a. J. Grodzinsky, "The Kinetics of Chemically Induced Nonequilibrium Swelling of Articular Cartilage and Corneal Stroma," Journal of Biomechanical Engineering, vol. 109, no. 1, p. 79, 1987. [Online]. Available: http://biomechanical.asmedigitalcollection.asme.org/article.aspx?articleid=1397498

[250] A. J. Grodzinsky, Fields, Forces, and Flows in Biological Systems, 1st ed. Garland Science, 2001. [Online]. Available: http://www.garlandscience.com/product/isbn/9780815342120

[251] X. Wu, Z. Li, X.-X. Chen, J. S. Fossey, T. D. James, and Y.-B. Jiang, "Selective sensing of saccharides using simple boronic acids and their aggregates," Chemical Society Reviews, vol. 42, no. 20, p. 8032, oct 2013. [Online]. Available: http://xlink.rsc.org/?DOI=c3cs60148j

[252] T. Wallmersperger, B. Kroeplin, J. Holdenried, and R. W. Guelch, "Coupled multifield formulation for ionic polymer gels in electric fields," in Proceedings of SPIE - The International Society for Optical Engineering, Y. Bar-Cohen, Ed., vol. 4329, jul 2001, pp. 264–275. [Online]. Available: http://proceedings.spiedigitallibrary.org/proceeding.aspx?articleid=1279378

[253] T. Wallmersperger and D. Ballhause, "Coupled chemo-electro-mechanical finite element simulation of hydrogels: II. Electrical stimulation," Smart Materials and Structures, vol. 17, no. 4, p. 045012, aug 2008. [Online]. Available: http://stacks.iop.org/0964-1726/17/i=4/a=045012?key=crossref.c4fb2a99c8f1ad7c4111aa2d0e63dcb3

[254] T. Wallmersperger, K. Keller, B. Kroplin, M. Günther, and G. Gerlach, "Modeling and simulation of pH-sensitive hydrogels," Colloid and Polymer Science, vol. 289, no. 5-6, pp. 535–544, apr 2011. [Online]. Available: http://link.springer.com/10.1007/s00396-011-2404-1

[255] T. Tanaka and D. J. Fillmore, "Kinetics of swelling of gels," The Journal of Chemical Physics, vol. 70, no. 3, p. 1214, jul 1979. [Online]. Available: http://scitation.aip.org/content/aip/journal/jcp/70/3/10.1063/1.437602

[256] J. Wike-Hooley, J. Haveman, and H. Reinhold, "The relevance of tumour pH to the treatment of malignant disease," Radiotherapy and Oncology, vol. 2, no. 4, pp. 343–366, dec 1984. [Online]. Available: http://www.sciencedirect.com/science/article/pii/S0167814084800778

[257] J. Radej, M. Matejovic, A. Krouzecky, R. Sykora, J. Chvojka, and I. Novak, "How Severe Acidosis Can a Human Survive? Successful Hemofiltration Use," Dialysis & Transplantation, vol. 36, no. 11, pp. 608–610, nov 2007. [Online]. Available: http://doi.wiley.com/10.1002/dat.20163

[258] R. M. Sawant, J. P. Hurley, S. Salmaso, A. Kale, E. Tolcheva, T. S. Levchenko, and V. P. Torchilin, ""SMART" Drug Delivery Systems: Double-Targeted pH-Responsive Pharmaceutical Nanocarriers," Bioconjugate Chemistry, vol. 17, no. 4, pp. 943–949, jul 2006. [Online]. Available: http://pubs.acs.org/doi/abs/10.1021/bc060080h

[259] R. D. Harter, "Effect of Soil pH on Adsorption of Lead, Copper, Zinc, and Nickel1," Soil Science Society of America Journal, vol. 47, no. 1, p. 47, 1983. [Online]. Available: https://dl.sciencesocieties.org/publications/sssaj/abstracts/47/1/SS0470010047https://www.soils.org/publications/sssaj/abstracts/47/1/SS0470010047

[260] B. Merriman, I. T. R&D Team, and J. M. Rothberg, "Progress in Ion Torrent semiconductor chip based sequencing," ELECTROPHORESIS, vol. 33, no. 23, pp. 3397–3417, dec 2012. [Online]. Available: http://doi.wiley.com/10.1002/elps.201200424

[261] "MiniLab ISFET pH Meter." [Online]. Available: http://uk.hach.com/minilab-h138-isfet-ph-meter-ip67-3-point-cal-ph-0-01-resolution/product?id=25141975219

[262] N. K. Rajan, D. a. Routenberg, and M. a. Reed, "Optimal signal-to-noise ratio for silicon nanowire biochemical sensors," Applied Physics Letters, vol. 98, no. 26, p. 264107, jun 2011. [Online]. Available: http://scitation.aip.org/content/aip/journal/apl/98/26/10.1063/1.3608155

[263] M. J. Deen, M. W. Shinwari, J. C. Ranuarez, and D. Landheer, "Noise considerations in field effect biosensors," Journal of Applied Physics, vol. 100, no. 7, p. 074703, 2006. [Online]. Available: http://scitation.aip.org/content/aip/journal/jap/100/7/10.1063/1.2355542

[264] S. Martinoia and G. Massobrio, "A behavioral macromodel of the ISFET in SPICE," Sensors and Actuators B: Chemical, vol. 62, no. 3, pp. 182–189, mar 2000. [Online]. Available: http://linkinghub.elsevier.com/retrieve/pii/S0925400599003779

[265] K. S. Kundert and O. Zinke, The Designer's Guide to Verilog-AMS, June 2004, ser. The Designer's Guide Book Series. Boston: Springer US, 2004. [Online]. Available: http://link.springer.com/10.1007/b117108

[266] J. Santana and R. Van Den Hoven, "A Capacitive MEMS Verilog-A based sensor system for building integrity monitoring," International Journal of Information Acquisition, vol. 08, no. 02, pp. 153–159, jun 2011. [Online]. Available: http://www.worldscientific.com/doi/abs/10.1142/S0219878911002409

[267] H.-J. Park, P. Ko, and C. Hu, "A charge conserving non-quasi-state (NQS) MOSFET model for SPICE transient analysis," IEEE Transactions on Computer-Aided Design of Integrated Circuits and Systems, vol. 10, no. 5, pp. 629–642, may 1991. [Online]. Available: http://ieeexplore.ieee.org/lpdocs/epic03/wrapper.htm?arnumber=79500

[268] H. Park, P. Ko, and C. Hu, "A nonquasi-static MOSFET model for SPICE-transient analysis," IEEE Transactions on Electron Devices, vol. 36, no. 3, pp. 561–576, mar 1989. [Online]. Available: http://ieeexplore.ieee.org/lpdocs/epic03/wrapper.htm?arnumber=19969

[269] Ping Yang, B. Epler, and P. Chatterjee, "An Investigation of the Charge Conservation Problem for MOSFET Circuit Simulation," IEEE Journal of Solid-State Circuits, vol. 18, no. 1, pp. 128–138, feb 1983. [Online]. Available: http://ieeexplore.ieee.org/lpdocs/epic03/wrapper.htm?arnumber=1051909

[270] L. Bousse and P. Bergveld, "On the impedance of the silicon dioxide/electrolyte interface," Journal of Electroanalytical Chemistry and Interfacial Electrochemistry, vol. 152, no. 1-2, pp. 25–39, aug 1983. [Online]. Available: http://www.sciencedirect.com/science/article/pii/S0022072883800308http://linkinghub.elsevier.com/retrieve/pii/S0022072883800308

[271] Y. Cao, "Predictive Technology Model." [Online]. Available: http://ptm.asu.edu/modelcard/2006/130nm{_}bulk.pm

[272] L.-L. Chi, J.-C. Chou, W.-Y. Chung, T.-P. Sun, and S.-K. Hsiung, "Study on extended gate field effect transistor with tin oxide sensing membrane," Materials Chemistry and Physics, vol. 63, no. 1, pp. 19–23, feb 2000. [Online]. Available: http://linkinghub.elsevier.com/retrieve/pii/S0254058499001844

[273] L.-T. Yin, J.-C. Chou, W.-Y. Chung, T.-P. Sun, and S.-K. Hsiung, "Separate structure extended gate H+-ion sensitive field effect transistor on a glass substrate," Sensors and Actuators B: Chemical, vol. 71, no. 1-2, pp. 106–111, nov 2000. [Online]. Available: http://linkinghub.elsevier.com/retrieve/pii/S0925400500006134

[274] W. Seo, W. Yu, T. Tan, J. Zhou, T. Zhang, B. Ziaie, and B. Jung, "Diaper-embedded urinary tract infection monitoring system powered by a urine-powered battery," in 2015 IEEE Biomedical Circuits and Systems Conference (BioCAS). IEEE, oct 2015, pp. 1–4. [Online]. Available: http://ieeexplore.ieee.org/lpdocs/epic03/wrapper.htm?arnumber=7348431

[275] C. D. Chin, V. Linder, and S. K. Sia, "Commercialization of microfluidic point-of-care diagnostic devices," Lab on a Chip, vol. 12, no. 12, p. 2118, jun 2012. [Online]. Available: http://xlink.rsc.org/?DOI=c2lc21204h

[276] K. Famm, B. Litt, K. J. Tracey, E. S. Boyden, and M. Slaoui, "Drug discovery: A jump-start for electroceuticals," Nature, vol. 496, no. 7444, pp. 159–161, apr 2013. [Online]. Available: http://www.nature.com/doifinder/10.1038/496159a

[277] A. P. Alivisatos, A. M. Andrews, E. S. Boyden, M. Chun, G. M. Church, K. Deisseroth, J. P. Donoghue, S. E. Fraser, J. Lippincott-Schwartz, L. L. Looger, S. Masmanidis, P. L. McEuen, A. V. Nurmikko, H. Park, D. S. Peterka, C. Reid, M. L. Roukes, A. Scherer, M. Schnitzer, T. J. Sejnowski, K. L. Shepard, D. Tsao, G. Turrigiano, P. S. Weiss, C. Xu, R. Yuste, and X. Zhuang, "Nanotools for Neuroscience and Brain Activity Mapping," ACS Nano, vol. 7, no. 3, pp. 1850–1866, mar 2013. [Online]. Available: http://pubs.acs.org/doi/abs/10.1021/nn4012847

[278] S.-W. Hwang, H. Tao, D.-H. Kim, H. Cheng, J.-K. Song, E. Rill, M. A. Brenckle, B. Panilaitis, S. M. Won, Y.-S. Kim, Y. M. Song, K. J. Yu, A. Ameen, R. Li, Y. Su, M. Yang, D. L. Kaplan, M. R. Zakin, M. J. Slepian, Y. Huang, F. G. Omenetto, and J. a. Rogers, "A Physically Transient Form of Silicon Electronics," Science, vol. 337, no. 6102, pp. 1640–1644, sep 2012. [Online]. Available: http://www.sciencemag.org/cgi/doi/10.1126/science.1226325

[279] C. W. Park, S.-K. Kang, H. L. Hernandez, J. A. Kaitz, D. S. Wie, J. Shin, O. P. Lee, N. R. Sottos, J. S. Moore, J. A. Rogers, and S. R. White, "Thermally Triggered Degradation of Transient Electronic Devices," Advanced Materials, vol. 27, no. 25, pp. 3783–3788, jul 2015. [Online]. Available: http://doi.wiley.com/10.1002/adma.201501180

APPENDIX

A. CODES

A.1 Droplet Characterization

Sentaurus Structure Editor

Command: sde -e -l filename.scm

```
; code for constant-area mode

;
;(define pi 3.141593)

; Device geometry parameters
(define xorigin 0.0)
(define yorigin 0.0)

; dimensions of the electrode
(define width 400.0)
(define height 0.01)

; determine debye length
(define ni 6e13)
(define e0 8.85e-14)
(define ew (* e0 78.9))
(define q 1.6e-19)
(define vt .0259)
(define Ld (* 1e4 (sqrt (/ (* ew vt) (* 2 ni q)))))
(display "Debye_Length")
(display Ld)

; geometry of the droplet
(define contact-radius 400.0)
(define initial-angle-degrees 20.0)


(define half_distance 10.0)     ; half times the distance between the electrodes

; Create droplet structures for different contact angles (i.e. 20 to 160 degrees)
(do ( (j 2 (+ j 1)) ) ( (= j 16) )

        (begin

        (define contact-angle-degrees (* j 10.0))
                        (display contact-angle-degrees) (newline)
        (define contact-angle-radians (convert-to-radian contact-angle-degrees))
        (define radius (/ contact-radius (sin contact-angle-radians)))       ; droplet radius in um

        (define filename (string-append "sdevice_input/droplet_angle_" (number->string
             contact-angle-degrees)))

        ; calculated parameters

        ; defining electrode
        (define X1electrode1 half_distance)
        (define X2electrode1 width)
        (define Y1electrode1 yorigin)
        (define Y2electrode1 yorigin) ; (+ yorigin height))

        ;defining circular droplet
        (define Xdrop xorigin)
        (define Ydrop (- yorigin (* radius (cos contact-angle-radians))))

        ; defining rectangle covering upper hemisphere of the water droplet (to make things
             easier I take the maximum possible rectangle)

        (define X1drop (- xorigin (* 1.0  radius)))
        (define X2drop (+ xorigin (* 1.0  radius)))
        (define Y1drop yorigin)
```

```
(define Y2drop (+ yorigin (* 2.0 radius)))

(sdegeo:set-default-boolean "ABA")

; Creating geometrical structure

; Creating circular droplet
(if (<= contact-angle-degrees 90.0)
(begin
        (define start-angle (- 90 contact-angle-degrees))
        (define end-angle 90)
        ;(define end-angle (+ 90 contact-angle-degrees))
        (display contact-angle-radians) (newline)
        (display start-angle) (newline)
        (display end-angle) (newline)
        (if (= contact-angle-degrees 90.0)
                (set! Ydrop 0)
        )

        (sdegeo:create-circular-sheet
                (position Xdrop Ydrop 0)
                radius "Solution" "R.droplet" start-angle end-angle)
)
)

(if (> contact-angle-degrees 90.0)
        (begin
        (sdegeo:create-circular-sheet
                (position Xdrop Ydrop 0)
                radius "Solution" "R.droplet" -90 90)
        )
)

; cutting out part of the circle with the defined rectangle to form a droplet shape
        (sdegeo:2d-cut
         (position X1drop Y1drop 0)
 (position X2drop Y2drop 0))



; Contact declarations
(sdegeo:define-contact-set "Celectrode1"
 4.0 (color:rgb 1.0 0.0 0.0) "##")
;(sdegeo:define-contact-set "Celectrode2"
; 4.0 (color:rgb 0.0 1.0 0.0) "##")
(sdegeo:define-contact-set "Ground"
 4.0 (color:rgb 0.0 0.0 1.0) "##")


(sdegeo:insert-vertex (position X1electrode1 Y1electrode1 0))

; Contact placement
(sdegeo:define-2d-contact
 (find-edge-id (position (/ (+ X1electrode1 X2electrode1) 2) Y1electrode1 0))
 "Celectrode1")



(sdegeo:set-current-contact-set "Ground")
(sdegeo:set-contact-edges (list (car (find-edge-id (position Xdrop (* (+ Ydrop radius )
     0.1) 0))) (car (find-edge-id (position Xdrop (* (+ Ydrop radius) 0.3) 0))) (car
     (find-edge-id (position Xdrop (* (+ Ydrop radius) 0.5) 0))) (car (find-edge-id
     (position Xdrop (* (+ Ydrop radius) 0.7) 0))) (car (find-edge-id (position Xdrop (*
     (+ Ydrop radius) 0.9) 0)))) "Ground")



; Biggest Refinement Placement
(sdedr:define-refinement-size "Ref.droplet" (/ radius 10) (/ radius 10) (/ radius 20) (/
     radius 20))
(sdedr:define-refinement-region "RefPlace.droplet1" "Ref.droplet" "R.droplet")

(define N1 25)
(define N4 25)
(define N5 10)

(define M2 25)
(define M3 25)


; Horizontal Refinement 6
(sdedr:define-refeval-window "RefEvalWindow6.droplet" "Rectangle"
        (position 380 yorigin 0)
        (position 410 (* 1.10 height) 0))
(sdedr:define-refinement-size "RefFine6.droplet" 1 0.010 0.05 0.005)
(sdedr:define-refinement-placement "RefPlaceFine6.droplet" "RefFine6.droplet"
     "RefEvalWindow6.droplet")

; Vertical Refinement 1 (finest refinement)
```

```
        ;(xcut)
        (sdedr:define-refeval-window "RefEvalWindow0.droplet" "Rectangle"
                (position xorigin (- height 0.001) 0)
                (position X2electrode1 (+ height (/ Ld 3)) 0))
        (sdedr:define-refinement-size "RefFine0.droplet" (/ width 10) (/ Ld 100) (/ width 20) (/
            Ld 200))
        (sdedr:define-refinement-placement "RefPlaceFine0.droplet" "RefFine0.droplet"
            "RefEvalWindow0.droplet")

        (sdedr:define-refeval-window "RefEvalWindow1.droplet" "Rectangle"
                (position xorigin (/ Ld 3) 0)
                (position X2electrode1 (+ height Ld) 0))
        (sdedr:define-refinement-size "RefFine1.droplet" (/ width 10) (/ Ld 25) (/ width 20) (/
            Ld 50))
        (sdedr:define-refinement-placement "RefPlaceFine1.droplet" "RefFine1.droplet"
            "RefEvalWindow1.droplet")

        (sdedr:define-refeval-window "RefEvalWindow2.droplet" "Rectangle"
                (position xorigin (+ height Ld) 0)
        (position X2electrode1 (+ height (* 2 Ld)) 0))
        (sdedr:define-refinement-size "RefFine2.droplet" (/ width 10) (/ Ld 12.5) (/ width 20) (/
            Ld 25))
        (sdedr:define-refinement-placement "RefPlaceFine2.droplet" "RefFine2.droplet"
            "RefEvalWindow2.droplet")

        ; Horizontal Refinement 3 (ycut)
        (sdedr:define-refeval-window "RefEvalWindow3.droplet" "Rectangle"
                (position (- half_distance Ld)  yorigin 0)
                (position (- half_distance (* .33 Ld)) height 0))
        (sdedr:define-refinement-size "RefFine3.droplet"  (/ Ld 25) (/ height 10) (/ Ld 50) (/
            height 20))
        (sdedr:define-refinement-placement "RefPlaceFine3.droplet" "RefFine3.droplet"
            "RefEvalWindow3.droplet")

        (sdedr:define-refeval-window "RefEvalWindow4.droplet" "Rectangle"
                (position (- half_distance (* 2 Ld))  yorigin 0)
                (position (- half_distance Ld) height 0))
        (sdedr:define-refinement-size "RefFine4.droplet"  (/ Ld 25) (/ height 10) (/ Ld 50) (/
            height 20))
        (sdedr:define-refinement-placement "RefPlaceFine4.droplet" "RefFine4.droplet"
            "RefEvalWindow4.droplet")

        (sdedr:define-refeval-window "RefEvalWindow5.droplet" "Rectangle"
                (position (- half_distance (* .33 Ld))  yorigin 0)
                (position (+ half_distance 0.001) height 0))
        (sdedr:define-refinement-size "RefFine5.droplet"  (/ Ld 100) (/ height 10) (/ Ld 200) (/
            height 20))
        (sdedr:define-refinement-placement "RefPlaceFine5.droplet" "RefFine5.droplet"
            "RefEvalWindow5.droplet")


        (sde:set-meshing-command "snmesh -a -c boxmethod")
        (sdedr:append-cmd-file "-")
        (sde:build-mesh "snmesh" "-a -c boxmethod" filename)
        (sde:save-model filename)
        ) ; end of begin
) ; end of do loop
```

Sentaurus Device Simulation

Command: sdevice filename.cmd

```
File {
        Grid = "sdevice_input/droplet_angle_90_msh.tdr"
        Plot = "sdevice_output/droplet_angle_90"
        Current = "sdevice_output/droplet_angle_90"
        Output = "sdevice_output/droplet_angle_90"
        Parameter ="solution_oxide.par"
}

Electrode {
        { Name="Celectrode1" Voltage=0 Workfunction=4.61}
        { Name="Ground" Voltage=0 Workfunction=4.61}
}

Plot {
        eDensity hDensity Potential SpaceCharge ElectricField
        IntrinsicDensity EffectiveIntrinsicDensity
        ConductionBandEnergy ValenceBandEnergy
```

```
        eQuasiFermiEnergy hQuasiFermiEnergy
        DielectricConstant
        ElectricField/Vector
}

Solve {
        Poisson

        Quasistationary ( MaxStep= 0.4
                        Goal {Name="Celectrode1" Voltage=0.2} )
                { Poisson}
}
```

A.2 Droplet Desalting

Sentaurus Structure Editor

Command: sde -e -l filename.scm

```
; Device geometry parameters
(define xorigin 0.0)
(define yorigin 0.0)

; dimensions of the electrode
(define width 70)
(define height 1.0)

(define ni 6e17)
(define e0 8.85e-14)
(define ew (* e0 78.9))
(define q 1.6e-19)
(define vt .0259)

(define Ld_old (* 1e4 (sqrt (/ (* ew vt) (* 2 ni q)))))

(define hstern (* 7.5391e-3 Ld_old)) ;6e17 0.5V

(define hnet (+ height hstern))

(define Ld (* Ld_old 1))

(display "Debye_Length")
(display Ld)

; geometry of the droplet
(define contact-radius 70)

; half_distance of electrode from center of droplet contact
(define half_distance 10.0)

(define contact-angle-degrees 48)
                (display contact-angle-degrees) (newline)
(define contact-angle-radians (convert-to-radian contact-angle-degrees))
(define radius (/ contact-radius (sin contact-angle-radians)))      ; droplet radius in um

(define filename (string-append "sdevice_input/droplet_angle_" (number->string
    contact-angle-degrees)))

; calculated parameters

(define X1electrode1 half_distance)
(define X2electrode1 width)
(define Y1electrode1 yorigin)
(define Y2electrode1 (+ yorigin height))

(define X1stern (- half_distance hstern))
(define X2stern (+ width hstern))
(define Y1stern yorigin)
(define Y2stern (+ yorigin height hstern))

;defining circular droplet
(define Xdrop xorigin)
(define Ydrop (- yorigin (* radius (cos contact-angle-radians))))
```

```
; defining rectangle covering upper hemisphere of the water droplet
; (to make things easier I take the maximum possible rectangle)

(define X1drop (- xorigin (* 1.0  radius)))
(define X2drop (+ xorigin (* 1.0  radius)))
(define Y1drop yorigin)
(define Y2drop (+ yorigin (* 2.0 radius)))

(sdegeo:set-default-boolean "ABA")

; Creating geometrical structure

; Creating circular droplet
(if (<= contact-angle-degrees 90.0)
(begin
        (define start-angle (- 90 contact-angle-degrees))
        (define end-angle 90)
        ;(define end-angle (+ 90 contact-angle-degrees))
        (display contact-angle-radians) (newline)
        (display start-angle) (newline)
        (display end-angle) (newline)
        (if (= contact-angle-degrees 90.0)
                (set! Ydrop 0)
        )

        (sdegeo:create-circular-sheet
                 (position Xdrop Ydrop 0)
                 radius "Solution" "R.droplet" start-angle end-angle)
)
)

(if (> contact-angle-degrees 90.0)
        (begin
        (sdegeo:create-circular-sheet
                 (position Xdrop Ydrop 0)
                 radius "Solution" "R.droplet" -90 90)
        )
)

; Contact declarations
(sdegeo:define-contact-set "Celectrode1" 4.0 (color:rgb 1.0 0.0 0.0) "##")
(sdegeo:define-contact-set "Ground" 4.0 (color:rgb 0.0 0.0 1.0) "##")

; cutting out part of the droplet
(sdegeo:2d-cut  (position X1drop Y1drop 0) (position X2drop Y2drop 0))
(sdegeo:create-rectangle (position X1stern Y1stern 0) (position X2stern Y2stern 0) "SiO2"
    "R.stern")

(define dummy2 (sdegeo:create-rectangle (position X1electrode1 Y1electrode1 0) (position
    X2electrode1 Y2electrode1 0) "Aluminum" "R.dummy2"))
(sdegeo:set-current-contact-set "Celectrode1")
(sdegeo:set-contact-boundary-edges dummy2 (sdegeo:get-current-contact-set))
(sdegeo:delete-region dummy2)


(sdegeo:insert-vertex (position (* half_distance 1.05) Y1electrode1 0))
(sdegeo:insert-vertex (position (* X2electrode1 0.95) Y1electrode1 0))

; Contact placement
(sdegeo:define-2d-contact (find-edge-id (position Xdrop (/ (+ Ydrop radius ) 2) 0)) "Ground")

; defining meshing strategy

; Biggest Refinement Placement
(sdedr:define-refinement-size "Ref.droplet" (/ radius 10) (/ radius 10) (/ radius 20) (/ radius
    20))
(sdedr:define-refinement-region "RefPlace.droplet1" "Ref.droplet" "R.droplet")


; Horizontal refinement
(define r 2)

; Horizontal Refinement 1
(sdedr:define-refeval-window "REW_H1.droplet" "Rectangle" (position (- X2stern (/ Ld 1e20))
    yorigin 0) (position (+ X2stern (* Ld 10)) (* 1.10 hnet) 0))
(sdedr:define-multibox-size "REF_H1.droplet" (/ Ld 1) (/ hnet 5) (/ Ld 1e20) (/ hnet 10) 2.5 1.1)
(sdedr:define-multibox-placement "RPF_H1.droplet" "REF_H1.droplet" "REW_H1.droplet")

; Horizontal Refinement 2
(sdedr:define-refeval-window "REW_H2.droplet" "Rectangle" (position (- X1stern (* Ld 10)) yorigin
    0) (position X1stern (* 1.10 hnet) 0))
(sdedr:define-multibox-size "REF_H2.droplet" (/ Ld 1) (/ hnet 5) (/ Ld 1e20) (/ hnet 10) -2.5 1.1)
(sdedr:define-multibox-placement "RPF_H2.droplet" "REF_H2.droplet" "REW_H2.droplet")

; Vertical Refinement 2
(sdedr:define-refeval-window "Rew_v1.droplet" "Rectangle" (position xorigin (- hnet (/ Ld 1e10))
    0) (position X2stern (+ hnet (* Ld 10)) 0))
(sdedr:define-multibox-size "Ref_v1.droplet" (/ width 20) (/ Ld 1) (/ width 50) (/ Ld 1e10) 1 2.5)
(sdedr:define-multibox-placement "Rpf_v1.droplet" "Ref_v1.droplet" "Rew_v1.droplet")
```

```
(sde:set-meshing-command "snmesh -a -c boxmethod")
(sdedr:append-cmd-file "")
(sde:build-mesh "snmesh" "-a -c boxmethod" filename)
(sde:save-model filename)
```

Sentaurus Device Simulation

Command: sdevice filename.cmd

```
File {
        Grid = "sdevice_input/droplet_angle_48_msh.tdr"
        Plot = "sdevice_output/droplet_angle_48"
        Current = "sdevice_output/droplet_angle_48"
        Output = "sdevice_output/droplet_angle_48"
        Parameter ="solution.par"
}

Electrode {
        { Name="Celectrode1" Voltage=0 Workfunction=4.61}
        { Name="Ground" Voltage=0 Workfunction=4.61}
}

Physics(Region="R.stern"){
   Traps((FixedCharge Conc=0))

}

CurrentPlot{
        eDensity(
        Average(Semiconductor)
        Integrate(Semiconductor)
        )

        hDensity(
        Average(Semiconductor)
        Integrate(Semiconductor)
        )

        eTrappedCharge(
        Average(Insulator)
        Integrate(Insulator)
        )

        hTrappedCharge(
        Average(Insulator)
        Integrate(Insulator)
        )
}


Plot {
        eDensity hDensity Potential SpaceCharge ElectricField
        IntrinsicDensity EffectiveIntrinsicDensity
        ConductionBandEnergy ValenceBandEnergy
        eQuasiFermiEnergy hQuasiFermiEnergy
        DielectricConstant
        ElectricField/Vector
        eTrappedCharge
        hTrappedCharge
}

Solve {
        Poisson

      Quasistationary ( MaxStep= 0.1 Goal {Name="Celectrode1" Voltage=0.5} )
                { Poisson
                  CurrentPlot(Time= (0; 0.2; 0.4; 0.6; 0.8; 1.0))}
      }
```

A.3 Droplet Heating

A.3.1 Sentaurus Code for Solving Electrical Equations

Sentaurus Structure Editor

Command: sde -e -l filename.scm

```
; Device geometry parameters
(define offset 10)
(define radius 35)       ; droplet radius in um
(define dlength (+ radius offset))              ; device half width
(define hwidth_ch 1)     ; half width of the channel
(define tbox 0.145)              ; thickness of bottom oxide
(define tsi 30e-3)               ; thickness of the channel
(define tox 30e-3)               ; thickness of the top oxide
(define tbulk 5)                 ; thickness of bulk silicon

; defining geometry for bulk silicon
(define X1bulk (- dlength))
(define X2bulk dlength)
(define Y1bulk (- (+ tbox tbulk)))
(define Y2bulk (- tbox))

; defining geometry for bottom oxide
(define X1box (- dlength))
(define X2box dlength)
(define Y1box (- tbox))
(define Y2box 0)

; defining geometry for silicon channel
(define X1ch (- hwidth_ch))
(define X2ch hwidth_ch)
(define Y1ch 0)
(define Y2ch tsi)

; defining geometry for the top-oxide layer covering

(define X1tox (- X1ch tox))
(define X2tox (+ X2ch tox))
(define Y1tox Y1ch)
(define Y2tox (+ Y2ch tox))


;defining circular droplet
(define Xdrop 0)
(define Ydrop 0)

; defining rectangle covering upper hemisphere of the water droplet
(define X1drop (- Xdrop radius))
(define X2drop (+ Xdrop radius))
(define Y1drop Ydrop)
(define Y2drop (+ radius Ydrop))


; defining lengths from the center of the device geometry
(define lbulk (* 2 dlength))
(define lbox (* 2 dlength))
(define ltox (* 2 hwidth_ch))
(define width_ch (* 2 hwidth_ch))

; defining the coordinates for refinement window
(define X1ref1 (- (* 2 hwidth_ch)))
(define X2ref1 (* 2 hwidth_ch))
(define Y1ref1 Y1tox)
(define Y2ref1 (* 10 Y2tox))

(define x-max-ref1 (/ (- X2ref1 X1ref1) 200))
(define x-min-ref1 (/ x-max-ref1 2))
(define y-max-ref1 (/ (- Y2ref1 Y1ref1) 100))
(define y-min-ref1 (/ y-max-ref1 2))

; Overlap resolution: New replaces old
(sdegeo:set-default-boolean "ABA")


; Creating geometrical structure
```

```
; Creating circular droplet
(sdegeo:create-circular-sheet
        (position Xdrop Ydrop 0)
         radius "Water" "R.drop")

; cutting out semi-circle from droplet region
(sdegeo:2d-cut
        (position X1drop Y1drop 0)
        (position X2drop Y2drop 0))

; Creating bulk silicon region
(sdegeo:create-rectangle
        (position X1bulk Y1bulk 0)
        (position X2bulk Y2bulk 0)
"Silicon" "R.bulk")

; Creating bottom oxide region
(sdegeo:create-rectangle
        (position X1box Y1box 0)
        (position X2box Y2box 0)
        "SiO2" "R.box")


; Creating top oxide region
(sdegeo:create-rectangle
        (position X1tox Y1tox 0)
        (position X2tox Y2tox 0)
        "SiO2" "R.tox")


; Creating silicon channel region
(sdegeo:create-rectangle
        (position X1ch Y1ch 0)
        (position X2ch Y2ch 0)
        "Silicon" "R.channel")

; Contact declarations
(sdegeo:define-contact-set "bulk"
        4.0 (color:rgb 1.0 0.0 0.0) "##")
(sdegeo:define-contact-set "source"
        4.0 (color:rgb 0.0 1.0 0.0) "##")
(sdegeo:define-contact-set "bodytie"
        4.0 (color:rgb 0.0 0.0 1.0) "##")


; Contact placement
(sdegeo:define-2d-contact
        (find-edge-id (position (/ (+ X1bulk X2bulk) 2) Y1bulk 0))
        "bulk")
(sdegeo:set-current-contact-set "source")
(sdegeo:set-contact-boundary-edges (list (car (find-body-id (position (/ (+ X1ch X2ch) 2) (/ (+
    Y1ch Y2ch) 2) 0)))) "source")

; defining doping profile

(sdedr:define-constant-profile "Profile.channel"
         "BoronActiveConcentration" 1e16)
(sdedr:define-constant-profile-region "Placement.channel"
        "Profile.channel" "R.channel")


(sdedr:define-constant-profile "Profile.bulk"
         "BoronActiveConcentration" 1e15)
(sdedr:define-constant-profile-region "Placement.bulk"
        "Profile.bulk" "R.bulk")

;(sdedr:define-constant-profile "Profile.sd"
;         "PhosphorusActiveConcentration" 1e20)
;(sdedr:define-constant-profile-region "Placement.s"
;        "Profile.sd" "R.s")
;(sdedr:define-constant-profile-region "Placement.d"
;        "Profile.sd" "R.d")



; defining meshing strategy

; channel
(sdedr:define-refinement-size "Ref.channel" (/ width_ch 8) (/ tsi 16) (/ width_ch 16) (/ tsi 32))
(sdedr:define-refinement-region "RefPlace.channel" "Ref.channel" "R.channel")

; top oxide
(sdedr:define-refinement-size "Ref.tox" (/ ltox 8) (/ tox 8) (/ ltox 16) (/ tox 16))
(sdedr:define-refinement-region "RefPlace.tox" "Ref.tox" "R.tox")

; bottom oxide
(sdedr:define-refinement-size "Ref.box" (/ lbox 35) (/ tbox 8) (/  lbox 140) (/ tbox 16))
(sdedr:define-refinement-region "RefPlace.box" "Ref.box" "R.box")
```

```
; droplet
(sdedr:define-refinement-size "Ref.drop" (/ radius 35) (/ radius 35) (/ radius 140) (/ radius
    140))
(sdedr:define-refinement-region "RefPlace.drop" "Ref.drop" "R.drop")

; bulk silicon
(sdedr:define-refinement-size "Ref.bulk" (/ lbulk 35) (/ tbulk 5) (/ lbulk 140) (/ tbulk 20))
(sdedr:define-refinement-region "RefPlace.bulk" "Ref.bulk" "R.bulk")

; creating refinement reference windows for fine gridding strategy
(sdedr:define-refeval-window "RefEvalWin_1" "Rectangle"  (position X1ref1 Y1ref1 0) (position
    X2ref1 Y2ref1 0))
(sdedr:define-refinement-size "Ref.REW1" x-max-ref1 y-max-ref1 x-min-ref1 y-min-ref1)
(sdedr:define-refinement-placement "RefPlace.REW1" "Ref.REW1" "RefEvalWin_1" )

(sde:set-meshing-command "snmesh -a -c boxmethod")
(sdedr:append-cmd-file "_")
(sde:build-mesh "snmesh" "-a -c boxmethod" "./droplet_device1")
(sde:save-model "./droplet_device1")
```

Sentaurus Device Simulation

Command: sdevice filename.cmd

```
File {
        * input files:
        Grid = "droplet_device1_msh.tdr"
        * output files:
        Plot = "droplet_device1_35"
        Current = "droplet_device1_35"
        Output = "droplet_device1_35"
        Parameter ="water.par"
}


Electrode {
        { Name="bulk" Voltage=-35}
        { Name="source" Voltage=0}
}

Plot {
        eDensity hDensity Potential SpaceCharge ElectricField eQuasiFermi hQuasiFermi
        eMobility hMobility eVelocity hVelocity eQuasiFermiEnergy hQuasiFermiEnergy
        DielectricConstant Doping DonorConcentration AcceptorConcentration
        ConductionBandEnergy ValenceBandEnergy
        ElectricField/Vector
}

Math {
        CurrentPlot (Digits = 2)
}

Solve {
        Poisson
}
```

A.3.2 Matlab Code for Solving Thermal Equation

```
% Temperature profiling code

% File runs properly on MATLAB R2012a

%%
% close all;
clear all;
clc

% Defining units
um=1e-6;
mm=1e-3;
```

```
cm=1e-4;
nm=1e-9;


Air.thermal_conductivity=0.024; % 0.15;
vrms=[20 22 24 26 28 30 32 34 36 38 40];
abs_voltage=vrms*sqrt(2);



radius_array=[10,20,30,35,40]*1*um;
initial_temperature=298;

power=zeros(1,length(vrms));
integral_EsquareField_droplet=zeros(1,length(vrms));
integral_EsquareField_SiO2=zeros(1,length(vrms));

radius=35*um;



for vrmsindex=1:length(vrms)
    voltage_rms=vrms(vrmsindex);
    frequency=10e6;
    proportionality_constant=0.20;
    fileToRead=['N:\summer2012\device_may27_' num2str(radius/um) 'um\scalar_field_offset_0_35V.txt
        '];
    filename=['Vrms_' num2str(floor(voltage_rms))];
    foldername=['F:\network_drives\Purdue\May2016\2013_PNAS\droplet_' num2str(radius/um) 'um'];
    if ~exist(foldername,'dir')
    eval(['mkdir_' foldername]);
end

e0=8.85e-12;
Water.epsilon=79*e0;
Water.eimg=1e3*e0;

SiO2.epsilon=3.9*e0;
SiO2.loss_tangent=1e-4;

Air.specific_heat=1000;          % oil 1670
Air.mass_density=1.2;           % 800

voltage=sqrt(2)*voltage_rms;

SiO2.eimg=SiO2.loss_tangent*SiO2.epsilon;

Water.thermal_conductivity=0.58;%0.58;
SiO2.thermal_conductivity=1.4;
Silicon.thermal_conductivity=149;%149;

Water.specific_heat=4180;
SiO2.specific_heat=1000;
Silicon.specific_heat=710;

Water.mass_density=1000;
SiO2.mass_density=2600;
Silicon.mass_density=2300;



SiO2.epsilon=3.9*e0;

max_time_estimate=4*(Water.mass_density*Water.specific_heat*radius^2)/(Water.thermal_conductivity)
    ;
max_time=1e-3;
% step_time=max_time/10;
gp_step_time=max_time/1.8^20; % For T vs. Time (Plot)
time=[0,gp_step_time*1.8.^[0:20]]; % For T vs. Time (Plot)
% time=[0,0.5,1,2,4,8,16,32]*1e-3; % Works fine for steady state

% Device geometry parameters
 dwidth=radius+5*um;              % half width of the device in meters
 radius_air=dwidth;
 tol=dwidth-radius+0.05*um;

 tbox=145*nm;                % thickness of bottom oxide
 tsi=30*nm;                  % thickness of the channel
 tox=30*nm;                  % thickness of the top oxide
 tbulk=5*um;                     % thickness of bulk silicon
 hwidth=1*um;                % half width of silicon channel

%defining geometry for bulk silicon
 X1bulk=-dwidth;
 X2bulk=dwidth;
 Y1bulk=-(tbox+tbulk);
 Y2bulk=-tbox;
```

```
%defining geometry for bottom oxide
 X1box=-dwidth;
 X2box=dwidth;
 Y1box=-tbox;
 Y2box=0;

%defining geometry for silicon channel
 X1ch=-hwidth;
 X2ch=hwidth;
 Y1ch=0;
 Y2ch=tsi;


 % defining geometry for the top-oxide layer
 X1tox=X1ch-tox;
 X2tox=X2ch+tox;
 Y1tox=Y1ch;
 Y2tox=Y2ch+tox;


% defining circular droplet
 Xdrop=0;
 Ydrop=0;

 Xair=0;
 Yair=0;


% defining rectangle covering lower semicircle of the air covering (and
% water droplet)

 X1drop=Xair-radius_air;
 X2drop=Xair+radius_air;
 Y1drop=Yair-radius_air;
 Y2drop=Yair;

%%%%%%%%%%%%%%%%%

% Creating geometrical structure

rcair=create_circular_sheet([Xair Yair],radius_air,'Air','Rair');
% Creating circular droplet
rdroplet=create_circular_sheet([Xdrop Ydrop],radius,'Water','Rdrop');
%  cutting out semi-circle from droplet region
rcut=create_rectangle([X1drop Y1drop],[X2drop Y2drop],'','Rcut');

% Creating bulk silicon region
rbulk=create_rectangle([X1bulk Y1bulk],[X2bulk Y2bulk],'Silicon','Rbulk');
% Creating bottom oxide region
rbox=create_rectangle([X1box Y1box],[X2box Y2box],'SiO2','Rbox');
% Creating top oxide region
rtox=create_rectangle([X1tox Y1tox],[X2tox Y2tox],'SiO2','Rtox');
% Creating silicon channel region
rch=create_rectangle([X1ch Y1ch],[X2ch Y2ch],'Silicon','Rch');


regions=[rdroplet,rcut,rbulk,rbox,rtox,rch,rcair];
[gd ns]=geometry_description_matrix(regions);
sf='((Rdrop+Rair)-Rcut)+Rbulk+Rbox+Rtox+Rch';

% removing unnecessary internal subdomain borders
[dl1,bt1]=decsg(gd,sf,ns);

CIRC=1;
BOUND=0;
Ytol=Yair+radius_air;
cs=find(dl1(1,:)==CIRC);
keepcs=[find(abs(dl1(4,:)-Ytol)<=tol) find(abs(dl1(5,:)-Ytol)<=tol)];
bl=setdiff(cs,keepcs);

[dl,bt]=csgdel(dl1,bt1,bl);
[p,e,t]=initmesh(dl);


 % mapping subdomain numbers with the polygons
 % find a triangle index corresponding to each subdomain number

 no_of_subdomains=max(t(4,:));
 sdindex=zeros(1,no_of_subdomains);
 for i=1:no_of_subdomains
     sdindex(i)=find(t(4,:)==i,1);
 end

% find the centers of all the traingles in the geometry
tcom=zeros(2,length(t));
for i=1:length(t)
     p1=p(:,t(1,i));
     p2=p(:,t(2,i));
```

```
    p3=p(:,t(3,i));
    tcom(:,i)=(p1+p2+p3)/3;
end
%

scalarData= importdata(fileToRead);
electric_field=scalarData(:,3)*1e2;      % converting from V/cm to V/m
electric_field(find(isnan(electric_field)))=1;
index=find(electric_field<1);
electric_field(index)=1;

% the scaling law of the electrid field has been verified with simulation
%  (since it is just a dielectric capacitor)
electric_field=electric_field*voltage/35;

xdata=scalarData(:,1)*1e-6;                    % converting from um to m
ydata=scalarData(:,2)*1e-6;
get_electric_field=TriScatteredInterp([xdata ydata],abs(electric_field));

xlim=[min(xdata) max(xdata)];
ylim=[min(ydata) max(ydata)];

xq=[xlim(1):(xlim(2)-xlim(1))/500: xlim(2)];
 yq=[Y1bulk:(Y2bulk-Y1bulk)/25:Y2bulk,Y1box:(Y2box-Y1box)/50:Y2box,Y1tox:(Y2tox-Y1tox)/50:10*Y2tox
      ,10*Y2tox:(ylim(2)-10*Y2tox)/100:ylim(2)];
[Xq,Yq]=meshgrid(xq,yq);

eq=get_electric_field(Xq,Yq);

eq(isnan(eq))=0;
Esquare=eq.^2;
norm_matrix=ones(size(Xq));
norm_matrix(isnan(eq))=0;
norm=trapz(Yq(:,1),trapz(Xq(1,:),norm_matrix,2));

Esquare_avg=trapz(Yq(:,1),trapz(Xq(1,:),Esquare,2))/norm;

a=0;

c=zeros(1,length(t));
f=zeros(1,length(t));
d=zeros(1,length(i));


fail.x=[];
fail.y=[];
thermal_conductivity=zeros(1,length(t));
mass_density=zeros(1,length(t));
specific_heat=zeros(1,length(t));
Q=zeros(1,length(t));
material_name=zeros(1,length(t));
% field=zeros(1,length(t));
index_droplet=[];
index_SiO2=[];
for i=1:length(t)
    xcoor=tcom(1,i);
    ycoor=tcom(2,i);


    if((xcoor-Xair)^2+(ycoor-Yair)^2<=radius_air^2)
        mname='Air';
    end

    if((xcoor-Xdrop)^2+(ycoor-Ydrop)^2<=(radius)^2)
        mname='Water';
    end

    % Note the order of the
    if(inpolygon(xcoor,ycoor,[X1box X2box],[Y1box Y2box])||inpolygon(xcoor,ycoor,[X1tox X2tox],[
        Y1tox Y2tox]))
        mname='SiO2';
    end
    if(inpolygon(xcoor,ycoor,[X1bulk X2bulk],[Y1bulk Y2bulk])||inpolygon(xcoor,ycoor,[X1ch X2ch],[
        Y1ch Y2ch]))
        mname='Silicon';
    end

    if(strcmpi(mname,'Water'))
    material_name(i)=1;
    end

    thermal_conductivity(i)=eval([mname '.thermal_conductivity']);
    mass_density(i)=eval([mname '.mass_density']);
    specific_heat(i)=eval([mname '.specific_heat']);
      c(i)=thermal_conductivity(i);
     E=get_electric_field(xcoor,ycoor);
    d(i)=mass_density(i)*specific_heat(i);
    if(isnan(E)~=1)
        if(strcmpi(mname,'Water'))
```

```
            index_droplet=[index_droplet i];

            if xcoor>X1tox && xcoor<X2tox
                electric_conductivity=conductivity(ycoor-abs(Y2tox-Y1tox));
            else
                electric_conductivity=conductivity(ycoor);
            end
         local_relative_permittivity=proportionality_constant*electric_conductivity/(2*pi*
             frequency*e0);
           Q(i)=1/2*local_relative_permittivity*e0*E^2*2*pi*frequency;

           f(i)=Q(i);
        elseif(strcmpi(mname,'SiO2'))
            index_SiO2=[index_SiO2 i];
            Q(i)=1/2*SiO2.eimg*E^2*2*pi*frequency;
          f(i)=Q(i);
        elseif(strcmpi(mname,'Silicon'))
        end


    else
            fail.x=[fail.x xcoor];
            fail.y=[fail.y ycoor];
    end

end

field=zeros(1,length(t));
for indext=1:length(t)
    xcoor=tcom(1,i);
    ycoor=tcom(2,i);
    field(indext)=get_electric_field(xcoor,ycoor);
end

field_droplet=zeros(1,length(t));
field_SiO2=zeros(1,length(t));

field_droplet(index_droplet)=field(index_droplet);
field_SiO2(index_SiO2)=field(index_SiO2);

power(vrmsindex)=integral_calculator(p,t,Q);
integral_EsquareField_droplet(vrmsindex)=integral_calculator(p,t,field_droplet.^2);
integral_EsquareField_SiO2(vrmsindex)=integral_calculator(p,t,field_SiO2.^2);



 bc=[1 1 1 1 1 3 '0' '0' '1' num2str(initial_temperature)]';
 b=repmat(bc,1,length(dl));

 deltaTmax=time(end)*frequency*pi*Water.eimg*Esquare_avg/(Water.mass_density*Water.specific_heat);

 T1=parabolic(initial_temperature,time,b,p,e,t,c,a,f,d);
 final_sol=T1(:,size(T1,2));
 maxTemp=max(T1(:,:)-273)

 saturation_time=(Water.mass_density*Water.specific_heat)*(maxTemp(end)-(initial_temperature-273))
     /(0.5*2*pi*frequency*Water.eimg*Esquare_avg)


    xmin=min(p(1,:)); xmax=max(p(1,:));
    ymin=min(p(2,:)); ymax=max(p(2,:));
    xlimT=[xmin xmax];
    ylimT=[ymin ymax];
    nxy=200;
    xtemp=[xlimT(1):(X1tox-xlimT(1))/200:X1tox,X1tox:(X2tox-X1tox)/200:X2tox,X2tox:(xlimT(2)-X2tox
        )/200: xlimT(2)];
    ytemp=[Y1bulk:(Y2bulk-Y1bulk)/50:Y2bulk,Y1box:(Y2box-Y1box)/50:Y2box,Y1tox:(Y2tox-Y1tox)
        /100:10*Y2tox,10*Y2tox:(ylimT(2)-10*Y2tox)/100:ylimT(2)];
    [xydata,tn,a2,a3]=tri2grid(p,t,final_sol,xtemp,ytemp);


clear i index bc b f a b  material_name mname fail


save([foldername filesep filename]);


end


function array=create_circular_sheet(vertex,radius,mname,rname)
geometry=[1 vertex(1) vertex(2) radius];
array.geometry=geometry';
array.rname=rname;
array.mname=mname;


function array=create_rectangle(vertex1,vertex2,mname,rname)
geometry=[3 4 vertex1(1) vertex2(1) vertex2(1) vertex1(1) vertex1(2) vertex1(2) vertex2(2) vertex2
    (2)];
```

```
array.geometry=geometry';
array.rname=rname;
array.mname=mname;


%% To determine the conductivity of the solution
%% we are considering only the conductivity due to Na+ and Cl- ions
%% the function takes the ycoordinate in meters and returns conductivity of the ionic solution in
     SI units (S/m)
% Navo=6.023e23/mol
% 1 mol/liter = 1e-3 mol/cm^3

 function cond=conductivity(ycoord)

% all units in the code are in cm unless otherwise specified

ycoord=ycoord*1e2; % changing ycoord from meters to cm

pH=7;


q = 1.6e-19;
kT = 0.0259 * q;
e0 = 8.85e-14;
ew = 78.8*e0;
Navo=6.023e20;

I0=0.225; % in molar
n0 = I0 * Navo;    % electrolyte concentration in cm^-3
Ns = 5e14;   % total density of amphoteric sites (OH) /cm^2
pKa = -2;
pKb = 6;

Ka = 10^(-pKa);
Kb = 10^(-pKb);

aHB = 10.^(-pH);
c1 = aHB./Ka;
c2 = Kb./aHB;

grahame_cons=sqrt(8*ew*kT*n0);


bp=17; % no of base pairs
molecule_charge=bp*(-2);
molecule_density=0*1e13; %cm-2;

debye_length=sqrt(ew*kT/(2*q^2))/(sqrt(n0));

x0=0;
options=optimset('Display','off');

phi0 = fsolve(@(phi0) ((-grahame_cons*sinh(q*phi0/(2*kT))+q*Ns*(c1*exp(-q*phi0/kT)-c2*exp(q*phi0/
     kT))/(1+c1*exp(-q*phi0/kT)+c2*exp(q*phi0/kT))+molecule_density*molecule_charge*q)/grahame_cons
     ),x0,options);  % Call solver

% reference wikipedia
molar_conductivity_Na= 50; % Scm^2/mol
molar_conductivity_Cl=76; % Scm^2/mol

ion_charge=1;
gamma=abs(tanh(phi0*q*ion_charge/(4*kT)));

% Reference: Bard & Faulkner (Page 548, Electrochemical Methods: Fundamentals and Applications)
charge_positive=((1+gamma*exp(-ycoord./debye_length))./(1-gamma*exp(-ycoord./debye_length))).^2;
charge_negative=((1-gamma*exp(-ycoord./debye_length))./(1+gamma*exp(-ycoord./debye_length))).^2;

molar_concentration_Na=n0*charge_positive/Navo; % # of moles / liter
molar_concentration_Cl=n0*charge_negative/Navo; % # of moles / liter


cond=molar_concentration_Na*molar_conductivity_Na+molar_concentration_Cl*molar_conductivity_Cl;  %
     in Scm^2/liter

% changing conductivity to SI units Scm^2/liter ->S/m
cond=cond*1e-1;
```

A.4 MoS_2 Code

Sentaurus Structure Editor

```
Command: sde -e -l filename.scm
```

```
; Define Origin
 (define x0 0.0)
 (define y0 0.0)

; Define channel thickness, oxide thickness and dummy insulator thickness at top MoS2 interface
 (define tch 0.07)
 (define tox 0.3)
 (define tins 0.001)

; Define channel length, gate length, and length of the dummy insulator
 (define lg 11.6)
 (define lch 11.6)
 (define lins 11.6)

; Define Gate Oxide Coordinates
 (define X1ox (- x0 (/ lg 2.0)))
 (define X2ox (+ x0 (/ lg 2.0)))
 (define Y1ox y0)
 (define Y2ox (+ y0 tox))

; Define Channel Coordinates
 (define X1ch (- x0 (/ lch 2.0)))
 (define X2ch (+ x0 (/ lch 2.0)))
 (define Y1ch Y2ox)
 (define Y2ch (+ Y2ox tch))

; Define Dummy Insulator Coordinates
 (define X1ins (- x0 (/ lins 2.0)))
 (define X2ins (+ x0 (/ lins 2.0)))
 (define Y1ins Y2ch)
 (define Y2ins (+ Y2ch tins))

; Define Source/Drain Coordinates
 (define Xe1 X1ch)
 (define Y1e1 Y1ch)
 (define Y2e1 Y2ch)

 (define Xe2 X2ch)
 (define Y1e2 Y1ch)
 (define Y2e2 Y2ch)

; Create Gate Oxide, Channel, and Dummy Insulator Region
 (sdegeo:create-rectangle (position X1ox Y1ox 0) (position X2ox Y2ox 0) "SiO2" "R.ox")
 (sdegeo:create-rectangle (position X1ch Y1ch 0) (position X2ch Y2ch 0) "MoS2" "R.ch")
 (sdegeo:create-rectangle (position X1ins Y1ins 0) (position X2ins Y2ins 0) "Solution" "R.ins")

; Define Colors for Source/Drain/Gate Contacts
 (sdegeo:define-contact-set "source" 4.0 (color:rgb 1.0 0.0 0.0) "##")
 (sdegeo:define-contact-set "drain" 4.0 (color:rgb 0.0 1.0 0.0) "##")
 (sdegeo:define-contact-set "gate" 4.0 (color:rgb 0.0 0.0 1.0) "##")

; Define Doping Profiles
 (sdedr:define-constant-profile "Profile.ch" "PhosphorusActiveConcentration" 1e16)
 (sdedr:define-constant-profile-region "Placement.ch" "Profile.ch" "R.ch")

; Create Refinement For Gridding
 (sdedr:define-refeval-window "RefWin.ox1" "Rectangle" (position X1ox Y1ox 0) (position (+ X1ox
     (/ lg 2)) Y2ox 0))
 (sdedr:define-multibox-size "MBdef.ox1" (/ lg 10) (/ tox 10) (/ lg 5000) (/ tox 20) 1.2 1.0)
 (sdedr:define-multibox-placement "MBPlace.ox1" "MBdef.ox1" "RefWin.ox1")


 (sdedr:define-refeval-window "RefWin.ox3" "Rectangle" (position (- X2ox (/ lg 2)) Y1ox 0)
     (position X2ox Y2ox 0))
 (sdedr:define-multibox-size "MBdef.ox3" (/ lg 10) (/ tox 10) (/ lg 5000) (/ tox 20) -1.2 1.0)
 (sdedr:define-multibox-placement "MBPlace.ox3" "MBdef.ox3" "RefWin.ox3")


 (sdedr:define-refeval-window "RefWin.ch11" "Rectangle" (position X1ch Y1ch 0) (position (+ X1ch
     (/ lch 2)) (/ (+ Y1ch Y2ch) 2) 0))
 (sdedr:define-multibox-size "MBdef.ch11" (/ lch 10) (/ tch 10) (/ lch 5000) (/ tch 30) 1.2 1.15)
 (sdedr:define-multibox-placement "MBPlace.ch11" "MBdef.ch11" "RefWin.ch11")

 (sdedr:define-refeval-window "RefWin.ch31" "Rectangle" (position (- X2ch (/ lch 2)) Y1ch 0)
     (position X2ch (/ (+ Y1ch Y2ch) 2) 0))
 (sdedr:define-multibox-size "MBdef.ch31" (/ lch 10) (/ tch 10) (/ lch 5000) (/ tch 30) -1.2 1.15)
 (sdedr:define-multibox-placement "MBPlace.ch31" "MBdef.ch31" "RefWin.ch31")


 (sdedr:define-refeval-window "RefWin.ch13" "Rectangle" (position X1ch (/ (+ Y1ch Y2ch) 2) 0)
     (position (+ X1ch (/ lch 2)) Y2ch 0))
 (sdedr:define-multibox-size "MBdef.ch13" (/ lch 10) (/ tch 10) (/ lch 5000) (/ tch 30) 1.2 -1.15)
 (sdedr:define-multibox-placement "MBPlace.ch13" "MBdef.ch13" "RefWin.ch13")

 (sdedr:define-refeval-window "RefWin.ch33" "Rectangle" (position (- X2ch (/ lch 2)) (/ (+ Y1ch
     Y2ch) 2) 0) (position X2ch Y2ch 0))
 (sdedr:define-multibox-size "MBdef.ch33" (/ lch 10) (/ tch 10) (/ lch 5000) (/ tch 30) -1.2
     -1.15)
```

```
(sdedr:define-multibox-placement "MBPlace.ch33" "MBdef.ch33" "RefWin.ch33")


(sdedr:define-refeval-window "RefWin.ins1" "Rectangle" (position X1ins Y1ins 0) (position (+
    X1ins (/ lins 10)) Y2ins 0))
(sdedr:define-multibox-size "MBdef.ins1" (/ lins 100) (/ tins 10) (/ lins 500) (/ tins 20) 1.03
    1.0)
(sdedr:define-multibox-placement "MBPlace.ins1" "MBdef.ins1" "RefWin.ins1")


(sdedr:define-refeval-window "RefWin.ins3" "Rectangle" (position (- X2ins (/ lins 10)) Y1ins 0)
    (position X2ins Y2ins 0))
(sdedr:define-multibox-size "MBdef.ins3" (/ lins 100) (/ tins 10) (/ lins 500) (/ tins 20) -1.03
    1.0)
(sdedr:define-multibox-placement "MBPlace.ins3" "MBdef.ins3" "RefWin.ins3")

; Define the Source, Drain and Gate contacts
(sdegeo:define-2d-contact (find-edge-id (position Xe1 (/ (+ Y1e1 Y2e1) 2) 0)) "source")
(sdegeo:define-2d-contact (find-edge-id (position Xe2 (/ (+ Y1e2 Y2e2) 2) 0)) "drain")
(sdegeo:define-2d-contact (find-edge-id (position (/ (+ X1ox X2ox) 2) Y1ox 0)) "gate")

; Create Meshing and Save the File
(sde:set-meshing-command "snmesh -a -c boxmethod")
(sde:set-meshing-command "snmesh -a -c boxmethod")
(sde:build-mesh "snmesh" "-a -c boxmethod" "./fet")
(sde:save-model "./fet")
```

Sentaurus Device Simulation

Command: sdevice filename.cmd

```
File {
        Grid = "fet_msh.tdr"
        Plot = "fet_des.tdr"
        Current = "fet_des.plt"
        Output = "fet_des.log"
        Parameter = "materials.par"
}

Electrode {
        { Name = "source" Voltage = 0.0 Area=12.5}
        { Name = "drain" Voltage = 0.0 Area=12.5}
        { Name = "gate" Voltage = [expr "-4.8154+1.97"] Material="PolySi"(P=6.0e20) Area=12.5}
}

Math {
        Number_of_Threads=Maximum
        Digits=5
        Extrapolate
        NoCheckTransientError
        RelErrControl
        NotDamped=200
        TrapDLN=50
}


Plot {
        Potential ElectricField ElectricField/Vector
        ConductionBandEnergy ValenceBandEnergy
        eQuasiFermiEnergy hQuasiFermiEnergy
        eDensity hDensity EffectiveIntrinsicDensity
        eEffectiveStateDensity hEffectiveStateDensity
        Doping SpaceCharge
        BandGap ElectronAffinity DielectricConstant
        eCurrent hCurrent
        eMobility hMobility
     }

Physics(MaterialInterface="Solution/MoS2") {
        Traps(
                (FixedCharge Conc=2.8e11
                (Donor
                #Acceptor
                Uniform
                Conc=0e15
                EnergyMid=0.75
                fromCondBand
                EnergySig=0.55
                eXsection=1e-14 hXsection=1e-14
```

```
                )
                )
        }


Physics (MaterialInterface="MoS2/Oxide") {
        Traps(
                (FixedCharge Conc=2.6e11)
                (Acceptor
                Uniform
                Conc=0e12
                EnergyMid=0.10
                fromCondBand
                EnergySig=0.10
                eXsection=1e-14 hXsection=1e-14
                )
                (Donor
                Uniform
                Conc=8e11
                EnergyMid=0.75
                fromCondBand
                EnergySig=0.75
                eXsection=1e-14 hXsection=1e-14
                )
        )
}
CurrentPlot {
        ElectrostaticPotential((0 0.30) (0 0.37))

}

Solve {
        Poisson
        Coupled {Poisson Electron}
        Plot(FilePrefix="output/vgfb_vd0")
        Save(FilePrefix="output/vgfb_vd0")

        Quasistationary (MaxStep =0.2
                Goal { Name="gate" Voltage=0.0} )
                {
                Plugin{
                Poisson
                Coupled {Poisson Electron}
                }
                }
        Plot(FilePrefix="output/vg0_vd0")

        Quasistationary (MaxStep =0.2
                Goal { Name="drain" Voltage=1.0} )
                {
                Plugin{
                Poisson
                Coupled {Poisson Electron}
                }
                Plot(FilePrefix="output/vg0_vd" Time=(1.0) NoOverwrite)
                }
        Save(FilePrefix="output/vg0_vd1")


        Quasistationary (MaxStep =0.4 InitialStep=0.01 MinStep=1e-9
                Goal { Name="gate" Voltage=[expr "40"] } )
                {
                 Plugin{
                 Poisson
                 Coupled {Poisson Electron}
                 }
                Plot(FilePrefix="output/vd1_Vgp40" Time=(0.0; 0.5; 1.0) NoOverwrite)
                }

        NewCurrentPrefix="vd1_vg"
        Quasistationary (MaxStep = 0.02 InitialStep=0.01 MinStep=1e-9
                Goal { Name="gate" Voltage=[expr "10"]} )
                {
                Coupled {Poisson Electron}
                }


        Quasistationary (MaxStep = 0.02 InitialStep=0.01 MinStep=1e-9
                BreakCriteria{
                Current(Contact="drain" minval=1e-13)
                }
                Goal { Name="gate" Voltage=[expr "-0"]} )
                {
                Coupled {Poisson Electron}
                #Plot(FilePrefix="output/vd1_Vgn1" Time=(0.5;1.0) NoOverwrite)
                }

        Quasistationary (MaxStep = 0.02 InitialStep=0.01 MinStep=1e-9
                BreakCriteria{
```

```
                Current(Contact="drain" minval=1e-13)
                }
                Goal { Name="gate" Voltage=[expr "-10"]} )
                {
                Coupled {Poisson Electron}
                Plot(FilePrefix="output/vd1_Vgn10" Time=(0;0.2;0.4;0.6;0.8;1.0) NoOverwrite)
                }

        Quasistationary (MaxStep =0.3 InitialStep=0.01 MinStep=1e-9
                BreakCriteria{
                Current(Contact="drain" minval=1e-13)
                }
                Goal { Name="gate" Voltage=[expr "-15"]} )
                {
                Coupled {Poisson Electron}
                Plot(FilePrefix="output/vd1_Vgn15" Time=(0.4;0.8) NoOverwrite)
                }

        Quasistationary (MaxStep =0.05 InitialStep=0.01 MinStep=1e-9
                BreakCriteria{
                Current(Contact="drain" minval=1e-13)
                }
                Goal { Name="gate" Voltage=[expr "-20"]} )
                {
                Coupled {Poisson Electron}
                Plot(FilePrefix="output/vd1_Vgn20" Time=(0.2;0.6;1.0) NoOverwrite)
                }

        Quasistationary (MaxStep =0.2 InitialStep=0.01 MinStep=1e-9
                BreakCriteria{
                Current(Contact="drain" minval=1e-13)
                }
                Goal { Name="gate" Voltage=[expr "-40"]} )
                {
                Coupled {Poisson Electron}
                Plot(FilePrefix="output/vd1_Vgn40" Time=(0; 0.2; 0.4; 0.6; 0.8; 1.0) NoOverwrite)
                }
}
"
```

A.5 Hydrogel Code

A.5.1 Numerical Model

```
%% Code written by Piyush Dak, Purdue University, 2016 (Advisor: Prof. Muhammad A. Alam)

% The code determines the time dependence of osmotic pressure exerted by
% Hydrogel sandwiched between a rigid porous membrane and a deformable
% membrane on a deformable membrane.
%                                   SKETCH
%                          -->  |----------|------------|
%                          -->  |   Rigid  |  Hydrogel  |
%          (solution) H+   -->  | Membrane |            |
%                          -->  |----------|------------|
%                               <--lporous-><-lhydrogel->
%% The code uses following functions:

% SolvePoissonEquationEquilibrium (Solves equilibrium poisson equation)
% SolvePoissonEquationNonEquilibrium (Solves non-equilibrium poisson equation)
% smoothen_stepfunction (smoothens the ionizable group density from 0 to the vlaue in hydrogel for
    convergence)
% pHfunction (smoothens out the pH boundary condition for convergence)
% CreateJacobianMatrix
% bernoulli_function

clc; clear; close all

%% Definition of fundamental constants

Navg=6.023e23;                          % Avogadro number in #/Mole
e0=8.85e-12;                            % Permittivity in vaccuum in SI units
q=1.6e-19;                              % Electronic Charge in columbs
kB=1.3806488e-23;                       % Boltzmann Constant in m^2 kg sec^-2 K-1

%% Definition of parameters related to the liquid comprising sample

Kw_mM=1e-8;                             % Ionization constant of water at room temperature, Kw
    in mM
er=80;                                  % Relative permittivity of Water
```

```
%% Geometric Dimensions of Hydrogel in x-dimension

lporous_um=5;                                   % length of porous membrane in um
lhydrogel_um=20;                                % length of hydrogel membrane in um
ltotal_um=lporous_um+lhydrogel_um;              % Total length of hydrogel in um (These are input
    parameters to the function)

%% Hydrogel Composition
% Here, we assume that hydrogel is composed of 2 type of anionic groups and
% 1 type of cationic groups
pKa1=5;                                         % pKa of anionic group 1
pKa2=7;                                         % pKa of anionic group 1
pKb=6;                                          % pKb of cationic groups

Nanionic1_mM=100;                               % The number density in mM and pKa of anionic group 1
    in Hydrogel
Nanionic2_mM=0;                                 % The number density in mM and pKa of anionic group 2
    in Hydrogel
Ncationic_mM=0;                                 % The number density in mM and pKb of cationic group in
     Hydrogel

%% Diffusion slowdown factors

DH_modified_factor=1;                           % The factor by which the diffusion is slowed down in
    hydrogel due to steric hindrance (relative to pure water)
porous_diffusion_factor=1;                      % The factor by which the diffusion in porous membrane
    is slowed down relative to the pure water.

%% Operating Conditions

salt_concentration=100;                         % Salt Concentration in mM

Temperature_degrees=25;                         % Temperature in Degree Centigrade

% Buffer Parameters
Nbasic=0;                                       % Number density in mM of basic buffer groups
Dbasic=1/1e4;                                   % Diffusion coefficient (normalized to DH+ in pure
    water)
Kbasic=1e3*10^-6;                               % Acid dissociation constant of basic buffer groups

Nacidic=0;                                      % Number density in mM of acidic buffer groups
Dacidic=1/10;                                   % Diffusion coefficient (normalized to DH+ in pure
    water)
Kacidic=1e3*10^-4;                              % Acid dissociation constant of basic buffer groups

parlist.tarr=[0 10]*60;                         % Array of time values
parlist.pHarr=[5 5.1 5];                        % Array of pH values denoting the corresponding pH
    boundary condition at various time points listed in parlist.tarr.
% (For the values listed above, pH takes a jump from pH=5 to pH=5.1 at t=0 and then it goes down
    to 5 at t=10 min.)
stpar=100;                                      % Smoothening parameter to make sure that the pH doesn'
    t shoot up abruptly in time space (to improve convergence)


%% Gridding Parameters for x-space and t-space

nx=500;                                         % Total number of grid points for distance
nt=400;                                         % Total number of grid points for time (increase if
    resolution is not good, and having convergence issues)

%% Control parameters for turning on/off different models

field_turned_off=0;                             % If 1, the field is turned off (only diffusion is
    solved for), if 0 (includes both drift and diffusion components)
buffer_model_on=1;                              % If 1, the buffer model is turned on (Note, that
    buffer concentation, Nbuff must be non-zero for buffer to have any effect)
modify_mobility=0;                              % If 1, the mobility of the buffer is modified in
    accordance with analysis

%% The Actual Code Starts Here
%%%%%%%%%%%%%%%%%%%%%%%%%%%%%%%%%%%%%%%%%%%%%
%% Setting Scales for x, t, and D and Pressure

um=1e-6;
time_scale=1;                                   % 1 sec
DH_scale=9.31e-9;                               % Diffusion constant of protons in pure water (m^2/sec)
x_scale=sqrt(DH_scale*time_scale);              % m

T=273+Temperature_degrees;                      % Temperature of solution in Kelvin
pressure_scale=kB*T*Navg;                       % In Pascal /mM

%% Creating time and space grid points

tmax=20*60;             % Time for which simulation is to be run (in seconds)
t=linspace(0,tmax,nt);  % Array of grid points for time (make the grid points smaller if there is
    resolution is not good enough).

xmax=ltotal_um*um;   % Convert the total length of the system into meters.
```

```
x=linspace(0,xmax/x_scale,nx) ; % Scale it with respect to diffusion distance for 1 sec travel of
    protons in pure water.

%%
% Determine Ka and Kb values from the pKa's and convert these into mM.

Ka1_M=10^-pKa1; Ka1_mM=Ka1_M*1e3;
Ka2_M=10^-pKa2; Ka2_mM=Ka2_M*1e3;
Kb_mM=10^-pKb*1e3;

%%
% Analytical Estimate of Time Response
% Hana=1e3*10.^-parlist.pHarr;

pHana=[min(parlist.pHarr):0.1:max(parlist.pHarr)];
Hana=1e3*10.^-pHana;

Deff_estimate=1./(1+Ka1_mM*Nanionic1_mM./(Ka1_mM+Hana).^2+Ka2_mM*Nanionic2_mM./(Ka2_mM+Hana).^2+
    Kb_mM*Ncationic_mM./(Kb_mM+Hana).^2);

L_ana=xmax/x_scale-lporous_um*um/x_scale;
time_estimate=L_ana.^2./(2*Deff_estimate)+(lporous_um*um/x_scale)^2/(2*porous_diffusion_factor);
tmax=max(time_estimate)/60;
tmin=min(time_estimate)/60;
sprintf('Tmin: %.1f \nTmax: %.1f',tmin,tmax)


%%
% Determine smoothening parameter for x-space, so that the value of
% ionizable group density doesn't shoot up abruptly from porous membrane to
% hydrogel

sxmax=xmax/x_scale;
smpar=sxmax*1e3;          % Smoothening Parameter

%%
Dbasic_arr=Dbasic*ones(size(x));
Dacidic_arr=Dacidic*ones(size(x));

Nbasic_arr=Nbasic*ones(size(x));
Nacidic_arr=Nacidic*ones(size(x));

Kbasic_arr=Kbasic*ones(size(x));
Kacidic_arr=Kacidic*ones(size(x));
%% Setting up boundary conditions

Na_bc=salt_concentration;
Cl_bc=salt_concentration;
Na_ic=salt_concentration;
Cl_ic=salt_concentration;

pHinit=parlist.pHarr(1);
H0_ic=10^-pHinit*1e3; % mM

%% Setting up parameters in Region1 (Porous Membrane) and Region2 (Hydrogel)

parlist.Region1.DH=porous_diffusion_factor;
parlist.Region1.Ncationic=0;
parlist.Region1.Nanionic1=0;
parlist.Region1.Nanionic2=0;
parlist.Region1.Kb=0;
parlist.Region1.Ka1=0;
parlist.Region1.Ka2=0;

parlist.Region2.DH=DH_modified_factor;
parlist.Region2.Ka1=10^-pKa1*1e3;
parlist.Region2.Ka2=10^-pKa2*1e3;
parlist.Region2.Kb=10^-pKb*1e3;
parlist.Region2.Ncationic=Ncationic_mM;
parlist.Region2.Nanionic1=Nanionic1_mM;
parlist.Region2.Nanionic2=Nanionic2_mM;

%%
xpm=lporous_um*um/x_scale;                              % The location of the porous/hydrogel
    interface in terms of scaled distance

parlist.xpm=xpm;

DHxx=smoothen_stepfunction(x,xpm,parlist.Region1.DH,parlist.Region2.DH,smpar);
Ka1_vec=smoothen_stepfunction(x,xpm,parlist.Region1.Ka1,parlist.Region2.Ka1,smpar);
Ka2_vec=smoothen_stepfunction(x,xpm,parlist.Region1.Ka2,parlist.Region2.Ka2,smpar);
Kb_vec=smoothen_stepfunction(x,xpm,parlist.Region1.Kb,parlist.Region2.Kb,smpar);

Ncationic_vec=smoothen_stepfunction(x,xpm,parlist.Region1.Ncationic,parlist.Region2.Ncationic,
    smpar);
Nanionic1_vec=smoothen_stepfunction(x,xpm,parlist.Region1.Nanionic1,parlist.Region2.Nanionic1,
    smpar);
Nanionic2_vec=smoothen_stepfunction(x,xpm,parlist.Region1.Nanionic2,parlist.Region2.Nanionic2,
    smpar);
```

```
%%

c0=1*1e-3*Navg/1e-3;  % 1 mM in #/m^3;
Ld=sqrt(e0*kB*T/(q^2*c0)); % Debye lenth corresponding to 1 mM concentration in m

parlist.H0ic=H0_ic;

nx=length(x);
nt=length(t);
x0_Ld=(x_scale/Ld);

exx=er*ones(nx,1);


%%  Determining the Equibrium Solution
rho_param.dpsi=0;
rho_param.ddpsi_dx=0;

% Solve the equilibrium case with the initial conditions
rho_param.Na0=Na_ic;
rho_param.H0=H0_ic;

rho_param.Nanionic1_vec=Nanionic1_vec;
rho_param.Nanionic2_vec=Nanionic2_vec;

rho_param.Ka1_vec=Ka1_vec;
rho_param.Ka2_vec=Ka2_vec;

rho_param.Ncationic_vec=Ncationic_vec;
rho_param.Kb_vec=Kb_vec;

rho_param.x0_Ld=x0_Ld;
rho_param.Kw=Kw_mM;
rho_param.tolerance=1e-16;

% Determine equilibrium solution to the poisson equation

psi_guess=zeros(1,nx);

psi_equilibrium=SolvePoissonEquationEquilibrium(x,psi_guess,exx,rho_param);

psi_numerical=psi_equilibrium(end);
lambda_solution=exp(-psi_equilibrium);
Na_distance=Na_ic*lambda_solution;
Cl_distance=Cl_ic./lambda_solution;
H_distance=H0_ic*lambda_solution;
OH_distance=(Kw_mM/H0_ic)./lambda_solution;

rho_fixed=Ncationic_vec'-Ncationic_vec'.*Kb_vec'./(Kb_vec'+H_distance)-Nanionic1_vec'.*Ka1_vec'./(
    Ka1_vec'+H_distance)-Nanionic2_vec'.*Ka2_vec'./(Ka2_vec'+H_distance);

rho_distance=Na_distance-Cl_distance+H_distance-OH_distance+rho_fixed;


pressure_initial=(Na_distance+Cl_distance+H_distance+OH_distance-Na_ic-Cl_ic-H0_ic-Kw_mM/H0_ic)*
    pressure_scale;



%%

npos=2; % Number of Mobile Positive Charges  (H+ and Na+)
nneg=1; % Number of Mobile Negative Charges  (Cl-)


bc.psi=0; % Left Boundary Condition for psi
bc.dpsi_dx=0; % Right Boundary Condition for dpsi_dx

bc.u=[H0_ic Na_bc Cl_bc];
bc.du_dx=[0 0 0];

umatrix=zeros(nt,nx,npos+nneg);
Efield_arr=zeros(nt,nx-1);

dx=diff(x);

exx=er*ones(nx,1);
psi=zeros(nt,nx);


%%
rho_param.Na_bc=Na_bc;


    umatrix(1,:,1)=H_distance;
    umatrix(1,:,2)=Na_distance;
    umatrix(1,:,3)=Cl_distance;
    rho_param.Hplus=H_distance;
    psi(1,:)=psi_equilibrium';
```

```
% Changing the boundary conditions appropriately
    for idx=1:npos+nneg
        umatrix(1,1,idx)=bc.u(idx);
    end

    tidx=2;

    cmat=ones(nx,1);


    H0_bc_arr=zeros(size(t));
    pH_bc_arr=zeros(size(t));
    H0_bc_arr(1)=H_distance(1);
    pH_bc_arr(1)=pHfunction(-4,parlist.tarr,parlist.pHarr,stpar);

    cmat_matrix=ones(size(umatrix(:,:,1)));

while tidx<=nt

    pHbc=pHfunction(t(tidx),parlist.tarr,parlist.pHarr,stpar);

    H0_bc=10.^-pHbc*1e3;
    bc.u=[H0_bc Na_bc Cl_bc];
    H0_bc_arr(tidx)=H0_bc;
    pH_bc_arr(tidx)=pHbc;


    cmat_cationic=  Kb_vec.*Ncationic_vec./((Kb_vec+umatrix(tidx-1,:,1)).^2);
    cmat_anionic1=Ka1_vec.*Nanionic1_vec./((Ka1_vec+umatrix(tidx-1,:,1)).^2);
    cmat_anionic2=Ka2_vec.*Nanionic2_vec./((Ka2_vec+umatrix(tidx-1,:,1)).^2);

     dtj=t(tidx)-t(tidx-1);

   % Solve Continuity Equation for Hplus ions
     bcondition.n=bc.u(1);
     bcondition.dn_dx=bc.du_dx(1);

     soln_previous=umatrix(tidx-1,:,1);
     soln_previous=soln_previous(:);

     charge_type=1;

     psi_previous=psi(tidx-1,:);
     Efield_previous=-diff(psi_previous)./dx;
     Efield_arr(tidx-1,:)=Efield_previous;


     %%
         cmat_basic_buffer=Nbasic_arr.*Kbasic_arr./(umatrix(tidx-1,:,1)+Kbasic_arr).^2;
         cmat_acidic_buffer=Nacidic_arr.*Kacidic_arr./(umatrix(tidx-1,:,1)+Kacidic_arr).^2;

          cmat=1+cmat_cationic+cmat_anionic1+cmat_anionic2;

          if buffer_model_on
            cmat_buffer=cmat_basic_buffer+cmat_acidic_buffer;
            cmat=cmat+cmat_buffer;
          end

            cmat=cmat';

         cmat_matrix(tidx,:)=cmat;
     % Note: In normalized units mu and D are same values

     if buffer_model_on
        if modify_mobility
            mu_eff=DHxx+Dbasic_arr.*(Nbasic_arr./(Kbasic_arr+umatrix(tidx-1,:,1)));
        else
            mu_eff=DHxx;
        end

        D_eff=DHxx+Dbasic_arr.*(Nbasic_arr.*Kbasic_arr./(umatrix(tidx-1,:,1)+Kbasic_arr).^2)+...
              Dacidic_arr.*(Nacidic_arr.*Kacidic_arr./(umatrix(tidx-1,:,1)+Kacidic_arr).^2);

%               Dacidic_arr.*(Nacidic_arr./(umatrix(tidx-1,:,1)+Kacidic_arr));


     else
         mu_eff=DHxx;
         D_eff=DHxx;
     end
     %%

    if field_turned_off
     mu_eff=0*D_eff;
    end
```

```
        [spAmatrix,yvector]=CreateJacobianMatrix(Efield_previous,D_eff,mu_eff,cmat,dx,dtj,charge_type
            ,bcondition);
        rhsvector=yvector+cmat(2:nx).*soln_previous(2:nx);
        soln_present=[bc.u(1); spAmatrix\rhsvector];
        umatrix(tidx,:,1)=soln_present;
        psi_guess=zeros(1,nx);
        rho_param.Hplus=soln_present;

        psi(tidx,:)=SolvePoissonEquationNonEquilibrium(x,psi_guess,exx,rho_param);

        lambda_factor=exp(-psi(tidx,:));
       umatrix(tidx,:,2)=Na_bc*lambda_factor;
       umatrix(tidx,:,3)=Cl_bc./lambda_factor;
        pressure_Hion(tidx,:)=(umatrix(tidx,:,1)+Kw_mM./umatrix(tidx,:,1)-(H0_bc+Kw_mM/H0_bc));
        tidx=tidx+1


end

pressure_mat=umatrix(:,:,2)+umatrix(:,:,3)-2*Na_bc+pressure_Hion;
pressure_exerted=pressure_mat(:,end)'*pressure_scale/1e3;

%%

figure('Units','inches','Position',[3,1,6.6,4.4],'DefaultAxesLineWidth',2,'DefaultAxesFontSize'
    ,24,'DefaultAxesFontName','Arial',...
    'DefaultTextFontSize',24,'DefaultLineLineWidth',4,'DefaultAxesTickLength',[0.015,0.03],'
        PaperPositionMode','auto');
plot(t/60,pH_bc_arr,'b');
xlabel('Time (in min)');
ylabel('pH(t)');
legend('N_f=100mM');

figure('Units','inches','Position',[3,1,6.6,4.4],'DefaultAxesLineWidth',2,'DefaultAxesFontSize'
    ,24,'DefaultAxesFontName','Arial',...
    'DefaultTextFontSize',24,'DefaultLineLineWidth',4,'DefaultAxesTickLength',[0.015,0.03],'
        PaperPositionMode','auto');
plot(t/60,pressure_exerted-pressure_exerted(1),'b');
xlabel('Time (in min)');
ylabel('\DeltaP (kPa)');
legend('N_f=100mM');
ylim([0 3]);


function psi_solution=SolvePoissonEquationEquilibrium(x,psi_guess,exx,rho_param)

% Function to solve for Equilibrium Poisson Equation

x=x(:);
exx=exx(:);
psi_old=psi_guess(:);


nx=length(x);
dx=diff(x);

% Boundary Conditions for x=x1 (dirichlet) anx x=xk (neumann)
y_bc=rho_param.dpsi;
dydx_bc=rho_param.ddpsi_dx;

Na0=rho_param.Na0;
H0=rho_param.H0;
Kw=rho_param.Kw;
x0_Ld=rho_param.x0_Ld;
tolerance=rho_param.tolerance;

% Nanionic_vec=rho_param.sigma0_vec(:);
Nanionic1_vec=rho_param.Nanionic1_vec(:);
Ka1_vec=rho_param.Ka1_vec(:);

Nanionic2_vec=rho_param.Nanionic2_vec(:);
Ka2_vec=rho_param.Ka2_vec(:);

Ncationic_vec=rho_param.Ncationic_vec(:);
Kb_vec=rho_param.Kb_vec(:);

Na1_cap=Nanionic1_vec./Na0;
Na2_cap=Nanionic2_vec./Na0;

Nb_cap=Ncationic_vec./Na0;

alpha=(x0_Ld)^2.*Na0;          % Charge Density Scaling Factor for Poisson Equation
OH0=Kw/H0;


%% Create Main Matrix

% Helper vectors for defining the lhs matrix Ax=b
```

```
avec=zeros(nx-1,1);
bvec=zeros(nx-1,1);
cvec=zeros(nx-1,1);

% Matrix for solving the Poisson Equation
Amatrix=zeros(nx-1,nx-1);

for ii=2:nx-1
    iix=ii-1;
    dxb=dx(ii-1);
    dxf=dx(ii);
    dxavg=(dxb+dxf)/2;
    eb=(exx(ii)+exx(ii-1))/2;
    ef=(exx(ii+1)+exx(ii))/2;

    avec(iix)=eb/(dxavg*dxb);
    bvec(iix)=-1/dxavg*(ef/dxf+eb/dxb);
    cvec(iix)=ef/(dxavg*dxf);

end

avec(end)=exx(end-1)/dx(end)^2;
bvec(end)=-exx(end-1)/dx(end)^2;

for iix=2:nx-2

   Amatrix(iix,iix)=bvec(iix);
   Amatrix(iix,iix-1)=avec(iix);
   Amatrix(iix,iix+1)=cvec(iix);
end

Amatrix(1,1)=bvec(1);
Amatrix(1,2)=cvec(1);
Amatrix(end,end-1)=avec(end);
Amatrix(end,end)=bvec(end);

spAmatrix=sparse(Amatrix);

%%
% For Equilibrium Solution of Non-Linear Poisson Equation

% Normalize The Charges by the Sodium Ion Concentration

continue_tag=1;

num_iterations=1;
while continue_tag
% num_iterations
num_iterations=num_iterations+1;
exp_npot=exp(-psi_old(2:nx));
exp_pot=exp(psi_old(2:nx));
cosh_pot=(exp_pot+exp_npot)/2;
sinh_pot=(exp_pot-exp_npot)/2;

Hplus=H0.*exp_npot;
OHminus=OH0.*exp_pot;

% dpsi_Nf_coeff=Na_cap(2:nx).*Ka_vec(2:nx).^2.*exp_npot./(Ka_vec(2:nx)+H0.*exp_npot).^2;   %
    Previous Mistake

% Defining Vectors for the Derivative of rho with respect to psi
dNa1_dpsi=-Na1_cap(2:nx).*Ka1_vec(2:nx).*Hplus./(Ka1_vec(2:nx)+Hplus).^2;   % (Corrected on
    4/11/2015) (inclusive of the charge)
dNa2_dpsi=-Na1_cap(2:nx).*Ka2_vec(2:nx).*Hplus./(Ka2_vec(2:nx)+Hplus).^2;   % (Corrected on
    4/11/2015) (inclusive of the charge)


dNb_dpsi=-Nb_cap(2:nx).*Kb_vec(2:nx).*Hplus./(Kb_vec(2:nx)+Hplus).^2;  % (inclusive of the charge)

drhoM_dpsi=-alpha*(2*cosh_pot+OHminus/Na0+Hplus/Na0);
drhoF_dpsi=alpha*(dNa1_dpsi+dNa2_dpsi+dNb_dpsi);
drho_dpsi=drhoM_dpsi+drhoF_dpsi;

spWmatrix=sparse(diag(drho_dpsi));

% Defining vectors for calculation of net charge density at each iteration
N1_anionic=Na1_cap(2:nx).*Ka1_vec(2:nx)./(Ka1_vec(2:nx)+Hplus);    % Number density of the anionic
    groups (normalized with respect to salt concentration)
N2_anionic=Na2_cap(2:nx).*Ka2_vec(2:nx)./(Ka2_vec(2:nx)+Hplus);    % Number density of the anionic
    groups (normalized with respect to salt concentration)


N_cationic=Nb_cap(2:nx)-Nb_cap(2:nx).*Kb_vec(2:nx)./(Kb_vec(2:nx)+Hplus); % Number density of the
    cationic groups (normalized with respect to salt concentration)

Nfixed=N_cationic-N1_anionic-N2_anionic; % Charge density of the fixed groups (normalized with
    respect to the salt concentration)

rho_fixed=alpha*Nfixed;
```

```
rho_mobile=alpha*(-2*sinh_pot+Hplus/Na0-OHminus/Na0);
rho_total=rho_mobile+rho_fixed;


rhs_vector=-spAmatrix*psi_old(2:nx)-rho_total;

% rhs_vector=-spAmatrix*psi_old(2:nx)+alpha*(2*sinh_pot+OH0/Na0*exp_pot-H0/Na0*exp_npot+Nfixed);



rhs_vector(1)=rhs_vector(1)-avec(1)*y_bc;
rhs_vector(end)=rhs_vector(end)-dydx_bc/dx(end);


spModAmatrix=spAmatrix+spWmatrix;

dpsi_new=[y_bc; spModAmatrix\rhs_vector];

continue_tag=norm(dpsi_new)/nx>tolerance;

if continue_tag
    psi_old=psi_old+dpsi_new;
else
    psi_solution=psi_old+dpsi_new;
end
%     psi_old(end)

end


function psi_solution=SolvePoissonEquationNonEquilibrium(x,psi_guess,exx,rho_param)

% Function to solve for non-equilibrium Poisson Equation

x=x(:);
exx=exx(:);
psi_old=psi_guess(:);

x0_Ld=rho_param.x0_Ld;
tolerance=rho_param.tolerance;

% Boundary Conditions for x=x1 (dirichlet) anx x=xk (neumann)
y_bc=rho_param.dpsi;
dydx_bc=rho_param.ddpsi_dx;

Na_bc=rho_param.Na_bc;

Hplus=rho_param.Hplus(:);
Kw=rho_param.Kw;

Nanionic1_vec=rho_param.Nanionic1_vec(:);
Nanionic2_vec=rho_param.Nanionic2_vec(:);

Ncationic_vec=rho_param.Ncationic_vec(:);

Ka1_vec=rho_param.Ka1_vec(:);
Ka2_vec=rho_param.Ka2_vec(:);

Kb_vec=rho_param.Kb_vec(:);




nx=length(x);
dx=diff(x);

OHminus=Kw./Hplus;

Nanionic1_cap=Nanionic1_vec./Na_bc;
Nanionic2_cap=Nanionic2_vec./Na_bc;

Ncationic_cap=Ncationic_vec./Na_bc;


alpha=(x0_Ld)^2.*Na_bc;

%%
% Helper vectors for defining the lhs matrix Ax=b

avec=zeros(nx-1,1);
bvec=zeros(nx-1,1);
cvec=zeros(nx-1,1);

% Matrix for solving the Poisson Equation

Amatrix=zeros(nx-1,nx-1);


for ii=2:nx-1
```

```
    iix=ii-1;
    dxb=dx(ii-1);
    dxf=dx(ii);
    dxavg=(dxb+dxf)/2;
    eb=(exx(ii)+exx(ii-1))/2;
    ef=(exx(ii+1)+exx(ii))/2;
    avec(iix)=eb/(dxavg*dxb);
    bvec(iix)=-1/dxavg*(ef/dxf+eb/dxb);
    cvec(iix)=ef/(dxavg*dxf);
end

avec(end)=exx(end-1)/dx(end)^2;
bvec(end)=-exx(end-1)/dx(end)^2;

for iix=2:nx-2

   Amatrix(iix,iix)=bvec(iix);
   Amatrix(iix,iix-1)=avec(iix);
   Amatrix(iix,iix+1)=cvec(iix);
end

Amatrix(1,1)=bvec(1);
Amatrix(1,2)=cvec(1);
Amatrix(end,end-1)=avec(end);
Amatrix(end,end)=bvec(end);

spAmatrix=sparse(Amatrix);
%%

% For Quasi-Equilibrium Solution of Non-Linear Poisson Equation


N1_anionic=Nanionic1_cap.*Ka1_vec./(Ka1_vec+Hplus);
N2_anionic=Nanionic2_cap.*Ka2_vec./(Ka2_vec+Hplus);

N_cationic=Ncationic_cap-Ncationic_cap.*Kb_vec./(Kb_vec+Hplus);


N_fixed=Hplus/Na_bc-OHminus/Na_bc+N_cationic-N1_anionic-N2_anionic; % Fixed Positive Charge
    Density

continue_tag=1;

num_iterations=1;
while continue_tag

    num_iterations=num_iterations+1;
    exp_npot=exp(-psi_old(2:nx));
    exp_pot=exp(psi_old(2:nx));
    cosh_pot=(exp_pot+exp_npot)/2;
    sinh_pot=(exp_pot-exp_npot)/2;


    drho_dpsi=-alpha*(2*cosh_pot);
    spWmatrix=sparse(diag(drho_dpsi));


    rho_mobile=-alpha*(2*sinh_pot);
    rho_fixed=alpha*N_fixed(2:nx);

    rho_total=rho_mobile+rho_fixed;
    rhs_vector=-spAmatrix*psi_old(2:nx)-rho_total;

    rhs_vector(1)=rhs_vector(1)-avec(1)*y_bc;
    rhs_vector(end)=rhs_vector(end)-dydx_bc/dx(end);

    spModAmatrix=spAmatrix+spWmatrix;


    dpsi_new=[y_bc; spModAmatrix\rhs_vector];

    continue_tag=norm(dpsi_new)/nx>tolerance;

    if continue_tag
       psi_old=psi_old+dpsi_new;
    else
       psi_solution=psi_old+dpsi_new;
    end
%    psi_old(end)

end


function [spAmatrix,yvector]=CreateJacobianMatrix_Buffer(Efield,D_eff,mu_eff,Carr,dx,dtj,
    charge_type,bc)

% Function to calculate the Jacobian Matrix
nx=length(dx)+1;
RHSmatrix=zeros(nx-1);
```

```
yvector=zeros(nx-1,1);

Rarr=zeros(nx-1,1);
Sarr=zeros(nx-1,1);
Tarr=zeros(nx-1,1);

muavg=(mu_eff(1:nx-1)+mu_eff(2:nx))/2;
Davg=(D_eff(1:nx-1)+D_eff(2:nx))/2;
rmat=charge_type*dx.*Efield.*(muavg./Davg);
bpi=bernoulli_function(rmat);
bmpi=bernoulli_function(-rmat);

Cmatrix=diag(Carr(2:nx));


bc_n=bc.n;
bc_J=bc.dn_dx;

% S2 T2 .......
% R3 S3 T3 ....
% ..............
% ... Rkm1 Skm1

for ii=2:nx

    iix=ii-1;

    if ii~=nx
      dxf=dx(ii);
    else
      dxf=dx(nx-1);
    end

    dxb=dx(ii-1);

    dxavg=(dxf+dxb)/2;

    dx2f=dxavg*dxf;
    dx2b=dxavg*dxb;


    bb_pos=bpi(ii-1);
    bb_neg=bmpi(ii-1);


    if ii~=nx
        bf_pos=bpi(ii);
        bf_neg=bmpi(ii);
        Df=Davg(ii);
    end

    Db=Davg(ii-1);

    if ii~=nx

        Rarr(iix)=-(dtj/dx2b)*Db*bb_neg;
        Sarr(iix)=Db*bb_pos*(dtj/dx2b)+Df*bf_neg*(dtj/dx2f);
        Tarr(iix)=-(dtj/dx2f)*Df*bf_pos;

    elseif ii==nx
        Rarr(iix)=-Db*bb_neg*(dtj/dxb^2);
        Sarr(iix)=Db*bb_pos*(dtj/dxb^2);
    end

end

% S2 R2 .......
% T3 S3 R3 ....
% ..............
% ... Tkm1 Skm1

RHSmatrix(1,1)= Sarr(1);
RHSmatrix(1,2)=Tarr(1);

RHSmatrix(nx-1,nx-2)=Rarr(nx-1);
RHSmatrix(nx-1,nx-1)=Sarr(nx-1);

for ii=2:nx-2
    RHSmatrix(ii,ii-1)=Rarr(ii);
    RHSmatrix(ii,ii)=Sarr(ii);
    RHSmatrix(ii,ii+1)=Tarr(ii);
end

spAmatrix=sparse(RHSmatrix+Cmatrix);

yvector(1)=-Rarr(1)*bc_n; % For the dirichlet boundary condition at x(1)
yvector(nx-1)=-bc_J*dtj/dx(nx-1); % For the neumann boundary condition at x(end+1/2)

check_nan=max(isnan(RHSmatrix(:)));
```

```
if check_nan
sprintf('Nan_Value_Found');
end


function berno=bernoulli_function(x)

berno=zeros(size(x));
for i=1:length(x)
    if abs(x(i))<1e-15
        berno(i)=1/(1+x(i)/2+x(i)^2/6+x(i)^3/24);
    else
        berno(i)=x(i)/(exp(x(i))-1);
    end
end
```

A.5.2 Analytical Model

```
% Code written by Piyush Dak, Purdue University, 2016 (Advisor: Prof. Muhammad A. Alam)

% Code to Determine Osmotic Pressure for a Hydrogel based pH Sensor
% as a function of the solution pH

clc; clear; close all
%% Fundamental Constants

kB=1.3806488e-23;           % Boltzmann constant (m^2 kg sec^-2 K-1)
Navo=6.023e23;              % Avagadro's Number

%% Known Constants

Kw_mM=1e-8;                 % Ionic product of water in mM at room temperature
Temperature_degrees=25;     % Temperature in Degree Centigrade

%% Constants for a particular Hydrogel
pKh=7.4;                    % pKa of the acidic/basic group
Nf_mM=50;                   % Ionizable group density in mM

%% Opearting Conditions

cs_mM=50;                   % Salt concentration in mM
pHarr=(4:0.2:10);           % pH array

%%

T=273+Temperature_degrees;  % Temperature in Kelvins
pressure_scale=kB*T*Navo;   % In Pascal /mM


for i=1:length(pHarr)

        pH=pHarr(i);

        Kh_mM=10^-pKh*1e3;
        H_mM=10^-pH*1e3;

        c3=H_mM^2/Kh_mM*(cs_mM+H_mM);
        c2=H_mM*(cs_mM+H_mM);
        c1=-H_mM*((H_mM*cs_mM+Kw_mM)/Kh_mM+Nf_mM);
        c0=-((H_mM*cs_mM)+Kw_mM);

        c1=c1+Nf_mM*H_mM;
        c2=c2+Nf_mM*H_mM^2/Kh_mM;

        coeff_mat=[c3 c2 c1 c0];
        roots_equation=roots(coeff_mat);
        lambda=max(roots_equation);
        spressure_Hcontribution=(lambda*H_mM+Kw_mM/(lambda*H_mM))-(H_mM+Kw_mM/H_mM);
        spressure=(lambda+1/lambda-2)*cs_mM+spressure_Hcontribution;

        spressure_arr(i)=spressure;
end

% Final pressure value in Pascals
pressure_arr=spressure_arr*pressure_scale;


%%
% Plotting Osmotic Pressure vs. pH

figure('Units','inches','Position',[3,1,6.6,4.4],'DefaultAxesLineWidth',2,'DefaultAxesFontSize'
    ,24,'DefaultAxesFontName','Arial',...
    'DefaultTextFontSize',24,'DefaultLineLineWidth',4,'DefaultAxesTickLength',[0.015,0.03],'
        PaperPositionMode','auto');
plot(pHarr, pressure_arr/1e3,'b');
```

```
xlabel('pH');
ylabel('Pressure (kPa)');
xlim([4 10]);


%% The following references provide more detail on the code above.

% [1]. Numerical and Analytical Modeling to Determine Performance Trade-offs in Hydrogel based pH
    Sensors
%     P. Dak and M. A. Alam
%     IEEE Transactions on Electron Devices, 63, 6 (2016)
%
% [2]. A Predictive Model for Hydrogel Based Wireless Implantable Bio-Chemical Sensors
%     P. Dak and M. A. Alam
%     Device Research Conference (DRC) (June 21st - June 24th, 2015, Columbus, OH)
```

A.6 Compact Model for pH-FET Sensor

A.6.1 DC Model:

Verilog-A Code:

```
`include "constants.vams"
`include "disciplines.vams"

//define relative permittivity of water
`define RP_EPSw 80
//conversion constant from moles/liter to #/m^3
`define N_AVG 6e26

module pH_robust_model_1_0_1(lgate,interface,pHnode);

 input pHnode;
 output lgate,interface;                // lgate is connected to the reference electrode,
     interface is in contact with the surface
 electrical lgate,interface,pHnode,nodeint1, nodeint2;

 branch (nodeint1,nodeint2) BRseries;
 branch (nodeint2,interface) BCdl;
 branch (nodeint2,interface) BRart;

//Convention for Ka, Kb: Ka=[A-OH][Hs+]/([AOH2+], Kb=[AO-][Hs+]/[AOH]
//NOH_SI denotes the charge density of the surface groups: NOH_SI=[AOH]+[AO-]+[AOH2+]
// pH=-log10[H+], pKa=-log10[Ka], pKb=-log10[Kb]

//Parameters characterizing electrolyte and electrolyte-oxide interface
parameter real version          =   1.00;                                   // pHsensor surface
    potential model version = 1.0.1
parameter real sternmod         =   1       from [0:1];                     // Parameter to turn on/
    off the stern model. 0 means that the model is off.
parameter real pKa              =   -2.0    from (-inf:inf);                // pKa of the acidic [A-
    OH2+] surface group
parameter real pKb              =   6.0     from (-inf:inf);                // pKb of the basic [A-OH
    ] surface group
parameter real i0               =   0.1     from [0.0:inf];                 // ionic concentration in
     moles/liter
parameter real Cstern           =   0.2     from (0.0:inf];                 // Stern capacitance in F
    /m^2
parameter real NOH              =   5e14    from (0.0:inf);                 // Number density of
    surface OH groups in cm^-2
parameter real Rart             =   1e50     from (0.0:inf);
parameter real mup              =   5.1e-8  from (0:inf);       //m^2/Vs      // Mobility of Na+
     ions in water
parameter real mun              =   7.6e-8  from (0:inf);       //m^2/Vs      // Mobility of Cl-
     ions in water
parameter real AFET             =   1.0e-12  from (0:inf);       //m^2          Area of Field
    effect transistor

parameter real noise_model     =   0        from [0:1];


real pH;
real ew;
real n0;
real pzc, deltapK;
real NOH_SI;
real c, deltapH;
real Rseries, sigma, Cdl, Cdiff, Cdiff0, COH;
```

```
//parameters to be used for calculation
real Q0dl, Q0, Qratio, dpH;
real vfi, tanhvfi, norm_QOH;
real Vbias;

analog begin
        pzc             =       (pKa+pKb)/2.0;
        deltapK         =       pKb-pKa;
        pH              =       V(pHnode);
        deltapH         =       pH-pzc;
        c               =       limexp(`M_LN10*deltapK/2.0);
        Q0              =       2*`P_Q*NOH_SI;
        dpH             =       `M_LN10*deltapH;
        NOH_SI          =       NOH * 1e4;                              // conversion from cm^-2
            to m^-2
        n0              =       `N_AVG*i0;                              // conversion to #/m^3  (
            ionic concentration)
        ew              =       `RP_EPSw*`P_EPS0;                       // permittivity of the
            electrolyte, in units of F/m
        Q0dl            =       sqrt(8.0 * ew * $vt * `P_Q * n0);       // prefactor for the
            double layer charge (in units of columb/cm^2)
        sigma           =       `P_Q*n0*(mup+mun);                      // Conductivity of the
            solution (for Rseries calculation)
        Qratio          =       Q0/Q0dl;
        vfi             =       V(nodeint1,lgate);
        tanhvfi         =       tanh(vfi/$vt+dpH);
        norm_QOH        =       tanhvfi/ (2.0+c*sqrt(1.0-tanhvfi*tanhvfi));

    if(sternmod == 0) begin
            V(nodeint1,lgate) <+ 2*$vt*asinh(-Qratio*norm_QOH);       // Refer Section 3.2.1 of
                the manual
        end
    else begin
            V(nodeint1,lgate) <+ 2*$vt*asinh(-Qratio*norm_QOH)-Q0/Cstern*norm_QOH;     // Refer
                Section 3.2.2 of the manual
        end

        Vbias           =       V(nodeint1,lgate);
        Cdiff0          =       AFET*sqrt(2.0*`P_Q*ew*n0/$vt);
        Cdiff           =       Cdiff0*cosh(Vbias/(2.0*$vt));
        Cdl             =       1.0/(1.0/Cdiff+1.0/(Cstern*AFET));
        COH             =       AFET*(Q0/$vt)*(c*cosh(vfi/$vt+dpH)+2.0)/pow((c+2.0*cosh(vfi/$vt+
            dpH)),2.0);
        Rseries         =       (1.0/sigma)*sqrt(`M_PI/AFET);

        I(BRart)        <+      V(BRart)/Rart;
        I(BCdl)         <+      (Cdl+COH)*ddt(V(BCdl));
        V(BRseries)     <+      I(BRseries)*Rseries;
    if(noise_model == 1)  begin
        V(BRseries)     <+      white_noise(4*`P_K*$temperature*Rseries,"thermal");

    end

    end

endmodule


//Noiseless Resistor
`include "discipline.vams"

module resistor(p,n);
       parameter real r=0;  //resistance (Ohms)
       inout p,n;
       electrical p,n;

       analog begin
          V(p,n) <+ r*I(p,n);
       end
endmodule
```

Spice Code:

Command: hspice filename.sp

```
* SPICE Analysis

.hdl "../pH_robust_model_1_0_1.va"
.hdl "../resistor.va"

.option dccap=1
```

```
.option measform=3
.option post

.include "model_130nm.par"


.param vd = 0.1
.param vs = 0.0
.param vfg = 1.0
.param vbg = 0
.param pH = 4.0
.param length=1u width=100u
.param Afet='length*width'
.param ionic_concentration=1e-3
.param noise_mod=1

VpH pHnode 0 pH
Vdd rnode 0 vd
Vsource source 0 vs
Vlgate lgate 0 vfg AC 1 0
Vbgate bgate 0 vbg

X1 lgate fgate pHnode pH_robust_model_1_0_1 AFET=Afet i0=ionic_concentration noise_model=noise_mod
M1 drain fgate source bgate nfet L=length W=width
X2 rnode drain resistor r=1

.DC VpH 2.0 10.0 0.001

.END
```

A.6.2 Transient Model:

Verilog-A Code:

```
`include "constants.vams"
`include "disciplines.vams"

//define relative permittivity of water
`define RP_EPSw 80
//conversion constant from moles/liter to #/m^3
`define N_AVG 6e26

module pH_robust_model_1_0_2(n1,n4,pHnode);

 input pHnode;
 output n1,n4;                  // n1 is connected to the reference electrode, n5 is in contact with
       the surface
 electrical pHnode, n1,n2,n3,n4;

 branch (n1,n2) BRseries;
 branch (n2,n3) BCdl;
 branch (n2,n4) BCoh;
 branch (n3,n4) BCstern;


//Convention for Ka, Kb: Ka=[A-OH][Hs+]/([AOH2+], Kb=[AO-][Hs+]/[AOH]
//NOH_SI denotes the charge density of the surface groups: NOH_SI=[AOH]+[AO-]+[AOH2+]
// pH=-log10[H+], pKa=-log10[Ka], pKb=-log10[Kb]

//Parameters characterizing electrolyte and electrolyte-oxide n5
parameter real version          =   1.01;                                   // pHsensor surface
     potential model version = 1.0.1
parameter real sternmod         =   1       from [0:1];                     // Parameter to turn on/
     off the stern model. 0 means that the model is off.
parameter real pKa              =   -2.0    from (-inf:inf);                // pKa of the acidic [A-
     OH2+] surface group
parameter real pKb              =   6.0     from (-inf:inf);                // pKb of the basic [A-OH
     ] surface group
parameter real i0               =   0.1     from [0.0:inf];                 // ionic concentration in
      moles/liter
parameter real Cstern           =   0.2     from (0.0:inf];                 // Stern capacitance in F
     /m^2
parameter real NOH              =   5e14    from [0.0:inf);                 // Number density of
     surface OH groups in cm^-2
//parameter real Rseries          =   0     from   [0.0:inf);
parameter real mup              =   5.1e-8  from (0:inf);       //m^2/Vs        // Mobility of H+
     ions in water
parameter real mun              =   7.6e-8  from (0:inf);       //m^2/Vs        // Mobility of OH-
      ions in water
```

```
parameter real AFET             =    1.0e-12  from (0:inf);        //m^2            Area of Field
     effect transistor

real pH;
real ew;
real n0;
real pzc, deltapK;
real NOH_SI;
real c, deltapH;
real sigma, Rseries;
real Q0dl, Q0oh, dpH;
real voh, tanhvoh, norm_QOH;
real vdl, Qoh, Qdl;
real Qstern;
real Qtotal;

analog begin
        pzc             =         (pKa+pKb)/2.0;
//pHpzc is the point of zero charge i.e. pH at which the surface charge is zero assuming that
     surface potential is zero
        deltapK         =         pKb-pKa;
        pH              =         V(pHnode);
        deltapH         =         pH-pzc;
        c               =         limexp(`M_LN10*deltapK/2.0);
        ew              =         `RP_EPSw*`P_EPS0;                                    // permittivity
             of the electrolyte, in units of F/m
        n0              =         `N_AVG*i0;                                         // conversion to #/
             m^3  (ionic concentration)
        NOH_SI          =          NOH * 1e4;                                      // conversion from cm^-2
              to m^-2

        Q0oh              =         2*`P_Q*NOH_SI;
        Q0dl            =         sqrt(8.0 * ew * $vt * `P_Q * n0);        // prefactor for the
             double layer charge (in units of columb/cm^2)

        dpH             =         `M_LN10*deltapH;
        sigma           =         `P_Q*n0*(mup+mun);                                  // Conductivity of the
              solution (for Rseries calculation)

        voh             =        -V(BCoh);
        vdl             =        -V(BCdl);
        tanhvoh         =         tanh(voh/$vt+dpH);
        norm_QOH        =         tanhvoh/ (2.0+c*sqrt(1.0-tanhvoh*tanhvoh));

        Qoh             =         -Q0oh*norm_QOH;
        Qdl             =         -Q0dl*(limexp(vdl/(2.0*$vt))-limexp(-vdl/(2.0*$vt)))/2.0;
        Qstern          =         Cstern*V(BCstern);
        Qtotal          =         Qoh+Qdl;

        Rseries         =          (1.0/sigma)*sqrt(`M_PI/AFET);

        I(BCdl)       <+        AFET*ddt(Qdl);
        //I(BCstern)        <+     AFET*ddt(Qstern);
        V(BRseries)   <+         I(BRseries)*Rseries;
        I(BCoh)       <+        AFET*ddt(Qoh);
        V(BCstern)    <+       idt(I(BCstern))/(AFET*Cstern);

        $strobe("Print pH: %0.2g V(n1,n4): %.4g, V(n2,n3): %.4g, V(n3,n4): %0.4g,  Qdl: %0.4g, Qoh
             : %0.4g, Qstern: %0.4g, Qtotal: %0.4g",pH, V(n1,n4), V(n2,n3),V(n3,n4), Qdl, Qoh,
             Qstern,Qtotal);

    end

endmodule
```

Spice Code:

Command: hspice filename.sp

```
* SPICE Analysis

.hdl "../pH_robust_model_1_0_2.va"
.hdl "../resistor.va"

.option dccap=1 RELTOL=1e-15 RELQ=1e-3 RUNVL=6 MEASFORM=3 DVDT=2 DELMAX=1m

.include "../130nm_bulk_modified.par"

.SET_SAMPLE_TIME twindow 0 2.0 period 0.01

.param vd = 1.0
.param vs = 0.0
```

```
.param vfg = 1.0
.param vbg = 0
.param vpH = 4.0
.param Length=10u
.param Width=100u

.param AFET='Length*Width'

VpH pHnode 0 pwl(
+ 0 2.0
+ 1 2.0
+ 2 4.0
+ 3 4.0
+ 4 2.0
+ 5 2.0
+ 6 10.0
+ 7 10.0
+ 8 2.0)

Vdd rnode 0 vd
Vsource source 0 vs
Vlgate lgate 0 pwl(
+ 0 0.0
+ 1 0.0
+ 2 0.0
+ 3 1.0
+ 4 1.0
+ 5 0.0
+ 6 0.0
+ 7 1.0
+ 8 1.0
+) AC 1 0

Vbgate bgate 0 vbg

X1 lgate fgate pHnode pH_robust_model_1_0_2 AFET=AFET NOH=5e14
M1 drain fgate source bgate nfet L=Length W=Width
X2 rnode drain resistor r=1


.tran 0.01m 10.0

.option post

.ALTER
Vlgate lgate 0 pwl(0 0.0 1 0.0 2 0.0 3 1.0 4 1.0) AC 1 0

.END
```

VITA

VITA

Piyush Dak received his B.Tech. in Engineering Physics and M.Tech. in Engineering Physics with specialization in nanoscience from Indian Institute of Technology Bombay, Mumbai, India in June 2010. After working as a Software Engineer in OnMobile Global Ltd. for 6 months, he joined Prof. Muhammad Ashraful Alam's research group at Purdue University, West Lafayette in Jan. 2011 to pursue his Ph.D. degree. His research interests include modeling, simulation and design considerations of nanoscale electronic devices for logic, memory and health-care applications.